Inhibition of Bcl-3 as a novel therapeutic approach for metastatic breast cancer

Jitka Soukupová

Thesis submitted for the award of PhD,
14th June 2013

Under the supervision of Dr. Richard Clarkson
School of Biosciences, Cardiff University

Co-supervised by Dr. Andrea Brancale and
Dr. Andrew Westwell
School of Pharmacy and Pharmaceutical Sciences, Cardiff University

DECLARATION

This work has not previously been accepted in substance for any degree and is not concurrently submitted in candidature for any degree.

Signed …… (candidate) Date ……

STATEMENT 1

This thesis is being submitted in partial fulfilment of the requirements for the degree of PhD.

Signed …… (candidate) Date ……

STATEMENT 2

This thesis is the result of my own independent work/investigation, except where otherwise stated. Other sources are acknowledged by explicit references.

Signed …… (candidate) Date ……

STATEMENT 3

I hereby give consent for my thesis, if accepted, to be available for photocopying and for inter-library loan, and for the title and summary to be made available to outside organisations.

Signed …… (candidate) Date ……

STATEMENT 4: PREVIOUSLY APPROVED BAR ON ACCESS

I hereby give consent for my thesis, if accepted, to be available for photocopying and for inter-library loans **after expiry of a bar on access previously approved by the Graduate Development Committee.**

Signed …… (candidate) Date ……

Abstract

B-Cell Lymphoma 3 (Bcl-3) is a proto-oncogene modulating the nuclear factor κB (NF-κB) signalling pathway, which had been first identified at the site of a t (14,19) translocation in B-cell chronic lymphocytic leukemia. Deregulated Bcl-3 expression has been reported in various tumours and in breast tumours Bcl-3 was found to be significantly elevated compared to the normal adjacent tissue. Activated NF-κB signalling is detected in 86% of ER-negative and HER2+ breast tumours. The currently used monoclonal antibody against HER2 (trastuzumab), produces remissions in 10-15 % of HER2+ breast cancers, thus the identification of novel therapeutic targets is essential.

Previous *in vivo* studies used ErbB2 (MMTV/neu) mouse models deficient in Bcl-3 to understand the role and underlying mechanism of Bcl-3 in mammary tumour formation and progression. Even though Bcl-3 deficiency *in vivo* did not affect the primary tumor growth, the occurrence of developed lung metastases was reduced by 40%. Despite these effects on tumour progression, no effect on normal mammary gland function was observed. Based on the this evidence, the inhibition of Bcl-3 seems a promising therapeutic strategy, especially for HER2+ breast cancers, mainly in the prevention of secondary-tumour seeding and spread at distal sites.

Using a Bcl-3 binding mutant we have shown that Bcl-3 function can be inhibited by disruption of binding to its cognate partners, p50 and p52 from the NF-κB family. Using molecular modelling we constructed a model of the Bcl-3-p50 complex, identified a novel protein-protein interaction domain and performed initial virtual screening for potential small molecule inhibitors. Candidate compounds were evaluated in human tumorigenic (MDA-MB-231) and non-tumorigenic cell lines (HEK-293) in cell based assays determining the effect on disruption of Bcl-3—p50 binding, as well as the change in NF-κB activity and migration ability. A lead compound was identified with low nM activities in all three cell based assays. Analogues of the lead compound were designed and synthesized in order to evaluate the structure-activity relationships (SAR). Important moieties in the structure were identified and the structural analogue 15f had almost 10 fold increase in the activity over the lead compound. More structural analogues will be analysed in the near future to further explore the SAR of the lead compound. Meanwhile *in vivo* xenografts experiments are evaluating the efficacy of the lead compound and its analogue 15f on the ability to suppress the spread and growth of secondary tumours.

Acknowledgements

Firstly I would like to thank to my supervisor, Dr. Richard Clarkson. He has provided me with valuable support and guidance throughout the project. His critical views on my work helped me to quickly improve not only my understanding of the project and techniques, but also the presentation of my work. He was a great support when I was writing my thesis by giving me critical comments on my work in a short time. Dr. Alison Wakefield was of a great help in understanding the background of the project and providing me with any materials when required. My acknowledgments also go to previous and current members of the RWEC lab, Rhiannon French, Olivia Hayward and Dr. James Knight. Dr. Syn Kok Yeo was always willing to help and provided me with a packaged p52WT lentivirus construct; Dr. Luke Piggott helped me with FACS analysis. Final year project student, Steffan Seal and a master project student, William Yang, helped with immunohistochemistry analysis of xenograft study using MDA-MB 231 cells.

I am really grateful to Alain Chariot for providing me with a Bcl-3 WT and Bcl-3 ANK M123 construct.

My gratitude also extents to my supervisors in the School of Pharmacy and Pharmaceutical Sciences. Dr. Andrea Brancale gave me many advices and support when I was performing molecular modelling studies and his lab was always very friendly and welcoming. Dr. Andrew Westwell helped me with organic synthesis and with the understanding of NMR spectra. His recommendation on this PhD project and his willingness to always help is much appreciated. I would also like to thank him for giving me the opportunity to attend PAMM conferences and to meet interesting people from the field. Members of his lab, mainly Jan-Philip Meyer and Winnie Velangparackel were of a great support when I was attempting the chemistry. Final year project student, Sunaiya Varsani, helped me with the synthesis of hydrochloric salt of the lead compound and novel di- and tri- substituted structural analogues of the lead compound.

I am also grateful to President's research scholarship for sponsoring my PhD and the opportunity to work under the Drug Discovery and Development Scheme. I would also like to thank all the members of this scheme, Áine Flynn, Brendan O Ruadhain, Alan Stone, Blanka Gonczy and Athanasios Anthopoulos for

being so friendly and supportive, Prof. Chris McGuigan for organising seminars and lab visits during this 3 years and Dr. Richard Clarkson for organising a visit to GE Heathcare.

I would like to thank BACR, EACR and IMPAKT for sponsoring me to attend various conferences.

My gratitude also goes to my friends in Cardiff that supported me through the project and also in my writing up period, mainly Antoaneta Georgieva, Charmmy Ka Lio, Shun Ming Yuen and Golnaz Rafiei. And last not least, the support from Spain from Diego López Valera and from my family in the Czech Republic.

List of abbreviations

AKT1	Ak strain transforming 1
ALCLs	Anaplastic large-cell lymphomas
ANK	Ankyrin repeat
AP	Alkaline phosphatase
AP-1	Activator protein-1
BARD1	BRCA1- associated RING domain protein 1
Bcl-2	B-cell Lymphoma 2
Bcl-3	B-cell Lymphoma 3
Bcl-X_L	B-cell Lymphoma-extra large
bCSCs	Breast cancer stem cells
BRCA1	Breast cancer susceptibility gene 1
BSA	Bovine serum albumin
BTC	Betacellulin
Cc3	Cleaved caspase 3
cDNA	complementary deoxyribonucleic acid
CHL	Classical Hodgkin lymphoma
c-FLIP	Cellular FLICE inhibitory protein
cIAP	Cellular inhibitor of apoptosis
CtBP	C-terminal binding protein
CXCR4	C-X-C chemokine receptor type 4
CYLD	Cylindromatosis/turban tumour syndrome gene
DCM	Dichloromethan
DD	Dimerisation domain
dH_20	Distilled H_2O
DHMEQ	Dehydroxymethylepoxyquinomicin
DMEM	Dulbecco's modified Eagle's medium
DMF	Dimethyl formamide
DMSO	Dimethyl sulfoxide
DNA	Deoxyribonucleoside acid
dNTPs	Deoxyribonucleoside triphosphates
ECL	Enhanced chemiluminescence
EC_{50}	Half maximal effective concentration
E.coli	*Escherichia coli*
ECM	Extracellular matrix
EDTA	Ethylene diamine tetraacetic acid
EGFR	Epidermal growth factor receptor
EGTA	Ethylene glycol tetraacetic acid
ELISA	Enzyme-linked immunosorbent assay
EMT	Epithelial-to-mesenchymal transition
EPG	Epigen
EPR	Epiregulin
ER	Oestrogen receptor
ErbB2	v-erb-b2 erythroblastic leukemia viral oncogene homolog 2
FACS	Fluorescence activated cell sorting
FBS	Foetal bovine serum
GATA3	GATA-binding protein 3

GFP	Green fluorescent protein
GRR	Glycine-rich regions
GSK3	Glycogen synthase kinase 3
HA-tag	Human influenza hemagglutinin protein tag
HDAC1	Histone deacetylase 1
Hdm2	Human double minute 2
HER2	Human epidermal growth factor receptor 2
HRP	Horseradish peroxidase
Hz	Hertz
IGF1R	Insulin-like growth factor 1 receptor
IGFBP	Insulin-like growth factor binding protein
IC_{50}	Half maximal inhibitory concentration
Ig	Immunoglobulin
IKK	Inhibitor of NF-κB Kinase subunit
IL	Interleukin
IR	Infrared light
IκB	Inhibitors of NF-κB
Jab1	c-Jun activation domain-binding protein 1
JAK-STAT	Janus kinase and signal transducer and activator of transcription
JNK1	c-Jun N-terminal kinase 1
LPS	Lipopolysaccharide
LZ	Leucine zipper
MAPK	Mitogen-activated protein kinase
MFUs	Mammosphere forming units
miRNAs	Micro-RNAs
MMPs	Matrix metalloproteinases
MMTV/neu	Mouse mammary tumour virus promoter driving neu oncogene
MOE	Molecular Operating Environment
Mp	melting point
mRNA	Messenger Ribonucleic acid
MS	Mass spectrometry
mTOR	Mammalian target of rapamycin
NEMO	NF-κB essential modifier
NF-κB	Nuclear factor binding to the intronic kappa-light-chain enhancer element in B cells
NIK	NF-κB inducing kinase
NLS	Nuclear localisation sequence
NRG	Neuregulin
NSAIDs	Non-steroid anti-inflammatory drugs
PARP	Poly ADP ribose polymerase
PBS	Phosphate buffered saline
PBS/T	Phosphate buffered saline/Tween
PCR	Polymerase chain reaction
PDB	Protein Data Bank
PEST	proline-, glutamic acid-, serine- and threonin- rich regions
PET	Polyethylene terephthalate
PgR	Progesteron receptor
PI3K	Phosphatidylinositol 3-kinase

pNPP	para-nitrophenylphosphate
PPIs	Protein-protein interactions
PSMB1	Proteasome subunit β type-1
PVDF	Polyvinylidene difluoride
QRT-PCR	Quantitative real-time polymerase chain reaction
RANK	Receptor activator of NF-κB
RANKL	Receptor activator of NF-κB ligand
RHD	Rel Homology Domain
RIPA	Radio-immunoprecipitation assay buffer
RLU	Relative light units
RMSD	Root mean square deviation
RNA	Ribonucleic acid
r.t.	room temperature
SDS	Sodium dodecyl sulphate
SDS-PAGE	Sodium dodecyl sulphate polyacrylamide gel electrophoresis
SEM	Standard error of the mean
SiRNA	Small interfering RNA
STAT	Signal transducer and activator of transcription
TAD	Transactivation domain
TAM	Tumour associated macrophages
TBS	Tris-buffered saline
TEMED	N'N'N'N' tetra methyl ethylene diamine
TGFα	transforming growth factor-α
TIMPs	Tissue inhibitors of metalloproteinases
TIP_{60}	60 kDa Tat-interactive protein
TLC	Thin layer chromatography
TNBC	Triple negative breast cancer
TNFα	Tumour necrosis factor-α
uPA	urokinase-type plasminogen activator
uPAR	urokinase-type plasminogen activator receptor
UV	Ultraviolet light
VEGF	Vascular endothelial growth factor
VEGFR	Vascular endothelial growth factor receptor
WT	Wild type

Table of contents

DECLARATION ..... **ii**

Abstract ..... **iii**

Acknowledgements ..... **iv**

List of abbreviations ..... **vi**

Table of contents ..... **ix**

Table of figures ..... **xviii**

Table of tables ..... **xx**

Table of schemes ..... **xxi**

1. General Introduction **2**

1.1 Breast cancer 2

1.1.1 Breast cancer development and metastatic progression 3

1.1.2 Heterogeneity of breast cancer 6

1.1.3 Classification of breast cancers based on expression patterns 6

1.1.3.1 Luminal subtypes 6

1.1.3.2 HER2 enriched subtype 7

1.1.3.3 The basal subtype 9

1.1.3.4 Claudin-low subtype 9

1.1.3.5 Normal breast-like subtype 10

1.1.4 Targeted therapies for breast cancer 11

1.1.4.1 HER2 targeted treatment 11

1.1.4.2 Targeting pathways downstream of HER2 receptor 12

1.1.4.3 EGFR targeted treatment 12

1.1.4.4 Targeting VEGFR 13

1.1.4.5 NF-κB signalling as a target 13

1.2 NF-κB signalling 14

1.2.1 NF-κB family members 14

1.2.2 IκB family members 14

1.2.3 NF-κB signalling pathways 17

1.2.3.1 Canonical (classical) pathway 17

1.2.3.2 Non-canonical (alternative) pathway 17

1.2.4 NF-κB and cancer development 19
1.2.5 NF-κB signalling in mammary gland 19
1.2.5.1 The role of NF-κB in established tumours 20
1.2.5.2 The role of NF-κB in metastatic progression 21
1.2.6 Inhibition of NF-κB signalling 21
1.2.6.1 Inhibition of the IKK complex 22
1.2.6.2 Proteasome inhibitors 22
1.2.6.3 Inhibition of phosphorylation, nuclear translocation and DNA binding of NF-κB heterodimers 22
1.2.6.4 Conclusion 23
1.3 B-cell Lymphoma 3 25
1.3.1 Introduction 25
1.3.2 Regulation of NF-κB signalling by Bcl-3 25
1.3.3 Regulation of Bcl-3 26
1.3.3.1 Transcriptional regulation 26
1.3.3.2 Phosphorylation and degradation 26
1.3.4 The role of Bcl-3 in immune responses 29
1.3.5 Bcl-3 and cancer 29
1.3.6 Bcl-3 and breast cancer 31
1.4 Project Aims 35
2. Materials and Methods 37
2.1 Cloning procedures 37
2.1.1 Amplification of DNA constructs 37
2.1.1.1 Transformation of *E. coli* with DNA 37
2.1.1.2 Isolation of DNA from bacterial cells 37
2.1.1.3 Restriction digest reactions 37
2.1.1.4 Agarose gel electrophoresis 38
2.1.2 Bcl-3 constructs 38
2.1.3 A p52 construct within a lentiviral vector 41
2.1.4 NF-κB Luciferase reporter plasmid 41
2.2 Cell culture maintenance and storage 41
2.2.1 Experimental cell lines 41
2.2.1.1 HEK-293 41
2.2.1.2 MDA-MB-231 42

2.2.1.3 SKBR3 42
2.2.1.4 ZR-75-1 42
2.2.1.5 MCF-10A 42
2.2.2 Maintenance of cell lines 43
2.2.3 Long term cell storage 44
2.2.4 Cell counting 44
2.3 Transfection and transduction of cells 45
2.3.1 Transient siRNA transfection 45
2.3.2 Transfection of cells with plasmid DNA 46
2.3.3 Generation of stable overexpressing clones 47
2.3.4 Lentiviral transduction of cell lines 47
2.3.5 Transfection of cells with reporter plasmids 47
2.4 Cell based assays 48
2.4.1 Cell Titre Blue viability assay 48
2.4.2 Cell count 48
2.4.3 Determination of caspase activity in cells 49
2.4.4 NF-κB luciferase reporter assay 49
2.4.5 Boyden chamber migration assay 50
2.4.5.1 Visualization of migrated cells 50
2.4.5.2 Mounting of membranes 51
2.4.5.3 Invasion index 51
2.4.6 Mammosphere assay 51
2.4.7 Flow cytometry 53
2.4.7.1 Cell cycle analysis 53
2.4.7.2 Live/dead analysis 54
2.4.7.3 GFP analysis 54
2.5 Protein analysis 54
2.5.1 Protein extraction from cells 54
2.5.1.1 Whole cell protein extraction under denaturing condition 54
2.5.1.2 Whole cell protein extraction under non-denaturing condition 55
2.5.2 Determination of protein concentrations 55
2.5.3 Western analysis 56
2.5.3.1 Preparation of protein samples 56
2.5.3.2 Casting of polyacrylamide gels 56
2.5.3.3 Gel electrophoresis 56

2.5.3.4 Transfer of proteins to PVDF membranes 57
2.5.3.5 Probing of membranes 57
2.5.3.6 Visualisation of protein bands 58
2.5.3.7 Stripping and reprobing of membranes 59
2.5.4 ELISA assay 59
2.5.4.1 Indirect and sandwich ELISA assay 60
2.6 RNA analysis 61
2.6.1 Isolation of RNA 61
2.6.2 Reverse transcription 61
2.6.3 Quantitative-real time-polymerase chain reaction (QRT-PCR) 62
2.6.3.1 Primer design 62
2.6.3.2 QRT-PCR reaction 62
2.6.3.3 Analysis of QRT-PCR data 63
2.7 Molecular modelling 64
2.8 Statistical analysis 64
2.8.1.1 Student's t-test 64
3. Biological Outcome of Bcl-3 Suppression in Human Cell Lines 66
3.1 Introduction 66
3.1 The outcome of Bcl-3 suppression in human breast cancer cell lines 67
3.1.1 Bcl-3 expression among human cell lines 67
3.1.2 Suppression of Bcl-3 decreases NF-κB activity in human cell lines 67
3.1.3 Suppression of Bcl-3 reduced the viability and proliferation capacity of breast cancer cell lines in adherent growth conditions 69
3.1.4 The effect of Bcl-3 deficiency on cell cycle 72
3.2 Generation and characterisation of Bcl-3 overexpressing clones 74
3.2.1 Generation of Bcl-3 WT and Bcl-3 binding mutants in MDA-MB-231 cells 74
3.2.1.1 The effect of Bcl-3 expression on NF-κB activity 75
3.2.1.2 The effect of Bcl-3 expression on cell viability and proliferation 77
3.2.1.3 The effect of Bcl-3 expression on cell cycle 77
3.2.1.4 The effect of Bcl-3 on cell motility and cell invasion 81
3.2.1.5 The effect of Bcl-3 expression on mammosphere forming potential 86
3.2.2 Generation of Bcl-3 WT and Bcl-3 binding mutants in HEK-293 cells 89
3.2.2.1 Effect of Bcl-3 expression on basal NF-κB activity in HEK-293 cells 91
3.2.2.2 Effect of Bcl-3 on cell viability and cell cycle in HEK-293 cells 91

3.2.3 Detection of Bcl-3-p50 binding 92
3.2.4 Overexpression of p52 WT in HEK-293 95
3.2.4.1 Effect of p52 expression on NF-κB basal activity 95
3.2.4.2 Effect of co-expression of Bcl-3 and p52 on cell viability 98
3.3 Discussion 100
3.3.1 The outcome of Bcl-3 suppression in human breast cancer cell lines 100
3.3.2 Modelling disruption of Bcl-3-p50 binding in MDA-MB-231 cell line 101
3.3.3 Overexpression of Bcl-3 WT in MDA-MB-231 cells 102
3.3.4 Metastatic properties of Bcl-3 104
3.3.5 Bcl-3 expression and mammosphere forming potential 106
3.3.6 Overexpression of Bcl-3 in non-tumorigenic HEK-293 cells 107
3.4 Conclusion 108
4. Generation and Evaluation of Small-Molecule Inhibitors 110
4.1 Introduction to molecular modelling 110
4.1.1 Molecular mechanics 110
4.1.2 Molecular dynamics 111
4.2 Introduction to virtual screening 112
4.3 Introduction to Bcl-3 structure 113
4.3.1 Characterisation of Bcl-3 structure 114
4.3.2 Binding partners of Bcl-3 114
4.3.3 IκBα comparison 118
4.4 Generation of Bcl-3 models 120
4.4.1 Model of Bcl-3-p50 and Bcl-3-p52 complex 120
4.4.1.1 Validation of the model of Bcl-3-p50 complex 120
4.5 Structure-based virtual screening 123
4.5.1 Identification of binding sites for p50 123
4.5.2 Characterisation of a novel binding pocket 124
4.5.3 Generation of a pharmacophore model 124
4.5.4 Virtual screening for inhibitors of Bcl-3-p50 interaction 127
4.5.5 Evaluation of selected compounds for Bcl-3-p52 inhibition 128
4.5.6 Predicted binding of compound 1 132
4.6 Biological evaluation of selected compounds 134
4.6.1 Cell toxicity 134

4.6.2 Biological evaluation of disruption of Bcl-3-p50 binding 136
4.6.2.1 Indirect Sandwich ELISA assay 136
4.6.2.2 NF-κB assay 136
4.6.2.3 Cell motility assay 136
4.6.3 Biological evaluation of disruption of Bcl-3-p52 binding 140
4.7 Discussion 142
4.7.1 Generation and optimisation of a Bcl-3-p50 and Bcl-3-p52 complex 142
4.7.2 Virtual screening for Bcl-3 inhibitors 143
4.7.3 Biological evaluation of potential inhibitors in cell based assays 144
4.8 Summary 144
5. Establishing the Structure-Activity Relationships (SAR) 147
5.1 Design of novel analogues 149
5.2 General method for synthesis 149
5.3 Results of synthesis 152
5.3.1 Synthesis of series 1 152
5.3.2 Synthesis of series 2 153
5.3.3 Synthesis of series 3 154
5.4 Characterization of the lead compound (15a) 156
5.4.1 Cell toxicity of the lead compound *in vitro* 157
5.4.2 Establishing IC_{50} of the lead compound by Indirect Sandwich ELISA assay .. 159
5.4.3 Establishing IC_{50} of the lead compound by NF-κB assay 159
5.4.4 Establishing IC_{50} of the lead compound by cell motility assay 159
5.5 Biological evaluation of mono substituted analogues 163
5.5.1 Cell toxicity 163
5.5.2 NF-κB assay 163
5.5.2.1 Indirect Sandwich ELISA assay 164
5.5.2.2 Cell motility assay 164
5.6 Biological evaluation of di- and tri- substituted analogues 172
5.6.1 Cell toxicity 172
5.6.2 NF-κB assay 172
5.7 Discussion 175
5.7.1 Characterisation of the lead compound 175

5.7.2 Biological evaluation of mono-substituted analogues 176
5.7.3 Biological evaluation of di- and tri- substituted analogues 177
6. Experimental chemistry 180
6.1 General information 180
6.2 Synthesis of series 1 181
6.2.1 General method for the first step 181
6.2.2 General method for the second step 181
6.2.3 Synthesis of 2-(2-fluorophenyl)-4*H*-3,1-benzoxazin-4-one (**13 a**) 183
6.2.4 Synthesis of 2-(3-fluorophenyl)-4*H*-3,1-benzoxazin-4-one (**13b**) 184
6.2.5 Synthesis of 2-(4-fluorophenyl)-4*H*-3,1-benzoxazin-4-one (**13c**) 185
6.2.6 Synthesis of 2-(2-methoxyphenyl)-4*H*-3,1-benzoxazin-4-one (**13d**) 186
6.2.7 Synthesis of 2-(3-methoxyphenyl)-4*H*-3,1-benzoxazin-4-one (**13e**) 187
6.2.8 Synthesis of 2-(4-methoxyphenyl)-4*H*-3,1-benzoxazin-4-one (**13f**) 188
6.2.9 Synthesis of 2-(2-nitrophenyl)-4*H*-3,1-benzoxazin-4-one (**13g**) 189
6.2.10 Synthesis of 2-(3-nitrophenyl)-4*H*-3,1-benzoxazin-4-one (**13h**) 190
6.2.11 Synthesis of 2-(4-nitrophenyl)-4*H*-3,1-benzoxazin-4-one (**13i**) 191
6.2.12 Synthesis of 2-(*o*-tolyl)-4*H*-3,1-benzoxazin-4-one (**13j**) 192
6.2.13 Synthesis of 2-phenyl-4*H*-3,1-benzoxazin-4-one (**13k**) 193
6.2.14 2-(3,4-dimethoxyphenyl)-4*H*-3,1-benzoxazin-4-one (**13l**) 194
6.2.15 2-(3,5-dimethoxyphenyl)-4*H*-3,1-benzoxazin-4-one (**13m**) 195
6.2.16 2-(3,4,5-trimethoxyphenyl)-4*H*-3,1-benzoxazin-4-one (**13n**) 196
6.2.17 2-(3,5-difluorophenyl)-4*H*-3,1-benzoxazin-4-one (**13o**) 197
6.2.18 2-(2,6-difluorophenyl)-4*H*-3,1-benzoxazin-4-one (**13p**) 198
6.2.19 2-(2,4-difluorophenyl)-4*H*-3,1-benzoxazin-4-one (**13q**) 199
6.2.20 Synthesis of 2-[(2-fluorobenzoyl)amino]-N-(2-morpholin-4-ylethyl)benzamide (**15a**) 200
6.2.21 Synthesis of 2-[(3-fluorobenzoyl)amino]-N-(2-morpholin-4-ylethyl)benzamide (**15b**) 201
6.2.22 Synthesis of 2-[(4-fluorobenzoyl)amino]-N-(2-morpholin-4-ylethyl)benzamide (**15c**) 202
6.2.23 Synthesis of 2-[(2-methoxybenzoyl)amino]-N-(2-morpholin-4-ylethyl)benzamide (**15d**) 203
6.2.24 Synthesis of 2-[(3-methoxybenzoyl)amino]-N-(2-morpholin-4-ylethyl)benzamide (**15e**) 204
6.2.25 Synthesis of 2-[(4-methoxybenzoyl)amino]-N-(2-morpholin-4-ylethyl)benzamide (**15f**) 205

6.2.26 Synthesis of 2-[(2-nitrobenzoyl)amino]-N-(2-morpholin-4-ylethyl)benzamide (**15g**) 206

6.2.27 Synthesis of 2-[(3-nitrobenzoyl)amino]-N-(2-morpholin-4-ylethyl)benzamide (**15h**) 207

6.2.28 Synthesis of 2-[(4-nitrobenzoyl)amino]-N-(2-morpholin-4-ylethyl) benzamide (**15i**) 208

6.2.29 Synthesis of 2-[(2-methylbenzoyl)amino]-N-(2-morpholin-4-ylethyl) benzamide (**15j**) 209

6.2.30 Synthesis of 2-benzamido-N- (2-morpholin-4-ylethyl)benzamide (**15k**) 210

6.2.31 Synthesis of 3,4-dimethoxy-*N*- (2-[(2-morpholin-4-ylethyl) carbamoyl] phenyl) benzamide (**15l**) 211

6.2.32 Synthesis of 3,5-dimethoxy-*N*- (2-[(2-morpholin-4-ylethyl) carbamoyl] phenyl) benzamide (**15m**) 212

6.2.33 Synthesis of 3,4,5-trimethoxy-*N*- (2-[(2-morpholin-4-ylethyl) carbamoyl] phenyl) benzamide (**15n**) 213

6.2.34 Synthesis of 3,5-difluoro -*N*- (2-[(2-morpholin-4-ylethyl) carbamoyl] phenyl) benzamide (**15o**) 214

6.2.35 Synthesis of 2,6-difluoro -*N*- (2-[(2-morpholin-4-ylethyl) carbamoyl] phenyl) benzamide (**15p**) 215

6.2.36 Synthesis of 2,4-difluoro -*N*- (2-[(2-morpholin-4-ylethyl) carbamoyl] phenyl) benzamide (**15q**) 216

6.3 Synthesis of series 2 217

6.3.1 Synthesis of 2-[(2-fluorobenzoyl)amino]-N-(2-morpholin-4-ylpropyl)benzamide (**17a**) 218

6.3.2 Synthesis of 2-[(4-fluorobenzoyl)amino]-N-(pyridin-3-ylmethyl)benzamide (**17b**) 219

6.3.3 Synthesis of 2-[(4-fluorobenzoyl)amino]-N-(pyrrolidin-3-ylmethyl)benzamide (**17c**) 220

6.3.4 Synthesis of 2-[(4-fluorobenzoyl)amino]-N-(piperidin-3-ylmethyl)benzamide (**17d**) 221

6.3.5 Synthesis of 2-[(4-fluorobenzoyl)amino]-N-(piperazin-3-ylmethyl)benzamide (**17e**) 222

6.3.6 Synthesis of *N*- (2-aminoethyl)-2-(2-fluorobenzamido) benzamide (**17f**)..... 223

6.4 Synthesis of series 3 224

6.4.1 General method for the first step 224

6.4.2 General method for the second step 224

6.4.3 Synthesis of 2-(2-fluorophenyl)-8-methoxy-3,1-benzoxazin-4-one (**19a**)..... 226

6.4.4 Synthesis of 2-(2-fluorophenyl)-8-methoxy-3,1-benzoxazin-4-one (**19b**) 227

6.4.5 Synthesis of 2-(2-fluorophenyl)-8-methoxy-3,1-benzoxazin-4-one (**19c**) 228

6.4.6 Synthesis of 5-chloro-2- (2-fluorophenyl)-3,1-benzoxazin-4-one (**19d**) 229

6.4.7 Synthesis of 2-[(2-fluorobenzoyl)amino]-3-methoxy-N-(2-morpholin-4-ylethyl) benzamide (**20a**) 230

6.4.8 Synthesis of 2-[(2-fluorobenzoyl)amino]-3-methyl-N-(2-morpholin-4-ylethyl) benzamide (**20b**) 231

6.4.9 Synthesis of 2-[(2-fluorobenzoyl)amino]-5-iodo-N-(2-morpholin-4-ylethyl) benzamide (**20c**) 232

6.4.10 Synthesis of 2-[(2-fluorobenzoyl)amino]-2-chloro-N-(2-morpholin-4-ylethyl) benzamide (**20d**) 233

6.5 Synthesis of hydrochloride salt of 2-fluoro-*N*- (2-((2-morpholinoethyl) carbamoyl) phenyl) benzamide (HCl salt of 15a) 234

7. Discussion and future work 237

7.1 Bcl-3 as a therapeutic target 238

7.2 Modelling disruption of Bcl-3-p50 binding in MDA-MB-231 cell line 239

7.3 Does Bcl-3 act as an oncogene? 240

7.4 Targeting Bcl-3-p50 protein-protein interactions 241

7.4.1 Virtual screening targeted against a novel Bcl-3 binding pocket 242

7.4.2 Biological evaluation of potential inhibitors in cell based assays 242

7.4.3 Structure activity relationships of a lead compound 243

7.5 Future directions 244

7.5.1 Further chemical modification of structural analogues 244

7.5.2 Further *in vivo* studies to support therapeutic potential of Bcl-3 245

7.5.3 Future perspectives of Bcl-3 inhibitors 245

References 247

Appendices 259

1. List of purchased and synthesised compounds 259

Table of figures

Figure 1.1 Incidence and mortality of breast cancer in Western Europe between 1975-2010 2
Figure 1.2 Increase in relative survival in breast cancer in England and Wales 3
Figure 1.3 Progression from non-invasive carcinoma to invasive metastatic carcinoma 5
Figure 1.4 ErbB (HER) family 8
Figure 1.5 NF-κB family members 16
Figure 1.6 NF-κB signalling pathways 18
Figure 1.7 Targeting NF-κB signalling 24
Figure 1.8 The role of Bcl-3 in NF-κB signalling 28
Figure 1.9 Bcl-3 deficiency does not affect tumour growth but reduces ErbB2 metastatic tumour burden 34
Figure 2.1 Bcl-3 constructs 40
Figure 2.2 Expression of receptors in human breast cancer cell lines 43
Figure 2.3 Mammosphere assay 52
Figure 2.4 Schematic representation of an Indirect and Sandwich ELISA assay 59
Figure 3.1 Bcl-3 expression in a human cell lines and the effect of Bcl-3 suppression on NF-κB activity 68
Figure 3.2 Cell viability and proliferation in Bcl-3 suppressed human breast cancer cells 70
Figure 3.3 Cell death and cyclin D1 expression in Bcl-3 suppressed breast cancer cells ... 71
Figure 3.4 The effect of Bcl-3 suppression on cell cycle 73
Figure 3.5 Generation of Bcl-3 WT and Bcl-3 ANK M123 clones and their effect on NF-κB activity in MDA-MB-231 cells 76
Figure 3.6 The effect of Bcl-3 expression on cell proliferation in MDA-MB-231 cells 79
Figure 3.7 Bcl-3 expression reduced the proportion of cells in G0/1 phase of cell cycle .. 80
Figure 3.8 Bcl-3 suppression by siRNA decreases cell motility 83
Figure 3.9 Bcl-3 expression affects cell motility 84
Figure 3.10 The effect of Bcl-3 on TIMP 1 and TIMP 2 expression 85
Figure 3.11 The effect of Bcl-3 knock down on mammosphere forming potential 87
Figure 3.12 The effect of Bcl-3 WT or Bcl-3 ANK M123 overexpression on mammosphere forming potential 88
Figure 3.13 Stable overexpression of Bcl-3 WT and Bcl-3 ANK M123 in HEK-293 cells 90

Figure 3.14 Effect of Bcl-3 expression on basal NF-κB activity and cell viability in HEK-293 cells 93
Figure 3.15 Optimisation of Indirect Sandwich ELISA 94
Figure 3.16 GFP expression in HEK-293 – p52 cells 96
Figure 3.17 Stable overexpression of p52 WT in HEK-293 cells and its effect on basal NF-κB activity 97
Figure 3.18 The effect of p52 overexpression on cell viability in the HEK-293 cell line 99
Figure 4.1 Schematic representation of key contributors to a molecular mechanics force field 111
Figure 4.2 Structure of Bcl-3 116
Figure 4.3 Characterisation of Bcl-3 structure 117
Figure 4.4 Comparison of Bcl-3 and IκBα structure 119
Figure 4.5 Model of Bcl-3 in a complex with p50 and p52 homodimers 121
Figure 4.6 Validation of the model of Bcl-3-p50 complex 122
Figure 4.7 Characterisation of novel binding pocket for p50 125
Figure 4.8 Interacting residues in the “MYSGS” binding pocket 126
Figure 4.9 Selection process 129
Figure 4.10 Compound 1 docked into Bcl-3 133
Figure 4.11 Cell toxicity 135
Figure 4.12 ELISA assay evaluating Bcl-3-p50 binding 137
Figure 4.13 NF-κB assay in HEK-293 and MDA-MB-231 cells 138
Figure 4.14 Cell motility assay in MDA-MB-231 139
Figure 4.15 NF-κB assay in HEK-293-p52 141
Figure 5.1 Ligand interaction of the lead compound 6 in the “MYSGG” binding pocket . 148
Figure 5.2 Modification of the lead compound 149
Figure 5.3 Cell toxicity of the lead compound 158
Figure 5.4 Establishing IC_{50} of the lead compound by Indirect Sandwich ELISA assay 160
Figure 5.5 Establishing IC_{50} of the lead compound by NF-κB assay 161
Figure 5.6 Establishing IC_{50} of the lead compound by cell motility assay 162
Figure 5.7 Cell toxicity 166
Figure 5.8 NF-κB assay in MDA-MB-231 cells 167
Figure 5.9 Establishing IC_{50} of selected analogues by NF-κB assay in MDA-MB-231 cells 168

Figure 5.10 Establishing IC_{50} of selected analogues by Indirect Sandwich ELISA assay ... 169
Figure 5.11 Establishing IC_{50} of selected analogues by cell motility assay 170
Figure 5.12 The effect of analogue 15f on cell viability 171
Figure 5.13 Biological evaluation of di- and tri- substituted analogues 173
Figure 5.14 Establishing IC_{50} of selected di- and tri- substituted analogues by NF-κB assay in MDA-MB-231 cells 174
Figure 7.1 Structure activity relationships (SAR) of the lead compound 244

Table of tables

Table 1.1 Intrinsic subtypes of breast cancer..... 10
Table 2.1 Reaction volumes and components for single or double restriction enzyme digest..... 38
Table 2.2 ON Target plus SMART pool sequences 45
Table 2.3 Volumes and concentration of reagents for transient siRNA transfection in different culture plates 46
Table 2.4 Number of cells plated for siRNA transient transfection, stable transfection or transfection of cells with reporter plasmids for NF-κB reporter plasmids..... 46
Table 2.5 Volumes of reagents for stable transfection of cells with plasmid DNA in 24 well plate format 46
Table 2.6 Volumes of reagents for transfection of cells with NF-κB reporter plasmids in 96 well plate format..... 48
Table 2.7 Seeding densities for Cell Titre blue viability assays and cell count 48
Table 2.8 Composition of buffers for whole cell protein extraction 55
Table 2.9 Composition of gels for SDS-PAGE 56
Table 2.10 Composition of buffers used in Western analysis 57
Table 2.11 Details of primary antibodies used for Western blotting analysis 58
Table 2.12 Details of secondary antibodies used for Western blotting analysis..... 58
Table 2.13 Details of antibodies used in ELISA assay 60
Table 2.14 Master mix components for reverse transcription..... 62
Table 2.15 Primer sequences used for QRT-PCR..... 62
Table 2.16 QRT-PCR reaction components 63
Table 4.1 Structures of 10 purchased compounds..... 130
Table 4.2 Scoring results for 10 purchased compounds 131

Table 4.3 Model system used for biological evaluation 134
Table 5.1 Solubility of the lead compound in organic solvents 156
Table 5.2 Comparison of novel analogues 178

Table of schemes

Scheme 5.1 General synthesis route 150
Scheme 5.2 Suggested mechanism of the two-step synthesis 151
Scheme 5.3 Synthesis of series 1 153
Scheme 5.4 Synthesis of series 2 154
Scheme 5.5 Synthesis of series 3 155
Scheme 6.1 Synthesis of series 1 182
Scheme 6.2 Synthesis of series 2 217
Scheme 6.3 Synthesis of series 3 225

Chapter 1

General Introduction

1. General Introduction

1.1 Breast cancer

Breast cancer is the most common cancer in the UK and the most prevalent cancer in women worldwide (Rachet et al., 2009, Polyak, 2007). There were 1.38 million new cases diagnosed worldwide in 2008, which accounts for 23% of all new cases in 2008 and 11% overall incidence. An increase of incidence of breast cancer mainly in Western Europe was observed, rising from an average of 50 per 100,000 women in 1975 to current level of 89.7 per 100,000 women (Figure 1.1A) (Ferlay et al., 2010, Rachet et al., 2009)

Even though breast cancer is the most prevalent cancer in the UK, it ranks as the fifth more common cause of death, mainly due to the improvements in therapy. Despite the rise of incidence, breast cancer mortality has declined by about 10% in UK between 1975-2010 to current standardized rate of 18 per 100,000 women in UK (Figure 1.1B)(Ferlay et al., 2010, Rachet et al., 2009).

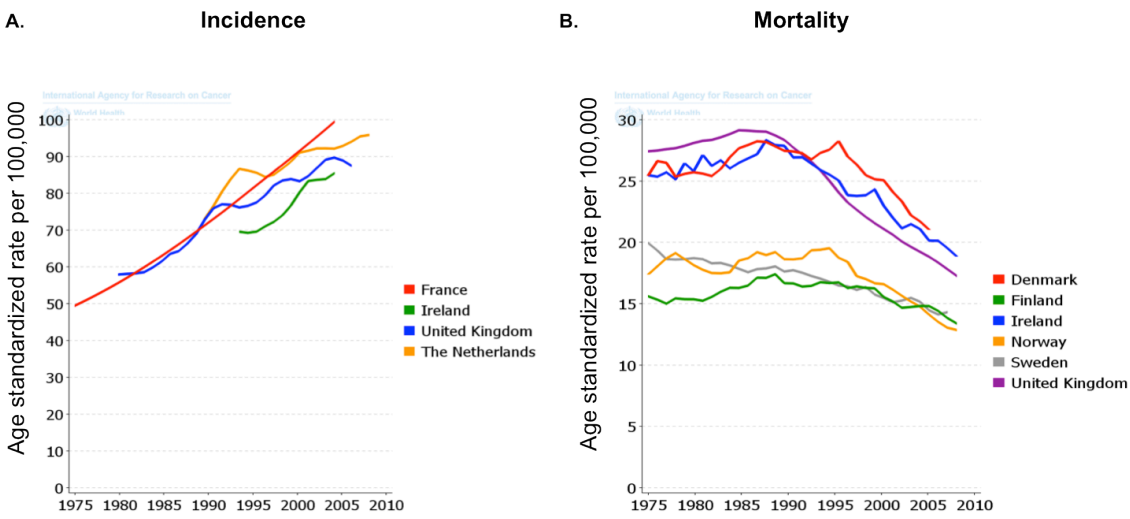

Figure 1.1 Incidence and mortality of breast cancer in Western Europe between 1975-2010
Figure adapted from (Ferlay et al., 2010).

The relative survival of breast cancer patients has increased dramatically over the last 35 years, with 1 year survival now being almost 100% and 10 years survival 80% (Figure 1.2) (Rachet et al., 2009). Localized disease is largely curable, however up to 20% of patients are likely to develop metastatic disease, which still has a poor prognosis (Place et al., 2011, Eckhardt et al., 2012). Therefore understanding of breast cancer progression towards aggressive metastatic forms and tumour cell-specific molecular pathways is necessary to further improve current therapies.

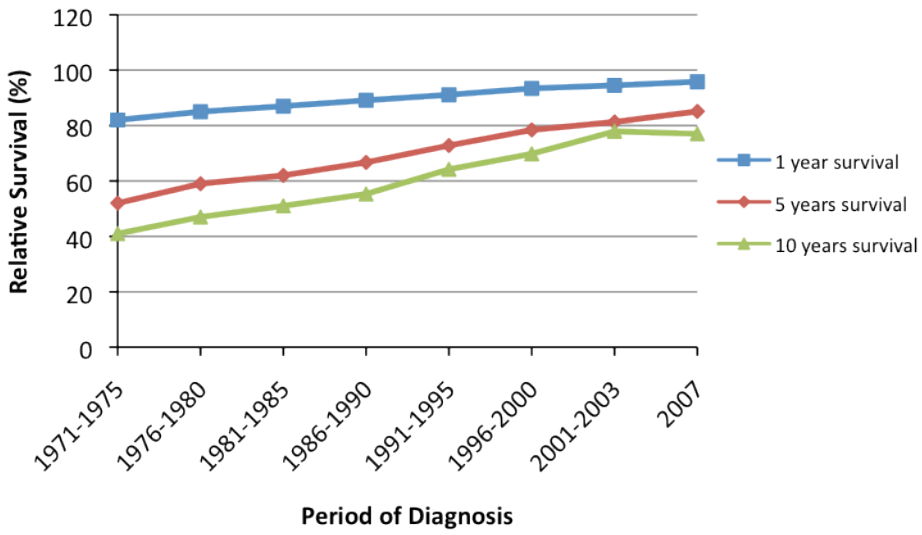

Figure 1.2 Increase in relative survival in breast cancer in England and Wales
Relative survival of breast cancer patients in England and Wales over 1971 – 2007. Data extracted from (Rachet et al., 2009).

1.1.1 Breast cancer development and metastatic progression

The normal breast duct consists of a luminal epithelial cell layer surrounded by myoepithelial cells, which are attached to the basement membrane. The breast microenvironment is composed of extracellular matrix (ECM) and numerous stromal cells, such as endothelial cells, immune cells, fibroblasts and adipocytes (Place et al., 2011). Breast tumours evolve via sequential progression through defined pathological and clinical stages (Figure 1.3), starting with ductal hyperproliferation followed by evolution into in situ and invasive carcinoma (Polyak, 2007). In order to form metastasis, tumour cells first migrate from the primary

tumour, penetrate blood vessels and then colonize distant sites (Mehlen et al., 2006) possibly through mechanism involving epithelial-to-mesenchymal (EMT) transition (Huber et al., 2005, Guarino, 2007, Thiery et al., 2006). The epithelial phenotype is characterised by cell surface polarization into apical and basolateral domains and intercellular adhesion controlled by a junctional complex, whereas EMT transition is associated with the downregulation of E-cadherin that controls cell polarity and tight junctions (Kim et al., 2006). Most of the tumour cells die during this process, however several studies have shown that tumour cells can remain dormant in the tissue, either as single cells or as micrometastases, leading to the long latency between initial therapy and the onset of metastatic disease (Meng et al., 2004, MacDonald et al., 2002). Interestingly, in order to establish growth at the secondary site, the tumour cells have to undergo a mesenchymal to epithelial transition (Eckhardt et al., 2012). The common sites for metastasis originated from breast tumours are bone, lung and liver (Weigelt et al., 2005).

There are various difficulties associated with targeting metastases and discovering novel molecular targets. The differences between the early stages and metastases development require novel targeted therapy that will differ from targeted therapy for primary tumours. Moreover, the target gene has to be detectable in the disseminated tumour cells or in the primary tumour before the metastases occurs (Eckhardt et al., 2012). Due to the potential long latency between primary tumour development to metastatic disease, targeted therapy needs to be administered for a long period and therefore with fewer side effects than conventional therapy.

In order to find a new molecular target, we need better understanding of the metastases-regulating genes and also of the concept of dormancy of the tumour cells, which can be up to 20 years in breast cancer patients. Although the development of targeted therapy for metastatic disease still remains a challenge, the use of Denosumab, an antibody targeting receptor activator of NF-κB ligand (RANKL) has proven to be successful in the treatment of bone metastases by preventing further spread of secondary tumours in patients with advanced disease (Eckhardt et al., 2012).

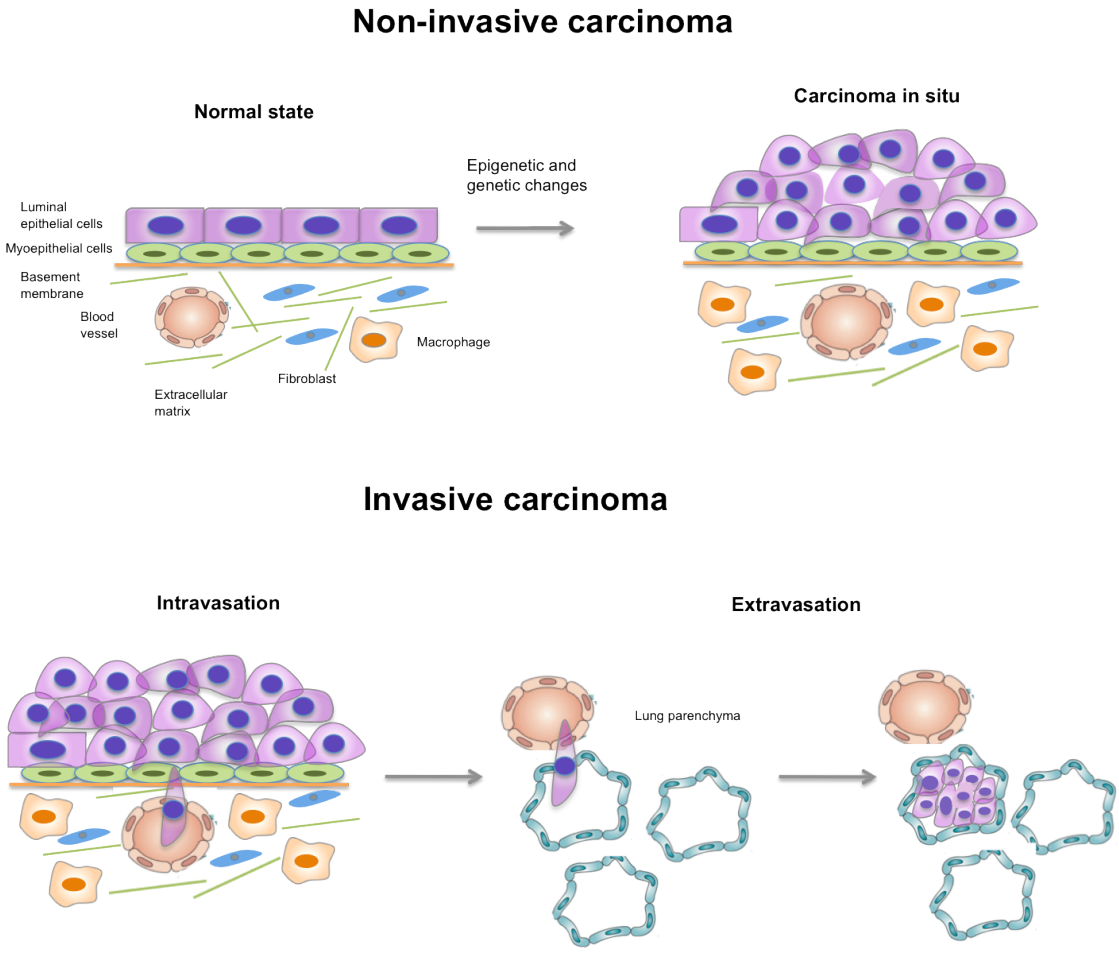

Figure 1.3 Progression from non-invasive carcinoma to invasive metastatic carcinoma

Invasive metastatic carcinoma evolves via progression through carcinoma in situ into invasive carcinoma. In order to form metastases, cells must invade through the basement membrane, enter the vasculature (intravasate), survive in the absence of adhesion, exit the vasculature (extravasate) and establish a new tumour in a foreign microenvironment (here in lung parenchyma). Figure adapted from (Polyak, 2007).

1.1.2 Heterogeneity of breast cancer

Human breast cancers are phenotypically heterogeneous with unpredictable clinical outcomes (Biswas et al., 2004) and can be classified into subtypes based on differences in their gene expression patterns. Clinicians rely on the expression of two important growth factor receptors, the nuclear estrogen receptor (ER) and the membrane receptor tyrosine kinase, ErbB2 (HER2/neu) to classify human breast cancers into therapeutic and prognostic groups (Biswas et al., 2004). According to (Sorlie et al., 2001) the cellular and molecular heterogeneity of breast tumours emphasize the importance of studying multiple genetic alterations using systematic investigation of expression patterns of thousand of genes using cDNA microarrays as discussed below.

1.1.3 Classification of breast cancers based on expression patterns

Breast cancer tumours show distinct and reproducible subtypes of breast carcinoma associated with different clinical outcomes (Perou et al., 2000, Sorlie et al., 2001, Carey, 2010, Livasy et al., 2007). Breast cancers can be clustered into six intrinsic subtypes, luminal A, luminal B, HER2 enriched, basal-like, Claudin-low and normal-like (Carey, 2010). More recently, a genomic study of 2000 breast tumours revealed at least 10 different subtypes of breast cancer (Curtis et al., 2012), while another study identified 6 subtypes of triple negative breast cancer (Lehmann et al., 2011). Improvement in molecular subtyping is necessary for the development and use of molecular-based cancer therapies.

1.1.3.1 Luminal subtypes

Two hormone receptor-positive subtypes, luminal A and luminal B are the most common of all subtypes, comprising approximately 40% and 20% respectively of breast cancers. These tumours typically express luminal cytokeratins (8 and 18), estrogen receptor (ER) and progesterone receptor (PgR) (Perou et al., 2000). Moreover, these subtypes were found to express genes associated with ER activation, such as LIV1, GATA3 and CCND1 (Sotiriou et al., 2003). The expression of ER-related genes is usually higher in luminal A tumours and the expression of proliferation genes is generally higher in luminal B tumours (Perou et al., 2000,

Carey, 2010). Luminal B subtype is highly proliferative and often carry mutations in p53 (Bild et al., 2009). Patients with luminal A tumours have significantly better prognosis for overall and relapse free survival than patients with luminal B tumours (Sorlie et al., 2001). The therapeutic approach for these subtypes remains endocrine therapy, but these tumours can also benefit from a variety of adjuvant cytotoxic therapy, such as aromatase inhibitors (Carey, 2010). A fraction of luminal B subtype tumours was also found to have activated PI3K or SRC pathways and might benefit from targeted therapy such as AKT1 or mTOR inhibitors (Bild et al., 2009).

1.1.3.2 HER2 enriched subtype

The ErbB2-positive (HER2 enriched) subtype is characterized by high expression of HER2 genes, low expression of the hormone receptor-related gene cluster and high expression of the proliferation cluster. This subtype is relatively uncommon, comprising only 5-10% of all breast cancers (Carey et al., 2006, Carey, 2010). A key clinical consideration is that only about half of HER2-driven breast cancers fall into this category, while the rest co-express the luminal cluster (Carey, 2010). This subtype has relatively poor prognosis and does not respond to endocrine therapy, thus novel HER2-targeted therapy is routinely incorporated into adjuvant therapy (discussed more in depths in section 1.1.4.1) (Carey, 2010).

The ErbB family includes four different receptor tyrosine kinases: EGFR (ErbB-1), HER2 (ErbB-2), HER3 (ErbB-3), and HER4 (ErbB-4) (Normanno et al., 2009). Binding of ligands induces either homo- or hetero- dimerization of the receptor and activation of signalling cascade, while HER2 being the preferred heterodimeric binding partner (Figure 1.4 A). This sequence of events promotes cell proliferation, survival and migration, events that are associated with breast cancer progression (Morrow et al., 2009). Interestingly it was found that HER2 activates not only PI3K/Akt signalling pathway, but also canonical NF-κB signalling through activation of IKKα (Figure 1.4 B). Both pathways contribute to the invasiveness of HER2 overexpressing breast cancers (Meckhofer et al., 2010).

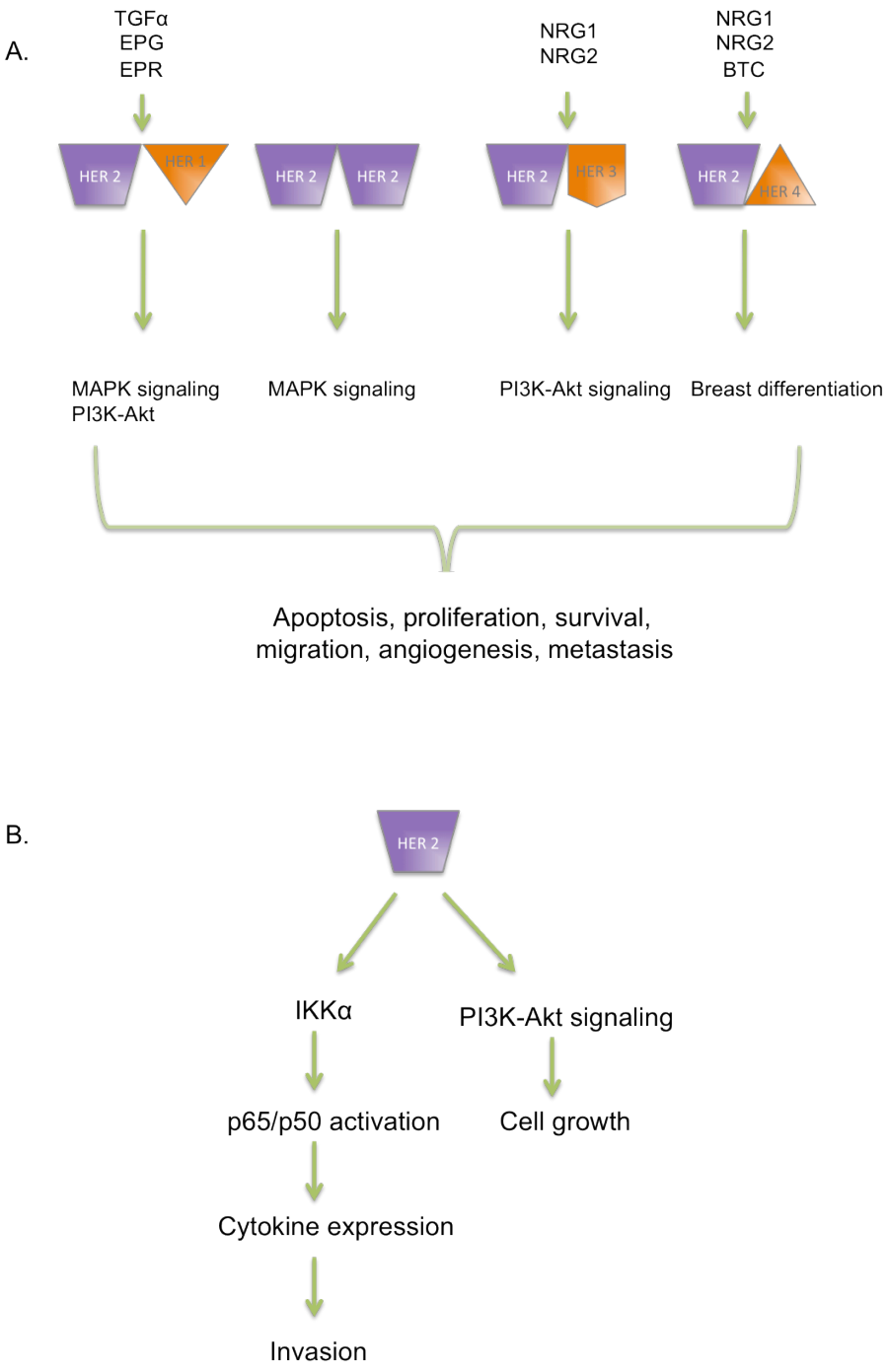

Figure 1.4 ErbB (HER) family

A. The binding of ligands, including TGFα (transforming growth factor-α), EPG (epigen), EPR (epiregulin), NRG (neuregulin) and BTC (betacellulin) leads to activation of signalling cascades involving MAPK signalling (mitogen-activated protein kinase) and PI3K-Akt signalling (phosphoinositide 3-kinase-Akt). This sequence of events leads to apoptosis, proliferation, survival, migration, angiogenesis and metastasis of HER2+ breast cancers. Figure adapted from (Spector et al., 2007, Morrow et al., 2009). **B.** Her2 activates IKKα and PI3K-Akt signalling, which leads to promotion of cells growth and invasion. Figure adapted from (Meckhofer et al., 2010).

1.1.3.3 The basal subtype

The basal-like subtype comprises about 15-20% of all breast cancers and is characterized by low expression of the hormone receptor-related luminal genes and of the HER2-related genes, therefore this subtype is frequently called triple negative breast cancer (TNBC). Additionally, this subtype has high expression of the proliferation gene cluster and high expression of the basal cluster, including basal epithelial cytokeratins (5, 14 and 17) and epidermal growth factor receptor (Carey, 2010). One of the risk factors for developing basal like breast cancer is BRCA1 mutation (Foulkes et al., 24) and the inhibition of poly(ADP-ribose) polymerase (PARP) has shown high efficacy in these patients (Eckhardt et al., 2012).

The clinical outcome of the basal-like subtype, like that of HER2 enriched subtype, is associated with the shortest overall and relapse free survival (Sorlie et al., 2001). The basal-like subtype is often high grade with high proliferation rate and necrosis (Laurentiis et al., 2010). Moreover the treatment of basal-like breast cancer is challenging due to the lack of molecular targets, such as ER or HER2, thus patients cannot benefit from endocrine therapy or anti-HER2 agents. However up to 80% of basal-like breast cancers have high expression of EGFR and can therefore benefit from EGFR inhibitors (discussed more in depths in section 1.1.4.3) (Perou et al., 2000, Sorlie et al., 2001, Normanno et al., 2009, Carey, 2010, Carey et al., 2006).

1.1.3.4 Claudin-low subtype

The Claudin-low subtype is similar to TNBC, characterized by low expression of the hormone receptor-related luminal genes and of the HER2-related genes. Moreover it is determined by low expression of genes involved in cell-cell interaction and adhesions, such as claudins (3, 4 and 7) and E-cadherin (Carey, 2010). EMT is characterized by up-regulation of vimentin, Snail, Slug and Twist and down-regulation of E-cadherin, and all these events were found to occur in Claudin-low subtype. Further studies suggested that this subtype might arise from more immature precursor cells than other breast cancers due to the enrichment for stem-like cells (Hennessy et al., 2009). Furthermore, metaplastic carcinoma, an aggressive metastatic breast cancer characterized by mesenchymal/sarcomatoid metaplasia, demonstrates claudin-low features (Carey, 2010). Acquisition of EMT and stem cell-

like properties leads to therapeutic resistance and patients have overall poor survival (Prat et al., 2010).

1.1.3.5 Normal breast-like subtype

Approximately 10% of breast cancers have been classified as normal-like; these can be either ER+ or ER-. This classification might be a technical artefact of contaminating tumour samples with normal breast tissue, therefore the significance of this subtype has yet to be determined (Perou et al., 2000, Parker et al., 2009).

Subtype	Classification	Occurrence	Therapy
Luminal A	ER+/PR+/HER2-/low proliferation	40%	Endocrine therapy
Luminal B	ER+/HER2-/high proliferation ER+/HER2+	20%	Endocrine/ HER2-targeted
HER2	ER-/PR-/HER2+	5-10%	HER2-targeted
Basal like (triple-negative)	ER-/PR-/HER2-	15-20%	Chemotherapy EGFR inhibitors, PARP inhibitors
Claudin-low	ER-/PR-/HER2-/Low expression of tight junction proteins (claudins 3, 4 and 7 and E-cadherin)	5-10%	Chemotherapy
Normal breast-like	ER+/ER-	10%	Chemotherapy

Table 1.1 Intrinsic subtypes of breast cancer

1.1.4 Targeted therapies for breast cancer

Targeted therapy aims to provide more effective and less toxic treatment than conventional therapies, such as chemotherapy and radiotherapy and it is the fastest growing field in cancer drug development worldwide (BCCResearch, 2008). An understanding of the underlying biology of breast cancer led to the development of novel therapeutics targeting specific molecular pathways (Higgins et al., 2011, Palma et al., 2012).

The identification of hormone dependent (ER+ and PR+) subtypes of breast cancer led to the development of endocrine therapy, which is the first example of targeted therapy. Consequently, other targeted therapies have been developed, such as HER2 inhibitors, inhibitors of intracellular signalling pathways (PI3K, Akt, mTor) and angiogenesis therapy (Normanno et al., 2009, Schlotter et al., 2008).

The concept of targeted therapy raised high expectations; however only a fraction of patients with tumours responded to given targeted therapy in clinic. This led to the realization that understanding of the specific complexity and variability of tumours in the context of the individual is needed in order to predict the benefits for the particular patient. The concept of personalized cancer medicine is therefore providing better advice on prognosis and therapeutic options for an individual and is opening a new way of targeted cancer treatment (Palma and Hanahan, 2012).

1.1.4.1 HER2 targeted treatment

HER2 represents an attractive target for cancer drug development. The humanized recombinant monoclonal antibody, trastuzumab, specifically targets the HER2/neu extracellular domain (Carney et al., 2007) and was approved as the first HER2 targeted therapy for the treatment of HER2+ metastatic breast cancer. In addition, trastuzumab with adjuvant chemotherapy significantly improved disease-free and overall survival rates in patients with early stage HER2+ breast cancer (Nahta et al., 2006).

However, there is still a large proportion of breast cancers overexpressing HER2 not responding to trastuzumab (Schlotter et al., 2008) or developing resistance. In the adjuvant setting, 15% of patients still relapse within one year of treatment initiation despite trastuzumab-based therapy (Nahta and Esteva, 2006).

Although mechanisms of trastuzumab resistance have been described, novel strategies to overcome resistance are still waiting to be developed (Morrow et al., 2009).

Another novel agent targeting HER2 is pertuzumab, which is a humanized recombinant monoclonal antibody against the extracellular dimerization domain of the HER2 receptor (Nahta and Esteva, 2006, Normanno et al., 2009). This antibody directly inhibits the dimerization of the HER2 protein with other HER family receptors, preventing the activation of downstream signalling pathways (Normanno et al., 2009). Lapatinib is a small-molecule dual inhibitor of the EGFR and HER2 receptor. Because lapatinib specifically targets the HER2 kinase domain, this agent was found active even in trastuzumab-resistant tumours. Therefore targeting other structural domains within the HER2 receptor is a promising strategy in the treatment of trastuzumab resistant breast tumours (Morrow et al., 2009).

1.1.4.2 Targeting pathways downstream of HER2 receptor

Inhibitors of pathways downstream of the HER2 receptor such as the PI3/Akt pathway may combat trastuzumab resistance (Nahta and Esteva, 2006). The PI3/Akt pathway regulates different functions that play an important role in tumour progression, such as cell growth, survival, invasion and migration (Liu et al., 2007). An example of an Akt inhibitor is perifosine, which has not achieved clinical development due to excessive toxicity in preclinical models (Nahta and Esteva, 2006). An alternative target of the PI3K/Akt signalling is the serine/threonine kinase mammalian target of rapamycin (mTOR). Rapamycin, the prototype of mTOR inhibitors, inhibited tumour growth in a wide range of experimental malignancies. Temsirolimus and everolimus are the rapamycin analogues currently in clinical development (Normanno et al., 2009).

1.1.4.3 EGFR targeted treatment

Hormone-resistant breast cancers (so called triple negative) are associated with an increase expression of both EGFR and EGFR ligands. Hence, EGFR and its downstream signalling pathways are promising targets for this specific type of breast cancer (Schlotter et al., 2008). According to Morrow *et al.* (2009), the results from preclinical studies of small-molecule EGFR tyrosine kinase inhibitors are

contradictory, therefore further studies are required. Unfortunately, the use of a monoclonal antibody against EGFR, cetuximab, had low preliminary efficacy, even in combination with chemotherapy, such as paclitaxel (Schlotter et al., 2008). The promising strategy seems to be the combination of EGFR and HER2 inhibition, as in the case of lapatinib.

1.1.4.4 Targeting VEGFR

Another key target in the treatment of breast cancer is vascular endothelial growth factor receptor (VEGFR) as it plays a central role in promoting angiogenesis (Schlotter et al., 2008). Angiogenesis, the formation of new blood vessels from the existing vasculature, is essential for the growth of the primary tumour and for the formation of metastasis (Normanno et al., 2009). Bevacizumab is a humanized monoclonal antibody that binds VEGF and prevents its interaction with VEGF receptors, thus leading to inhibition of VEGF-induced angiogenesis (Normanno et al., 2009).

1.1.4.5 NF-κB signalling as a target

Another attractive target in cancer drug development is the NF-κB signalling pathway. Even though NF-κB activation is known to be required for normal mammary gland development, its upregulation is connected with the etiology and progression of hormone-independent breast cancers, in part due to its transcriptional stimulation of genes that direct cell proliferation and invasion such as cyclin D1 (Zhou et al., 2005). A high level of NF-κB activation was found in 86% of HER2+/ER- breast cancers and in 33% of basal-like cancers (Biswas et al., 2006), which are associated with a shortened disease-free interval, poor survival and resistance to cancer therapy (Schlotter et al., 2008).

1.2 NF-κB signalling

Nuclear factor- κB (NF-κB) was first identified in 1986 as a transcription factor that binds to a 10bp sequence within the immunoglobulin (Ig) κ light chain enhancer (Sen et al., 1986). NF-κB transcription factors can both induce and repress gene expression by binding to DNA sequences, known as κB elements. NF-κB regulates numerous genes that control apoptosis, cell adhesion, proliferation, immunity and inflammation (Perkins, 2007).

1.2.1 NF-κB family members

The mammalian NF-κB family consists of five structurally related members (Figure 1.5 A), NF-κB1 (p50), NF-κB2 (p52), RelA (p65), RelB and c-Rel (Perkins, 2007). All five NF-κB members contain a conserved Rel homology domain (RHD) that is located towards the N terminus of the protein and is responsible for dimerization, interaction with IκBs and DNA binding. Rel subfamily members, RelA (p65), RelB and c-Rel contain C-terminal trans-activation domains (TADs) and directly promote gene transcription (Hayden et al., 2004). Both p50 and p52 proteins do not contain TADs and therefore can not directly stimulate gene transcription alone, only in heterodimeric combination with other members, such as p65 or RelB respectively (Perkins, 2007). All NF-κB family members can form homodimers or heterodimers, except for RelB, which only forms heterodimers (Gilmore, 2006). Resulting dimers are held in an inactive form in the cytoplasm by interaction with a member of the IκB family of proteins (Perkins, 2007).

1.2.2 IκB family members

In mammalian cells, there are several IκB proteins, IκBα, IκBβ, IκBε and IκBγ and they have different affinities for individual NF-κB dimers (Figure 1.5 B). Longer precursors of p50 and p52, p105 and p100 respectively, contain ankyrin-repeat motifs in their C termini, similar to those found in IκB (Perkins, 2007). The binding to the NF-κB subunits is mediated by ankyrin repeat domains (Karin et al., 2002), while one of their functions is to mask a conserved nuclear localization sequence that is found in the RHD of the NF-κB subunits (Perkins, 2007).

IκBα, IκBβ and IκBε contain two serines within N-terminal, which when phosphorylated are targeted to ubiquitine-dependent degradation by proteasome (Karin et al., 2002).

An atypical member of the IκB family, Bcl-3, contains similar ankyrin-repeat motifs, but unlike the other members is nuclear and has been shown to function as a transcriptional co-activator (Watanabe et al., 1997).

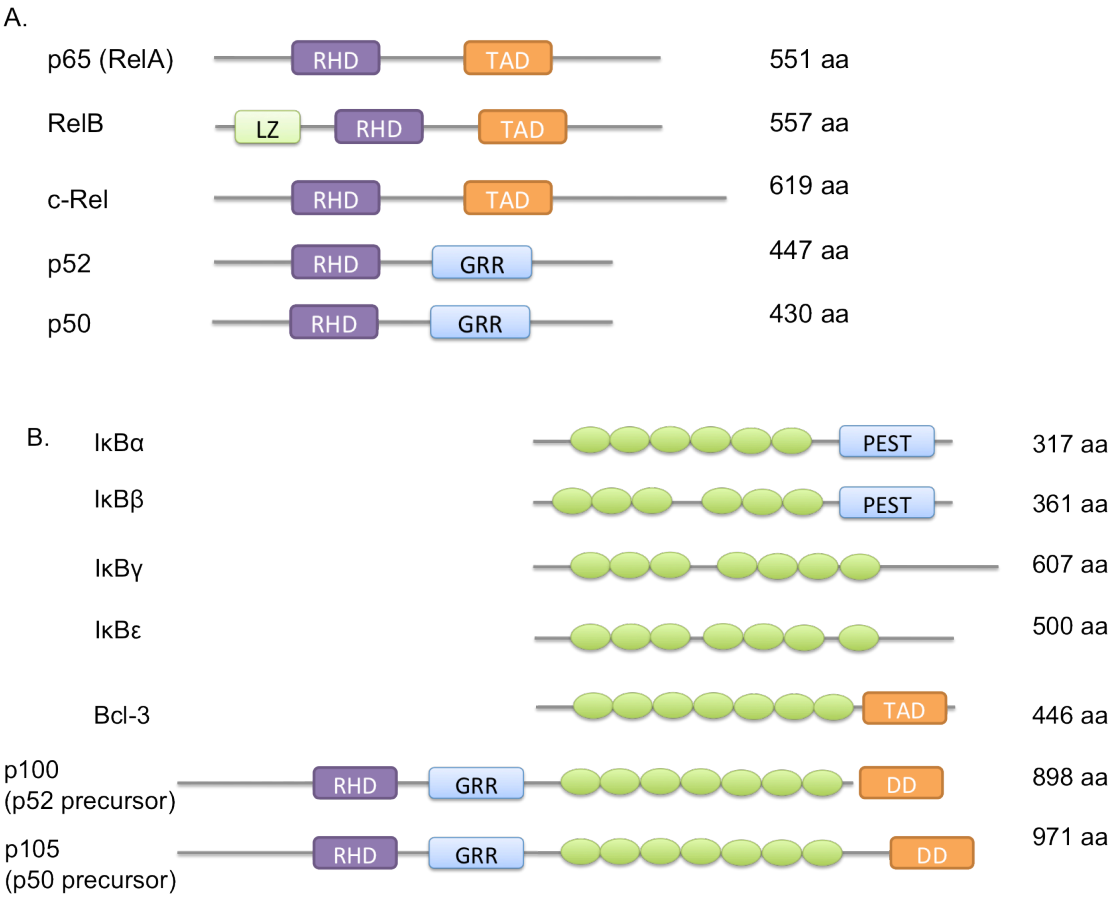

Figure 1.5 NF-κB family members

A. p65, RelB, c-Rel, p50 and p52 share a conserved, multifunctional Rel homology domain (RHD) of approximately 300 amino acids. p65, RelB and c-Rel additionally possess C-terminal transactivation domains (TAD), RelB has a leucine zipper (LZ), p52, p50 and their precursors have glycine-rich regions (GRR).

B. IκB proteins include IκBα, IκBβ, IκBγ, IκBε, Bcl-3 and p52 and p50 precursors p100 and p105 respectively. They contain several ankyrin-repeat motifs (denoted by green ovals). IκBα, IκBβ has proline-, glutamic acid-, serine- and threonine- rich regions (PEST), Bcl-3 posses TAD, p100 and p105 has dimerisation domain (DD), RHD and GRR.

1.2.3 NF-κB signalling pathways

NF-κB proteins are present in an inactive, IκB-bound complex in the cytoplasm and are mainly activated via two pathways known as a canonical (classical) and a non-canonical (alternative) pathway (Gilmore, 2006). In both cases activation by inductive stimuli leads to phosphorylation of IκB proteins by the IκB kinase (IKK) complex and subsequent proteasome-mediated degradation of IκB proteins. Activated NF-κB dimers migrate into the nucleus and regulate the expression of multiple target genes (Viatour et al., 2005).

1.2.3.1 Canonical (classical) pathway

The canonical pathway is induced by inflammatory stimuli, such as tumour necrosis factor-α (TNFα) or interleukin-1 (IL-1) (Perkins, 2007). Such activation leads to formation of an IKK complex (containing the α and β catalytic subunits and two molecules of the regulatory scaffold NEMO) which then phosphorylates IκB at two serine residues, which leads to its ubiquitination at residue K48 and degradation by the proteasome (Figure 1.6) (Gilmore, 2006). Activation by the canonical pathway results in translocation of predominately RelA-p50 heterodimers into the nucleus followed by induced gene expression. This pathway is crucial for the activation of innate immunity and inflammation, and for inhibition of apoptosis (Karin et al., 2004).

1.2.3.2 Non-canonical (alternative) pathway

In the non-canonical pathway, induction by CD40 or lymphotoxin-β leads to activation of the NF-κB-inducing kinase NIK. NIK phosphorylation activates an IKK complex, which in turn phosphorylates p100 two serine residues (S866, S870), leading to its partial proteolysis and liberation of the p52/RelB complex that target distinct κB elements (Figure 1.6) (Gilmore, 2006). This pathway is crucial for secondary lymphoid organ development, maturation of B cells and adaptive humoral immunity (Karin et al., 2004).

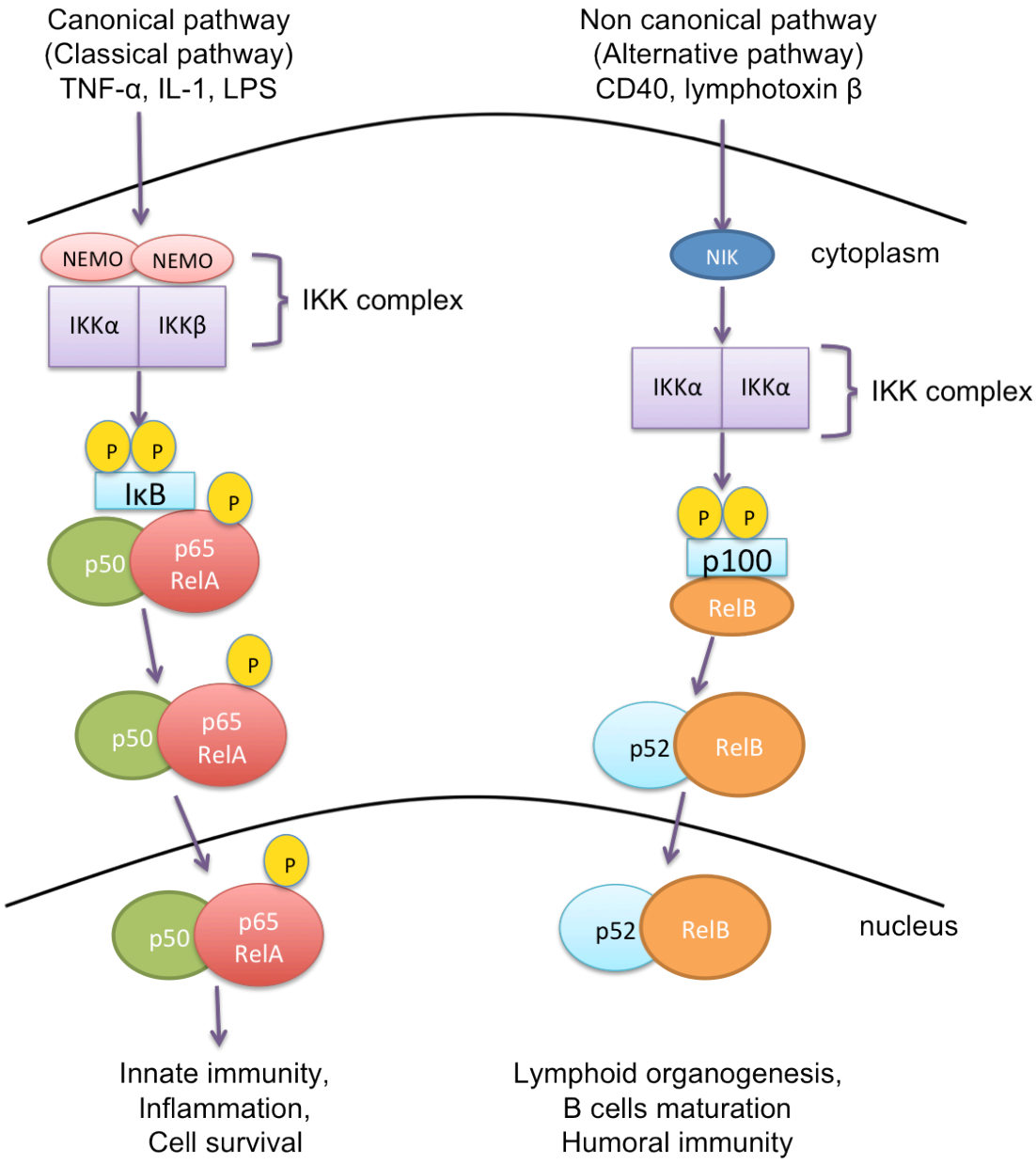

Figure 1.6 NF-κB signalling pathways

Two pathways, known as canonical and non-canonical pathways activate NF-κB signalling. Activation by TNF-α, IL-1 or LPS leads to formation of IKK complex, which phosphorylates IKBα to induce its degradation. This allows translocation of p65/p50 heterodimers to the nucleus. In the case of non-canonical pathway, activation by CD-40 or lymphotoxin-β leads to activation of NIK (NF-κB inducing kinase) and formation of IKK complex, which results in p100 processing and nuclear translocation of RelB-p52 heterodimers. Figure adapted from (Gilmore, 2006, Karin et al., 2004).

1.2.4 NF-κB and cancer development

Given the substantial role that NF-κB plays in both innate and acquired immunity, it is not surprising that experimental evidence are currently revealing the specific mechanisms, by which NF-κB provides the link between inflammation and cancer progression (Naugler et al., 2008, Kim et al., 2006).

A role of NF-κB in cancer is supported from numerous reports, showing the activation of NF-κB in many cancers, including solid cancers, such as breast cancer (Biswas et al., 2004), melanoma (Yang et al., 2007), lung cancer (Tew et al., 2007), colon cancer (Scartozzi et al., 2007), pancreatic cancer (Weichert et al., 2007), oesophageal adenocarcinoma (Izzo et al., 2007), and also in haematological malignancies (Vilimas et al., 2007).

NF-κB activation was shown to promote cell proliferation by activation of the cyclin D1 promoter (Baldwin, 2001). Moreover, NF-κB activation in tumour cells, tumour-associated stromal and endothelial cells plays a role in tumour progression and invasion (Kim et al., 2006).

1.2.5 NF-κB signalling in mammary gland

NF-κB activation in epithelial cells is essential for normal mammary gland development particularly during pregnancy and involution (Clarkson et al., 2000). Post-lactation involution of the mammary gland is characterised by an increase in apoptosis of milk-producing epithelial cells and their replacement by adipocytes (Watson, 2006). The lobuloalveolar development of the mammary gland during pregnancy is driven by the receptor activator of NF-κB ligand (RANKL). RANKL is produced by mammary epithelial cells and acts through its receptor RANK (Karin et al., 2002). NF-κB protects epithelial cells from pro-apoptic stimuli, which is important during involution, when apoptosis is initiated in the majority of epithelial cells (Haffner et al., 2006, Clarkson et al., 2000).

Even though NF-κB signalling is required for normal mammary gland development, inappropriate activation has been linked to tumour progression via stimulation of cell proliferation, pro-survival and metastasis (Haffner et al., 2006).

A number of oncoproteins have been shown to induce NF-κB activation. Importantly ErbB2 can activate NF-κB via the PI3-kinase dependent pathway (Biswas

et al., 2000) and a positive correlation between ErbB2 overexpression and NF-κB activation has been seen in several studies (Biswas et al., 2004, Zhou et al., 2005). Moreover the monoclonal antibody trastuzumab against ErbB2 was shown to block NF-κB activation (Biswas et al., 2004). Additionally, the positive link between ErbB2 expression and NF-κB activation was observed in estrogen receptor negative tumours, suggesting that ErbB2 positive tumours could be preferential targets of NF-κB inhibitors. Interestingly, NF-κB activation leads to the development of hormone-independent, aggressive forms of breast cancers (Zhou et al., 2005, Biswas et al., 2004).

Additionally, certain tumour suppressors can block NF-κB activation, such as CYLD, which has been demonstrated to block NF-κB activation through its deubiquitinating activity (Kim et al., 2006). Furthermore, it was reported that p53 inhibits NF-κB function (Webster et al., 1999).

1.2.5.1 The role of NF-κB in established tumours

NF-κB activation has been described in breast tumour samples and cell lines, *via* activation of the classical pathway by formation of p65/p50 heterodimers (Biswas et al., 2004, Zhou et al., 2005) or *via* non-canonical pathway by p52 and c-Rel subunits (Cogswell et al., 2000). Animal models support the evidence of the role of NF-κB in breast oncogenesis, the over-expression of c-Rel leads to the development of mammary tumours (Romieu-Mourez et al., 2003) and it was shown that activation of NF-κB signalling via c-Rel occurs early during the malignant transformation process (Kim et al., 2000).

Constitutive activation of NF-κB has been implicated in promoting cell survival by protecting cells from undergoing apoptosis (Sonenshein, 1997), which was confirmed by *in-vivo* and *in-vitro* studies. The anti-apoptotic factors that are regulated by NF-κB include cellular inhibitors of apoptosis (cIAPs), inhibitory protein (c-FLIP) and also members of the Bcl-2 family such as Bcl-X_L.

NF-κB controls cell growth through transcriptional regulation of cyclin D1, whose promoter contains NF-κB binding sites. The correlation between cyclin D1 expression and NF-κB activity was observed in breast tumours (Cogswell et al., 2000), while cyclin D1 expression was determined at the earliest stages of breast

cancer progression and once acquired it is detected in all stages of breast cancers (Bartkova et al., 1994).

1.2.5.2 The role of NF-κB in metastatic progression

It was shown that activation of the canonical NF-κB pathway may be implicated in EMT (Huber et al., 2005) by regulation of E-cadherin (Chua et al., 2007) and the transcription factor TWIST (Horikawa et al., 2007).

The degradation of extracellular matrix (ECM) may lead to the separation of the intracellular matrix promoting cell motility and metastatic abilities, while NF-κB regulates matrix metalloproteinases (MMPs) and urokinase-type plasminogen activator (uPA), which are involved in this process (Karin et al., 2002). Interestingly the uPA promoter contains an NF-κB binding site and promotes invasion by stimulating the conversion of plasminogen to plasmin. Plasmin has been shown to mediate invasion by degrading matrix proteins or by activating matrix metalloproteinases (MMPs). Additionally, uPA is also involved in cell adhesion and chemotaxis, therefore it is not surprising that uPA expression is a strong indicator of poor prognosis in breast cancers (Sliva et al., 2002).

Moreover, chemokines inducing cell migration and vascular endothelial growth factor (VEGR) promoting angiogenesis are also regulated by NF-κB (Haffner et al., 2006).

1.2.6 Inhibition of NF-κB signalling

An increasing body of evidence of the role of NF-κB signalling in the cancer development indicates that NF-κB is an interesting target for the development of new therapeutics. In addition, tumour cells in which NF-κB is activated are highly resistant to conventional cancer therapy and NF-κB inhibition substantially increases the sensitivity to treatment (Wang et al., 1999).

However the deletion of p65 was shown to be lethal due to extensive apoptosis of the hepatocytes in mice null for RelA as well as deletion of p65 in breast cancer cell lines caused cell death (Liu et al., 1996, Beg et al., 1995). This has led to the established view that broad spectrum anti-cancer therapy targeting NF-κB pathways may exhibit toxicity.

Despite the potential toxicity associated with a non-specific inhibition, several hundreds of compounds are known to target the NF-κB pathway with many in clinical trials. The NF-κB pathway can be inhibited at various stages as represented in Figure 1.7.

1.2.6.1 Inhibition of the IKK complex

The specific inhibitor against IKK complex is a BAY inhibitor, that irreversibly inhibits IkBα phosphorylation was found to have proapoptotic activity in a various tumour cell lines (Haffner et al., 2006). Interestingly, non-steroid anti-inflammatory drugs (NSAIDs) are known to inhibit Cox-2 activity, but they are also able to inhibit NF-κB activity through a mechanism that involved suppression of IKK (Basseres et al., 2006). There are many other known IKK inhibitors, such as thalidomide or curcumin, and novel inhibitors currently in clinical trials (Karin et al., 2004).

1.2.6.2 Proteasome inhibitors

The 26S proteasome is responsible for the degradation of ubiquitin-tagged proteins, in the case of NF-κB family, degradation of members of the IκB family. Inhibitors of the 26S proteasome were shown to inhibit IκB degradation and therefore the nuclear translocation of NF-κB subunits (Karin et al., 2004, Haffner et al., 2006). The developed reversible inhibitor of the 26S proteasome, Bortezomid, was capable of inducing apoptosis and sensitising cancer cells to chemotherapeutics (Orlowski et al., 2002).

1.2.6.3 Inhibition of phosphorylation, nuclear translocation and DNA binding of NF-κB heterodimers

p65 needs to be phosphorylated by various kinases; this process can be inhibited with compounds such as apigenin and emodin (Haffner et al., 2006). The actual translocation process can be inhibited with silibinin or antibiotic and anti-inflammatory compound known as DHMEQ (Haffner et al., 2006, Karin et al., 2004). DNA binding of NF-κB heterodimers can be inhibited using sesquiterpene lactones such as parthenolide and ergolide (Dey et al., 2008).

1.2.6.4 Conclusion

Even though many inhibitors of the NF-κB pathway are available, they lack the specificity and there is also a high risk of occurrence of side effects (Perkins, 2007, Perkins, 2012, Wu et al., 2005, Karin et al., 2004). In pre-clinical studies and in clinical trials the lack of specificity (e.g. proteasome inhibitors, Bortezomid), efficacy (e.g. inhibitors of the IKK complex) and toxicity (e.g. sesquiterpene lactones) was identified. Moreover, NF-κB activity is required for epithelial homeostasis and therefore its complete inhibition was shown to lead to the development of severe chronic inflammatory conditions (Pasparakis, 2009).

Therefore novel, more specific targets within the NF-κB pathway are essential for the development of novel therapeutics with beneficial outcome and reduced negative consequences. In particular, strategies to modulate, rather than completely inhibit NF-κB pathway have a strong potential (Perkins, 2012).

Disrupting specific interactions with key regulators could selectively regulate NF-κB activity. Targeting a known co-activator of the NF-κB pathway, such as Bcl-3, is a promising route for drug development and might provide a more selective inhibitor with decreased side effects.

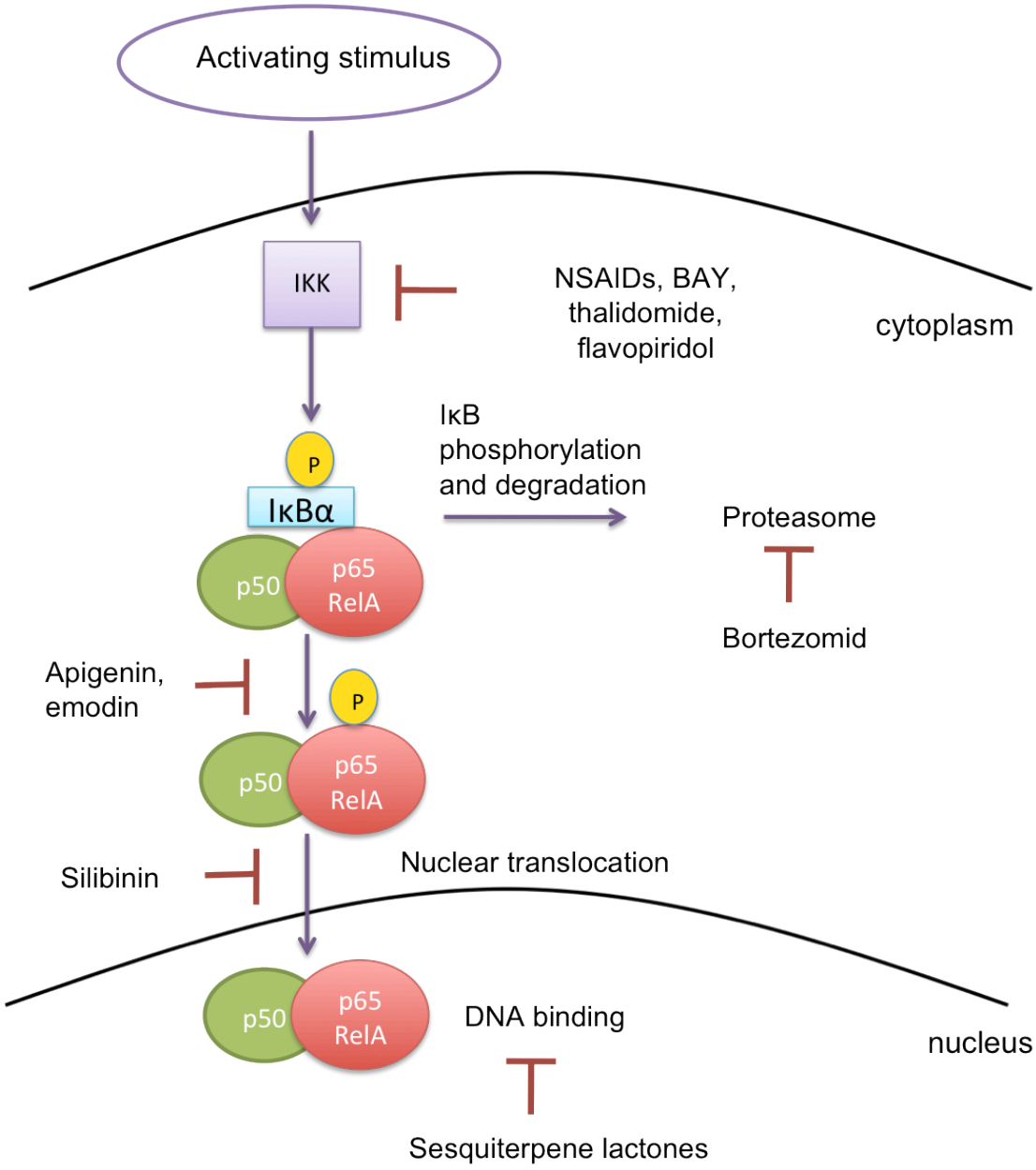

Figure 1.7 Targeting NF-κB signalling
Potential approaches to inhibit the NF-κB pathway can be divided into 5 groups: selective IKK inhibitors, proteasome inhibitors and unique events in the regulation of NF-κB heterodimers (phosphorylation, nuclear translocation and DNA binding). Figure adapted from (Dey et al., 2008, Haffner et al., 2006, Karin et al., 2004)

1.3 B-cell Lymphoma 3

1.3.1 Introduction

The proto-oncogene B-Cell Lymphoma 3 (Bcl-3) was first identified on chromosome 19 adjacent to the breakpoints in the translocation t(14;19)(q32; q13.1) (Ohno et al., 1990) during studies of neoplastic cells from patients with chronic lymphocytic leukemia (McKeithan et al., 1990). Bcl-3 is functionally related to, but distinct from, IκBα because it preferentially interacts with homodimers of NF-κB p50 (Franzoso et al., 1992, Hatada et al., 1992, Wulczyn et al., 1992) and p52 (p50B) (Bours et al., 1993), whereas the primary target for IκB-α is the p65 subunit of NF-κB (Thompson et al., 1995). Bcl-3 localizes predominantly to the nucleus (Bours et al., 1993, Franzoso et al., 1993, Naumann et al., 1993), whereas other members of the IκB family reside exclusively in the cytoplasm where they retain NF-κB dimers.

1.3.2 Regulation of NF-κB signalling by Bcl-3

It is known that Bcl-3 associates with p50 and p52 homodimers, however the precise role of Bcl-3 is controversial and might be also dependent on phoshorylation status (Nolan et al., 1993). Both p50 and p52 proteins from the NF-κB family are transcriptionally inactive, as they lack transactivation domains (Figure 1.5). First reports showed that Bcl-3 activates NF-κB signalling by removing repressive p50 and p52 complexes from NF-κB sites (Bours et al., 1993, Franzoso et al., 1992, Hatada et al., 1992). Subsequent studies revealed that Bcl-3 acts as a co-activator by binding to p50 and p52 homodimers and providing transactivation domains on both sides of the ankyrin repeat domain (Watanabe et al., 1997, Zhang et al., 1994, Naumann et al., 1993, Nolan et al., 1993). Moreover Bcl-3 can release p50 from cytosolic p105-p50 complex, form a complex with p50 homodimers and translocate the formed active complex to the nucleus (Heissmeyer et al., 1999, Watanabe et al., 1997).

Since Bcl-3 can interact with both p50 and p52 homodimers, it regulates both the canonical and non-canonical signalling pathways (Figure 1.8).

1.3.3 Regulation of Bcl-3

In diverse studies it was shown that Bcl-3 can either activate (Franzoso et al., 1993, Fujita et al., 1993) or repress (Kerr et al., 1992, Wulczyn et al., 1992) gene transcription by binding to p50 or p52 homodimers from the NF-κB family. This discrepancy could be caused by the complexity of Bcl-3 regulation as discussed below.

1.3.3.1 Transcriptional regulation

The Bcl-3 gene is approximately 11kb in length and contains nine exons (McKeihan et al., 1994). The expression of Bcl-3 can be regulated by inducible transcription factors such as STAT3 or AP-1. Analysis of the Bcl-3 promoter has identified two AP-1 binding sites and one STAT3 binding site (Brocke-Heindrich et al., 2006, Maldonado et al., 2010). Interestingly, it was found that IL-6 induced Bcl-3 expression is modulated through STAT3 binding to the intronic enhancer HS4 (Brocke-Heindrich et al., 2006).

As Bcl-3 is itself an NF-κB target, therefore its expression can be induced by a number of classic NF-κB stimuli, such as TNF-α and several cytokines (IL-4, IL-6, IL-10) (Heissmeyer et al., 1999, Rebollo et al., 2000, Kuwata et al., 2003). Bcl-3 is also regulated by NF-κB1 and by Bcl-3 itself, creating an autoregulatory loop (Brasier et al., 2001). Recent studies revealed critical functions of specific miRNAs, for instance miR-125b, which is able to downregulate Bcl-3 at the translational level (Guan et al., 2011).

Bcl-3 can be deubiquitinated by CYLD, which binds and removes lysine 63-linked ubiquitin chains from Bcl-3. This regulation mechanism prevents Bcl-3 accumulation in the nucleus and therefore activation of NF-κB signalling (Massoumi et al., 2006).

1.3.3.2 Phosphorylation and degradation

Bcl-3 is phosphorylated at the C-terminus and the phosphorylation status plays an important role in regulating its transcription potential (Dechend et al., 1999). GSK3 phosphorylates two serine residues in the C-terminal region (Viatour et al., 2004a), which leads to ubiquitylation of two lysines in the N-terminal region and subsequent degradation by proteasome subunit PSMB1 (Keutgens et al., 2010). This

mechanism limits intracellular levels of Bcl-3 and therefore prevents Bcl-3 oncogenicity (Viatour et al., 2004b).

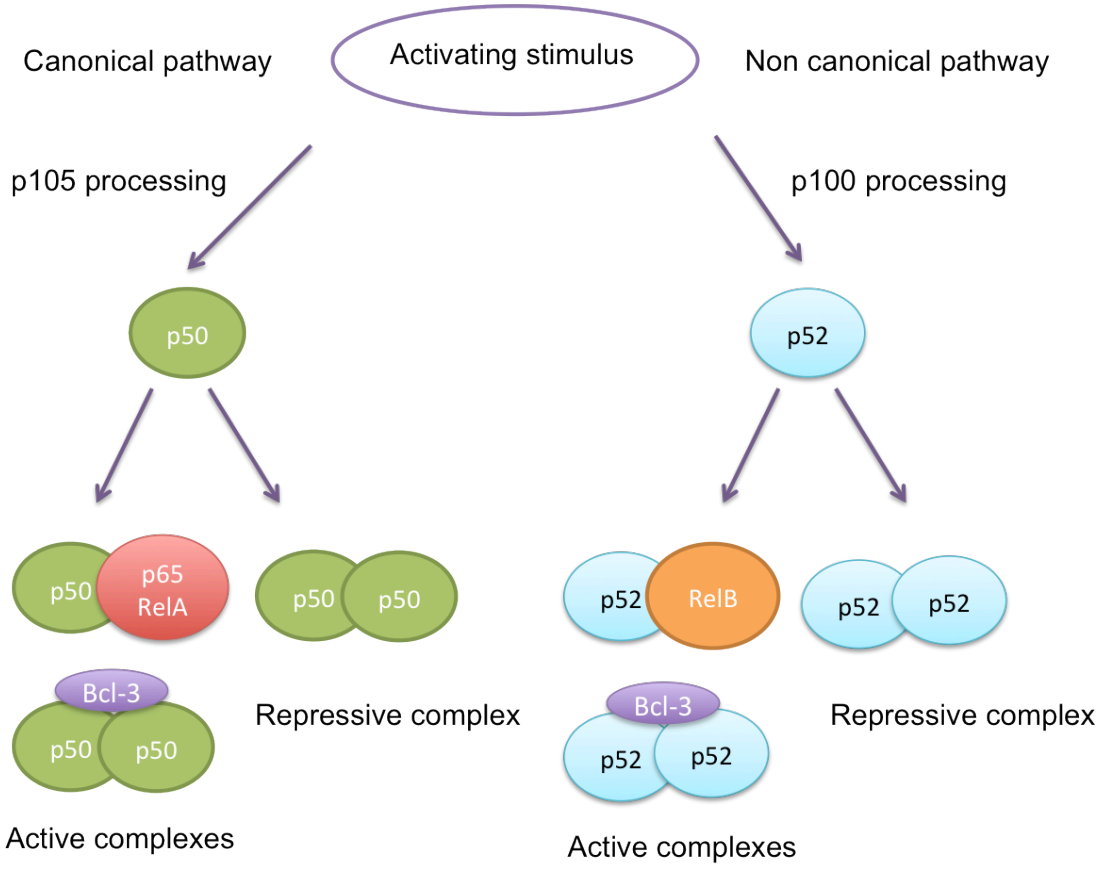

Figure 1.8 The role of Bcl-3 in NF-κB signalling
Bcl-3 plays a role in both the canonical and non-canonical signalling pathways by activation of p50 and p52 homodimers, which alone act as repressive complexes.

1.3.4 The role of Bcl-3 in immune responses

Bcl-3 deficient mice were generated in order to establish the role of Bcl-3 *in vivo*. Mice lacking Bcl-3 gene appeared developmentally normal and healthy, however were susceptible to certain pathogens, such as S. pneumoniae or Toxoplasma gonidii. These findings suggested the important role of Bcl-3 in immune responses. Bcl-3 expression is essential in germinal centre formation in secondary lymphoid organs and for the efficient production of antigen-specific antibodies (Franzoso et al., 1997, Schwarz et al., 1997) .

Similarly, p52 deficient mice failed to form germinal centres and were impaired in their response to certain pathogens (Franzoso et al., 1998). In contrast, mice deficient in p50 developed normal germinal centres and B cell follicles, suggesting that Bcl-3 and p52, but not p50, have several specific biologic functions during antigen-dependent stimulation of lymphocytes (Franzoso et al., 1998). Furthermore, double knock down mice for Bcl-3 and p52 failed to survive more than 4 weeks due to severe multi-organ inflammation (Zhang et al., 2007).

Moreover, Ong *et al.* (1998) reported that Bcl-3 overexpressing mice show splenomegaly and an accumulation of mature B cells in lymph nodes, bone marrow and peritoneal cavity. Even though Bcl-3 expression was not in itself sufficient for B-cell transformation, it led to a generalized accumulation of mature B cells, which was comparable with the pathogenic role of the t(14;19) translocation in B cell malignancies (Ong et al., 1998).

1.3.5 Bcl-3 and cancer

Bcl-3 was first identified in B-cell chronic lymphocytic leukemia in the genetic abnormality t(14;19) (q32;q13) chromosomal translocation. As a result of this translocation, Bcl-3 on 19q13 is juxtaposed to the α constant regions of immunoglobulin heavy chain gene (IgH) on 14q32, leading to increase expression of Bcl-3 mRNA (Ohno et al., 1990).

Bcl-3 overexpression has been reported in multiple myelomas and subtypes of lymphomas, such as anaplastic large-cell lymphomas (ALCLs), classical Hodgkin lymphomas (cHL) and non-Hodgkin's lymphomas, even in the absence of any chromosomal translocation (Au et al., 2002, Nishikori et al., 2003).

An anti-apoptotic role of Bcl-3 was identified in T lymphocytes (Mitchell et al., 2002), and it was suggested that Bcl-3 acts via blocking the known activator of T-cells death, Bim (Bauer et al., 2006). Bcl-3 overexpression was found in peripheral T-cell lymphomas using immunohistochemical staining and tissue microarrays of primary tumours (Mathas et al., 2005).

In addition to the established role of Bcl-3 in leukemias and lymphomas, deregulated Bcl-3 expression has also been reported in solid tumours. In primary tumour samples of nasopharyngeal carcinomas, high levels of p50 homodimers and Bcl-3 proteins were found by Western analysis (Thornburg et al., 2003). Moreover, Bcl-3 coimmunoprecipitated with p50, indicating that in nasopharyngeal carcinomas the repressive binding partner of p50, HDAC1, is replaced by transcriptionally activating Bcl-3 (Thornburg et al., 2003). Aberrant Bcl-3 nuclear expression was also found in 90% of hepatocarcinomas compared with the 26% expression in adjacent normal or cirrhotic liver tissue (O'Neil et al., 2007).

The underlying mechanism for the oncogenic Bcl-3 function has not yet been explained, however it was shown that Bcl-3 expression increases cell proliferation and survival via cyclin D1 upregulation *in vitro*. In a study by Westerheide *et al.* (2001) it was demonstrated that Bcl-3, in complex with p52, can activate cyclin D1 and cells overexpressing Bcl-3 had higher levels of cyclin D1 (Westerheide et al., 2001). Furthermore, cyclin D1 was previously found to be a p53 target (Guardavaccaro et al., 2000), and interestingly the induction of p53 can result in cyclin D1 inhibition via regulation of Bcl-3 protein levels. Bcl-3 repression in a human non-small-cell lung carcinoma cell line (H1299) resulted in an increased association of p52 homodimers with a repressive HDAC1, which led to a p53-induced repression of cyclin D1 (Rocha et al., 2003).

Human breast cancer MCF-7 cells overexpressing Bcl-3 were used in a study by Kashatus *et al.* (2006) to reveal the potential role of Bcl-3 in oncogenesis. Bcl-3 expression led to the suppression of p53 induction following DNA damage, and therefore to decreased apoptotic response than in control cells. p53 activation is controlled via interaction with its inhibitor, Hdm2, whereas overexpression of Bcl-3 resulted in an increase in Hdm2 expression, suggesting a potential mechanism for how Bcl-3 might inhibit p53 in these cells (Kashatus et al., 2006).

In a study by Ahmed *et al.* (2009), Bcl-3 was found to be involved in the basal regulation of cancer cell survival via JNK1/c-Jun. Bcl-3 was downregulated by c-Jun, and c-Jun silencing resulted in increased Bcl-3 expression. Furthermore, Bcl-3 silencing induced apoptosis in human colorectal (HCT116) cells that could not be rescued by co-silencing c-Jun, suggesting that Bcl-3 acts downstream of c-Jun (Ahmed et al., 2009).

The role of NF-κB and Bcl-3 in metastatic colorectal cancer was studied by Puvvada et al. (2010). NF-κB was found activated both in primary and metastatic sites as compared to normal tissue, suggesting that NF-κB activation occurs prior to metastatic spread. Importantly activation of p50 and p65 is associated with survival giving the opportunity for NF-κB as a prognostic factor. Bcl-3 expression was observed in both, normal mucosa and tumour tissue, however a strong positive correlation between tumour nuclear Bcl-3 levels and patient survival was observed. Moreover, a correlation between Bcl-3 and p50 subunit staining was found, suggesting activation of NF-κB via Bcl-3 association with p50. This study provides the first evidence for NF-κB and Bcl-3 as prognostic markers in metastatic colorectal cancer, however further studies in a larger subset of patient samples are clearly needed (Puvvada et al., 2010).

1.3.6 Bcl-3 and breast cancer

There haven't been many studies on Bcl-3 and its role in breast cancer, however published studies have confirmed the oncogenic potential of Bcl-3 in breast cancer as well.

Cogswell *et al.* (2000) was first to analyse breast cancer cell lines and human breast cancer tumour samples for NF-κB and Bcl-3 activation. NF-κB was found activated in various breast cancer cell lines, however the negative correlation between estrogen status and NF-κB activation reported by Biswas *et al.* (2000) was not observed. Seventeen breast carcinomas were analysed by immunohistochemistry and Western blot analysis for nuclear levels of NF-κB proteins. NF-κB subunits p50, p52 and c-Rel were found increased in tumours as compared to adjacent tissue. Interestingly Bcl-3 was found to be significantly elevated in the nuclear extracts of each of the four breast tumours analysed as compared to adjacent tissue obtained from the same patient. Even though a study

with larger patient cohort is needed, increase in Bcl-3 together with p50 and p52 nuclear levels provides a potential mechanism explaining the enhancement in NF-κB dependent gene expression observed in human breast cancer (Cogswell *et al*., 2000).

In a study by Pratt *et al.* (2003) ER+, but estrogen independent MCF-7/LCC1 cells were found not only to have activated NF-κB signalling, but also had elevated Bcl-3 protein levels compared to their ER+ and estrogen dependent parental controls, suggesting that estrogen withdrawal may promote the progression of breast cancer towards a hormone-independent phenotype by activation of NF-κB signalling and Bcl-3. In the same study it was reported that Bcl-3 overexpression *in vitro* in MCF-7 cells increased cyclin D1 levels. MCF-7 cells, overexpressing Bcl-3, transplanted into ovariectomized nude mice with estrogen-release pellets generated a significantly higher number of tumours and with increased tumour volume compared to control. However when the estrogen supply was removed, tumours regressed at the same rate as controls. Therefore Bcl-3 expression alone cannot promote the development of an estrogen-independent phenotype *in vivo* in this animal model, but can augment the growth and tumourigenicity of breast cancer cell lines (Pratt et al., 2003).

A study by Choi *et al.* (2010) identified C-terminal binding protein 1 (CtBP1) as a binding partner of Bcl-3 and a strong positive correlation between the protein levels of Bcl-3 and CtBP1 in human breast cancer cell lines and breast cancer tissues. Data suggested that Bcl-3 stabilizes anti-apoptotic CtBP1 by inhibiting its ubiquitination and provides a novel explanation for the mechanism underlying Bcl-3 oncogenic function. Bcl-3 protein levels were found higher in various breast cancer cell lines (MCF7, HCC1419, HCC38, BT20 and KPL4) than in a normal breast cell line (MCF10A) (Choi et al., 2010), as opposed to a study by Cogswell *et al.* (2000) where Bcl-3 protein levels was not detected in any of the breast cancer cell lines analysed (MCF-7, T47D, MDA231, SKBR3 and BT474) (Cogswell et al., 2000).

Overall, Bcl-3 expression was found higher in breast cancer cell lines and breast cancer patient samples as opposed to non-tumorigenic cell lines and adjacent tissue respectively. Moreover, cells overexpressing Bcl-3 generated

significantly higher number of tumours, which support the importance of Bcl-3 in breast cancer tumour progression.

A recent study conducted by Wakefield *et al.* (2013) showed that in contrast to the proliferation/survival effects of Bcl-3 observed in breast cancer cell lines *in vitro*, Bcl-3 specifically promoted the formation of metastasis of ErbB2 driven tumours in mouse models of breast cancer *in vivo*. Although primary tumour growth in the Bcl-3 deficient ErbB2 (MMTV/neu) mice model was not affected, the occurrence of developed lung metastasis was significantly reduced (by 40%) compared to control. Moreover, a significant reduction in mitotic index (Ki-67) and increase in apoptosis (cleaved caspase-3) was observed by immunohistochemistry of secondary lesions (Figure 1.9A-E) (Wakefield et al., 2013) that was not apparent in the primary lesion.

Consequently, Bcl-3 was knocked down by siRNA in an ErbB2 murine mammary cancer cell line derived from an activated Neu/ErbB2 mammary tumour (MG1361) and transplanted into ErbB2 mice by tail vein injection. The deletion of Bcl-3 resulted in an 80% decrease in lung metastases formation in this experimental model of metastasis as compared to control xenografts (Figure 1.9F). Moreover, suppression of Bcl-3 in MG1361 cells resulted in a significant decrease in cell migratory capacity *in vitro* as determined by the Boyden chamber migration assay (Figure 1.9G), with those cells that had migrated expressing higher levels of Bcl-3 than cells that did not (Wakefield et al., 2013).

Despite these effects on tumour behaviour, Bcl-3-deficiency did not affect normal mammary function (Wakefield et al., 2013). Therefore Bcl-3 is an attractive therapeutic target, at least on the current evidence in HER2 driven breast cancers, which accounts for around 30% of all breast cancers. We proposed therefore that therapeutic inhibition of Bcl-3, with the use of small molecule inhibitors, might prevent metastatic spread of this aggressive subtypes of breast cancers. Given the role of Bcl-3 in other types of cancers as discussed above, there is the added potential that a Bcl-3 inhibitor could also find therapeutic usage in patients with other types of cancers.

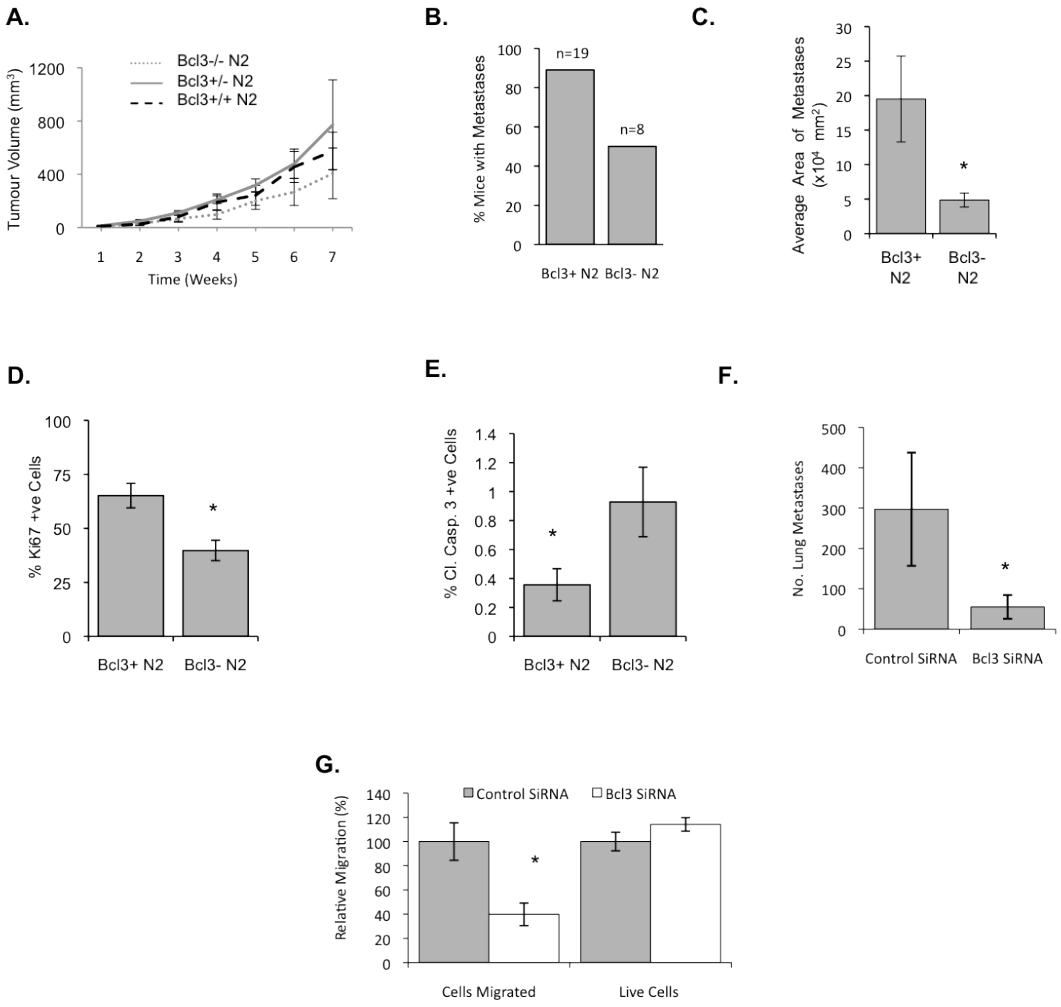

Figure 1.9 Bcl-3 deficiency does not affect tumour growth but reduces ErbB2 metastatic tumour burden

A. Growth rates of Bcl-3+/+ N2, Bcl-3 +/- N2, and Bcl-3 +/+ N2 primary mammary tumours. **B.** Percentage of mice harbouring metastatic lesions in the lung. **C.** Average area of secondary lesions in animals presenting with lung metastases. **D&E.** Quantification of the percentage of Ki-67 and cc3-positive cells respectively from 3 sections per lesion. **F.** Quantification of number of lung metastases per immunodeficient mouse that had received xenografts of Bcl-3 siRNA or control MG1361 cells. **G.** MG1361 cells were transfected either with Bcl-3 siRNA or control siRNA and the migratory ability was assessed by the Boyden chamber migration assay (left). Number of live cells remaining after 24hrs in adherent growth conditions (right). Figure adapted from (Wakefield et al., 2013)

1.4 Project Aims

As described in the introduction, Bcl-3 is a known proto-oncogene with a role in cancer progression. More specifically, it was established that Bcl-3 selectively promoted metastasis in HER2 driven breast cancers using ErbB2 (MMTV/neu) mice models and a HER2+ murine breast cancer cell line (MG1361). The first aim of this study was to:

- Further investigate the role of Bcl-3 in HER2+ and HER2- human breast cancer cell lines using Bcl-3 siRNA to suppress Bcl-3.

Bcl-3 acts as an NF-κB co-activator, we therefore aimed to establish whether Bcl-3 function could be inhibited by disruption of binding to its binding partners, proteins p50 and p52 from the NF-κB family to the same level as Bcl-3 knock down by siRNA.

- Determine the outcome of loss of Bcl-3-p50/Bcl-3-p52 interactions in human tumorigenic and non-tumorigenic cell lines.

As established previously, inhibition of Bcl-3 might be therapeutically beneficial, in particular in aggressive metastatic HER2+ breast cancers. Given that Bcl-3 suppression *in vivo* did not affect normal mammary gland development, inhibition of Bcl-3 is likely to have fewer side effects than global inhibition of NF-κB signalling. Currently there is no known inhibitor of Bcl-3 function. Therefore we aimed to:

- Analyse Bcl-3 structure through molecular modelling and design novel small molecule inhibitors by virtual screening.
- Test candidate compounds for biological activity.
- Establish structure-activity relationships of a panel of structural analogues derived from one or more lead compounds.

Chapter 2

Materials and Methods

2. Materials and Methods

2.1 Cloning procedures

2.1.1 Amplification of DNA constructs

2.1.1.1 Transformation of *E. coli* with DNA

The concentrations of DNA constructs were determined using a nanodrop spectrophotometer (ND-1000; Labtech International) and 50 ng of circular DNA was added to competent *E. coli* cells (C2984; NEB, Herts, UK) and incubated on ice for 30 min. *E.coli* cells were then immersed in a water bath at 42°C for 45 seconds followed by incubation on ice for 2 minutes. Consequently, 250 µl of S.O.C. media (NEB, Herts, UK) were added to *E.coli* cells, which were then left to incubate at 37°C for 1 hour. Transfected *E.coli* were then plated out onto plates coated with agar containing ampicilin at concentration 100 µg/ml (Invitrogen, San Diego, US). Plates were incubated for 12-16 hrs at 37°C. Resulting colonies were then picked and grown in 2 ml of Terrific Broth (TB) media supplemented with ampicilin at concentration 100 µg/ml (Invitrogen, San Diego, US) for 8 hours with constant agitation. For maxi-prep cultures, 1 ml of the resulting culture was removed and incubated with 200 ml of TB-Amp media in a 500 ml conical flask at 37°C for 12 hrs with constant agitation. For DNA isolation, cells were then pelleted by centrifugation at 5000 rpm for 10 min at room temperature.

2.1.1.2 Isolation of DNA from bacterial cells

DNA was isolated from pelleted bacterial growth cultures using QiaPrep MiniPrep Kit or EndoFree Plasmid Maxi Kit (Qiagen, Sussex, UK) depending on the size of cultures and amount of DNA to be extracted. Isolation was carried out according to the manufacturer's instructions. In cases where plasmids were to be used for transfections, the EndoFree Plasmid Maxi Kit was used.

2.1.1.3 Restriction digest reactions

Restriction digest was performed to verify the DNA construct, before being used for cell transfection. Restriction enzymes were obtained from Promega (Southampton, UK) or NEB (Herts, UK) and enzymatic reactions were carried out in

20 µl reaction volumes at 37°C for an hour (Table 2.1). In the case of double digests, the appropriate buffer recommended for optimal activity of both enzymes was used.

Restriction enzyme digest	Single digest	Double digest
Plasmid DNA	1 µg in 17 µl PCR-grade water (Sigma)	1 µg in 16 µl PCR-grade water (Sigma)
10x restriction enzyme buffer	2 µl	2 µl
Enzyme A	1 µl	1 µl
Enzyme B	-	1 µl
Total reaction volume	20 µl	20 µl

Table 2.1 Reaction volumes and components for single or double restriction enzyme digest.

2.1.1.4 Agarose gel electrophoresis

To analyze DNA digest, agarose gel electrophoresis was performed. To 50 ml of 1% w/v agarose gel was added 5 µl of Nucleic Acid Stain (Safe View, NBS Biologicals Ltd., Cambridgeshire, UK) and poured into a gel cast. The comb was inserted immediately and the gel was allowed to set for 30 min. Digested DNA (8 µl) was mixed with 2 µl of a loading dye (Blue/orange 6x loading dye, Promega) and 10 µl per sample was loaded into appropriate well along with 10 µl DNA molecular weight marker (Easy Ladder I, Bioline Reagents Ltd., London, UK). The gel was run at 150V for 30 min. DNA bands were visualized using a GelDoc (BioRad) and the size of bands was identified by comparison to the DNA molecular weight marker.

2.1.2 Bcl-3 constructs

Plasmids containing wild type (WT) or binding mutants (ANK M1, ANK M12 and ANK M123) sequences of Flag tagged Bcl-3 within a pcDNA 3.1 backbone were gifts from Dr. Alain Chariot, Interdisciplinary Cluster for Applied Genoproteomics, Liege. Dr. Alain Chariot generated binding mutants by mutagenesis within the second ankyrin repeat of Bcl-3 molecule (Figure 2.1A), which integrity is required for binding to p50 or p52 proteins, therefore generated mutants have disrupted Bcl-3-

p50 and Bcl-3-p52 binding. The sequence of Bcl-3 WT and selected binding mutant Bcl-3 ANK M123 was confirmed by sequencing (Figure 2.1B-D).

A.

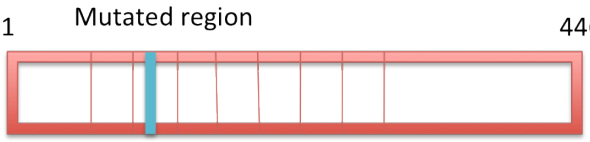

	161												174
Bcl-3 WT	N	N	L	R	Q	T	P	L	H	L	A	V	I	T
Bcl-3 ANK M1	N	N	L	R	Q	T	P	A	H	L	A	V	I	T
Bcl-3 ANK M12	N	N	L	R	Q	T	P	A	H	A	A	V	I	T
Bcl-3 ANK M123	N	N	L	R	Q	T	P	A	H	A	A	V	A	T

B.

Bcl-3 WT

AAC AAC CTA CGG CAG ACA CCG CTC CAC CTG GCT GTG ATC ACC

Bcl-3 ANK M123

AAC AAC CTA CGG CAG ACA CCG GCC CAC GCG GCT GTG GCC ACC

C. Bcl-3 WT

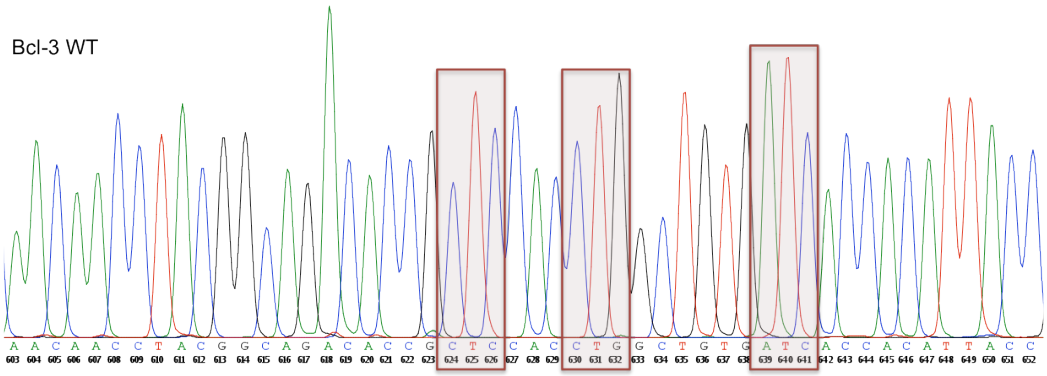

D. Bcl-3 ANK M123

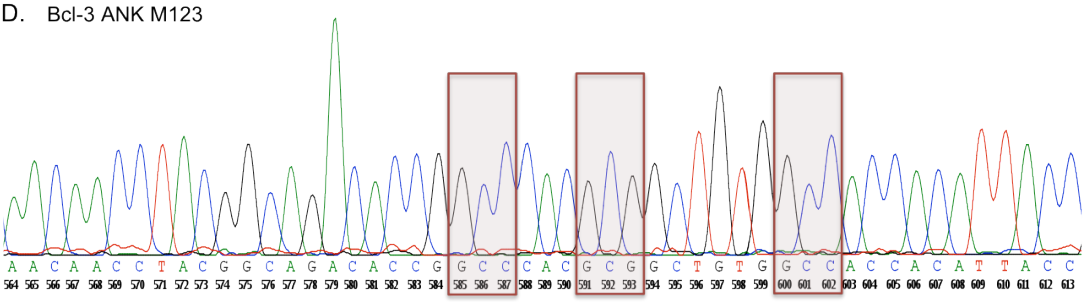

Figure 2.1 Bcl-3 constructs

A. The mutated region is shown in the second ankyrin repeat of Bcl-3. The FLAG-Bcl-3 constructs encode a FLAG-tagged Bcl-3 protein harbouring none, single, double, or triple mutation. The corresponding leucine and isoleucine residues were mutated into alanines, as indicated (Bcl-3 ANK M1, M12, or M123, respectively). **B-D.** Sequencing results showing the Bcl-3 WT construct and the Bcl-3 ANK M123 construct with appropriate mutated base sequence.

2.1.3 A p52 construct within a lentiviral vector

A pCMV-HA plasmid containing wild type (WT) sequence of human p52 was a kind gift from Professor Neil Perkins (Newcastle University, UK). The respective HA-p52 sequence was excised and ligated into p305 lentiviral plasmid by Dr. Syn Kok Yeo (Cardiff University, UK). Dr. Riccardo Brambilla (Cardiff University, UK) kindly packaged the lentiviral construct. The p305 plasmid contains an IRES-GFP sequence, which enables efficient selection of stable overexpressing cells by fluorescence assisted cell sorting (FACS).

2.1.4 NF-κB Luciferase reporter plasmid

NF-κB luciferase assays (detailed in section 2.4.3) were carried out using the 3x κB luciferase reporter plasmid, which was a kind gift from Professor Ron Hay (University of St. Andrews). A pcDNA3.1 plasmid containing the LacZ sequence was used as a control for transfection efficiency (gift from Professor Trevor Dale, School of Biosciences, Cardiff University). For positive and negative controls pGL3 luciferase reporter vectors (Promega) were used, pGL3control and pGL3basic respectively.

2.2 Cell culture maintenance and storage

2.2.1 Experimental cell lines

The human embryonic kidney cells (HEK-293) were a gift from Prof. Vladimir Buchman (School of Biosciences, Cardiff University). The human breast cancer cell lines, MDA-MB-231, SKBR3 and ZR-75-1 were a gift from Dr. Julia Gee (Department of Pharmacy and Pharmaceutical Sciences, Cardiff University). The human normal breast cancer cell line MCF-10A was a gift from Dr. Torsten Stein (Division of Cancer Sciences and Molecular Pathology, University of Glasgow). Descriptions of the main cell lines used are outlined below:

2.2.1.1 HEK-293

HEK-293 is a non-tumorigenic cell line derived from human embryonic kidney cells. HEK-293 cells are convenient for our investigation, because they are easily transfected and have undetectable basal level of Bcl-3 protein.

2.2.1.2 MDA-MB-231

MDA-MB-231 is a highly metastatic, human basal epithelial cell line isolated from the pleural effusion of an adenocarcinoma. The cells are 'triple negative' as they lack estrogen, progesterone and ERBB2 receptor and they strongly over-express EGFR. The expression of receptors in this line has been confirmed by the host laboratory (Figure 2.2) (Wakefield, 2012).

2.2.1.3 SKBR3

The SKBR3 cell line is a poorly metastatic human luminal epithelial cell line derived from a pleural effusion. SKBR3 cells are estrogen and progesterone receptor negative, over-express the ERBB2 receptor and have very low levels of the EGFR receptor. The expression of receptors in this line has been confirmed by the host laboratory (Figure 2.2) (Wakefield, 2012).

2.2.1.4 ZR-75-1

The ZR-75-1 cell line is a moderately metastatic human luminal epithelial cell line derived from a malignant ascitic effusion with infiltrating ductal carcinoma. ZR-75-1 cells are oestrogen and progesterone receptor positive. They express very low levels of the ErbB2 receptor and over-express EGFR. The expression of receptors in this line has been confirmed by the host laboratory (Figure 2.2) (Wakefield, 2012).

2.2.1.5 MCF-10A

MCF-10A is a mammary epithelial cell line and is considered as a model of non-tumorigenic mammary cells. MCF-10 cells were derived from a mammary tissue from a 36-year-old woman in a good health and the immortalized MCF-10A line can grow in culture and has a stable, near-diploid karyotype with modest genetic modifications typical of culture-adapted breast epithelial cells.

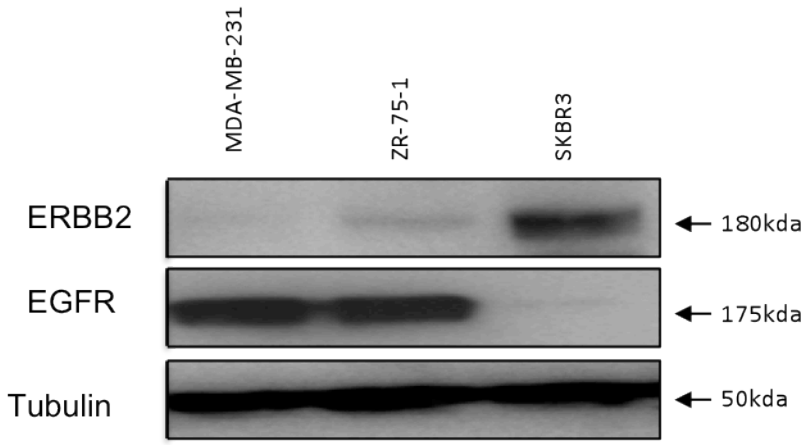

Figure 2.2 Expression of receptors in human breast cancer cell lines
Adapted from (Wakefield, 2012).

2.2.2 Maintenance of cell lines

The HEK-293 cell line was maintained in Dulbecco's modified Eagle's medium (DMEM, Invitrogen) supplemented with 10% v/v foetal bovine serum (FBS, Sigma, Dorset, UK), penicillin (50 u/ml, Invitrogen), streptomycin (50 u/ml, Invitrogen) and L-glutamine (2 mM, Invitrogen). The MDA-MB-231, ZR-75-1 and SKBR3 cell lines were maintained in RPMI medium (Invitrogen) supplemented with 10% v/v FBS, penicillin (50 u/ml Invitrogen) streptomycin (50 u/ml, Invitrogen) and L-glutamine (2 mM, Invitrogen).

MCF-10A cell line was maintained in Dulbecco's modified Eagle's medium nutrient mixture F-12 (DMEM/F-12, Invitrogen) supplemented with 5% v/v horse serum (Sigma, Dorset, UK), penicillin (50 u/ml, Invitrogen), streptomycin (50u/ml, Invitrogen), epidermal growth factor (EGF, 20 ng/ml, Sigma), hydrocortisone (0.5 mg/ml, Sigma), cholera toxin (100 mg/ml, Sigma) and insulin (10 µg/ml, Sigma).

All cell lines were incubated at 37°C and 5% CO_2 in T25 or T80 tissue culture flasks (Nunc, Leics, UK) and were routinely passaged every 3 – 8 days at a split ratio of 1:4 -1:12, when they became 80-90% confluent. Growth media was completely aspirated and the cells were washed with PBS to remove any remaining media. The wash was removed and 1.5 ml for T25 or 3 ml for T80 tissue culture flasks of 0.25% Trypsin/EDTA (Invitrogen) was added to the flask followed by incubation at 37°C for 5-10 min. When the cells were detached, as confirmed by

microscope observation, 3.5 ml for T25 and 7 ml for T80 tissue culture flask of growth media was added to the cells. These were then split at an appropriate ratio by the removal of excess cell suspension into waste. The remaining volume of cell suspension was made up to 5 ml for T25 or up to 15 ml for T80 tissue culture flasks with complete growth media.

2.2.3 Long term cell storage

In order to have sufficient aliquots of low passage number cell lines, cells were frozen and cryo-stored. Respective cells were detached using 0.25% Trypsin/EDTA (Invitrogen) and resuspended in a complete growth media in 15 ml falcon tube, followed by centrifugation at 1100 rpm for 5 min at room temperature. The supernatant was removed and cells were resuspended in a freezing media [complete growth medium containing 10% v/v dimethyl sulfoxide (DMSO; Sigma, Dorset, UK)] and aliquoted into 1 ml cryo tube vials (Nunc, Leics, UK). The tubes were then placed into a container with iso-propanol at room temperature (Fischer Scientific) to facilitate slow freezing at -80°C for 24 hrs before being transferred into liquid nitrogen storage. When cells were retrieved from cryo-storage, they were quickly defrosted to 37°C in a water bath before being resuspended in 10 ml of complete growth media and centrifuged at 1100 rpm at room temperature for 5 min. The cell pellet was resuspended in 5 ml of complete growth media and transferred to a T25 flask.

2.2.4 Cell counting

To allow the seeding of cells at appropriate density, cells were counted using an Improved Neubauer Counting Chamber (Hawksley, Lancing, UK). Cells were detached using 0.25% Trypsin/EDTA (Fisher Scientific) and pelleted by centrifugation at 1100rpm for 5 min at room temperature. Pellets were resuspended in an appropriate volume of complete growth media and 10 µl of cell suspension was loaded into the counting chamber. Cells were counted in four $1mm^2$ squares and the number of cells per ml of suspension was determined by calculating the average count per square and multiplying it by 1×10^4.

2.3 Transfection and transduction of cells

2.3.1 Transient siRNA transfection

In order to achieve Bcl-3 knock down in cell lines, respective cells were transfected with ON-Target plus SMART pool (Dharmacon, Thermo Scientific, Lafayette, USA). The SMART pool siRNA contains a mixture of four siRNAs that target the same gene to increase the efficiency of gene silencing. The negative control siRNA was designed to have minimal targeting of known genes in human (Table 2.2). The SMART pool siRNA (total amount 5.0 nmol) was resuspended according to manufacturer protocol in 250 µl of RNA-free water to obtain required concentration of 20 µM.

Cells were transfected with siRNA using lipofectamine RNAiMAX (Invitrogen, Paisley, UK). Volumes and concentrations of reagents used in different tissue culture plates are outlined in Table 2.3. The appropriate volume of siRNA was diluted in serum-free OPTIMEM (Invitrogen, Paisley, UK) in the well of a tissue culture plate and mixed gently. Lipofectamine RNAiMAX was mixed before use and then the appropriate volume was added to each well containing the siRNA in OPTIMEM. This was mixed and incubated for 20 min at room temperature to allow the siRNA-Lipofectamine complexes to form. Meanwhile, cells were diluted in complete growth media without antibiotics (for seeding concentrations see Table 2.4). Cells were then carefully added to each well containing siRNA-lipofectamine complexes and were incubated at 37°C in 5% CO_2 for 48 hrs before being harvested.

siRNA	Target sequence (5'-3')	Catalogue number
Human Bcl-3 ON-Target plus SMART pool	AGACACGCCUCUCCAUAUU	Dharmacon (Thermo Scientific) L-003874-00-0005
	GGCCGGAGGCGCUUUACUA	
	GCGCAAAUGUACUCCGGCA	
	GCCGGGAGCUCGACAUCUA	
Human control ON-Target plus SMART pool	UGGUUUACAUGUCGACUAA	Dharmacon (Thermo Scientific) D-001810-10
	UGGUUUACAUGUUGUGUGA	
	UGGUUUACAUGUUUUCUGA	
	UGGUUUACAUGUUUUCCUA	

Table 2.2 ON Target plus SMART pool sequences

Tissue culture vessel	Plating medium	Opti-MEM dilution medium	Final siRNA conc. (nM)	Volume of 20 µM siRNA	Lipofectamine RNAiMAX
24-well	500 µl	100 µl	20	0.8 µl	1 µl
6-well	2.5 ml	500 µl	20	4 µl	5 µl

Table 2.3 Volumes and concentration of reagents for transient siRNA transfection in different culture plates

Tissue culture vessel	Number of cells plated for si-RNA transient transfection			
	HEK-293	**MDA-MB-231**	**ZR-75-1**	**SKBR3**
Cells/ml	$2x10^5$	$2x10^5$	$2x10^5$	$3x10^5$
96-well	$2x10^4$	$2x10^4$	$2x10^4$	$3x10^4$
24-well	$1x10^5$	$1x10^5$	$1x10^5$	$1.5x10^5$
6-well	$5x10^5$	$5x10^5$	$5x10^5$	$7.5x10^5$

Table 2.4 Number of cells plated for siRNA transient transfection, stable transfection or transfection of cells with reporter plasmids for NF-κB reporter plasmids

2.3.2 Transfection of cells with plasmid DNA

To generate cells overexpressing either Bcl-3 WT or Bcl-3 ANK M123 (constructs are described in section 2.1.2), cells were transfected using Lipofectamine LTX reagent (Invitrogen, Paisley, UK). Cells were seeded at appropriate density (Table 2.4) into 24-well plates in antibiotic free culture media 24 hrs prior transfection. On the day of transfection, required amount of DNA was diluted in 100 µl serum-free OPTIMEM (Invitrogen, Paisley, UK) for each well of cells to be transfected. For MDA-MB-231 cell line, PLUS reagent (Invitrogen, Paisley, UK) was added to the plasmid mixture and cultivated at room temperature for 5 min. The experimentally determined amounts of Lipofectamine LTX reagent was added into previously diluted OPTIMEM-DNA solution (Table 2.5) mixed gently and cultivated at room temperature for 30 min. Consequently, the transfection mixture was added dropwise into wells and cells were incubated for 24 hrs at 37°C in 5% CO_2 before being selected for transgene expression.

	HEK-293	**MDA-MB-231**
DNA	500 ng	500 ng
Lipofectamine LTX	1.5 µl	1.75 µl
PLUS reagent	/	0.5 µl

Table 2.5 Volumes of reagents for stable transfection of cells with plasmid DNA in 24 well plate format

2.3.3 Generation of stable overexpressing clones

Stably transfected cells were selected by the addition of neomycin (G418, Sigma, Dorset, UK) to the culture medium for at least 7 days. Under selective conditions, resistant cells outgrow non-resistant cells, resulting in a polyclonal population of stably expressing cells. The required concentration of neomycin was determined experimentally for each cell line and varies in a range of 0.3-0.5 mg/ml. When needed, monoclonal populations were generated by diluting cells in 96-well plate to a concentration of 3 cells/well in 100 µl of complete growth media supplemented with neomycin. After about 2 weeks, resistant clones were selected, expanded and analysed for Bcl-3 expression (see individual experiments). The expression levels were regularly controlled by QRT-PCR (see section 2.6.3) and cells were passaged for a maximum of 20 passages.

2.3.4 Lentiviral transduction of cell lines

To generate cells stably overexpressing p52 WT, respective cells were seeded in 96-well plates at densities of $1x10^4$ cells per well. After 24 hours, media was removed from wells and replaced with 110 µl of complete growth culture media containing hexadimethrine bromide (Sigma, Dorset, UK) at a final concentration of 8 µg/ml. Plates were gently swirled and 5 µl/per well of p52 WT lentiviral construct was added. Cells were incubated at 37°C with 5% CO_2 for 18-20 hrs. After that, the media in wells was replaced with 120 µl of fresh culture media. Consequently, cells were passaged on to establish stably transduced cell lines.

2.3.5 Transfection of cells with reporter plasmids

For NF-κB luciferase assays (see section 2.4.3), cells were seeded into clear bottom black 96-well plates (Corning Inc., Lowell, US) in antibiotic free culture media in appropriate density (Table 2.6). After 24 hrs, cells were transfected with 10 ng of 3x κB luciferase plasmid and 10 ng of pcDNA3.1-LacZ plasmid per well. Empty pcDNA3.1 plasmid was also included to normalize the total weight of DNA transfected to 100 ng. For positive and negative controls respectively, 10 ng of pGL3control or pGL3basic were transfected in place of 3x κB luciferase plasmid. Transfection was carried out using Lipofectamine LTX reagents as described in section 2.3.2.

	HEK-293	MDA-MB-231	SKBR3	ZR-75-1
DNA	100 ng	100 ng	100 ng	100 ng
Lipofectamine LTX	0.3 µl	0.35 µl	0.35 µl	0.35 µl
PLUS reagent	/	0.1	/	0.1 µl

Table 2.6 Volumes of reagents for transfection of cells with NF-κB reporter plasmids in 96 well plate format

2.4 Cell based assays

2.4.1 Cell Titre Blue viability assay

The viability of cells at experimental endpoints for particular assays was determined using the Cell Titre Blue reagent (Promega, Southampton, UK). This reagent measures the cellular metabolic activity using resazurin as an indicator dye. Viable cells, therefore metabolically active, will reduce resazurin into highly fluorescent resofurin. The resulting fluorescence levels are measured and indicate cell viability.

Cells were plated at low confluency (Table 2.7) into 96 well plate in 100 µl of complete growth media in triplicates and were incubated at 37°C in 5% CO_2 for the desired test exposure period (see individual experiments). For each 100 µl of media in 96 well plate, 20 µl Cell Titre Blue reagent was added followed by incubation for an hour at 37°C in 5% CO_2. Fluorescence was then measured by setting excitation/emission wavelengths to 560/590 nm on a Flurostar Optima plate reader (BMG Labtech, Bucks, UK).

	Number of cells plated in 96-well format			
	HEK-293	**MDA-MB-231**	**SKBR3**	**ZR-75-1**
Plating medium	100 µl	100 µl	100 µl	100 µl
Cells per well	$5x10^3$	$5x10^3$	$1x10^4$	$1x10^4$
Cells per ml	$5x10^4$	$5x10^4$	$1x10^5$	$1x10^5$

Table 2.7 Seeding densities for Cell Titre blue viability assays and cell count

2.4.2 Cell count

To establish cell viability over time period of three days, respective cells were seeded at low confluency (Table 2.7) into 96 well plate in 100 µl of complete

growth media in triplicates and were incubated at 37°C in 5% CO_2. After 24 hrs, cells from triplicate wells for the first time point were detached using 0.25% Trypsin/EDTA (Invitrogen) and resuspended in complete growth media and individually counted. The same was done for each cell line at 48 hrs and 72 hrs post-seeding.

2.4.3 Determination of caspase activity in cells

Caspase-Glo 3/7 assay (Promega, Southampton, UK) is a luminescent assay that measure the activity of individual caspase 3/7 by providing a luminogenic substrates for individual caspases. Addition of the Caspase-Glo reagent to the sample results in cell lysis followed by caspase cleavage of the substrate and a resulting luminescent signal which is proportional to the amount of caspase activity present in the sample.

Analysed cells were removed from tissue culture plates using 0.25% w/v Trypsin/EDTA and centrifuged at 1100 rpm for 5 min before being resuspended in complete growth medium. Cells were counted and resuspended at a density of $1x10^5$ cells/ml and 100 µl of this suspension was plated into appropriate wells of a black-walled 96-well plate. At the same time, 100 µl of complete media alone was plated into triplicate wells to serve as a 'blank' control. The plate was incubated at 37°C and 5% CO_2 for 24 hrs. After incubation, Caspase-Glo reagent was prepared according to manufacturer's instructions. To each well containing cells or 'blank' controls, 100 µl of Caspase-Glo reagent was added. The plate was then gently agitated on a plate shaker at 400 rpm for 30 seconds before being incubated at room temperature for an hour. The luminescence of each sample was then measured on a FLUOstar Optima plate reader and the 'blank' control value was subtracted from all other values.

2.4.4 NF-κB luciferase reporter assay

After 48 hrs post-transfection with luciferase reporter plasmid, the media was aspirated and cells were lyzed using 50 µl/well of Glo-lysis buffer (Promega, Southampton, UK). The plate was left on a rocker for 20 min to facilitate complete cell lysis. Then, 20 µl of lysate from each well was removed and transferred into a new clear bottom black well plate for measuring LacZ activity as a transfection

efficiency control and followed by addition of 20 µl/well of Beta-Glo substrate (Promega, Southampton, UK) and cultivation at room temperature for at least 20 min. Subsequently, 30 µl/well of Bright-Glo luciferase substrate (Promega, Southampton, UK) was added to the original plate and asses immediately for luminescence activity. The luminescence produced from either reaction was read using a Flurostar Optima plate reader (BMG Labtech, Bucks, UK). The resulting luciferase activity was then normalized against lacZ activity obtained from Beta-glo measurement and is displayed as relative light units (R.L.U).

2.4.5 Boyden chamber migration assay

The migratory or invasive capacity of human mammary cancer cell lines was assessed by the Boyden chamber assay. Cells were seeded in low serum media in a chamber with porous membrane (transparent polyethylene terephthalate (PET) membranes with 8µm pores) as a solid support for motility assays or with a porous membrane coated with Matrigel Basement Membrane Matrix (BD BioCoat Growth factor reduced invasion chambers) for invasion assay. The cell insert was placed into a well with complete growth media, therefore cells are stimulated by a serum gradient to migrate or invade across the membrane through pores.

Total of 750 µl of complete growth media containing 10% of serum was added to appropriate wells of a 24 well cell culture insert companion plate (BD Biosciences, Oxford, UK). A cell culture insert (BD Biosciences, Oxford, UK) was then carefully placed into each well of the insert companion plate using tweezers. Cells were detached from tissue culture plates using 0.25% w/v Trypsin/EDTA (Invitrogen) and centrifuged at 13000 rpm for 5 min. Cells were washed twice in serum free media by resuspension and centrifugation. The appropriate number of cells ($2x10^5$ cells/ml for MDA-MB-231 cells) was resuspended in normal growth media containing only 0.1% serum. 350 µl of the cell suspension was added to the appropriate upper chambers of the cell culture inserts and plates were incubated for 24 hrs at 37°C and 5% CO_2.

2.4.5.1 Visualization of migrated cells

After incubation, cells on membranes were fixed by replacing the media in the top and bottom sections of the chamber with 70% ice-cold ethanol (Fisher

Scientific). Plates were incubated at -20°C for at least an hour. After fixation, inserts were immersed in tap water using tweezers to ensure all ethanol was removed. A moistened cotton wool bud was then used to mechanically remove all cells fixed on the upper side of the membranes. Cells were stained by individually immersing the inserts into filtered Harris' Haematoxylin (Sigma, Dorset, UK) for 1 min. Following this, inserts were washed in a beaker of tap water to remove the dye and immersed in 0.5% filtered Eosin (Sigma, Dorset, UK) for 2 min. Stained inserts were then washed again in a tap water.

2.4.5.2 Mounting of membranes

Glycerol Gelatin (Sigma, Dorset, UK) was heated in a beaker of boiling water and once liquefied, a drop was placed onto an appropriately labelled microscope slide (R.A.Lamb, Loughborough, UK). Membranes were cut out of the insert and transferred onto the corresponding slide with tweezers. Glycerol Gelatin was added to the top of the membranes and a cover slip was placed on the slide under firm pressure. Mounted slides were left to air dry before being analysed.

2.4.5.3 Invasion index

The number of cells invaded is represented as the percentage of cells invaded through the Matrigel Matrix membrane relative to the migration through the control membrane.

Determine Percent of invasion:

$$\% \text{ Invasion} = \frac{\text{Mean of cells invading through Matrigel Matrix membrane}}{\text{Mean of cells invading through Control insert membrane}} \text{ x } 100$$

2.4.6 Mammosphere assay

Mammosphere assay can be used to select breast cancer stem cells (bCSCs) based on their ability to survive under non-adherent conditions and to self renew. The resulting mammosphere colonies are enriched for mammary stem/early progenitor cells that are able to undergo self-renewal and form new colonies upon disaggregation and reseeding (Figure 2.3).

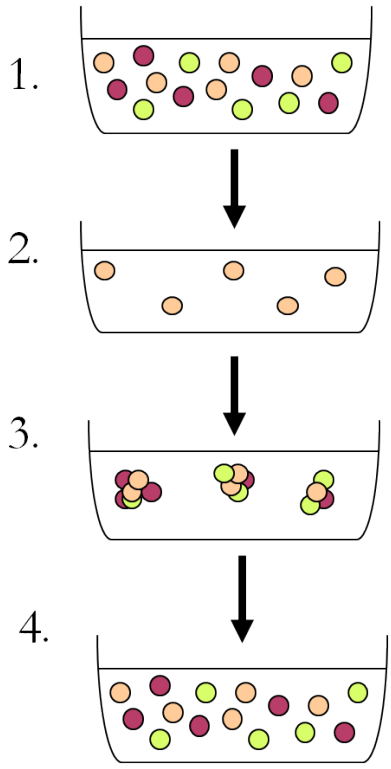

Figure 2.3 Mammosphere assay
1. Breast cancer cell lines from a monolayer are transferred to non-adherent condition
2. Non-stem cells die leaving only bCSCs
3. After 7 days the bCSCs have divided to form mammospheres forming units (MFUs), while 1MFU represents 1bCSC
4. MFUs contain both stem and differentiated cells, which can be disaggregated and re-subjected to the same assay to assess self-renewal ability

Cells were detached from tissue culture plates, dissociated into single cell suspension by centrifugation at 1300 rpm for 5 min and resuspended in mammosphere culture medium. This medium is serum-free epithelial growth medium (MEBM, Lonza, Slough, UK) supplemented with B27 (Invitrogen, Paisley, UK], 20 ng/ml Epidermal Growth Factor, 5 mg/ml Insulin, 0.0008% v/v β-mercaptoethanol and 1mg/ml hydrocortisone (all from Sigma, Dorset, UK). Cells were seeded at density of 2000 cells/well in 200 µl mammosphere medium into ultra-low attachment plates (Corning Inc., Lowell, USA) and incubated for 7 days at 37°C and 5% CO_2 to allow the formation of mammosphere colonies. The numbers of mammospheres formed per well were counted and represent the percentage of MFUs per number of cells seeded. To measure the size of spheres, images of individual spheres were obtained using Olympus BX41 Light Microscope (Olympus,

Essex, UK) and Colorview III camera (Soft Imaging Systems) and the diameter of spheres was measured with ImageJ software.

In order to determine the self-renewal capacity of cells, mammospheres were enzymatically dissociated into single cells using 0.25% w/v Trypsin/EDTA and re-seeded at density of 2000 cells/well in 200 µl mammosphere media into ultra-low attachment plates. The numbers of mammospheres were counted after 7 days of incubation at 37°C and 5% CO_2.

2.4.7 Flow cytometry

Fluorescence activated cell sorting (FACS) was performed on a FACS Canto Flow Cytometer (BD) and analysis of results was undertaken using a FlowJo software package. Gates were set to exclude >99% of cells labelled with appropriate dye. Flow cytometry was used to analyse the proportion of live/dead cells, cell cycle and GFP staining within respective samples. The analysis was performed either on stable transfected cells or siRNA transient transfected cells. For siRNA transfection respective cells were plated in 6-well format and transfected either with Bcl-3 siRNA or control siRNA for 48 hrs in triplicates. Cells were detached using 0.25% Trypsin/EDTA (Invitrogen) and resuspended in 10 ml of complete growth medium and centrifuged at 1300 rpm for 5 min. The cell pellet was washed twice in 1 ml PBS before being stained with appropriate dye.

2.4.7.1 Cell cycle analysis

For cell cycle analysis, cell pellets were resuspended in 100 µl of PBS and 900 µl of cold 100% Ethanol (Fisher Scientific) and stored at 4°C overnight. After fixation, cells were washed in PBS and resuspended in 1 ml of PBS. Cells were incubated with 10 µl of RNaseA (at concentration 10 mg/ml, Sigma, Dorset, UK) for 30 min at 37°C to remove any RNA present. Cells were washed in PBS and resuspended in 400 µl of PBS and 5 µl of Propidium Iodine (at concentration 1 mg/ml, Sigma, Dorset, UK) was added and incubated for at least 30 min on ice before being analyse by FACS at 585/42 PE-A.

2.4.7.2 Live/dead analysis

Cells were stained by adding 4 µl of 1:10 fixable near-IR live/dead stain (Invitrogen) to the cell pellet and incubated for 30 min at 4°C. Cells were then washed in PBS and resuspended in 400 µl of PBS before being analyze by FACS at 780/60 PE Cy7-A.

2.4.7.3 GFP analysis

To analyse the GFP staining, appropriate cells were resuspended in 400 µl of PBS and analysed by FACS at 530/30 FITC-A.

2.5 Protein analysis

2.5.1 Protein extraction from cells

Proteins were extracted from cells in order to be analyzed by Western blotting or ELISA assay. The media from tissue culture flask was removed and cells were rinsed with ice cold PBS (Sigma, Dorset, UK). Appropriate volume of PBS (5 ml for T25, 10 ml for T80) was added into the flask and cells were removed with a cell scraper (Nunc, Leics, UK). The cell suspension was then transferred to 15 ml tubes and centrifuged at 11000 rpm for 5 min at room temperature. The resulting pellet was used for protein extraction immediately or stored at -80° C prior use.

2.5.1.1 Whole cell protein extraction under denaturing condition

Denaturated whole cell protein extracts were isolated using RIPA buffer (Table 2.8) with the addition of complete mini protease inhibitor tablets (Roche, Welwyn Garden City, UK), 10 mM sodium fluoride (Fluka Biochemika), 1 mM sodium pyrophospate and 1 mM sodium orthovanadate (Sigma, Dorset, UK). Cell pellets from section 2.5.1 were resuspended in appropriate volume of RIPA buffer (50-200 µl). The cell suspension was passed through a 23G needle 10 times to ensure complete cell lysis and incubated on ice for 30 minutes. Lysates were centrifuged at 10000 rpm for 15 min at 4°C to pellet cell debris and the supernatant was aliquoted into fresh tubes and use immediately or stored at -20°C until required.

2.5.1.2 Whole cell protein extraction under non-denaturing condition

Non-denaturated protein extract was prepared using non-denaturing lysis buffer (Table 2.8) and used to analyze protein-protein interaction. Complete mini protease inhibitor tablets (Roche, Welwyn Garden City, UK), 10 mM sodium fluoride (Fluka Biochemika), 1 mM sodium pyrophospate and 1 mM sodium orthovanadate (Sigma, Dorset, UK) were added to the buffer prior use. Cell pellets from section 2.5.1 were resuspended in appropriate volume of non-denaturing buffer (50-200 µl) and incubated on ice 5 min. Cell suspensions were transferred to microcentrifuge tubes and sonicated on ice (3 times 5s) and centrifuged at 10000 rpm for 10 min at 4°C. The resultant supernatant was used immediately or stored at -20°C until required.

RIPA buffer pH 7.4	**Non-denaturing buffer**
50 mM Tris pH 8 (Sigma)	20 mM Tris pH 7.5 (Sigma)
150 mM sodium chloride (Sigma)	150 mM sodium chloride (Sigma)
1% v/v Nonidet-P40 (Roche)	1% v/v Nonidet-P40 (Roche)
0.1 % w/v sodium dodecyl sulphate (SDS, Sigma)	1 mM EDTA pH 8.0 (Fischer Scientific)
0.5 % w/v sodium deoxycholate (Sigma)	1 mM EGTA pH 8.0 (Fluka Biochemika)

Table 2.8 Composition of buffers for whole cell protein extraction

2.5.2 Determination of protein concentrations

Protein concentrations were analysed using the BCA protein Assay kit (Pierce, Loughborough, UK) according to manufacturer's instructions. Respective protein samples (5 µl) were added to 25 µl of BCA reagent and incubated at 37°C for 30 min. A blank sample was prepared by addition of RIPA buffer (5 µl) into 25 µl of BCA reagent. The resulting colometric changes were measured using a nanodrop spectrophotometer (ND-1000; Labtech International) at 562 nm. A standard curve was determined from a set of samples of known concentrations of bovine serum albumin and was used to extrapolate the relative concentration of protein extracts.

2.5.3 Western analysis

2.5.3.1 Preparation of protein samples

Protein extracts were diluted with RIPA buffer (see Table 2.8 for composition) to a final volume of 24 µl, while total amount of protein was kept between 30-60 µg. Then 6 µl of 5x Laemmli buffer (see Table 2.10 for composition) was added to each sample and proteins were denatured by heating to 95°C for 5 min.

2.5.3.2 Casting of polyacrylamide gels

SDS-PAGE gels consist of resolving and stacking phases, while the % of acrylamide used in the resolving phase depends on the size of proteins to be analysed. Because our proteins of interest were about 50 kDa, the 10% resolving gel was used (see Table 2.9 for composition). SDS-PAGE gels were set using Mini-Protean III (Bio-Rad, Hempstead, UK) gel casting apparatus. Casting plates were cleaned with 70% ethanol (Fisher Scientific) before being assembled in a gel casting apparatus and filled to approximately two thirds with the resolving gel. Once set, the stacking gel was poured over the resolving gel and a 10 or 15-well comb was inserted immediately. Consequently, the combs were removed and the wells were rinsed with distilled water.

10% Resolving gel	**4% Stacking gel**
4.1 ml distilled water	6.1 ml distilled water
3.3 ml 30% Acrylamide (Sigma)	1.3 ml 30% Acrylamide (Sigma)
100 µl 10% w/v sodium dodecyl sulphate (SDS, Sigma)	100 µl 10% w/v sodium dodecyl sulphate (SDS, Sigma)
2.5 ml 1.5M Tris-HCl pH 8.8 (Sigma)	2.5 ml 0.5M Tris-HCl pH 6.8 (Sigma)
100 µl 10% w/v ammonium persulphate (APS, Sigma)	100 µl 10% w/v ammonium persulphate (APS, Sigma)
15 µl TEMED (Sigma)	15 µl TEMED (Sigma)

Table 2.9 Composition of gels for SDS-PAGE

2.5.3.3 Gel electrophoresis

Protein separation was performed using the Mini-Protean III (Bio-Rad, Hempstead, UK) electrophoresis tank containing Tris-Glycine running buffer (see

Table 2.10 for composition). Protein molecular weight marker (PageRuler Plus; Fermentas, Loughborough, UK) was loaded into the first lane of each gel and prepared protein samples were loaded into the appropriate remaining wells and gels were run for 1 hour at 180V.

2.5.3.4 Transfer of proteins to PVDF membranes

Before transfer, Immobilon-P polyvinylidene difluoride membrane (PVDF, Milipore, Watfor, UK) was cut to a required size and soaked in methanol (Fisher Scientific, Loughborough, UK) for 10 sec and washed in PBS/T [phosphate buffer saline (PBS, Sigma, Dorset, UK) supplemented with 1% v/v Tween (Sigma, Dorset, UK)]. The membrane sandwich was assembled according to manufacturer's instructions in a wet electroblotting system (Bio-Rad, Hempstead, UK) using sponges, filter papers, membrane and the prepared gel. Air bubbles were carefully rolled out after the addition of each layer. An ice block was inserted into the transfer apparatus and proteins were transferred in 1 x Tris-Glycine transfer buffer (see Table 2.10 for composition) at 80V for 45 min.

Laemmli Buffer	**10x Electrophoresis buffer pH 8.3**	**1x Tris-Glycine running buffer**	**1x Tris-Glycine transfer buffer**	**Stripping buffer**
0.125 M Tris-HCl pH 6.8 (Sigma)	30.3 g Trisma base (Sigma)	50 ml 10x electrophoresis buffer	100 ml 10x electrophoresis buffer	62.5 mM Tris-HCl pH 6.8 (Sigma)
4% w/v SDS (Sigma)	144.4 g Glycine (Sigma)	5 ml 10% w/v SDS (Sigma)	200 ml methanol (Fisher Scientific)	2% w/v SDS (Sigma)
40% v/v glycerol (Sigma)	Distilled water up to 1 l	380 ml distilled water	700 ml distilled water	0.7% v/v beta-mercaptoethanol (Sigma)
0.1% w/v bromophenol blue (Sigma)				
6% v/v beta-mercaptoethanol (Sigma)				

Table 2.10 Composition of buffers used in Western analysis

2.5.3.5 Probing of membranes

Following transfer, membranes were washed in PBS/T and blocked in milk blocking solution (5% w/v non-fat milk in PBS/T) under agitation for at least an hour at room temperature. Membranes were then incubated in 5 ml of primary antibody

(Table 2.11) at 4°C on a roller mixer (Stuart, Merton, UK) overnight. After cultivation, membranes were washed in PBS/T followed by cultivation with appropriate secondary antibody (Table 2.12). Membranes were then washed again in PBS/T prior to protein detection by enhanced chemiluminesence.

Target	Species	Dilution ratio	Antigen size	Catalogue number
Bcl-3	Rabbit	1:200	~ 50 kDa	Santa Cruz (sc-185)
p52	Rabbit	1:200	~ 52 kDa	Santa Cruz (sc-848)
Flag	Mouse	1:1000	-	Sigma (F 3165)
HA	Rabbit	1:500	-	Cell signalling (C 29F4)
B-actin	Mouse	1:1000	~ 42 kDa	Sigma (A 5316)

Table 2.11 Details of primary antibodies used for Western blotting analysis

Target	Species	Dilution ratio	Catalogue number
Rabbit	Goat	1:2000	DAKO (P0448)
Mouse	Goat	1:2000	DAKO (P0447)

Table 2.12 Details of secondary antibodies used for Western blotting analysis

2.5.3.6 Visualisation of protein bands

Immobilised immuno-labelled proteins were detected using ECL or ECL Prime reagent (GE Healthcare, Bucks, UK) according to manufacturer's instruction. Prepared ECL/ECL+ solutions were mixed well and cultivated for 1 min, before addition on the membrane (1 ml per membrane). After the removal of excess reagent, the membrane was placed in a light-proof cassette, exposed to light sensitive films (Amersham Hyperfilm ECL; GE Healthcare, Bucks, UK) for varying lengths of time and developed on an automatic film processor (Xograph Compact X4). Processed films were then realigned with the original membrane and the target protein was identified by comparison to the molecular weight marker.

2.5.3.7 Stripping and reprobing of membranes

Membranes were stripped before being cultivated with subsequent antibody of interest. Membranes were washed in PBS/T and incubated in stripping buffer (see Table 2.10 for composition) for 30 minutes at 55°C under gentle agitation. Membranes were washed in PBS/T, blocked in milk blocking solution (5% w/v non-fat milk in PBS/T) and probed with a required antibody. Visualisation was performed as described in section 2.5.3.6.

2.5.4 ELISA assay

Enzyme-linked immunosorbent assay (ELISA) is a plate based assay designed to detect and quantify the amount of antigen present. In our case, ELISA assay was used to detect either the amount of Flag-Bcl-3 protein alone or Flag-Bcl-3 in complex with p50, using indirect or sandwich ELISA respectively (see Figure 2.4 for schematic representation).

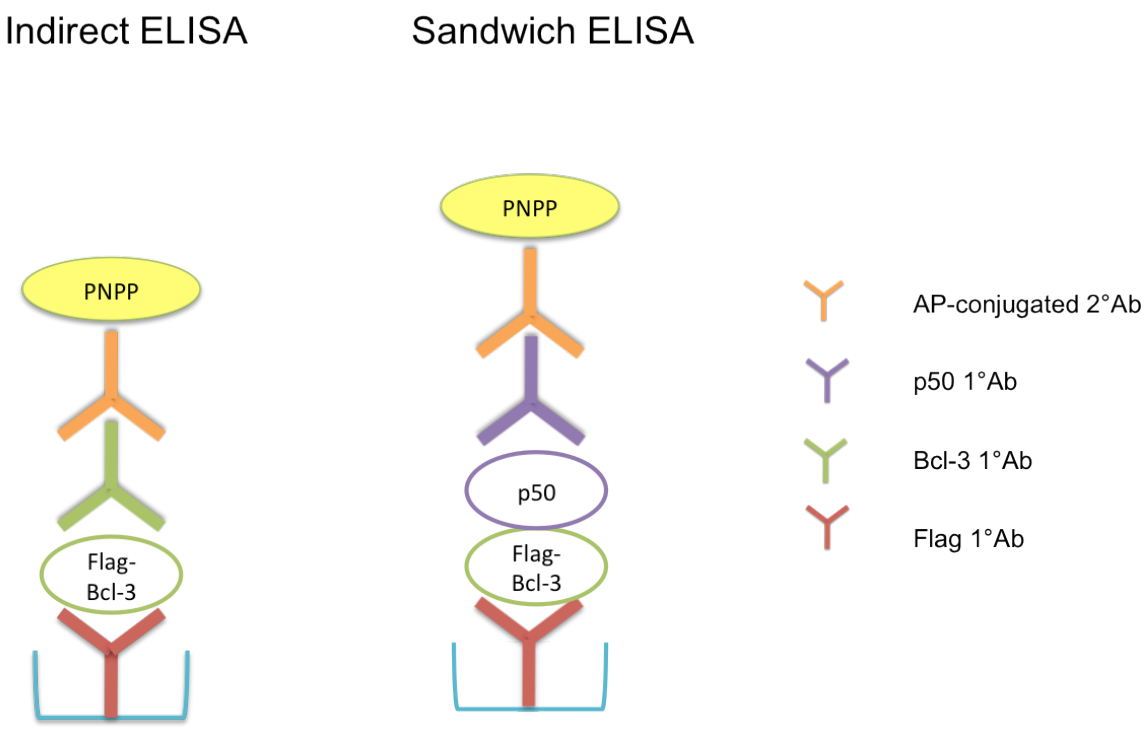

Figure 2.4 Schematic representation of an Indirect and Sandwich ELISA assay

2.5.4.1 Indirect and sandwich ELISA assay

Non-denaturing cell lysate (see 2.5.1.2 for preparation) was diluted with TBS/T [tris buffer saline (TBS, Calbiochem, Merck) supplemented with 0.5% v/v Tween (Sigma, Dorset, UK)] to a concentration of 0.5 – 1 µg/µl and 100 µl was added onto ANTI-Flag coated flat bottom ELISA plates (Sigma, Dorset, UK). Samples were added in triplicates, while TBS/T was used as a negative control.

The plate was cultivated at 37°C for an hour followed by 3x 200 µl washes with TBS/T. Primary antibodies, either Bcl-3 for indirect ELISA and p50 for sandwich ELISA (see Table 2.13 for detailed description of antibodies) were added in known volumes (125 µl) and concentrations to each well, incubated covered from light for an hour at room temperature. Another three 200 µl washes with TBS/T were performed before incubation with alkaline phospatase (AP) conjugated secondary antibody (see Table 2.13 for detailed description).

Meanwhile, para-nitrophenylphosphate solution (pNPP, Santa Cruz Biotechnology, California, USA) was prepared according to manufacture's instructions (5 mg of pNPP disodium salt in 5 ml of pNPP substrate buffer). The solution was mixed well and covered from light prior to use. pNPP is a substrate of choice for use with alkaline phosphatase and produces a soluble end product that is yellow in colour. Therefore colour changes can be measured and represent the amount of AP present.

After cultivation with secondary antibody, the wells were washed 3x200 µl TBS/T, pNPP solution was added (50 µl/well) and cultivated for an hour covered from light at room temperature. The reaction was stopped by addition of 3N NaOH (20 µl/well) and the colometric changes were measured at 405 nm using a plate reader.

Target	**Species**	**Dilution ratio**	**Catalogue number**
Primary antibodies			
Bcl-3	Rabbit	1/30	Santa Cruz (sc-185)
p-50	Rabbit	1/200	Abcam (ab 7549)
Secondary antibodies			
AP-conjugated rabbit	Goat	1/2500	Abcam (ab 97072)

Table 2.13 Details of antibodies used in ELISA assay

2.6 RNA analysis

Before working with RNA, all bench work surfaces and equipment were treated with RNAseZAP (Ambion, Paisley, UK) and RNAse free water (Sigma, Dorset, UK) was used throughout to prevent contamination by RNAses during isolation and purification of RNA.

2.6.1 Isolation of RNA

Purification of RNA from cell pellets (preparation of cell pellets as in section 2.5.1) was carried out using the RNeasy Mini Kit (Qiagen, Sussex, UK) according to manufacturer's instructions. Concentration and quality of RNA was quantified on a nanodrop spectrophotometer (ND-100, Labtech International).

2.6.2 Reverse transcription

Complementary DNA (cDNA) was synthesized from isolated RNA using RevertAID Premium Reverse Transcriptase (Fermentas, Loughborough, UK). RNA samples were diluted to concentrations between 0.5-1 µg in 12.5 µl of RNase free water. A master mix 1 (see Table 2.14 for composition) was added to each sample, mixed gently and heated to 65°C for 5 min. Then, a master mix 2 (see Table 2.14 for composition) was added to each sample and incubated for 10 min at 25°C, 30 min at 50°C and 5 min at 85°C before being cooled to 4°C. Samples were either used immediately or stored at -20°C until required.

Master Mix 1	**Volume Per Reaction**
dNTPs (10 mM; dATP, dCTP, dGTP, dTTP; Promega)	1 µl
Random Primers (500 µg/ml [Promega])	1 µl
Master Mix 2	**Volume Per Reaction**
5x RT Buffer (Fermentas)	5 µl
RNasin Plus (40 u/µl; Promega)	0.5 µl
RevertAID Premium Reverse Transcriptase (200 u/µl; Fermentas)	1 µl

Table 2.14 Master mix components for reverse transcription

2.6.3 Quantitative-real time-polymerase chain reaction (QRT-PCR)

2.6.3.1 Primer design

All primer sets were designed across exon boundaries using the Primer3 web-based software (http://frodo.wi.mit.edu/primer3/). All sequences were verified *in silico* using PCR software (http://genome.csdb.cn/cgi-bin/hgPcr). Sequences of used primers are shown in Table 2.15.

Target	**Species**	**Forward Primer Sequence (5' to 3')**	**Reverse Primer Sequence (5' to 3')**	**Product Size**
Bcl-3	Human	TAT TGC TGT GGT GCA GGG TA	GGT GTC TGC CGT AGG TTG TT	105bp
TIMP1	Human	GGG CTT CAC CAA GAC CTA CA	GAC TGG AAG CCC TTT TCA GA	141bp
TIMP2	Human	AAG CGG TCA GTG AGA AGG AA	GGG GGC CGT GTA GAT AAA CT	137bp
Cyclin D1	Human	CAA ATG TGT GCA GAA GGA GGT	CTC CTC GCA CTT CTG TTC CT	91bp
Cyclophilin	Human	CCA TCG TGT CAT CAA GGA CTT CAT	TTG CCA TCC AGC CAG GAG GTC T	216bp

Table 2.15 Primer sequences used for QRT-PCR

2.6.3.2 QRT-PCR reaction

QRT-PCR was performed using Step One Plus Realtime PCR System (Applied Biosystems) in conjunction with StepOne (v2.1; Applied Biosystems) software. Three technical replicates were analysed for each sample and a minimum of three separate biological samples were examined (see individual experiments). Human cyclophilin gene was used as a standard to normalize variations in the quantities of input cDNA.

Respective cDNA samples (or PCR grade water for negative control) were loaded into separate wells of a 96 well reaction plate (MicroAmp Fast Optical 0.1ml; Applied Biosystems, California, USA) and QRT-PCR mastermix (see Table 2.16 for composition) was added to each well and gently pipetted to ensure homogeneous mixing of cDNA and a master mix. The plate was then sealed with appropriate caps (MicroAmp Optical 8-capstrip; Applied Biosystems, California, USA) before being loaded into the Step One Plus Realtime PCR machine.

All reactions were run under the same cycling conditions of initial denaturation at 95°C for 10 min followed by 45 cycles of 95°C for 15 s and 60°C for 1 min (with a plate read after each cycle). A melting curve (95°C for 15 s, 60°C for 1 min [optics off], 60°C to 95°C at 0.2°C increments every 15 s [optics on]) was constructed at the end of the experiment and data was collected with Step one plus software.

QRT-PCR mastermix	QRT-PCR
cDNA Template	2.5 µl
PCR grade Water (Sigma)	12.65 µl
Go Taq PCR Buffer (Promega)	5 µl
Magnesium Chloride 25 mM (Promega)	2.5 µl
dNTPs 10 mM (Promega)	0.5 µl
Forward Primer 10 µM (Sigma Genosys)	0.25 µl
Reverse Primer 10 µM (Sigma Genosys)	0.25 µl
Go Taq DNA Polymerase (Promega)	0.1 µl
Sybr Green (Invitrogen)	1.25 µl
Total Reaction Volume	25 µl

Table 2.16 QRT-PCR reaction components

2.6.3.3 Analysis of QRT-PCR data

Data was initially examined using Step one plus software by ensuring that only one peak at the expected melting temperature was observed in respective melting curves and that the negative control samples produced no product.

Ct mean values of cyclophilin were subtracted from a Ct mean values of a target genes to give the value ΔCt. A relative value of the difference in transcript

levels between two samples was calculated as a difference between ΔCt of both samples, resulting in the ΔΔCt value. Relative fold changes were then calculated as $2^{-\Delta\Delta Ct}$.

2.7 Molecular modelling

All molecular modelling studies were performed on a MacPro dual 2.66GHz Xeon running Ubuntu 9. All protein crystal structures were downloaded from the PDB data bank (http://www.pdb.org/). Bcl-3 structure - PDB code 1K1A, p50 structure - PDB code 1SVC, p52 structure - PDB code 1A3Q and IκBα p65/p50 structure - PDB code 1NFI. Hydrogen atoms were added to the protein and the ionization of residues were set appropriate to pH 7.4, using Molecular operating Environment (MOE, 2009.10) and minimised keeping all the heavy atoms fixed until a RMSD gradient of 0.05 kcal mol^{-1} $Å^{-1}$ was reached. Protein complexes were built with MOE and minimized using the Amber 99 forcefield until a RMSD gradient of 0.05 kcal $mol^{-1}Å^{-1}$ was reached.

Molecular dynamics were performed using Gromacs 4.5 (Hess et al., 2008) on Bcl-3-p50 and Bcl-3-p52 complexes using Gromos 96 forcefield and NPT working environment. The simulation was conducted at 300K, 1 atmosphere, and time step 0.002 ps. Following minimization, the entire system was equilibrated for 100 ps followed by production phase of 10 ns. The minimized structure was solvated in a periodic dodecahedron simulation box using spc216 water molecules, providing a minimum of 9 Å of water between the protein surface and any periodic box edge.

The docking simulations were performed using Plants1.1 (Korb et al., 2006), Glide 5.5 (Schrodinger, 2009) and FlexX 3.0 (BiosolveITGmbH) using default parameters.

2.8 Statistical analysis

2.8.1.1 Student's t-test

The Student's T-test was used to determine statistical differences between normally distributed data sets and between data sets with sample sizes of n=3. This test was performed using Excel 2008 software.

Chapter 3

Biological Outcome of Bcl-3 Suppression in Human Cell Lines

3. Biological Outcome of Bcl-3 Suppression in Human Cell Lines

3.1 Introduction

Previous *in vivo* studies aimed to understand the role and underlying mechanism of Bcl-3 in mammary tumour formation and progression using ErbB2 (MMTV/neu) mouse models deficient in Bcl-3. Although loss of Bcl-3 did not affect the primary tumour growth, the occurrence of developed lung metastasis was significantly reduced by 40%. Moreover, a significant reduction in mitotic index (Ki-67) and increase in apoptosis (cleaved caspase-3) was observed using immunohistochemistry of secondary lesions (Wakefield et al., 2013).

To confirm the relevance of Bcl-3 in metastatic progression, Bcl-3 was knocked down by siRNA in an ErbB2 murine mammary cancer cell line derived from an activated Neu/ErbB2 mammary tumour (MG1361) and transplanted into ErbB2 mice by tail vein injection. The deletion of Bcl-3 resulted in an 80% decrease in lung metastases formation as compared to control xenografts. Moreover, suppression of Bcl-3 in MG1361 cells resulted in a significant decrease in cell migratory capacity *in vitro* as determined by the Boyden chamber migration assay, with those cells that had migrated expressing higher levels of Bcl-3 than cells that did not (Wakefield et al., 2013).

Similarly to *in vitro* studies in a murine breast cancer cell line, the anti-metastatic effect was observed in a panel of human breast cancer cell lines. In contrast to studies in murine breast cancer cells, deletion of Bcl-3 in human breast cancer cells significantly decreased cell viability, which was not associated with cyclin D1 expression (Wakefield et al., 2013). The exact mechanism for this reduced proliferation still remains to be determined.

Despite these effects on tumours no effect of Bcl-3-deficiency on normal mammary function was observed, which makes Bcl-3 an attractive therapeutic target (Wakefield et al., 2013). Therefore we propose that inhibiting Bcl-3 in breast tumours, for example with the use of small molecule inhibitors, may reduce the metastatic spread of aggressive forms of breast cancer.

The main aims of this chapter were to further explore the role of Bcl-3 in cancer progression and to investigate ways to inhibit Bcl-3 function. For the first aim we used Bcl-3 siRNA to suppress Bcl-3 expression in human breast cancer cell lines and looked at the biological outcome using various cell-based assays. The second aim was explored using a previously defined Bcl-3 binding mutant, proven to disrupt Bcl-3 interactions with the NF-κB subunits p50 and p52.

3.1 The outcome of Bcl-3 suppression in human breast cancer cell lines

3.1.1 Bcl-3 expression among human cell lines

It was demonstrated previously that Bcl-3 expression levels correlate with HER2 status (Wakefield et al., 2013). Therefore we confirmed the relative Bcl-3 levels among human breast cancer cell lines by QRT-PCR. We chose the triple negative cell line (MDA-MB-231), the HER2+ cell line (SKBR3) and the ER+ cell line (ZR-75-1). As expected, Bcl-3 levels were found to be significantly elevated in SKBR3 cells. Bcl-3 is also poorly expressed in non-tumorigenic cell lines, such as human embryonic kidney cells (HEK-293) (Figure 3.1A).

3.1.2 Suppression of Bcl-3 decreases NF-κB activity in human cell lines

We then looked whether Bcl-3 suppression affects NF-κB activity. Bcl-3 was suppressed using Bcl-3 siRNA in breast cancer cell lines (MDA-MB-231, SKBR3 and ZR-75-1). Cells were transfected with Bcl-3 or control siRNA for 48hrs before being analyzed for NF-κB activity by an NF-κB luciferase assay. We observed a significant decrease in NF-κB activity when Bcl-3 was knocked down in MDA-MB-231 and SKBR3 cells (Figure 3.1B) despite the fact that MDA-MB-231 cells exhibited relatively low Bcl-3 expression (Figure 3.1A). We did not observe any significant changes in NF-κB activity in ZR-75-1 cells, which may be attributed to the ER positivity of these cells as NF-κB activation is connected predominantly with ER negative breast cancer cells (Biswas et al., 2000). As the NF-κB luciferase assay was performed 96hrs after initial siRNA transfection, we confirmed that Bcl-3 was knocked in all three cell lines at this time point using QRT-PCR (Figure 3.1C-E).

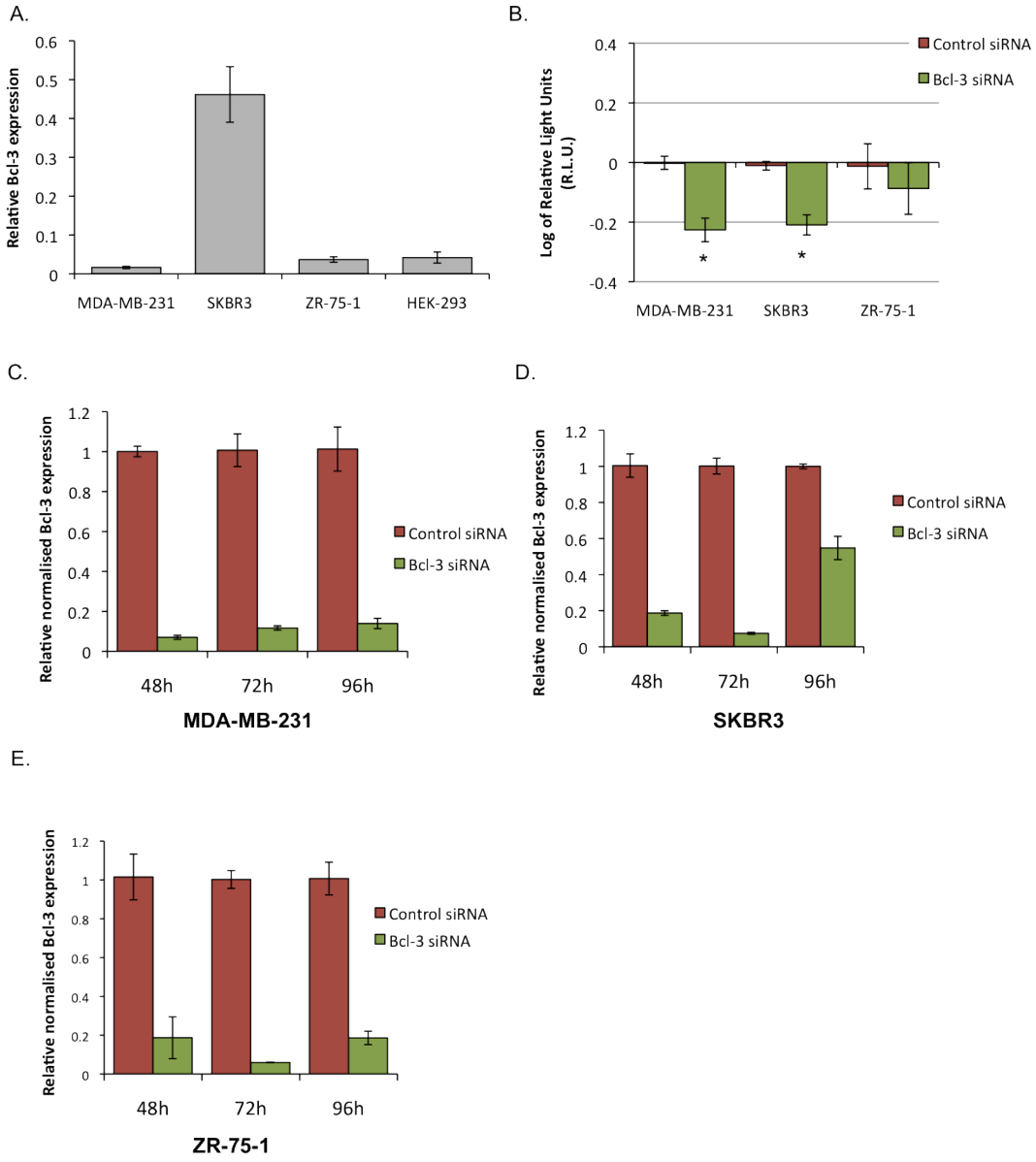

Figure 3.1 Bcl-3 expression in a human cell lines and the effect of Bcl-3 suppression on NF-κB activity

A. RNA was harvested from MDA-MB-231, SKBR3, ZR-75-1 and HEK-293 cell lines for QRT-PCR analysis. Bcl-3 mRNA expression was normalised to cyclophilin mRNA expression. Data represent three individual experiments and error bars represent ± SEM. **B.** MDA-MB-231, SKBR3 and ZR-75-1 cells were transfected with Bcl-3 or control siRNA for 48hrs before being transfected with NF-κB or LacZ reporter for 48hrs. NF-κB activity was measured as relative light units and normalised to LacZ activity before being normalised to the activity of the respective control siRNA and plotted on a log scale. Data represents 3 independent transfections. Error bars represent ± SEM. (T-test, *=$p<0.05$ as compared to control siRNA). **C.** (MDA-MB-231) + **D.** (SKBR3) + **E.** (ZR-75-1) cells were transfected with Bcl-3 or control siRNA. RNA was harvested at three time points post transfection (48hrs, 72hrs, 96hrs) for QRT-PCR analysis. Bcl-3 mRNA expression was normalised to cyclophilin mRNA expression. Data represent three individual experiments and error bars represent ± SEM.

3.1.3 Suppression of Bcl-3 reduced the viability and proliferation capacity of breast cancer cell lines in adherent growth conditions

It was demonstrated previously that Bcl-3 does not affect the growth of primary tumours *in vivo* (Wakefield et al., 2013) and the viability of a HER2+ murine cell line (MG1361) *in vitro* (Wakefield, 2012), however Bcl-3 suppression *in vitro* by siRNA decreased the viability of human HER2+ breast cancer cell line (SKBR3) and a triple negative cell line (MDA-MB-231) (Wakefield, 2012).

We wanted to confirm the effect of Bcl-3 on cell viability and cell proliferation; properties important for primary tumour growth. Bcl-3 was suppressed using Bcl-3 siRNA in human breast cancer cell lines (MDA-MB-231, SKBR3 and ZR-75-1). Cells were transfected with Bcl-3 or control siRNA for 48hrs before being seeded onto a 96-well plate. Cell viability was determined after 24hrs using the Cell Titre Blue viability assay and live cells were counted after 24hrs, 48hrs and 72hrs to analyse cell proliferation.

We confirmed that Bcl-3 suppression reduced the number of viable cells in MDA-MB-231 and SKBR3 cell lines (Figure 3.2A-D). However we observed no effect on cell numbers in ER+ ZR-75-1 cells (Figure 3.2E&F). The cell count determined that Bcl-3 suppression in MDA-MB-231 cells significantly reduced cell numbers after 48hrs from seeding and by 72hrs cell numbers were comparable to control siRNA. However in SKBR3 cells with suppressed Bcl-3 levels, the number of viable cells was significantly decreased from 24hrs from seeding and the rate of proliferation did not change until 72hrs post seeding.

Interestingly, the proportion of non-viable cells at 48hrs post Bcl-3 suppression as measured by flow cytometry was significantly increased in all three cell lines, yet the amplitude of these changes reflected the proliferation data (Figure 3.3A).

As cyclin D1 is a known regulator of cell proliferation and Bcl-3 expression is associated with increased cyclin D1 levels (Westerheide et al., 2001) we wanted to determine whether decrease in cell viability is associated with changes in cyclin D1 levels. However, no effect on cyclin D1 expression was observed following Bcl-3 suppression by Bcl-3 siRNA in neither of the analysed three cell lines (Figure 3.3B-D).

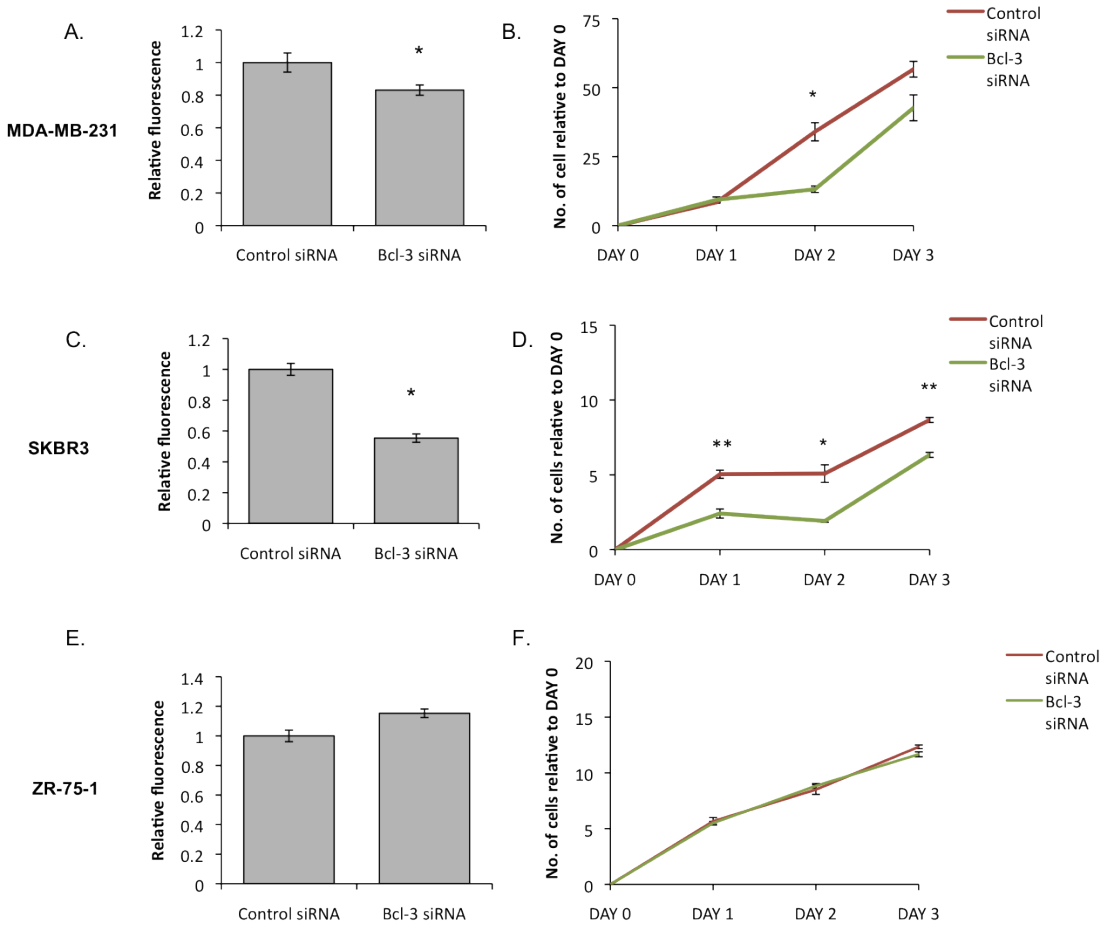

Figure 3.2 Cell viability and proliferation in Bcl-3 suppressed human breast cancer cells

MDA-MB-231 (**A&B**), SKBR3 (**C&D**) and ZR-75-1 (**E&F**) cells were transfected with Bcl-3 or control siRNA for 48hrs before being seeded in normal adherent growth conditions. **A&C&E.** Cell viability was determined after 24hrs by the Cell Titre Blue viability assay. Data represent average of six wells and resulting fluorescence was normalised against fluorescence of control siRNA. Error bars represent ± SEM. **B&D&F.** The number of cells in each well was counted at respective time points (DAY 1, DAY 2, DAY 3). Data represent average of six wells and error bars represent ± SEM. (T-test, *=$p<0.05$, **=$p<0.01$).

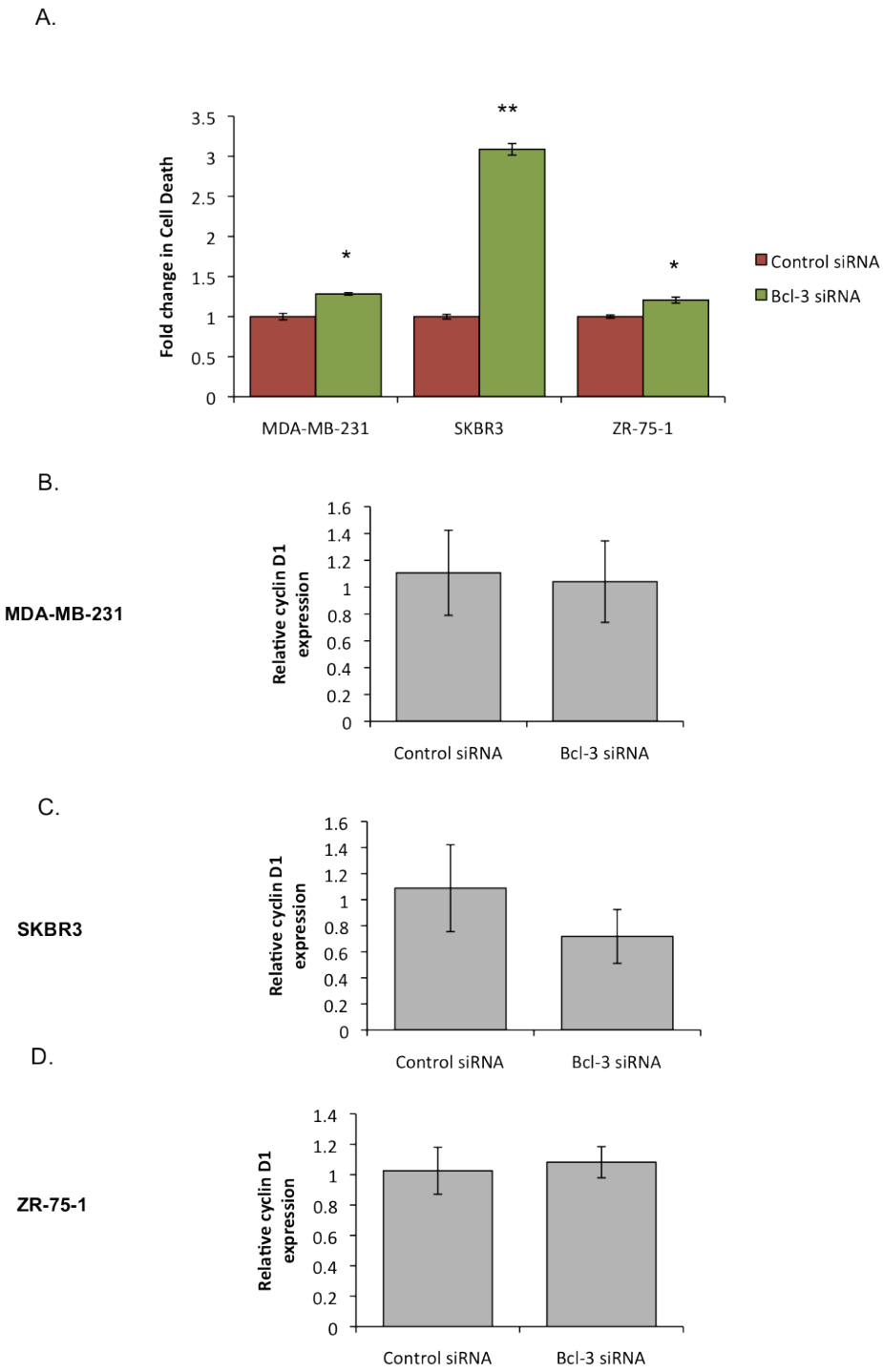

Figure 3.3 Cell death and cyclin D1 expression in Bcl-3 suppressed breast cancer cells

A. MDA-MB-231, SKBR3 and ZR-75-1 cells were transfected with Bcl-3 or control siRNA for 48hrs before being stained with 4 µl of 1:10 fixable near-IR live/dead stain and analysed by FACS at 780/60 PE Cy7-A. Data represent average of three measurements and error bars represent ± SEM. (T-test, *=p<0.05, **=p<0.01). **B-D.** MDA-MB-231 (**B**.), SKBR3 (**C.**) and ZR-75-1 (**D.**) cells were transfected with Bcl-3 or control siRNA for 48hrs before being analyzed for cyclin D1 expression by QRT-PCR. Cyclin D1 mRNA expression is relative to cyclophilin mRNA expression and normalised to the expression of control siRNA. Data represent average of three measurements and error bars represent ± SEM.

3.1.4 The effect of Bcl-3 deficiency on cell cycle

Previously it was shown that increased expression of Bcl-3 leads to a shortened G1 phase of the cell cycle, which could be explained by increased levels of Rb phosporylation in Bcl-3 overexpressing cells (Westerheide et al., 2001). Rb is a key cellular regulator of G1 transition and is activated by the cyclin D-cyclin-dependent kinase complex. Interestingly cyclin D1 protein levels correlated with Bcl-3 protein levels, suggesting that Bcl-3 may mediate its effects on the cell cycle via cyclin D1 (Westerheide et al., 2001).

In order to establish the effect of Bcl-3 suppression on the relative duration of cell cycle phases, Bcl-3 was suppressed using Bcl-3 siRNA in human breast cancer cell lines (MDA-MB-231, SKBR3 and ZR-75-1) for 48hrs. Consequently, cells were stained with propidium iodide and analysed using flow cytometry.

We observed lower percentage of cells entering the S phase in MDA-MB-231 and SKBR3 cells when Bcl-3 was suppressed. There were significantly more cells in G0/1 phase observed in a Bcl-3 deficient MDA-MB-231 cell line, while a similar trend was observed in a Bcl-3 deficient SKBR3 cells in conjunction with a greater proportion of cells in G2/M. Consistent with previous proliferation assays, no effect on the relative duration of cell cycle was observed when Bcl-3 was suppressed in ZR-75-1 cells (Figure 3.4).

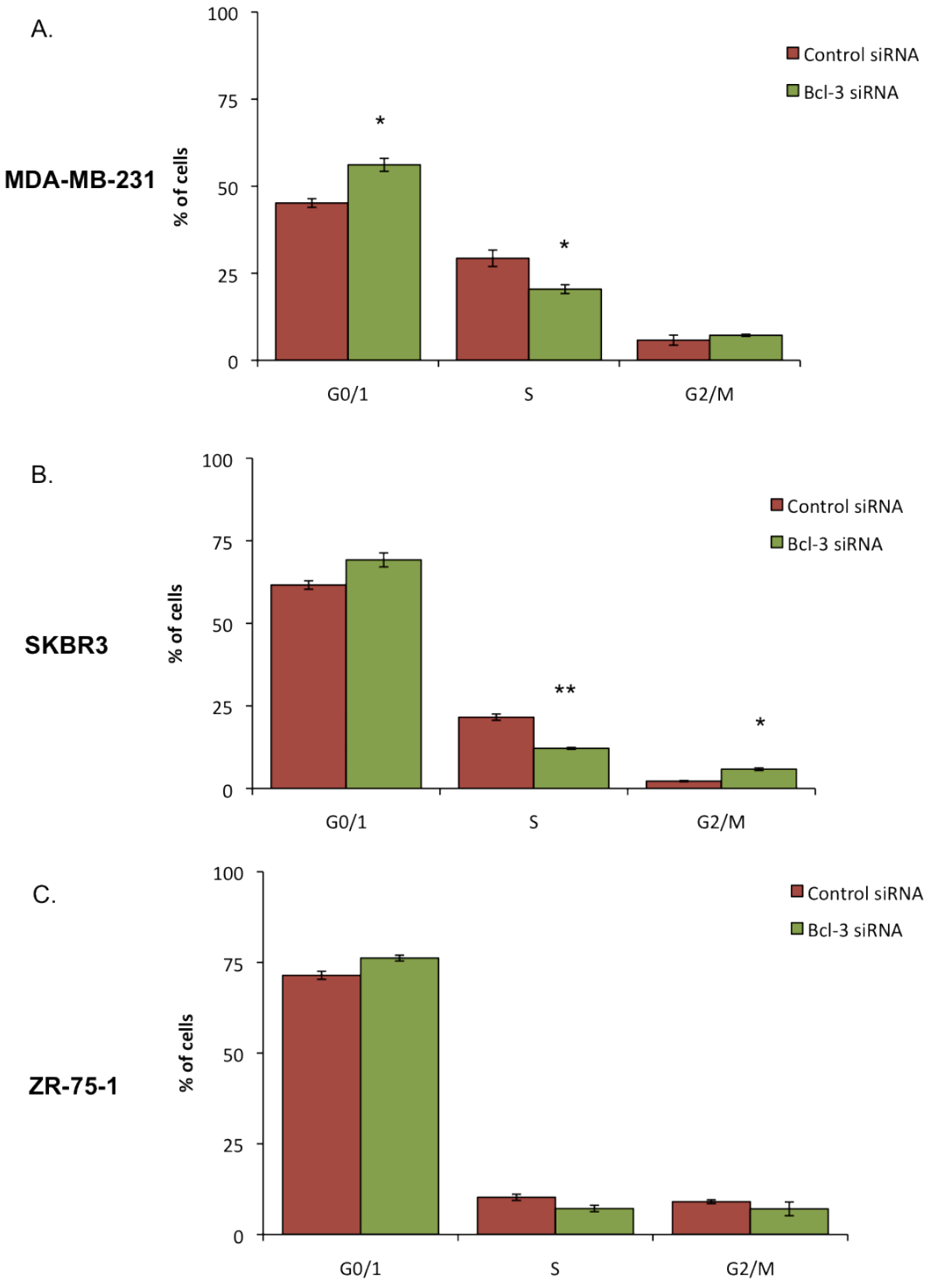

Figure 3.4 The effect of Bcl-3 suppression on cell cycle

MDA-MB-231 (**A.**), SKBR3 (**B.**) and ZR-75-1 (**C.**) cells respectively were transfected with Bcl-3 or control siRNA for 48h before being stained with propidium iodide and analysed for cell cycle stage by FACS at 585/42 PE-A. Data represent average of three measurements and error bars represent ± SEM. (T-test, *=$p<0.05$, **=$p<0.01$).

3.2 Generation and characterisation of Bcl-3 overexpressing clones

The current view is that Bcl-3 modulates NF-κB signalling through binding to proteins p50 and p52 from the NF-κB family (Franzoso et al., 1993, Watanabe et al., 1997, Wulczyn et al., 1992), therefore our approach to inhibit Bcl-3 function was to disrupt Bcl-3-p50/p52 binding.

In previous *in vitro* studies Bcl-3 was silenced using siRNA, therefore, we wanted to address whether disruption of Bcl-3 binding resulted in inhibition of Bcl-3 function equivalent to Bcl-3 knock down.

For this purpose, we obtained a FLAG-tagged constructs containing either Bcl-3 WT or Bcl-3 binding mutant (Bcl-3 ANK M123 as described in Material and Methods 2.1.2). This mutated form of Bcl-3 was not able to bind to proteins p50 and p52 (Keutgens et al., 2010). Bcl-3 is predominantly a nuclear protein, however overexpression of the Bcl-3 binding mutant resulted in equal Bcl-3 distribution in the cytoplasm and the nucleus. Moreover, binding to proteins p50 and p52 is required for its constitutive GSK-3 mediated Bcl-3 phosphorylation (Keutgens et al., 2010).

As we wanted to establish the functional outcome of cells overexpressing either Bcl-3 WT or Bcl-3 ANK M123 binding mutants, endogenous Bcl-3 expression is undesirable. Therefore we chose to use the triple negative cell line, MDA-MB-231, with low endogenous Bcl-3 expression (Figure 3.1A.) Moreover, triple negative cell lines were found to have constitutively activated NF-κB signalling (Yamaguchi et al., 2009).

In order to determine whether the functional outcome of Bcl-3 inhibition is cancer-related, for comparison we have selected non-tumorigenic human embryonic kidney cells HEK-293, because of their epithelial phenotype, exponential growth and low level of endogenous Bcl-3.

3.2.1 Generation of Bcl-3 WT and Bcl-3 binding mutants in MDA-MB-231 cells

MDA-MB-231 cells lines were transfected with Bcl-3 WT and Bcl-3 ANK M123 plasmids (FLAG-tagged constructs described in section 2.1.2). Individual overexpressing clones were then selected under neomycin conditions and

expanded prior to analyses for Bcl-3 expression. The expression levels of three selected clones overexpressing Bcl-3 WT and Bcl-3 ANK M123 were demonstrated by QRT-PCR (Figure 3.5 A&B). All selected clones expressed detectable levels of Bcl-3. The protein levels of selected clones with highest Bcl-3 expression, Bcl-3 WT-1 and Bcl-3 ANK M123-1 were confirmed by Western blotting (Figure 3.5 C). In order to confirm the stable expression of these clones, cell pellets were collected every 5 passages up to 20 passages and subjected to Western blotting (Figure 3.5 D&E). We observed an early decline in Bcl-3 expression in both, Bcl-3 WT and Bcl-3 ANK M123 overexpressing clones, however this decline was stabilized by passage 10.

3.2.1.1 The effect of Bcl-3 expression on NF-κB activity

An NF-κB luciferase assay was performed in order to determine the NF-κB activity in MDA-MB-231 cells overexpressing either Bcl-3 WT or Bcl-3 ANK M123. As established previously (Figure 3.1B), suppression of Bcl-3 by siRNA led to a significant decrease in NF-κB activity in MDA-MB-231 cells. Similarly, we observed a significant decrease of NF-κB activity when Bcl-3 activity was suppressed by overexpression of Bcl-3 ANK M123. As expected, NF-κB activity was increased when Bcl-3 WT was overexpressed (Figure 3.5 F).

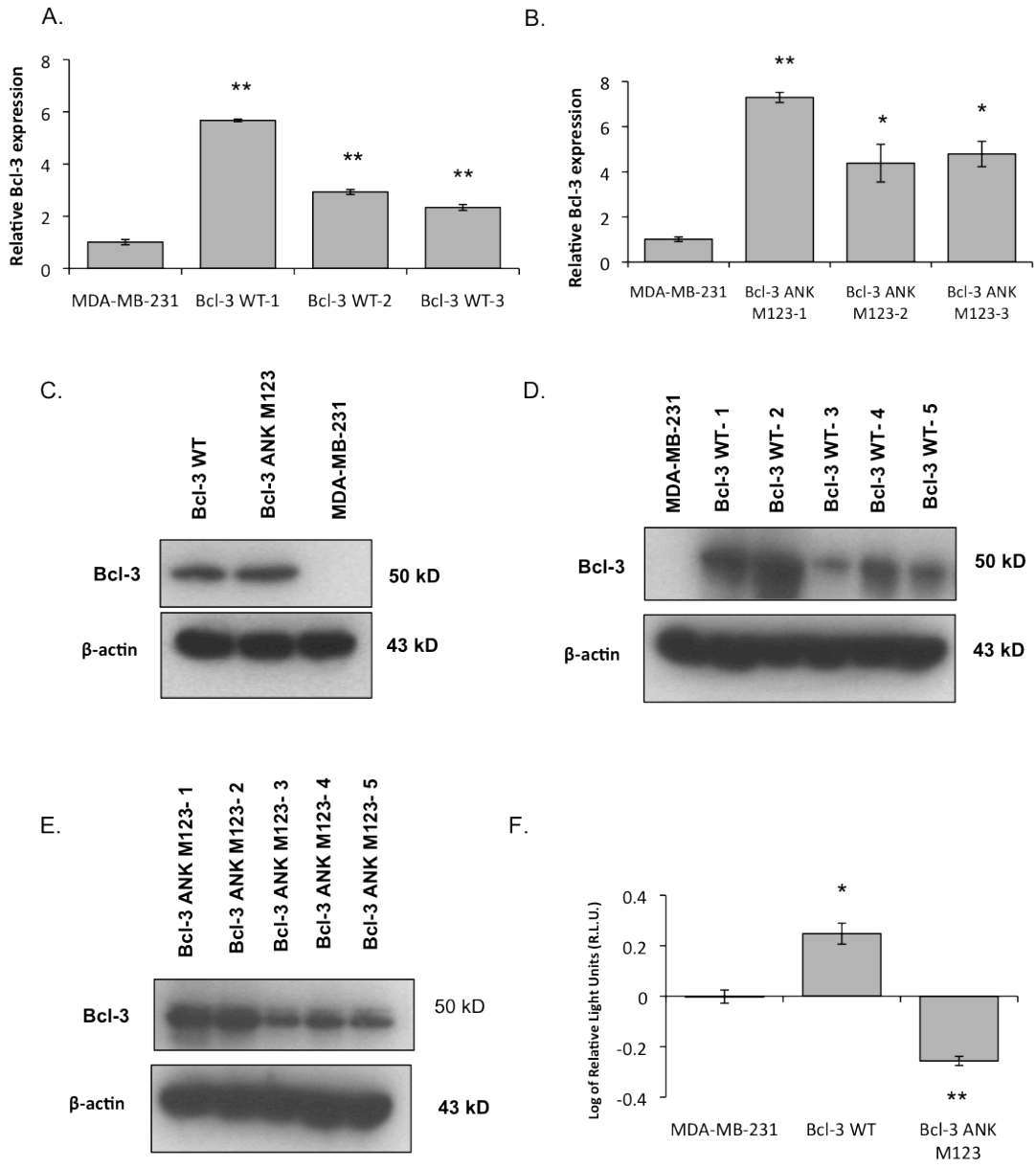

Figure 3.5 Generation of Bcl-3 WT and Bcl-3 ANK M123 clones and their effect on NF-κB activity in MDA-MB-231 cells

A&B. Data shows Bcl-3 mRNA expression of MDA-MB-231 Bcl-3 WT (**A.**) and MDA-MB-231 ANK M123 (**B.**) as measured by QRT-PCR relative to cyclophilin mRNA expression and normalised to MDA-MB-231. Error bars represent ± SEM of triplicate wells. (T-test, *=p<0.05, **=p<0.01). **C.** Total protein was extracted from MDA-MB-231 cells (parental, Bcl-3 WT and Bcl-3 ANK M123 overexpressing) and subjected to Western analysis with Bcl-3 primary antibody. Equal loading was confirmed by β-actin. **D&E.** Total protein was extracted from clone 1 of MDA-MB-231 Bcl-3 WT (**D.**) and clone 1 of Bcl-3 ANK M123 (**E.**) every five passages over 20 passages and subjected to Western analysis with Bcl-3 primary antibody. Equal loading was confirmed by β-actin. **F.**MDA-MB-231 [WT, Bcl-3-WT (1-3) and Bcl-3 ANK M123 (1-3)] cells were transfected with NF-κB or LacZ reporter for 48hrs. NF-κB activity was measured as relative light units, normalised to MDA-MB-231 and plotted on a log scale. Data represent 3 independent transfections. Error bars represent ± SEM. (T-test, *=p<0.05 and **=p<0.01 as compared to MDA-MB-231).

3.2.1.2 The effect of Bcl-3 expression on cell viability and proliferation

As determined previously, Bcl-3 inhibition by siRNA significantly decreased cell viability and cell proliferation (Figure 3.2.A&B). Our hypothesis therefore was that the Bcl-3 ANK M123 binding mutant would also suppress cell viability. Given the reciprocal regulation of NF-κB when Bcl-3 WT and Bcl-3 ANK M123 were overexpressed, we would expect that the overexpression of Bcl-3 WT would promote cell viability.

As expected, overexpression of Bcl-3 ANK M123 decreased cell viability and suppressed cyclin D1 expression. However Bcl-3 WT overexpression also suppressed cell viability despite an increase in cyclin D1 expression (Figure 3.6A-C). The cell count determined that overexpression of Bcl-3 ANK M123 significantly reduced cell numbers after 48hrs from seeding and by 72hrs cell numbers were not significantly different from MDA-MB-231 control (Figure 3.6B), which is in agreement with the effect of suppression of Bcl-3 by siRNA in MDA-MB-231 cells (Figure 3.2B.).

Our hypothesis then was that the decrease in cell counts for Bcl-3 WT overexpressing cells might be explained by increase in cell death, however we did not observe a significant increase in cell death as measured by flow cytometry (Figure 3.6D). We did observe a significant increase in activity of caspase 3/7 in Bcl-3 WT overexpressing cells as measured by the Caspase-Glo 3/7 assay compared to MDA-MD-231 cells (Figure 3.6E). The level of caspase 3/7 was comparable to MDA-MB-231 control in Bcl-3 ANK M123 overexpressing cells. These observations would suggest that Bcl-3 WT overexpression mediates apoptosis via caspase 3/7, which leads to the decrease in cell viability despite higher cyclin D1 expression.

3.2.1.3 The effect of Bcl-3 expression on cell cycle

As shown in Figure 3.4, suppression of Bcl-3 by siRNA suppresses entry into the cell cycle. Therefore we wanted to establish whether overexpression of Bcl-3 WT or Bcl-3 ANK M123 would affect entry of cells into the cell cycle. MDA-MB-231 control, Bcl-3 WT and Bcl-3 ANK M123 expressing cells were stained with propidium iodide and analysed using flow cytometry.

We observed a significant decrease of percentage of cells in the G0/1 phase when Bcl-3 WT was overexpressed, suggesting that a higher proportion of cells had

entered the cell cycle. However we did not observe any alteration in the cell cycle when Bcl-3 ANK M123 was overexpressed (Figure 3.7).

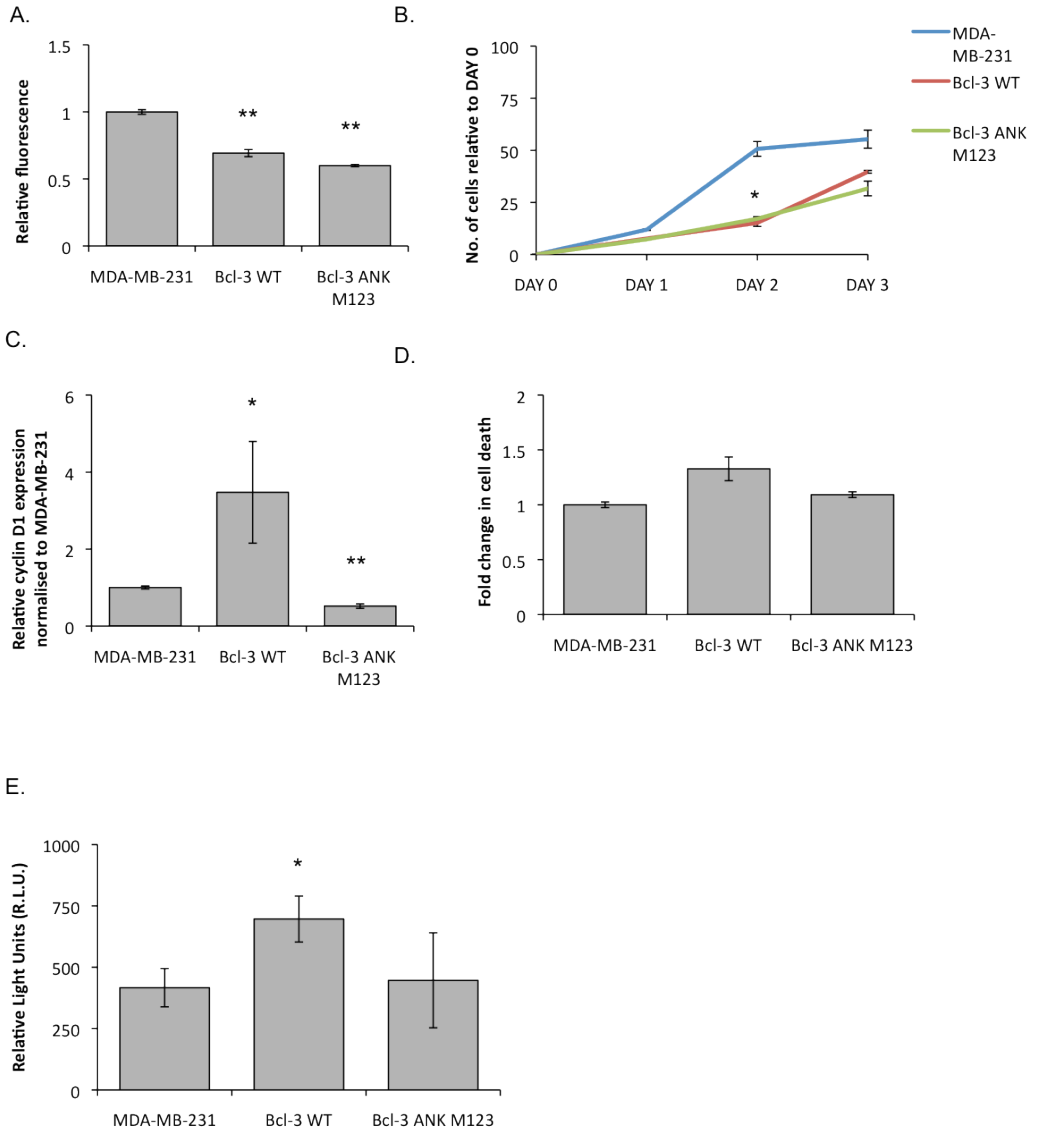

Figure 3.6 The effect of Bcl-3 expression on cell proliferation in MDA-MB-231 cells
A. MDA-MB-231 (WT, Bcl-3 WT and Bcl-3 ANK M123) cells were plated in normal adherent growth conditions. Cell viability was determined after 24hrs by the Cell Titre Blue viability assay. Data represent average of six wells and resulting fluorescence was normalised against fluorescence of MDA-MB-231. Error bars represent ± SEM. (T-test, **=p<0.01). **B.** MDA-MB-231 (WT, Bcl-3 WT and Bcl-3 ANK M123) cells were plated in normal adherent growth conditions. The number of cells in each well was counted at three time points (24hrs, 48hrs, 72hrs). Data represent average of six wells and error bars represent ± SEM. **C.** Data shows mRNA expression of cyclin D1 in MDA-MB-231 (WT, Bcl-3 WT, Bcl-3 ANK M123) cells. Expression levels are relative to cyclophilin and were normalised to mRNA levels of MDA-MB-231. Data represent three independent experiments and error bars represent ± SEM. (T-test, *=p<0.05, **=p<0.01). **D.** MDA-MB-231 (WT, Bcl-3 WT and Bcl-3 ANK M123 cells were stained with 4 µl of 1:10 fixable near-IR live/dead stain and analysed by FACS at 780/60 PE Cy7-A. Data represent average of three measurements and error bars represent ± SEM. **E.** MDA-MB-231 (WT, Bcl-3 WT and Bcl-3 ANK M123) cells were plated in normal adherent growth conditions. The caspase activity was determined after 24hrs by the Caspase-Glo 3/7 assay. The measured luminescence in R.L.U. is proportional to the amount of caspase activity present. Data represent average of three wells. Error bars represent ± SEM. (T-test, *=p<0.05).

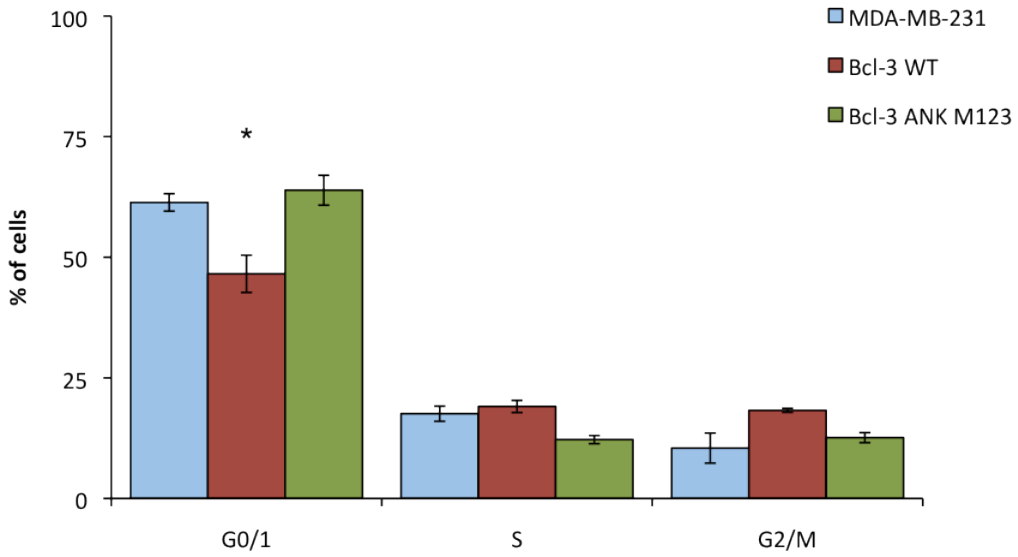

Figure 3.7 Bcl-3 expression reduced the proportion of cells in G0/1 phase of cell cycle

MDA-MB-231 (WT, Bcl-3 WT and Bcl-3 ANK M123 cells were stained with propidium iodide and analysed for cell cycle duration by FACS at 585/42 PE-A. Data represent average of three measurements and error bars represent ± SEM. (T-test, *=$p<0.05$).

3.2.1.4 The effect of Bcl-3 on cell motility and cell invasion

As discussed previously, Bcl-3 deletion results in a decrease in secondary tumour formation and a reduction in metastatic tumour growth (Wakefield et al., 2013). The metastatic properties of cancer cells can be modelled *in vitro* using the Boyden chamber motility assay, which measures cell migration through porous membrane based on serum gradient or invasion through matrigel.

Suppression of Bcl-3 resulted in a significant reduction of motility in a murine HER2+ breast cancer cell line (Wakefield et al., 2013) and in HER2+, ER+ and triple negative human breast cancer cell lines (Dr. Alison Wakefield, 2012, unpublished).

Therefore it was of interest to determine whether the migratory capacity would be altered in Bcl-3 overexpressing clones. Given the reciprocal effect on NF-κB signalling of Bcl-3 WT and Bcl-3 ANK M123 binding mutant it was hypothesised that Bcl-3 WT overexpressing cells would exhibit greater motility and Bcl-3 ANK M123 overexpressing cells would have suppressed motility.

Consistent with the previous observation, suppression of Bcl-3 by siRNA significantly reduced the migratory capacity of MDA-MB-231 cells by 50%. The invasion ability was also reduced, however when normalised to migration ability, no significant change was observed indicating that cell motility, but not invasive capacity were affected by Bcl-3 loss (Figure 3.8).

Cell motility was found to be significantly increased in MDA-MB-231 cells overexpressing Bcl-3-WT (Figure 3.9A). Overexpression of Bcl-3 ANK M123 decreased cell motility even below the basal level of parental MDA-MB-231 cells, while the number of live cells present in low serum medium was not affected. The ability to invade through matrigel was increased when Bcl-3 WT was overexpressed, however when normalised to migration ability, no significant increase was observed. Similarly, the invasion ability of Bcl-3 ANK M123 was decreased compared to the control, but when normalised to the migration activity, no significant decrease was observed (Figure 3.9C).

The molecular mechanism responsible for the change in migratory capacity is not yet defined. However, previous studies using microarray and QRT-PCR assays in murine MG1361 cells identified a number of metastasis-related genes whose

expression was altered following siRNA-mediated suppression of Bcl-3, among them the NME family, TIMP family and Arhgdib genes (Wakefield et al., 2013).

The expression of Nme gene (also called nm23) is associated with decreased metastatic potential in breast cancer patients (Hennessy et al., 1991), the family of Tissue Inhibitor of Metalloprotease (TIMPs) acts as an inhibitor of Matrix Metalloproteinases and is involved in tissue remodelling and tumour cell progression and was found to promote invasiveness in breast cancer (Zhang et al., 2008), while Arhgdib is a Rho GDP dissociation inhibitor that has been shown to act as a metastases suppressor (Gildea et al., 2002). These data suggests that Bcl-3 regulates invasion and migration by regulating a variety of motility and invasion associated genes (Wakefield et al., 2013).

However only the family of TIMPs genes was found affected in human breast cancer cell lines following suppression of Bcl-3 by siRNA (Wakefield, 2012), therefore it was of interest to determine the effect of TIMP 1 and TIMP 2 expression in MDA-MB-231 cells line overexpressing Bcl-3 WT and Bcl-3 ANK M123.

In agreement with previous study, TIMP 1 was found upregulated following the suppression of Bcl-3 by siRNA in MDA-MB-231 cells, whereas TIMP 2 was not affected. Similarly, overexpression of Bcl-3 ANK M123 increased TIMP1 expression, while not affecting TIMP 2 expression (Figure 3.10). Overexpression of Bcl-3 WT did not significantly affect the expression of either TIMP 1 or TIMP 2.

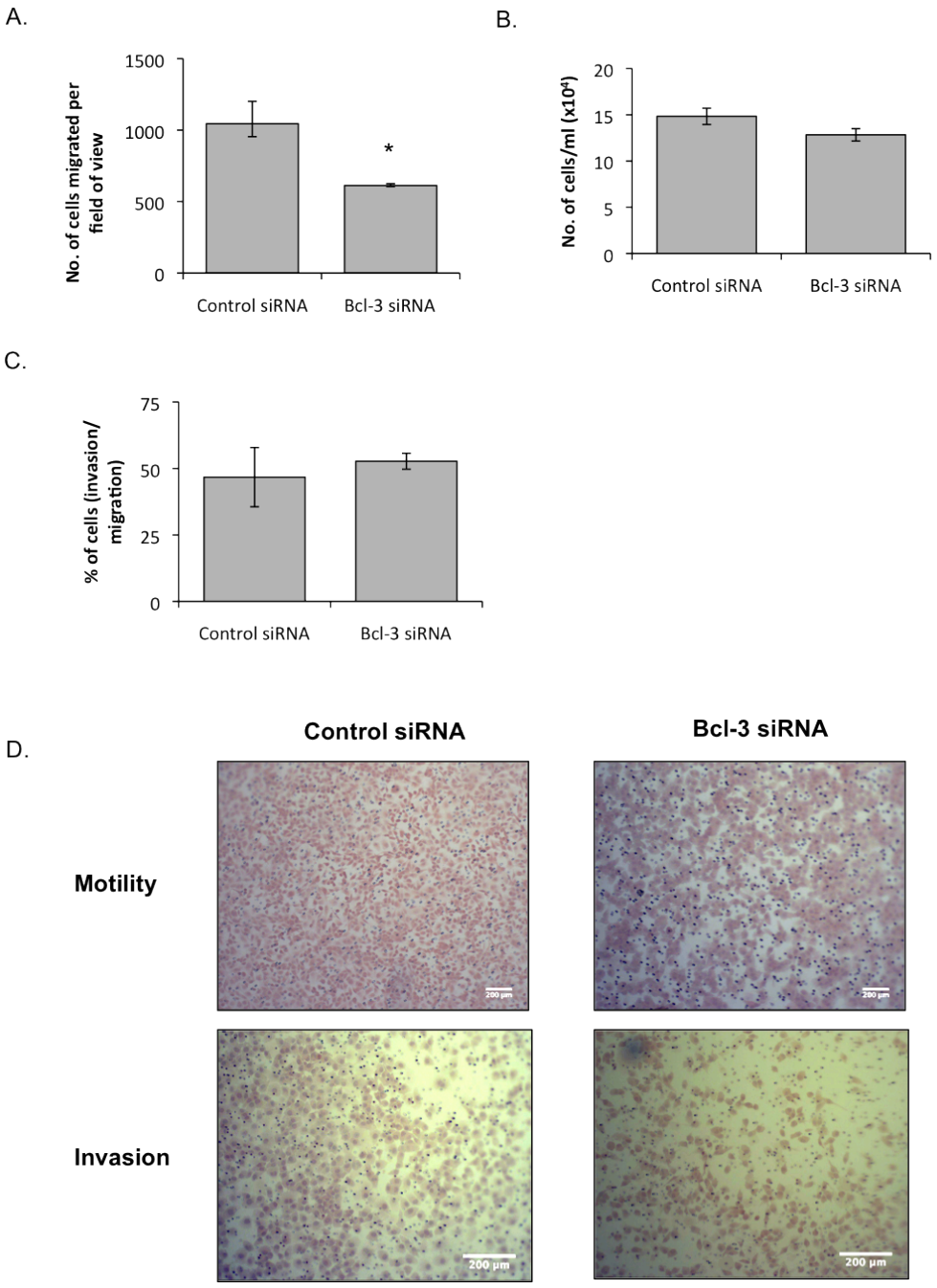

Figure 3.8 Bcl-3 suppression by siRNA decreases cell motility

MDA-MB-231 cells were transfected with Bcl-3 or control siRNA for 48hrs. **A**. Cells were seeded onto Boyden motility chambers for 24hrs. Migrated cells were counted from three fields of view of each of three replicate Boyden chambers. Error bars represent ± SEM. (T-test, *=$p<0.05$). **B.** Cells were seeded in normal adherent growth conditions for 24hrs and counted. **C**. Cells were seeded onto Boyden invasion chambers coated with matrigel for 24hrs. Invaded cells were counted from three fields of view of each of three replicate Boyden chambers. The number of invaded cells was normalised to number of migrated cells and is shown as % of invaded cells. Error bars represent ± SEM. **D.** Representative images of migrated and invaded cells for MDA-MB-231 (Control or Bcl-3 siRNA) cells. Scale bars represent 200 µm.

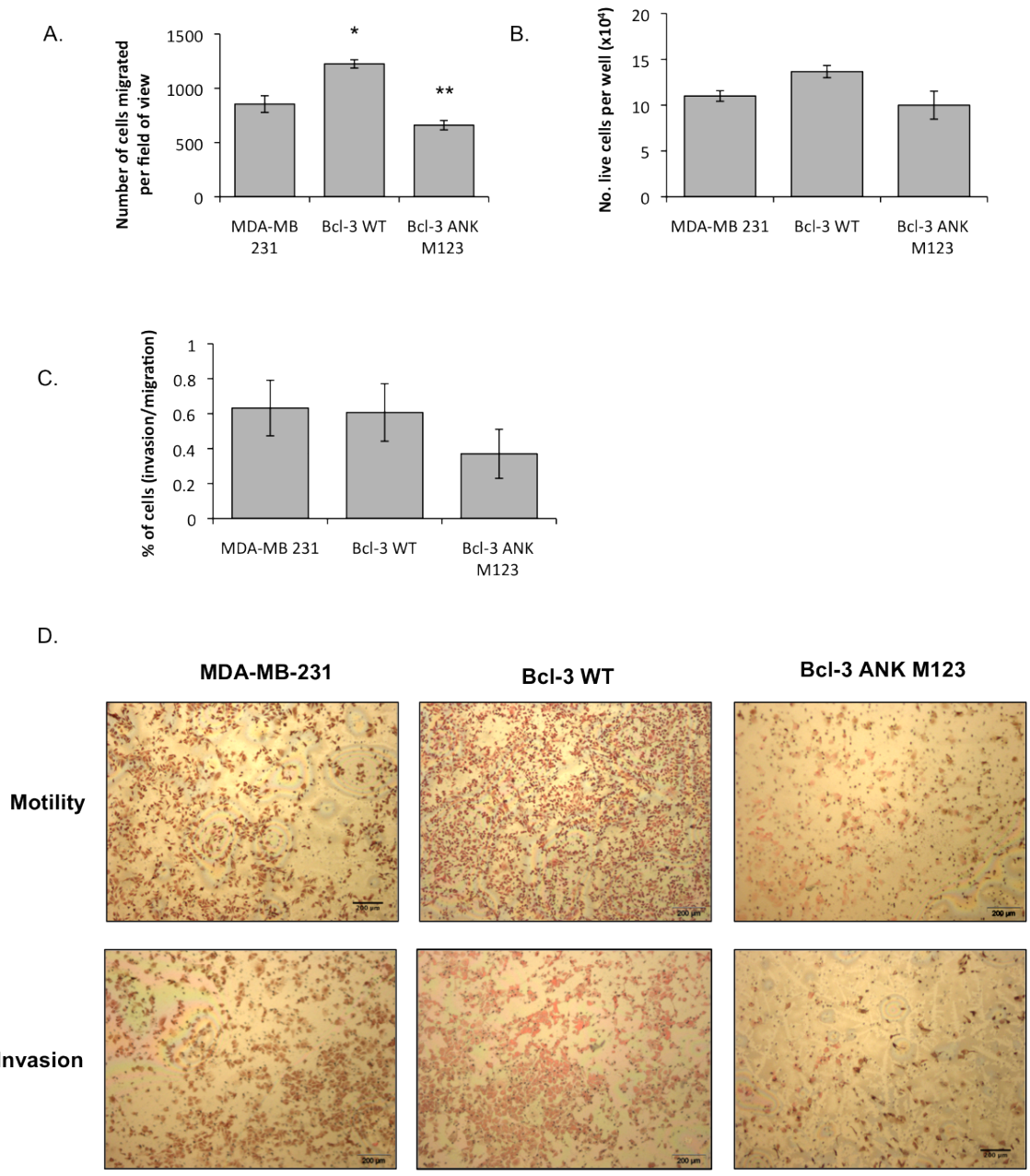

Figure 3.9 Bcl-3 expression affects cell motility

A. MDA-MD-231 (WT, Bcl-3 WT Bcl-3 ANK M123) cells were seeded onto Boyden motility chambers for 24hrs. Migrated cells were counted from three fields of view from three replicate Boyden chambers. The number of migrated cells was normalised to MDA-MB-231. Error bars represent ± SEM. (T-test, *=$p<0.05$). **B.** MDA-MD-231 (WT, Bcl-3 WT Bcl-3 ANK M123) cells were seeded in normal adherent growth conditions for 24hrs before being counted. **C.** MDA-MD-231 (WT, Bcl-3 WT Bcl-3 ANK M123) cells were seeded onto Boyden invasion chambers coated with matrigel for 24h. Invaded cells were counted from three fields of view of each of three replicate Boyden chambers. The number of invaded cells was normalised to number of migrated cells and is shown as % of invaded cells. Error bars represent ± SEM. **D.** Representative images of migrated cells and invaded cells for MDA-MB-231 (WT, Bcl-3 WT Bcl-3 ANK M123) cells. Scale bars represent 200 µm.

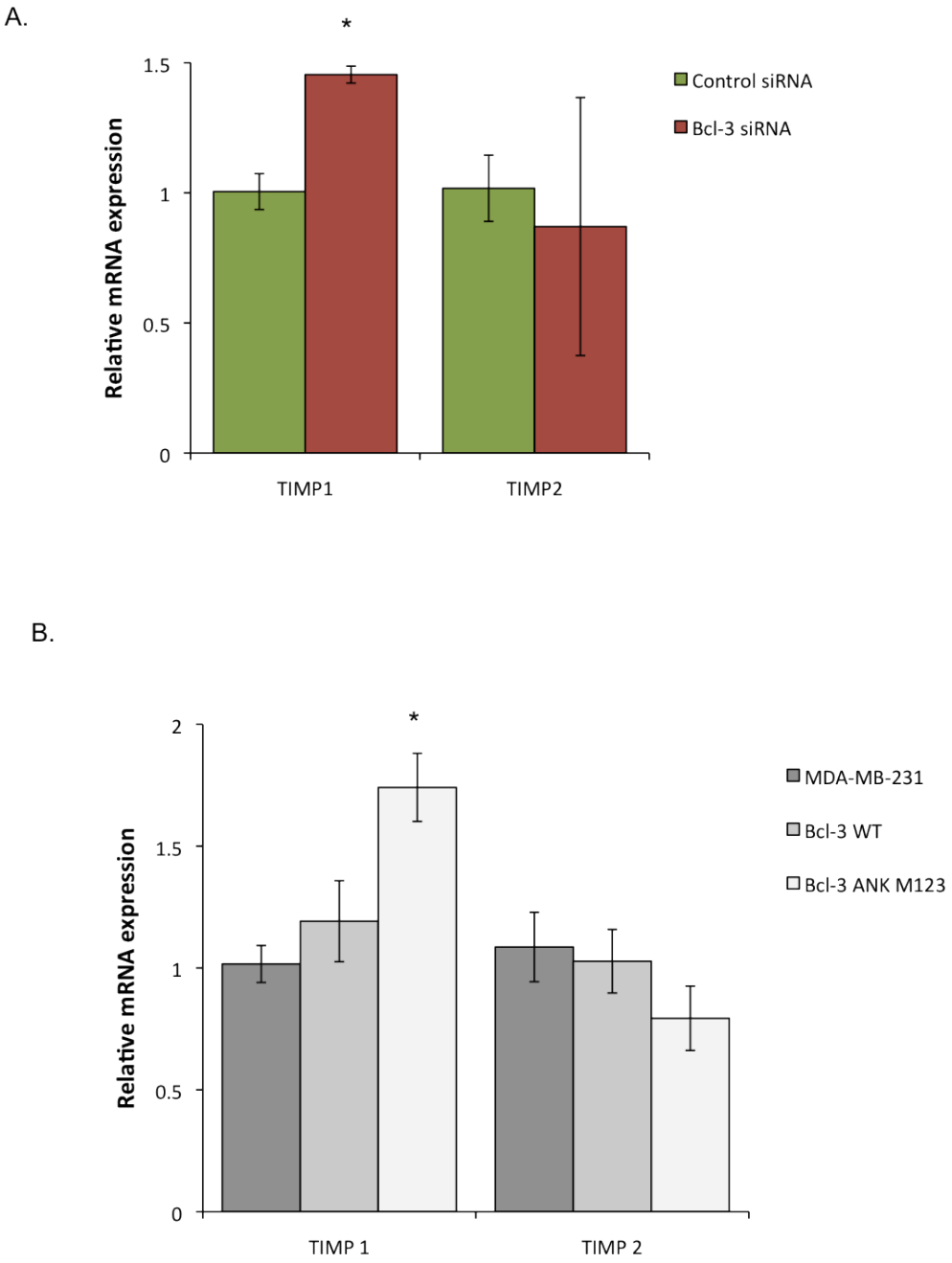

Figure 3.10 The effect of Bcl-3 on TIMP 1 and TIMP 2 expression

A. MDA-MB-231 cells were transfected with Bcl-3 or control siRNA for 48hrs before determination of expression of TIMP 1 and TIMP 2 by QRT-PCR. Expression levels are relative to cyclophilin and were normalised to mRNA levels of control siRNA. Data represent three independent transfection experiments and error bars represent ± SEM. **B.** Data show mRNA expression of TIMP 1 and TIMP 2 in MDA-MB-231 (WT, Bcl-3 WT, Bcl-3 ANK M123) cells. Expression levels are relative to cyclophilin and were normalised to mRNA levels of MDA-MB-231. Data represent three independent experiments and error bars represent ± SEM. (T-test, *=$p<0.05$, **=$p<0.01$).

3.2.1.5 The effect of Bcl-3 expression on mammosphere forming potential

Cancer stem cells make up a minority of the tumour cell population and it is proposed that these cells are responsible for seeding new tumour growth at distal sites (Shostak et al., 2011). In order to determine whether suppression of Bcl-3 function is correlated with changes in stem/progenitor subpopulation, we used the mammosphere assay (Dontu et al., 2003, Harrison et al., 2010, Charafe-Jauffret et al., 2009) as *in vitro* assay of cancer stem cell activity. As mammosphere forming ability was unaffected in murine mammary tumour cells (Wakefield et al., 2013), the hypothesis was that Bcl-3 suppression in human mammary tumour cells would have no effect on cancer stem cell activity.

Firstly, we looked at whether Bcl-3 suppression by siRNA had an effect on number and size of mammospheres formed. In the first passage, we did not observe any significant differences in the percentage of MFUs between MDA-MB-231 cells transfected with control siRNA or Bcl-3 siRNA. However, in the second passage we observed a significant decrease in MFUs for Bcl-3 siRNA cells (Figure 3.11 A+B), suggesting that Bcl-3 influenced the maintenance of stem cells in the population or their self renewing capacity.

The average size of mammospheres formed upon Bcl-3 suppression was significantly lower than that of control in both passages (Figure 3.11 C&D), suggesting that the proliferation of progenitor cells was also affected.

Having established that Bcl-3 suppression by siRNA has an effect on mammosphere formation, we wanted to determine whether disruption of Bcl-3-p50 binding as represented by overexpression of the Bcl-3 ANK M123 binding mutant would have the same effect. Therefore we compared the formation of MFUs of MDA-MB-231 cells overexpressing either Bcl-3 WT or Bcl-3 ANK M123 to parental MDA-MB-231 cells. In the first passage we observed a significant decrease in MFUs for Bcl-3 ANK M23 binding mutant, which was followed by the same trend in the second passage. This correlated with a decrease in the size of the mammospheres formed. Even though we observed a decrease in MFUs for Bcl-3 WT, the average size of mammospheres formed was significantly increased in both passages (Figure 3.12).

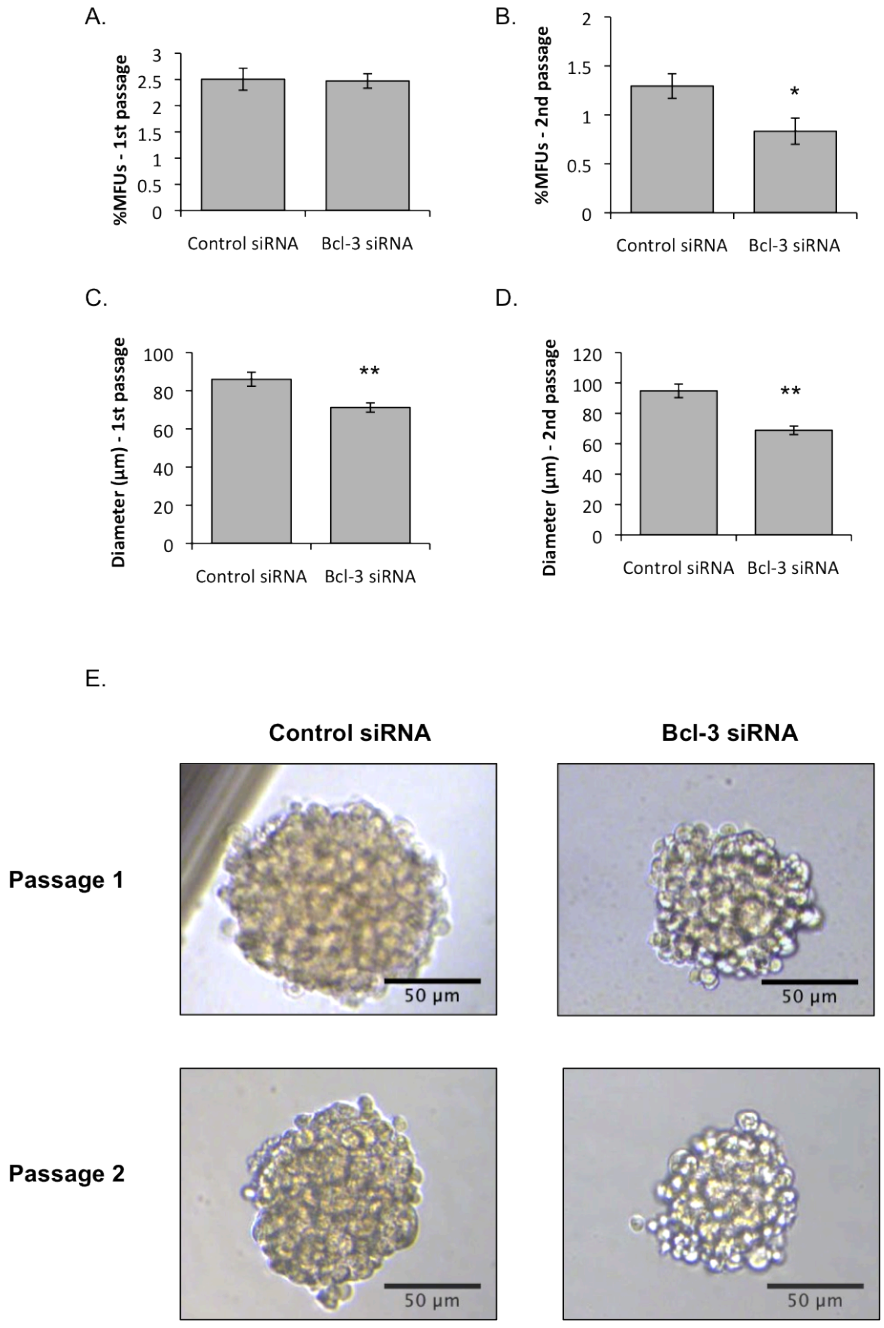

Figure 3.11 The effect of Bcl-3 knock down on mammosphere forming potential
MDA-MB-231 cells were transfected with Bcl-3 or control siRNA for 48hrs before being plated in non-adherent conditions. **A**. The number of mammospheres formed after 7 days is shown as % of MFUs in the first passage. Data represent average of 9 wells and error bars represent ± SEM. **B.** The number of mammospheres formed in the second passage is shown as % of MFUs. Data represents average of 9 wells and error bars represent ± SEM. (T-test, *=p<0.05 as compared to control siRNA) **C&D.** The size of mammospheres formed in the first passage (**C.**) and the second passage (**D.**) was measured using ImageJ software and is shown in µm. Data represent average of at least 50 measurements and error bars represent ± SEM. (T-test, **=p<0.01 as compared to control siRNA). **E.** Representative images of the mammospheres formed in first and second passage for Control siRNA and Bcl-3 siRNA. Scale bars represent 50 µm.

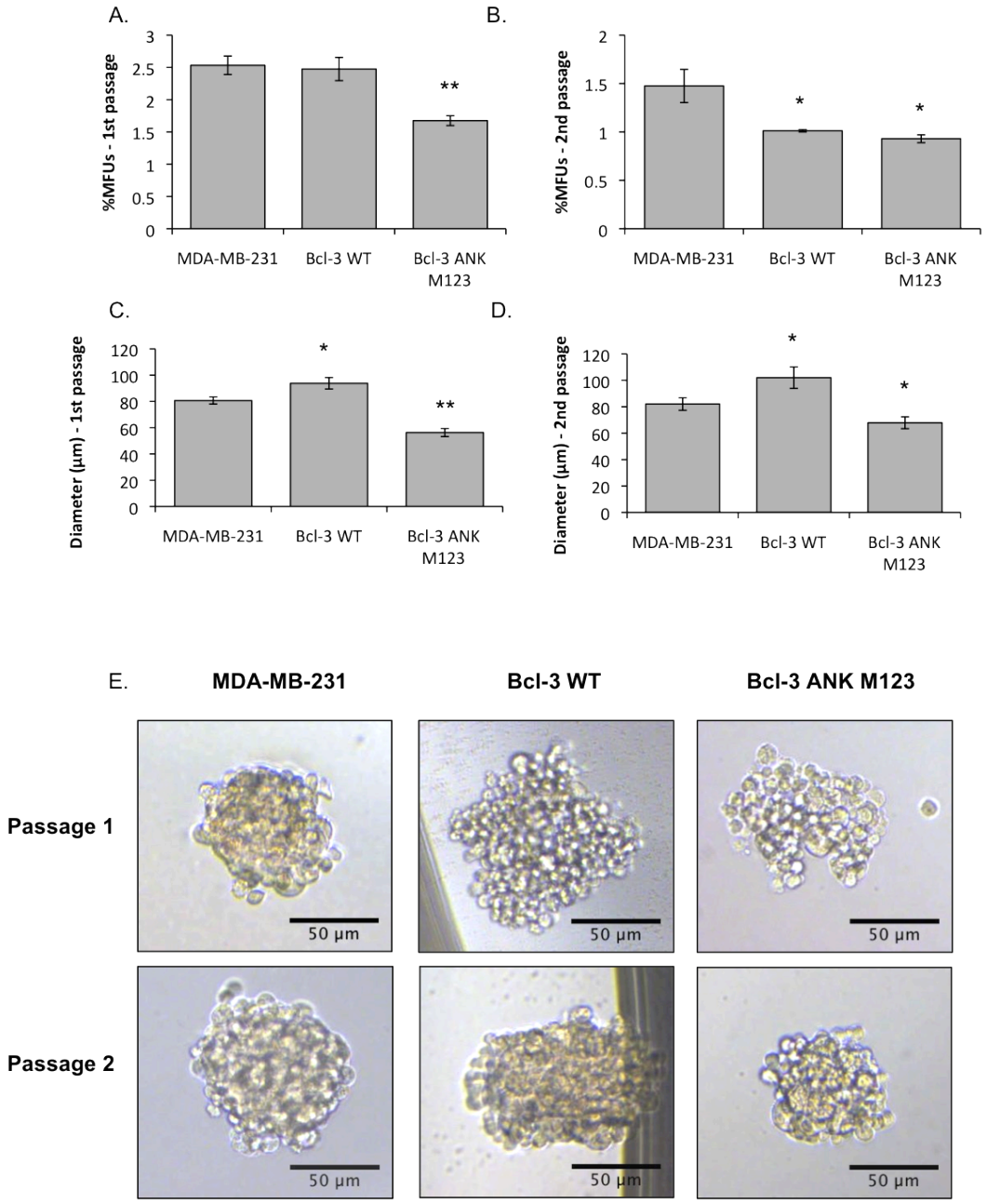

Figure 3.12 The effect of Bcl-3 WT or Bcl-3 ANK M123 overexpression on mammosphere forming potential

A. MDA-MB-231 (WT, Bcl-3 WT and Bcl-3 ANK M123) cells were plated in non-adherent conditions. The number of mammospheres formed after 7 days is shown as % of MFUs in the first passage. Data represent average of 6 wells and error bars represent ± SEM. (T-test, **=p<0.01 as compared to MDA-MB-231) **B.** The number of mammospheres formed is shown as % of MFUs in the second passage. Data represent average of 6 wells and error bars represent ± SEM. (T-test, *=p<0.05 as compared to MDA-MB-231) **C&D.** The size of mammospheres formed in the first passage (**C.**) and the second passage (**D.**) was measured using ImageJ software and is shown in µm. Data represent average of at least 30 measurements and error bars represent ± SEM. (T-test, *=p<0.05, **=p<0.01 as compared to MDA-MB-231). **E.** Representative images of the mammospheres formed in first passage for MDA-MB-231, Bcl-3 WT and Bcl-3 ANK M123 respectively. Scale bars represent 50 µm.

3.2.2 Generation of Bcl-3 WT and Bcl-3 binding mutants in HEK-293 cells

HEK-293 cells were originally chosen as the cell model to study Bcl-3 interactions with NF-κB subunits because they are easily manipulated and express negligible levels of endogenous Bcl-3 (A. Chariot, Personal Communication). The cell line was adopted for this project for the same reasons and provided consistency and continuity with the literature in terms of expected Bcl-3-p50 interactions *in vitro* (Keutgens et al., 2010). As these cells were also non-tumorigenic it also provided an opportunity to compare the function of Bcl-3 in cancer and non-cancer settings.

HEK-293 cells were transfected with Bcl-3 WT or Bcl-3 ANK M123 plasmids (FLAG-tagged constructs described in section 2.1.2), individual overexpressing clones were selected under neomycin conditions and expanded prior to analyses for Bcl-3 expression. The expression levels of five selected clones overexpressing Bcl-3 WT are demonstrated by Western blotting with Bcl-3 or FLAG primary antibodies (Figure 3.13 A). All selected clones expressed detectable levels of Bcl-3 WT and clone Bcl-3 WT-b, with highest Bcl-3 expression, was selected for future experiments. To confirm stable overexpression of clone Bcl-3 WT-b, cell pellets were collected every 5 passages up to 20 passages (Bcl-3 WT 1 - Bcl-3 WT 5). Expression levels were confirmed by Western blotting and QRT-PCR analysis (Figure 3.13 B&C) and did not show significant differences in expression with increasing passages. The Bcl-3 expression level of the selected Bcl-3 ANK M123 clone is comparable to that of the selected Bcl-3 WT clone as demonstrated by Western blotting and QRT-PCR analysis (Figure 3.13 D&E). The stable overexpression of clone Bcl-3 ANK M123 was confirmed by Western blotting (Figure 3.13 F). Similarly cell pellets were collected every 5 passages up to 20 passages (Bcl-3 ANK M123 1- Bcl-3 ANK M123 5).

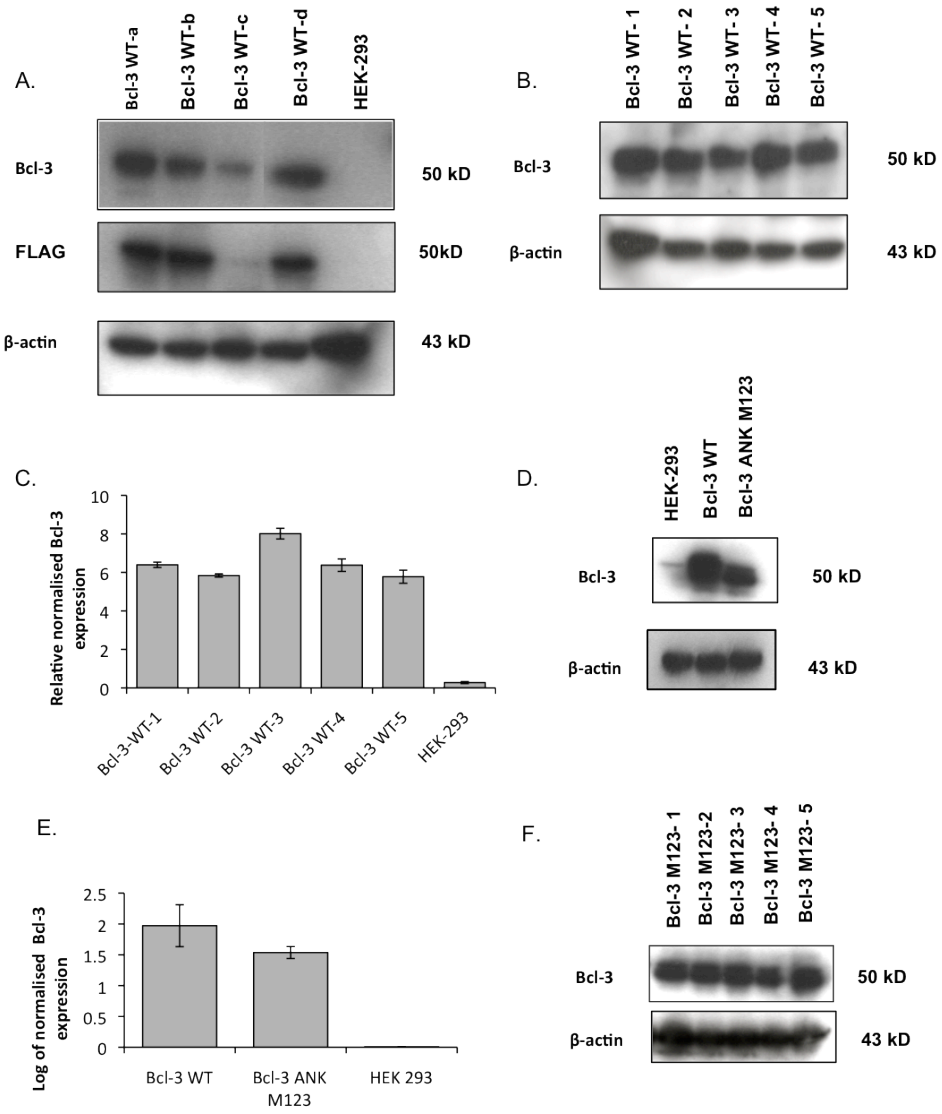

Figure 3.13 Stable overexpression of Bcl-3 WT and Bcl-3 ANK M123 in HEK-293 cells

A. Total protein was extracted from five clones of HEK-293 cells overexpressing Bcl-3 WT and subjected to Western blotting with Bcl-3 and FLAG primary antibodies. Equal loading was confirmed by β-actin. **B.** Total protein was extracted from clone of HEK-293 Bcl-3 WT-b every five passages over 20 passages and subjected to Western blotting with Bcl-3 primary antibody. Loading was confirmed by β-actin. **C.** Data shows Bcl-3 mRNA expression of clone Bcl-3 WT-b over 20 passages as measured by QRT-PCR relative to cyclophilin mRNA expression. Data represent three individual experiments and error bars represent ± SEM. **D.** Total protein was extracted from HEK-293 and selected clones of HEK-293 cells overexpressing Bcl-3 WT or Bcl-3 ANK M123 and subjected to Western blotting with Bcl-3 primary antibody. Equal loading was confirmed by β-actin. **E.** Bcl-3 mRNA expression of clone Bcl-3 WT and Bcl-3 ANK M123 was normalised to HEK-293 as measured by QRT-PCR relative to cyclophilin mRNA expression and plotted on a log scale. Error bars represent ± SEM. **F.** Total protein was extracted from clone of HEK-293 Bcl-3 M123 every five passages over 20 passages and subjected to Western blotting with Bcl-3 primary antibody. Equal loading was confirmed by β-actin.

3.2.2.1 Effect of Bcl-3 expression on basal NF-κB activity in HEK-293 cells

An NF-κB luciferase assay was performed in order to determine the basal NF-κB activity in HEK-293 cells. As expected, NF-κB activity was significantly increased when Bcl-3 WT was overexpressed as compared to WT HEK-293. Consistent with MDA-MB-231 cells, there was a reduction in NF-κB activity following Bcl-3 ANK M123 expression and although not significant this is suggesting that Bcl-3 cannot activate NF-κB signalling without binding to proteins p50 or p52 (Figure 3.14A).

3.2.2.2 Effect of Bcl-3 on cell viability and cell cycle in HEK-293 cells

Previously we determined that suppression of Bcl-3 reduce the number of viable cells in human breast cancer cell lines (Figure 3.2A-D and Figure 3.6C&D), therefore we aimed to establish the effect of Bcl-3 expression in non-tumorigenic HEK-293 cells. The number of viable cells was determined after 24hrs by the Cell Titre Blue viability assay and over three days by cell count. Consistent with previous observations, the number of viable cells was reduced when Bcl-3 ANK M123 binding mutant was overexpressed, while the most significant decrease in cell numbers was determined after 48hrs. However cyclin D1 expression of Bcl-3 ANK M123 binding mutant was higher than of HEK-293 control and comparable to Bcl-3 WT expressing cells (Figure 3.14). The cell viability of Bcl-3 WT overexpressing cells was comparable to the viability of HEK-293 cells after 24hrs cultivation, however after 48hrs cultivation the cell number was significantly decreased, even though cyclin D1 expression was found higher than that of HEK-293 control (Figure 3.14B&C). As previously determined that a higher proportion of Bcl-3 expressing cells than control cells enter cell cycle in MDA-MB-231, we aimed to establish whether Bcl-3 expression would have a similar effect in HEK-293 cells, however we did not observed any differences in the relative duration of cell cycle phases (Figure 3.14D).

3.2.3 Detection of Bcl-3-p50 binding

An indirect Sandwich ELISA assay was optimised to monitor Bcl-3-p50 protein interaction. This was initially developed in HEK-293 cells as Bcl-3-p50 interactions had previously been described in these cells (Keutgens et al., 2010).

We aimed to develop a high-throughput assay for the purpose of drug screening of compounds disrupting Bcl-3-p50 binding. Firstly, indirect ELISA was performed to establish Bcl-3 signal levels among samples (Figure 3.15A). Secondly, indirect sandwich ELISA was performed using the Bcl-3 WT and Bcl-3 ANK M123 overexpressing clones to detect the loss of signal of p50. The Bcl-3 ANK M123 binding mutant was used as a negative control (Figure 3.15B). These data demonstrated that the optimised ELISA assay could be used as a suitable method for monitoring Bcl-3-p50 protein-protein interaction.

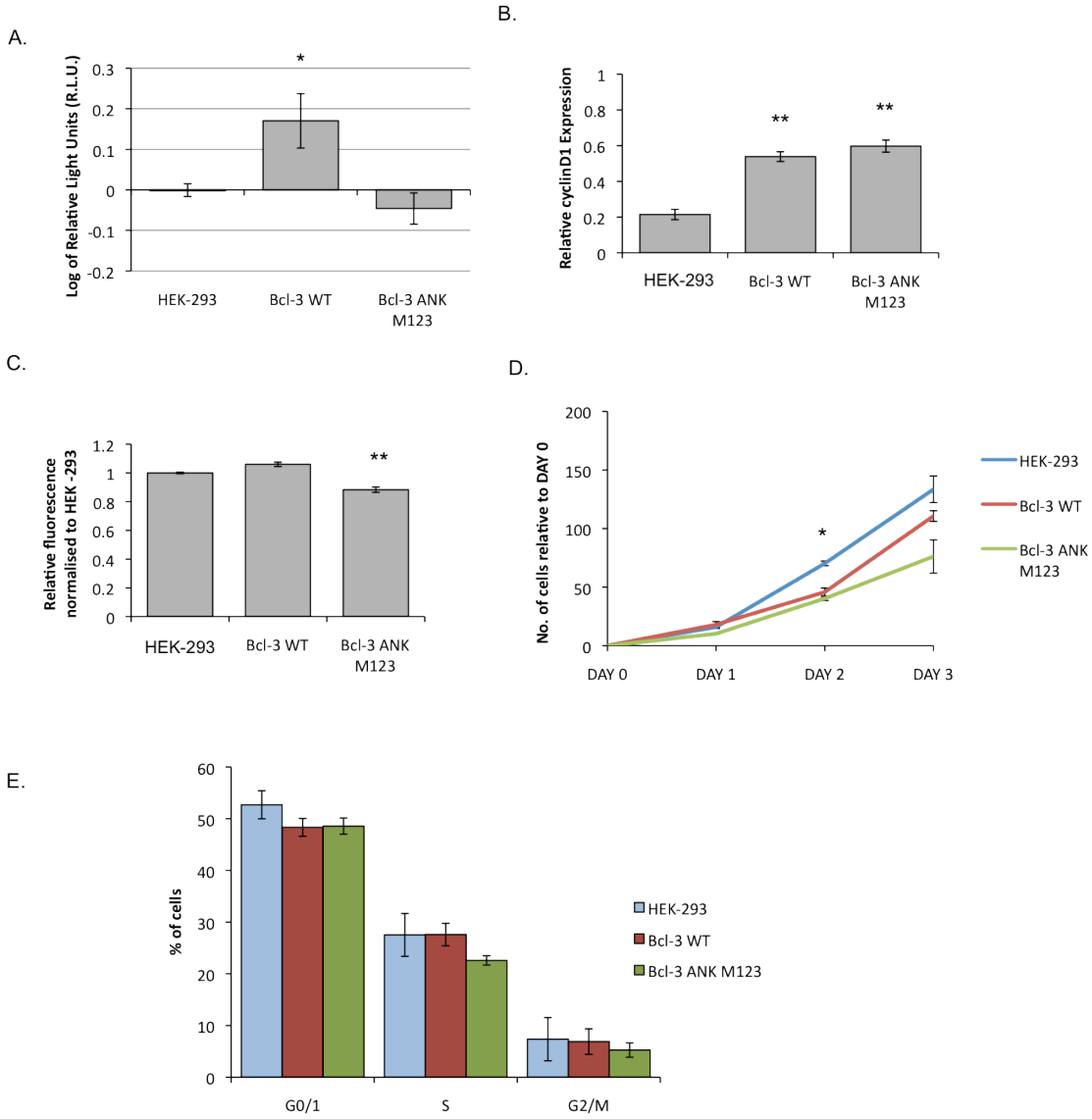

Figure 3.14 Effect of Bcl-3 expression on basal NF-κB activity and cell viability in HEK-293 cells

A.HEK-293 (WT, Bcl-3-WT and Bcl-3 ANK M123) cells were transfected with an NF-κB or LacZ reporter plasmid for 48hrs. NF-κB activity was measured as relative light units and normalised to LacZ activity before being normalised to the NF-κB activity of HEK-293 cells and plotted on a log scale. Data represent 3 independent transfections. Error bars represent ± SEM. (T-test, *=p<0.05 as compared to HEK-293). **B.** RNA was harvested from HEK-293 (WT, Bcl-3-WT and Bcl-3 ANK M123) cells for QRT-PCR analysis. Cyclin D1 mRNA expression was normalised to cyclophilin mRNA expression. Data represent three individual experiments and error bars represent ± SEM. (T-test, **=p<0.01). **C.** Cell viability in HEK-293 (WT, Bcl-3-WT and Bcl-3 ANK M123) cells was determined after 24hrs in adherent growth conditions by the Cell Titre Blue viability assay. Data represent average of six wells and error bars represent ± SEM. (T-test, **=p<0.01). **D.** HEK-293 (WT, Bcl-3-WT and Bcl-3 ANK M123) cells were plated in normal adherent growth conditions. The number of cells in each well was counted at three time points (24hrs, 48hrs, 72hrs). Data represent average of six wells and error bars represent ± SEM. **E.** HEK-293 (WT, Bcl-3-WT and Bcl-3 ANK M123) cells were stained with propidium iodide and analysed for cell cycle stage by FACS at 585/42 PE-A. Data represent average of three measurements and error bars represent ± SEM.

A.

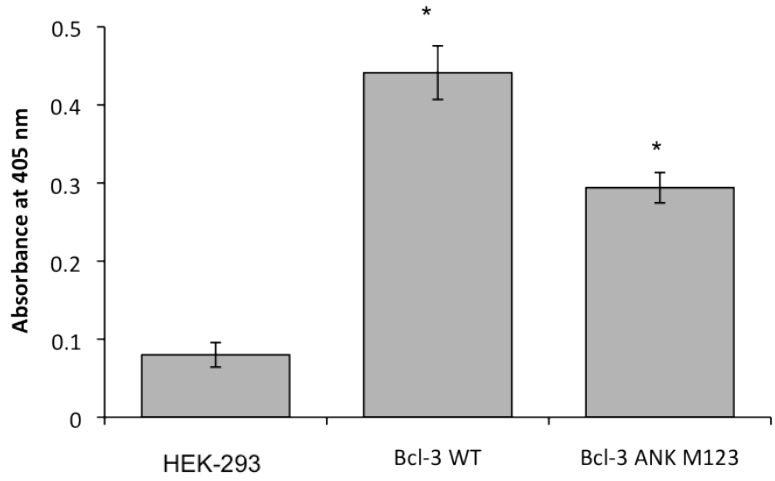

B.

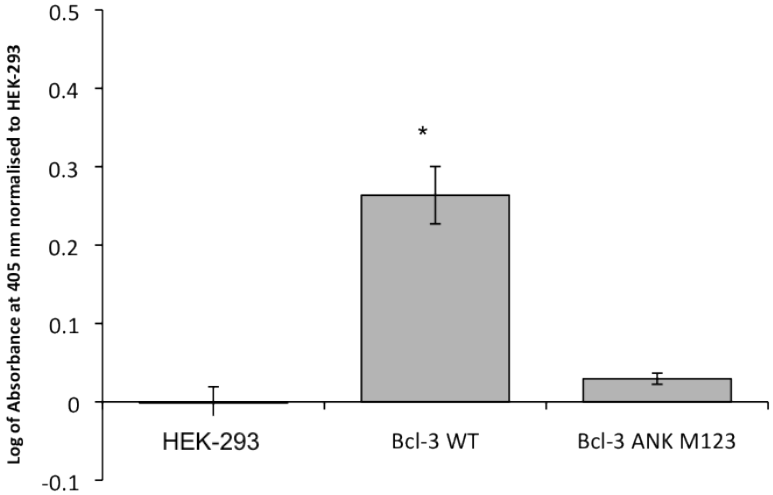

Figure 3.15 Optimisation of Indirect Sandwich ELISA

A. Indirect ELISA: HEK-293 (Bcl-3 WT, Bcl-3 ANK M123 and WT) cells were lysed under non-denaturing conditions and the indirect ELISA assay was performed on FLAG coated ELISA plates, using Bcl-3 primary antibody and an alkaline phosphatase conjugated secondary antibody. pnPP was used as a detection system and absorbance was measured at 405nm. Error bars represent ± SEM of three independent wells. (T-test, *=$p<0.05$ as compared to HEK-293). **B. Indirect Sandwich ELISA**: HEK-293 (WT, Bcl-3 WT and Bcl-3 ANK M123) cells were lysed under non-denaturing conditions and indirect sandwich ELISA assay was performed on FLAG coated ELISA plates, using a p50 primary antibody and an alkaline phosphatase conjugated secondary antibody. pnPP was used as a detection system and absorbance was measured at 405 nm normalised to the absorbance of HEK-293 and plotted on a log scale. Error bars represent ± SEM of three independent wells. (T-test, *=$p<0.05$ as compared to HEK-293).

3.2.4 Overexpression of p52 WT in HEK-293

Unlike p50, HEK-293 cells do not express detectable levels of endogenous p52 (Figure 3.17 A). In order to generate a suitable model for testing inhibitors disrupting Bcl-3-p52 binding and to determine the effect of inhibition of Bcl-3-p52 interaction, we overexpressed a WT p52 construct in parental HEK-293, HEK-293 Bcl-3 WT and HEK-293 Bcl-3 ANK M123. Cells were transduced with lentivirus encoding the GFP labelled, HA tagged, WT version of p52 in order to generate stable lines overexpressing p52 WT. The expression of GFP was confirmed by confocal microscopy and FACS analysis (Figure 3.16). The expression levels of p52 and Bcl-3 were confirmed by Western blotting (Figure 3.17 A&B).

3.2.4.1 Effect of p52 expression on NF-κB basal activity

An NF-κB luciferase activity assay was performed in order to determine the basal NF-κB activity in HEK-293 p52 expressing cells (Figure 3.17 C). As expected, NF-κB activity was significantly increased when Bcl-3 WT was overexpressed together with p52 as compared to HEK-293 p52 expressing cells. Importantly, no increase in the NF-κB activity was observed when Bcl-3 ANK M123 was overexpressed together with p52. In order to determine the effect of p52 overexpression on basal NF-κB activity, NF-κB activity of HEK-293 cells (Bcl-3-WT, Bcl-3 ANK M123 and WT) was compared to HEK-293 cells (Bcl-3-WT, Bcl-3 ANK M123 and WT) overexpressing p52 WT (Figure 3.17 D). We observed an increase in NF-κB activity when Bcl-3 WT and p52 WT were co-expressed, as p52 homodimers in a complex with Bcl-3 are known to increase NF-κB activity (Bours et al., 1993). However when p52 was expressed in either HEK-293 WT or Bcl-3 ANK M123, no effect on NF-κB activity was observed.

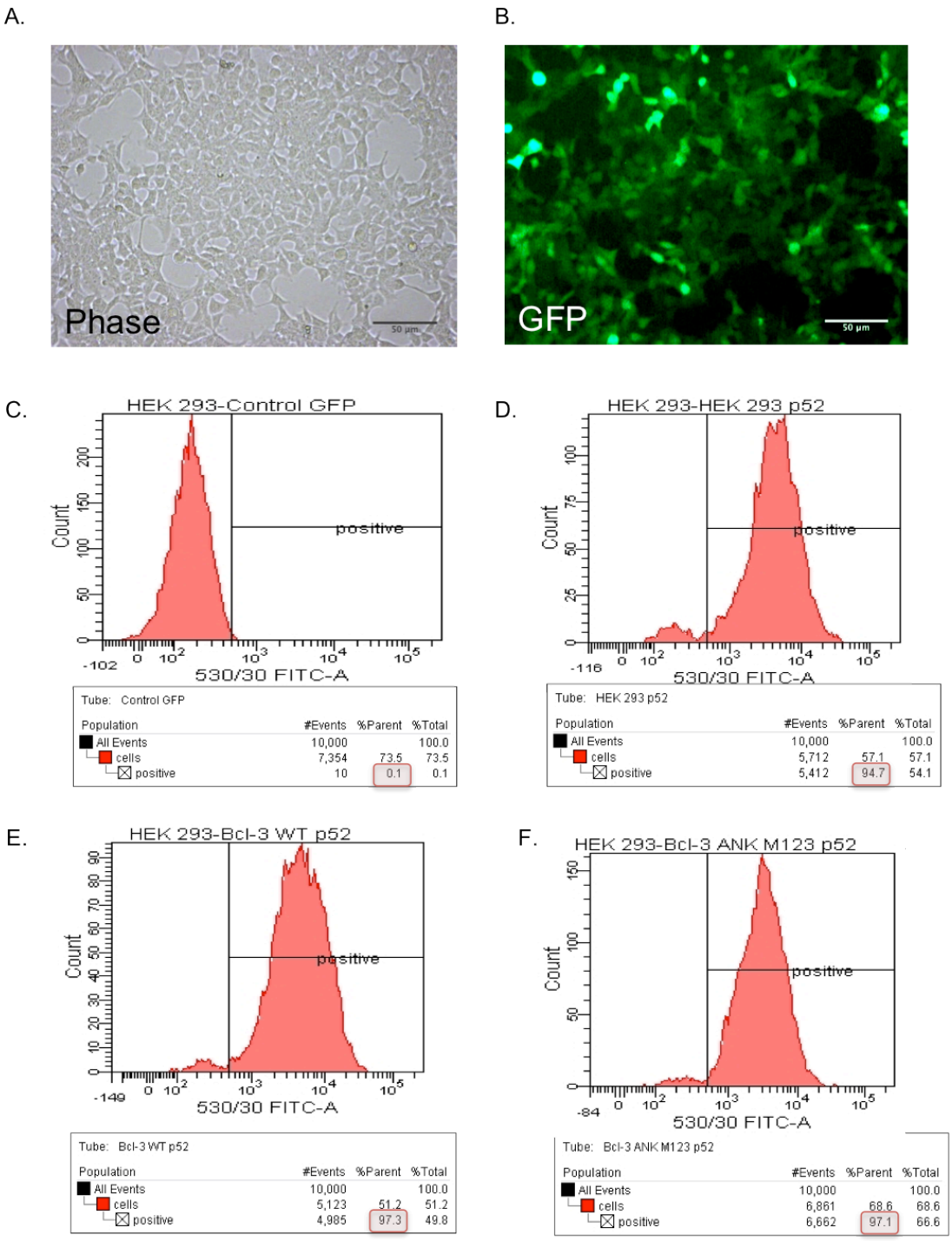

Figure 3.16 GFP expression in HEK-293 – p52 cells

Phase contrast (**A.**) and GFP (**B.**) images of HEK-293 cells transduced with p52 WT – GFP expression vector. Scale bars represent 50 µm. **C. - F.** Representative FACS plots of GFP expression (measured at 530/30 FITC-A) of HEK-293 cells transduced with p52 WT GFP expression vector. **C.** Control HEK-293 cells with gate set to exclude >99% non-labelled cells. **D**. HEK-293 cells overexpressing p52 showing 95% GFP expression. **E.** HEK-293 cells overexpressing Bcl-3 WT and p52 showing 97% GFP expression. **F.** HEK-293 cells overexpressing Bcl-3 ANK M123 and p52 showing 97% GFP expression.

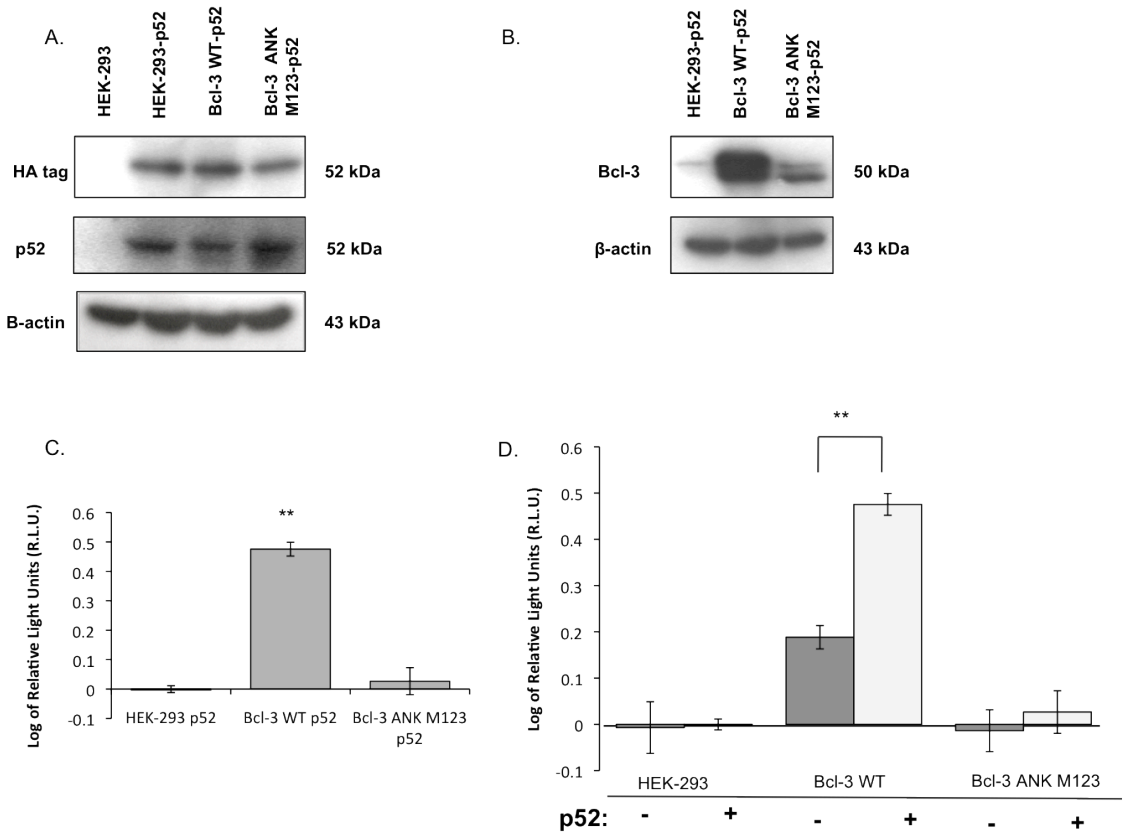

Figure 3.17 Stable overexpression of p52 WT in HEK-293 cells and its effect on basal NF-κB activity

A. Total protein was extracted from HEK-293 cells and HEK-293 overexpressing HA-tagged p52 WT (HEK-p52, Bcl-3 WT-p52, Bcl-3 ANK M123-p52) cells and subjected to Western blotting with HA tag and p52 primary antibodies. Equal loading was confirmed by β-actin. **B.** Total protein was extracted from HEK-293 cells overexpressing HA-tagged p52 WT (HEK-p52, Bcl-3 WT-p52, Bcl-3 ANK M123-p52) and subjected to Western blotting with Bcl-3 primary antibody. Equal loading was confirmed by β-actin. **C.** HEK-293 p52 (WT, Bcl-3-WT and Bcl-3 ANK M123) cells were transfected with NF-κB or LacZ reporter for 48hrs. NF-κB activity was measured as relative light units and normalised to LacZ activity before being normalised to the activity of HEK-293 p52 and plotted on a log scale. Data represent 3 independent transfections. Error bars represent ± SEM. (T-test, **=$p<0.01$ as compared to HEK-293 p52). **D.** HEK-293 (Bcl-3-WT, Bcl-3 ANK M123 and WT) cells and HEK-293 p52 (Bcl-3-WT, Bcl-3 ANK M123 and WT) cells were transfected with NF-κB or LacZ reporter for 48hrs. NF-κB activity was measured as relative light units and normalised to LacZ activity before being normalised to respective controls (HEK-293 and HEK-293 p52) and plotted on a log scale. Data represent 3 independent transfections. Error bars represent ± SEM. (T-test, **=$p<0.01$).

3.2.4.2 Effect of co-expression of Bcl-3 and p52 on cell viability

We aimed to establish the effect of co-expression of Bcl-3 and p52 on cell viability in HEK-293 cells. The co-expression of Bcl-3 ANK M123 binding mutant and p52 reduced the number of viable cells after 24hrs and over three days as compared to control. Even though co-expression of Bcl-3 WT and p52 did not affect the number of viable cells after 24hrs, the number of viable cells was significantly reduced after 48hrs and even more after 72hrs (Figure 3.18 A&B). These observations are consistent with the effect of Bcl-3 expression in MDA-MB-231 cells. We could also see a similar trend in cyclin D1 expression as in MDA-MB-231 cells overexpressing either Bcl-3 WT of Bcl-3 ANK M123, however changes in cyclin D1 expression were not significant as compared to HEK-293 p52 control.

As with HEK-293 expressing Bcl-3 we did not observe any differences in the relative duration of cell cycle phases when Bcl-3 was co-expressed with p52 (Figure 3.18 C).

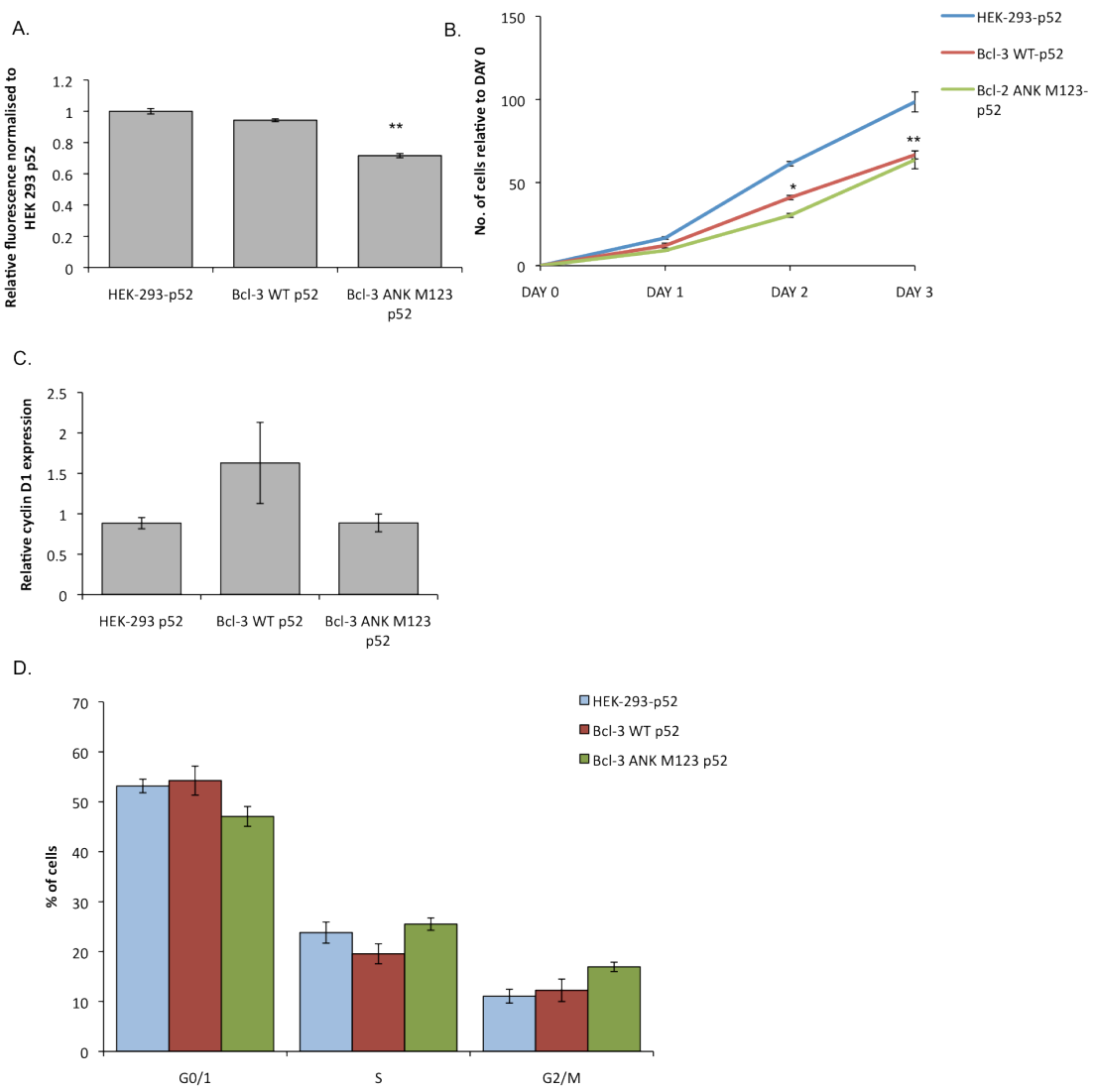

Figure 3.18 The effect of p52 overexpression on cell viability in the HEK-293 cell line

A. Cell viability in HEK-293 p52 (WT, Bcl-3-WT and Bcl-3 ANK M123) cells was determined after 24hrs in adherent growth conditions by the Cell Titre Blue viability assay. Data represent average of six wells and error bars represent ± SEM. (T-test, **=p<0.01). **B.** HEK-293 p52 (WT, Bcl-3-WT and Bcl-3 ANK M123) cells were plated in normal adherent growth conditions. The number of cells in each well was counted at three time points (DAY 1, DAY 2, DAY 3). Data represent average of six wells and error bars represent ± SEM. **C.** RNA was harvested from HEK-293 p52 (WT, Bcl-3-WT and Bcl-3 ANK M123) cells for QRT-PCR analysis. Cyclin D1 mRNA expression was normalised to cyclophilin mRNA expression. Data represent three individual experiments and error bars represent ± SEM. **D.** HEK-293 p52 (WT, Bcl-3-WT and Bcl-3 ANK M123) cells were stained with propidium iodide and analysed for cell cycle stage by FACS at 585/42 PE-A. Data represent average of three measurements and error bars represent ± SEM.

3.3 Discussion

In previous *in vivo* and *in vitro* studies it was determined that Bcl-3 specifically promoted murine metastatic tumour growth, mainly in ErbB2 positive mammary tumours (Wakefield et al., 2013). This chapter aimed to further explore the outcome of Bcl-3 suppression in human cell lines and to determine whether Bcl-3 function can be inhibited by disruption of binding with its binding partners, p50 and p52, from the NF-κB family.

3.3.1 The outcome of Bcl-3 suppression in human breast cancer cell lines

Bcl-3 was suppressed in three human breast cancer cell lines by Bcl-3 siRNA, in SKBR3, MDA-MB-231 and ZR-75-1 cell lines. Bcl-3 suppression in the HER2+, SKBR3 cell line and in the triple negative, MDA-MB-231 cell line led to a significant decrease in NF-κB activity (Figure 3.1B) despite the fact that MDA-MB-231 cells exhibit low Bcl-3 expression (Figure 3.1A). Interestingly we also observed a significant decrease in cell viability in these two cell lines (Figure 3.2) when Bcl-3 was suppressed, which was not seen previously in the HER2+ murine breast cancer cells (Wakefield et al., 2013).

The decrease in cell viability could be explained by changes in the cell cycle and increased cell death. We determined that a lower percentage of cells were entering the S phase of the cell cycle in both cell lines and in the case of the MDA-MB-231 cell line we also observed a significant increase in the percentage of cells resting in the G0/G1 phase when Bcl-3 was suppressed (Figure 3.4). Moreover, in both cell lines we observed a significant increase in cell death (Figure 3.3A), yet the amplitude of change was higher in SKBR3 cells where we also saw an almost 50% decrease in cell viability as opposed to 20% seen in MDA-MB-231 cells when Bcl-3 was suppressed.

We did not observe any change in NF-κB activity or cell viability when Bcl-3 was suppressed in the ZR-75-1 cell line, even though there was a significant increase in cell death following Bcl-3 suppression (Figure 3.3A). These findings might be attributed to ER positivity of these cells, as NF-κB activation was observed preferentially in HER2+/ER- mammary tumours (Biswas et al., 2004).

Cyclin D1 is an important gene regulated by the NF-κB signalling pathway that plays a critical role in the cell cycle. Induction of cyclin D1 in breast cancer shortens the G1 phase and increases the number of cells entering the cell cycle, which results in an increased proliferation (Musgrove et al., 1994). Therefore a decrease in cyclin D1 level would explain the decrease in cell viability and changes to cell cycle observed. However the levels of cyclin D1 did not change when Bcl-3 was suppressed in any of the cell lines (Figure 3.3B-D), suggesting that cell proliferation is regulated via other NF-κB regulated gene(s), which have yet to be identified.

3.3.2 Modelling disruption of Bcl-3-p50 binding in MDA-MB-231 cell line

We aimed to determine whether Bcl-3 function could be inhibited by disruption of its binding to proteins p50 and p52 from the NF-κB family. For this purpose we used a Bcl-3 binding mutant ANK M123 (construct described in section 2.1.2), which was proven not to be able to bind to protein p50 and p52 (Keutgens et al., 2010).

We hypothesised that the Bcl-3 binding mutant ANK M123 could behave as a dominant negative inhibitor of Bcl-3. Firstly, using modelling studies it was found that Bcl-3 binds p50 and p52 proteins as a dimer (Michel et al., 2001), therefore endogenous Bcl-3 might bind to the Bcl-3 binding mutant preventing the activity of the endogenous Bcl-3. Secondly, the Bcl-3 binding mutant is not able to bind to p50 and p52 homodimers, however its ability to bind other Bcl-3 binding partners could be preserved, therefore further experiments are clearly needed to explore the potential of Bcl-3 ANK M123.

We overexpressed the Bcl-3 ANK M123 construct in MDA-MB-231 cells, these cells were chosen because of their metastatic phenotype and low level of endogenous Bcl-3 expression. Bcl-3 ANK M123 overexpressing cells responded *in vitro* similarly to cells with Bcl-3 suppressed by siRNA, supporting the hypothesis that these cells act in a dominant negative manner. We observed a significant decrease in NF-κB activity along with down regulation of cyclin D1 (Figure 3.5&Figure 3.6). The cell viability was also decreased (Figure 3.6), even though cell cycle or number of dead/apoptotic cells was not affected (Figure 3.6&Figure 3.7),

therefore the mechanism by which the cell viability is affected will be explored further.

Previously it was shown that Bcl-3 deletion did not affect primary tumour growth *in vivo*, however metastasis formation was significantly reduced (Wakefield et al., 2013). Moreover, a significant reduction in mitotic index (Ki-67) and an increase in apoptosis (cleaved caspase-3) was observed only in secondary lung lesions with no changes seen in primary tumours (Wakefield et al., 2013).

As we observed a decrease in cell viability when Bcl-3 ANK M123 was overexpressed in MDA-MB-231 cells, consistent with the reduction in viability with Bcl-3 siRNA, we wanted to establish the effect of these cells on primary tumour growth *in vivo.* MDA-MB-231 cells overexpressing Bcl-3 ANK M123 were injected orthotopically by Dr. Richard Clarkson into 8 week old immune compromised female virgin mice, (Hsd: Athymic Nude-Foxn 1^{nu}) and the size of formed primary tumours was measured until the sacrifice of mice after 42 days post-surgery (manuscript in preparation).

In contrast to previous *in vivo* studies, a significantly reduced growth rate was observed as compared to parental MDA-MB-231 cells with a longer latency in tumour formation. Interestingly, primary tumours formed from Bcl-3 ANK M123 overexpressing cells exhibited a significant reduction in mitotic index (Ki-67) and an increase in apoptosis (cleaved caspase-3) with a histological appearance less aggressive and invasive than controls, properties previously observed only at secondary lesions (Steffan Seal, unpublished).

As only a few metastases were formed from these primary tumours both in Bcl-3 ANK M123 and parental MDA-MB-231 control, possibly due to early sacrification of mice, the effect on secondary lung lesion could not be evaluated. Additional *in vivo* experiments are required to verify the effects of Bcl-3 ANK M123 on metastatic frequencies.

3.3.3 Overexpression of Bcl-3 WT in MDA-MB-231 cells

Bcl-3 has been shown to stimulate cell growth as well as provide a survival function in various cell lines (Rebollo et al., 2000, Na et al., 1999). Bcl-3 overexpression in immortalized human breast epithelial cells, H16N2, led to a shortened G1 phase of the cell cycle and upregulation of cyclin D1. However no

increase in proliferation was observed despite cyclin D1 expression and shortened G1 phase (Westerheide et al., 2001).

We aimed to establish the effect of Bcl-3 WT overexpression in the triple negative human breast cancer cell line, MDA-MB-231, to better understand the oncogenic role of Bcl-3. Overexpression of Bcl-3 WT led to an increase in NF-κB activity together with cyclin D1 upregulation (Figure 3.5&Figure 3.6). We also observed a lower percentage of cells in G0/G1 phase (Figure 3.7) as seen previously in H16N2 cells (Westerheide et al., 2001), suggesting re-entry into the cell cycle. However despite this the cell count of Bcl-3 WT overexpressing cells was significantly decreased compared to parental MDA-MB-231 cells (Figure 3.6).

We anticipated that the Bcl-3 WT overexpressing cells were proliferating at a higher rate and that the decrease in cell count might be attributed to an increase in cell death. Even though we observed only a non-significant increase in cell death when Bcl-3 WT was overexpressed as analysed by FACS, the caspase 3/7 activities were significantly increased (Figure 3.6), suggesting that Bcl-3 overexpression mediated apoptosis via activation of caspase 3/7. We also speculated that unnatural ectopic overexpression of Bcl-3 could lead to physiological suppression of NF-κB activity, which might be attributed to a loss in homeostatic regulation of Bcl-3 binding to NF-κB subunits.

Indeed, in a study by Brasier *et al.* (2001) the presence of an NF-κB-Bcl-3 auto regulatory loop was identified, in which Bcl-3 transcription was negatively regulated by its own gene product thus preventing aberrant Bcl-3 accumulation (Brasier et al., 2001)

In another study by Bundy *et al.* (1997) Bcl-3 at low concentration was shown to act as a co-activator by increasing the rate of Bcl-3-p52 complexes binding to κB site and in higher concentrations to form inhibitory complexes with p52 homodimers, with these opposing roles dependent upon phosphorylation status of Bcl-3 (Bundy et al., 1997). Thus it may be that overexpression of Bcl-3 results in interactions with other signalling pathways, with opposing regulatory roles, resulting in an antagonistic action against its own pro-tumorigenic effects at higher concentrations. This is speculative at this stage and could be investigated further with a conditional regulator of Bcl-3 levels in an appropriate cell line.

Interestingly, Bcl-3 oncogenicity is also attenuated by GSK3-dependent phosphorylation on its C-terminal domain as this phosphorylation triggers Bcl-3 degradation via the proteasome pathway. This mechanism physiologically limits intracellular levels of Bcl-3 and therefore prevents Bcl-3 oncogenicity in normal cells (Viatour et al., 2004a). However translocation that causes Bcl-3 overexpression might then overcome GSK3-mediated Bcl-3 phosphorylation and degradation. The use of phosphorylation mutants would address this post-translational mechanism.

The overall negative effect of Bcl-3 overexpression on cell numbers *in vitro* was recently reflected in a mouse xenografts study, where a significant reduced growth rate was observed as compared to parental MDA-MB-231 cells with a longer latency in tumour formation (Dr. Richard Clarkson and Steffan Seal, unpublished data). Moreover, recombinant tumours exhibited a significant reduction in mitotic index (Ki-67) and apoptosis (cleaved caspase-3).

In comparison with a similar study by Pratt *et al.* (2003), utilising the MCF-7 breast cancer cell line transfected with FLAG-Bcl-3 constructs injected into nude mice, produced a near fourfold increase in the growth of Bcl-3 enriched tumours when compared with controls. The differences in primary tumour growth observed between these studies might be cell type dependent or it maybe due to the fact that cells were injected into mammary fat pad in our study as opposed to subcutaneous injections used by Pratt *et al.* (2003).

3.3.4 Metastatic properties of Bcl-3

We have previously shown that Bcl-3 deletion *in vivo* results in a decrease in secondary tumour formation and a reduction in metastatic tumour growth (Wakefield et al., 2013). Moreover a suppression of Bcl-3 *in vitro* by siRNA resulted in a significant reduction of motility in a murine HER2+ breast cancer cell line (Wakefield et al., 2013) and in both, HER2+ and triple negative human breast cancer cell lines (Figure 3.1)(manuscript in preparation).

Consistent with previous observations, suppression of Bcl-3 by siRNA significantly reduced the migratory capacity of MDA-MB-231 cells by 50% (Figure 3.8) and overexpression of the Bcl-3 ANK M123 binding mutant reduced migratory capacity by 30% (Figure 3.9). When Bcl-3 WT was overexpressed, the migratory capacity was significantly increased by 40% as compared to parental MDA-MB-231

cells (Figure 3.9), whereas none of the Bcl-3 alteration affected cell invasion (Figure 3.8&Figure 3.9).

These findings would suggest that Bcl-3 expression regulates cell proliferation and cell motility in a different way, as we observed that Bcl-3 WT overexpression led to a decrease in cell proliferation, but increase in cell migration ability. Indeed, a study by Janda *et al.* (2002) looked at the effect of Ras signalling pathways using a mammary epithelial EpH4/EpRas model. Ras induced two pathways, both of which activated NF-κB signalling in these cells (Huber et al., 2004b). A Raf/MEK/MAPK pathway was required for EMT and metastasis, while the PI3K/Akt signalling was found to be responsible for cell proliferation (Janda et al., 2002).

The molecular mechanism responsible for the change in migratory capacity is not yet defined. However, previous studies using microarray and QRT-PCR assays in murine MG1361 cells identified a number of metastasis-related genes whose expression was altered following siRNA-mediated suppression of Bcl-3, among them the NME family, TIMP family and Arhgdib genes (Wakefield et al., 2013).

However only the family of TIMPs genes was found to be affected in HER2+ and triple negative human breast cancer cell lines following suppression of Bcl-3 by siRNA (manuscript in preparation). Therefore the identity of the factors responsible for cell migration remains elusive. However, suppression of Bcl-3 by siRNA in MDA-MB-231 cells and overexpression of Bcl-3 ANK M123 caused a significant increase in TIMP1, which as a known inhibitor of matrix metalloproteinases has a role in inhibition of cell invasion.

Huber *et al.* (2004) suggested that NF-κB activation leads to activation of the epithelial-mesenchymal transition (EMT), an important processes in metastatic progression (Thiery, 2002). A large proportion of genes regulating EMT in a breast cancer cell line, EpH4, are also known as NF-κB targets, including Twist, various MMPs and cathepsin family members (Huber et al., 2004b, Huber et al., 2004a). Other target genes involved in tumour spread and metastasis of breast cancer regulated by NF-κB include those encoding IL-8, CXCR4 (Helbig et al., 2003), VEGF (Shibata et al., 2002) or urokinase-like plasminogen activator (uPA) (Sliva et al., 2002).

In a study by Andela *et al.* (2000) NF-κB activity was suppressed by retroviral delivery of a dominant negative inhibitor of NF-κB in a murine lung alveolar carcinoma cell line. Consistent with our published work (Wakefield et al., 2013), no effect on proliferation *in vitro* or on growth of primary tumours *in vivo* was observed. However total lung tumour burden was significantly decreased and formed metastases were smaller than those of control (Andela et al., 2000). The inhibition of NF-κB signalling in these murine lung alveolar carcinoma cells resulted in the down-regulation of MMP9, urokinase-like plasminogen activator (uPA) and reciprocal up-regulation of TIMP 1, TIMP 2 and PAI 2. This was repeated in a human breast cancer cell line, MDA-MB-231, and similar results were observed, suggesting that it was not specific to tumour type (Andela et al., 2000).

Even though further experiments are needed to determine the exact mechanism responsible for the significant changes in migratory ability, these data indicate that Bcl-3 plays an important role in promoting cell migration by affecting the expression of metastasis related genes, likely through activation of NF-κB signalling.

3.3.5 Bcl-3 expression and mammosphere forming potential

Cancer stem cells make up a minority of the tumour cell population and it is proposed that these cells are responsible for seeding new tumour growth at distal sites. NF-κB is believed to regulate the self-renewal of breast cancer stem cells in a model of HER2-dependent tumourigenesis (Shostak and Chariot, 2011). HER2 amplification led to an expansion of mammary stem cell numbers (Korkaya et al., 2008) and it is known that HER2 activates NF-κB via canonical signalling pathway (Biswas and Iglehart, 2006).

The mammosphere assay (Dontu et al., 2003, Harrison et al., 2010, Charafe-Jauffret et al., 2009) is a generally used *in vitro* assay to assess cancer stem cell activity.

In previous studies, mammosphere forming ability was unaffected in murine mammary tumour cells following Bcl-3 suppression by siRNA (Wakefield et al., 2013). However, in the human MDA-MB-231 cell line, suppression of Bcl-3 by siRNA led to the formation of significantly smaller mammospheres compared to control while the number of MFUs was not affected, suggesting that the

proliferation of progenitors arising from the presumptive CSCs was affected. In the second passage we observed not only a decrease in size of formed mammospheres, but also a significant decrease in MFU numbers (Figure 3.11), suggesting that Bcl-3 influenced the maintenance or self renewal of the cancer stem cell population during the first passage.

Although not performed, it is postulated that serial passaging of this population would result in the return of the self-renewing capacity of the CSCs population as the effect of transient siRNA depletion over time.

Moreover, when we overexpressed Bcl-3 ANK M123 binding mutant in MDA-MB-231 we observed a significant decrease in the proportion of MFUs, which was followed by the same trend in the second passage. This correlated also with a decrease in the size of the mammospheres formed.

Even though we observed no change in the first passage and a decrease in MFU numbers in the second passage when Bcl-3 WT was overexpressed in MDA-MB-231 cells, the average size of mammospheres formed was significantly increased in both passages (Figure 3.12).

The decrease of MFUs when Bcl-3 WT was overexpressed may reflect the increase in cell death in this population, which is especially surprising because the assay tests anoikis resistance and NF-κB was shown to be pro-survival in breast cancer (Biswas et al., 2003). However the increase in size is consistent with an increase in cell cycle, in this case of progenitors.

3.3.6 Overexpression of Bcl-3 in non-tumorigenic HEK-293 cells

Non-tumorigenic human embryonic kidney HEK-293 cells were originally chosen as a cell model to study Bcl-3 interactions with NF-κB subunits for the purpose of biological evaluation of designed Bcl-3 inhibitors, because they are easily manipulated and express negligible levels of endogenous Bcl-3 (A. Chariot, Personal Communication). As these cells were also non-tumorigenic it also provided an opportunity to determine the function of Bcl-3 in cancer and non-cancer settings.

Consistent with results obtained from the tumorigenic MDA-MB-231 cell line, overexpression of Bcl-3 ANK M123 in the HEK-293 cell line resulted in a decrease in NF-κB activity and cell viability (Figure 3.14). However we observed an unexpected increase in cyclin D1 expression with no effect on cell cycle (Figure

3.14). An overexpression of Bcl-3 WT in these cells led to an increase in NF-κB activity and cyclin D1 expression and a decrease in cell proliferation (Figure 3.14), which was consistent with previous observations in MDA-MB-231 cells.

Unlike p50, HEK-293 cells do not express detectable levels of endogenous p52 (Figure 3.17A). Therefore we overexpressed a WT p52 construct in HEK-293, HEK-293 Bcl-3 WT and HEK-293 Bcl-3 ANK M123 (Figure 3.16&Figure 3.17). Consistent with previous observations (Bours et al., 1993, Westerheide et al., 2001), co-expression of Bcl-3 and p52 significantly increased NF-κB activity as compared to expression of Bcl-3 alone. Expression of p52 alone had a repressive effect on NF-κB activity (Figure 3.17). However, co-expression of p52 with either Bcl-3 WT or Bcl-3 ANK M123 decreased cell viability without affecting cyclin D1 expression or the cell cycle (Figure 3.18).

However the main reason for overexpressing Bcl-3 WT, Bcl-3 ANK M123 and p52 in HEK-293 cells was to evaluate protein-protein interactions and the loss of these interactions for the purpose of screening compounds designed to disrupt Bcl-3-p50 binding. An indirect sandwich ELISA was optimised to detect Bcl-3-p50 binding and found as a suitable method for monitoring Bcl-3-p50 interactions (Figure 3.15).

3.4 Conclusion

Overall, suppression of Bcl-3 either by siRNA or by disruption of binding to proteins p50 and p52 from the NF-κB family was found to affect not only metastatic progression but also tumour growth of human breast cancer xenografts. The inhibition of Bcl-3, therefore seems a promising therapeutic strategy, especially for HER2+ and triple negative breast cancers. Therefore the next chapter will focus on designing novel inhibitors of Bcl-3-p50/p52 binding using a molecular modelling tool.

Chapter 4

Generation and Evaluation of Small-Molecule Inhibitors

4. Generation and Evaluation of Small-Molecule Inhibitors

Bcl-3 regulates NF-κB signalling via binding to proteins p50 and p52 from the NF-κB family (Franzoso et al., 1992, Hatada et al., 1992, Wulczyn et al., 1992). We have established in Chapter 3, that disrupting binding to these proteins can inhibit Bcl-3 function. Therefore our next step was to design small molecules targeting Bcl-3-p50 or Bcl-3-p52 interface using molecular modelling.

4.1 Introduction to molecular modelling

The rapid development of computational technology led to the integration of computational approaches into almost every aspect of chemical research (Richon, 2008, Bonvin, 2006). The increase in the number of structural targets is in part due to the improvement in techniques for structure determination, such as the successful generation of protein structural data by X-ray crystallography and nuclear magnetic resonance spectroscopy (Kitchen et al., 2004, Waszkowycz et al., 2011).

Protein-ligand docking has become a widely used tool in computer-aided drug design from hit identification to lead optimisation, moreover providing the benefit of fast and relatively cheap screening of large chemical databases (Waszkowycz et al., 2011).

Molecular modelling uses various computational techniques to mimic the behaviour of molecules and molecular systems. Molecules are depicted by molecular models, which enable the construction of their three-dimensional representations. Protein structural data are generated by X-ray crystallography and stored in the Protein Data Bank (PDB) database. Computer-based methods, such as molecular mechanics or simulations, are used to predict behaviour of these molecular systems (Leach, 2001).

4.1.1 Molecular mechanics

Molecular mechanics is a generic method for the simulation of molecules. As opposed to quantum mechanics, the energy of a system is calculated as a function of the nuclear positions, thus ignoring the electronic motions. Using molecular mechanics approach the energy calculation is less time consuming than using quantum mechanics and can therefore be used even on large molecular

systems (Leach, 2001). Molecular mechanics provides an equation for computing the conformational energy of a molecule (Young, 2009). This equation is a sum of changes in energy due to processes such as the stretching of bonds, the opening and closing of angles, and the rotations about single bonds. Non-bonded interactions, such as electrostatic and van der Waals interactions, also contribute to this equation (Figure 4.1) (Leach, 2001, Kitchen et al., 2004). Molecular mechanics calculations can determine the preferred conformation of a molecule as well as its interactions with other molecules. Molecular mechanics methods are the basis for other methods used in molecular modelling, such as a construction of a homology models, molecular dynamics or docking (Young, 2009).

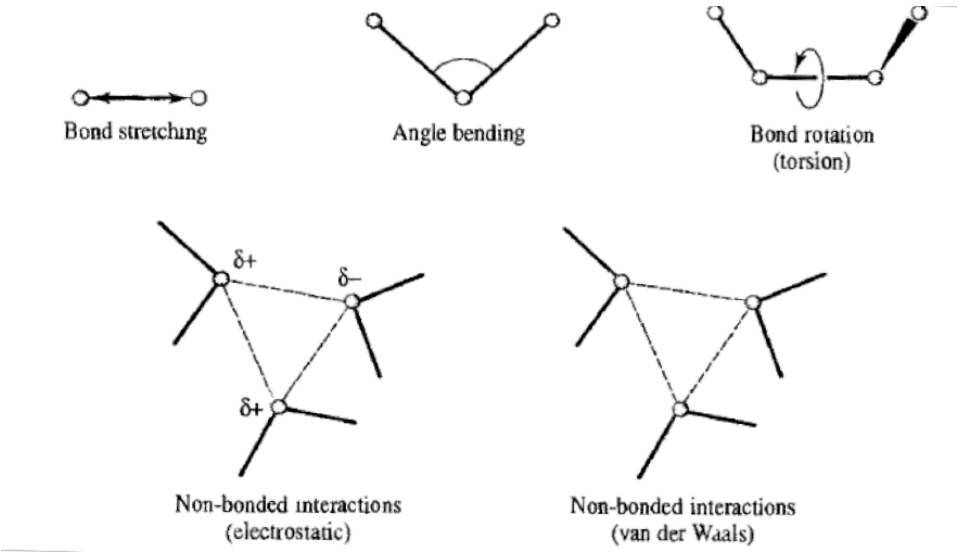

Figure 4.1 Schematic representation of key contributors to a molecular mechanics force field
Figure adapted from (Leach, 2001).

4.1.2 Molecular dynamics

To better understand the behaviour of complexes, a molecular dynamic simulation allows interaction of atoms and molecules for a period of time, generating a trajectory for the motion of the atoms. Molecular dynamics calculations incorporates Newton's equations of motion to simulate molecular vibration and movement within a solvent (Young, 2009). Molecular dynamics aims to mimic the way molecules explore their conformational space in a state as close to reality as possible with the use of current computational methods, being

particularly suited for the conformational study of proteins or other large molecules (Leach, 2001). The force on each atom is calculated from a change in a potential energy between current and new positions. Atomic forces and masses are then used to determine atomic positions over series of very small time steps (Kitchen et al., 2004). At each step, the forces on the atoms are computed and combined with the current positions and the force acting on each atom is assumed to be constant during the time interval. During the simulation, atoms are moved to the new position and an updated set of forces is computed. By this approach, molecular dynamics generates the trajectory that describes how the dynamic variables change with time (Leach, 2001).

4.2 Introduction to virtual screening

The term virtual screening describes the use of computational algorithms and models for the identification of bioactive compounds from large databases. Two different approaches can be applied. Ligand-based approach can be used when the three dimensional structure of the target is unknown and it selects compounds from databases based on the similarity to already known ligand (Hoelder et al., 2012).

Structure-based approach requires a three-dimensional structure of the target and evaluates the fit of compounds to a binding pocket. Structure-based approach is considered to have higher success rate than ligand-based approach and should be given priority when possible (Young, 2009).

The docking process is used in the structure-based approach to select active compounds and involves the prediction of ligand conformation and orientation within a targeted binding site. Docking is generally a multi-step approach and consists of the docking phase and the scoring phase. During the docking phase small molecules are posed in the binding site using various docking algorithms. The purpose of the docking phase is to identify the most favoured pose of the ligand. The protein is usually treated as conformationally rigid, and the ligand is given some degrees of freedom depending on docking algorithm (Young, 2009, Kitchen et al., 2004).

The identified favoured pose is evaluated and ranked using scoring algorithms. Most scoring functions are based on the molecular mechanics equation

and can be either force field based, empirical or knowledge-based (Kitchen et al., 2004). In our studies we used a combination of four scoring functions with different algorithms as described below.

In FlexX the binding site is characterized in terms of accessible chemical features in the protein active site, e.g. hydrogen bonding, hydrophobic or aromatic sites. These features are constructed geometrically around receptor atoms and are used to guide the placement of a ligand fragment (Kramer et al., 1999).

On the other hand the PLANTS algorithm treats the protein-ligand docking problem as a continuous optimization problem, where each component of the vector of variables corresponds to one of the degrees of freedom of the protein or the ligand. The goal of the optimization algorithm is to find a global minimum (Korb et al., 2009).

The goal of the XP Glide methodology is to semi quantitatively rank the ability of candidate ligands to bind to a specified conformation of the protein receptor. The rigid receptor approximation is utilized; ligands with steric clashes with the specified receptor conformation can bind effectively to alternative conformation. To overcome this problem XP Glide introduced a modest “induce fit” effect by scaling the van der Waals radii of nonpolar protein and ligand atoms (Friesner et al., 2006).

The docking function integrated into the MOE drug design software package (MOE, 2009.10) is based on London dG scoring function. The algorithm function consists of a directional hydrogen-bonding term, a directional hydrophobic interaction term and entropic term. It also computes an entropic penalty term for those atoms in the ligand, which become immobilized upon binding to the receptor (Prathipati et al., 2006).

4.3 Introduction to Bcl-3 structure

The human Bcl-3 is a 446-residue protein. Structural studies have revealed that Bcl-3 contains seven so-called ankyrin repeat domains (Ohno et al., 1990). Similar repeat motifs can be found in a number of diverse regulatory proteins, however the motifs of Bcl-3 are most closely related to those of IκB proteins (Michel et al., 2001).

The crystal structure of the ankyrin repeat of Bcl-3 was solved by Michel *et al.* (2001) in a resolution 1.86Å (PDB code 1K1A) spanning from residues 119-359. The N- and C- terminal domains could not be crystallized as they are poorly ordered and therefore could hamper crystallization. These domains cannot be modelled using homology modelling, since a suitable model sharing high similarity within these regions was not identified. However, numerous mutagenesis studies showed that the ankyrin repeat of Bcl-3 is sufficient for interaction with its binding partners (Wulczyn et al., 1992, Bours et al., 1993, Franzoso et al., 1993, Keutgens et al., 2010).

4.3.1 Characterisation of Bcl-3 structure

The seven ankyrin repeats of Bcl-3 form an elongated structure with a dimension of 75 x 25 x 25 Å (Michel et al., 2001). Each repeat consists of initial β-hairpin followed by inner and outer α-helix (Figure 4.2A). These repeats are uniform in backbone confirmation and share 27% sequence identity, although ankyrin repeat 1 lacks the initial β-hairpin (Figure 4.2B). The electrostatic surface potential of Bcl-3 gives theoretical pI value of 6.6 (Michel et al., 2001), which is due to presence of uncharged or basic residues. Notably, the large basic patch formed by seven arginine residues within ankyrin repeats 6 and 7 is believed to interact with Pirin (Figure 4.3A). The predicted interaction sites for p50 and p52 lie within the hydrophobic area observed spanning from ankyrin repeat 1 towards ankyrin repeat 7 in the area of outer α-helixes (Figure 4.3B).

4.3.2 Binding partners of Bcl-3

Mutagenesis studies of Bcl-3 indicated that all seven ankyrin repeats are required for the interaction with NF-κB proteins p50 and p52 (Wulczyn et al., 1992, Bours et al., 1993, Franzoso et al., 1993, Keutgens et al., 2010). The nuclear localization sequence (NLS) of Bcl-3 spans from amino acids 161 to 174 and shares high homology with the NLS of IκBα (Keutgens et al., 2010). Bcl-3 is phosphorylated by glycogen synthase kinase 3 (GSK-3) at phosphorylation sites S394, S398 (Viatour et al., 2004a). Bcl-3 is subjected to degradative, lys^{48} linked, polyubiquitination, which requires the residues K13 and K26 (Keutgens et al., 2010). A large basic patch

within ankyrin repeats six and seven (Figure 4.3C) was identified by modelling studies and was described to form a binding site for Pirin (Pang et al., 2004).

In addition to p50 and p52, Bcl-3 interacts with co activators such as Jab1, Bard1, Tip60 and Pirin (Dechend et al., 1999). A study by Kabuta *et al.* (2010) shows further enhancement of NF-κB activity when Bcl-3 is bound to the insulin substrate protein (IRS).

A.

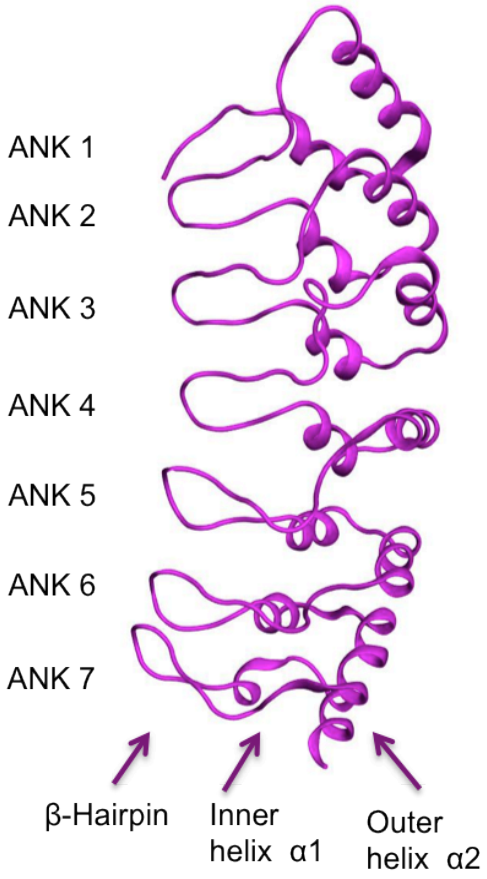

B.

		β-Hairpin	Inner helix α1	Outer helix α2	Linker
ANK 1	125	E-DGDTPLHIAVVQGNLPAVHRLVNLFQQGGRE			
ANK 2	157	LDIYNN-LRQTPLHLAVITTLPSVVRLLVTAGAS			
ANK 3	190	PMALDR-HGQTAAHLACEHRSPTCLRALLDSAAPGTLD—			
ANK 4	227	LEARNY-DGLTALHVAVNTECQETVQLLLERGAD			
ANK 5	260	IDAVDIKSGRSPLIHAVENNSSMVQLLLQHGAN			
ANK 6	294	VNAQMY-SGSSALHSASGRGLLPLVRTLVRSGAD			
ANK 7	327	SSLKNC-HNDTPLMVARSRRVIDILRG			

Figure 4.2 Structure of Bcl-3

A. The secondary structure of seven ankyrin repeats of Bcl-3 was solved (Michel et al., 2001) in a resolution of 1.86Å (PDB code 1K1A) and is shown in ribbon representation. Each repeat consists of a β-hairpin, inner α-helix and outer α-helix. **B.** Sequence alignment of seven ankyrin repeats showing high sequence similarity between individual repeats.

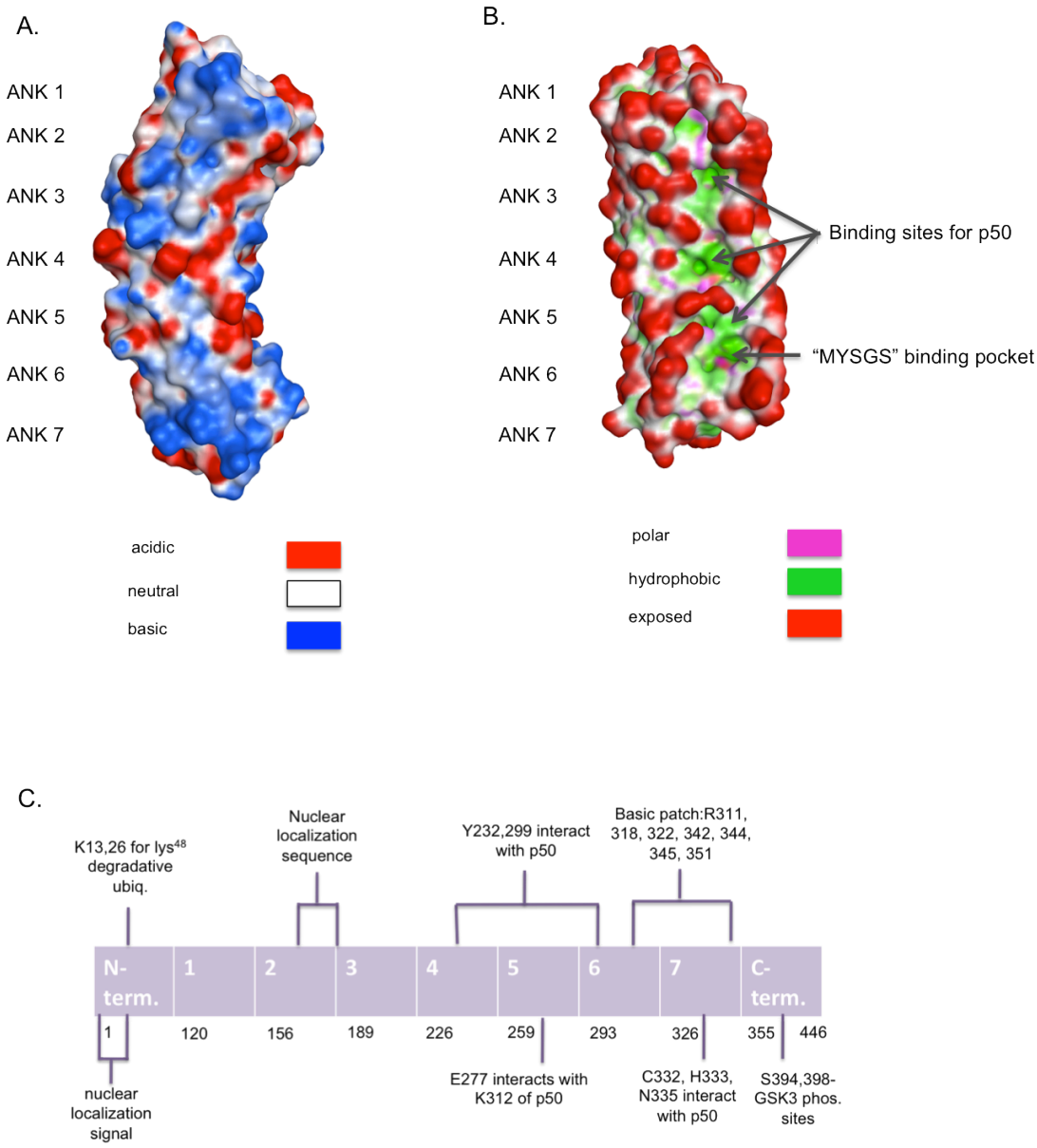

Figure 4.3 Characterisation of Bcl-3 structure

A. Surface of Bcl-3 with highlighted acidic and basic areas in red and blue respectively. **B.** Surface of Bcl-3 with polar (pink), hydrophobic (green) and exposed areas (red). **C.** Schematic representation of Bcl-3 structure with observed sites for p50 binding, ubiquitination sites, phosporylation sites, nuclear localization sequence (NLS) and basic patch for pirin.

4.3.3 IκBα comparison

The structurally most similar member of the IκB family, IκBα, has only 6 ankyrin repeats, but shares 35% sequence identity over these repeats (Figure 4.4A) and as expected, has very similar overall structure (Figure 4.4B). The crystal structure of Bcl-3 in a complex with its binding partners in not yet available, therefore we could use a model of IκBα crystallized in a complex with p65/p50 heterodimers (Jacobs et al., 1998) (shown in Figure 4.4 C) as a template for construction of our models. On the other hand, such structural similarity is undesirable when designing specific inhibitors; however, unique sites can be found within ankyrin repeat 6 and 7 of Bcl-3 structure, indicating a degree of novelty in its tertiary structure.

A.

Bcl-3	ANK 1	125	EDGDTPLHIAVVQGNLPAVHRLVNLFQQGGRE
IκBα		72	EDGDSFLHLAIIHEEKALTMEVIRQVKGDLAF
Bcl-3	ANK 2	157	LDIYNNLRQTPLHLAVITTLPSVVRLLVTAGAS
IκBα		104	LNFQNNLQQTPLHLAVITNQPEIAEALLGAGCD
Bcl-3	ANK 3	190	PMALDRHGQTAAHLACEHRSPTCLRALLDSAAPGTLD--
IκBα		137	PELRDFRGNTPLHLACEQGCLASVGVLTQSCTTPHLHIS
Bcl-3	ANK 4	227	LEARNYDGLTALHVAVNTECQETVQLLLERGAD
IκBα		176	LKATNYNGHTCLHLASIHGYLGIVELLVSLGAD
Bcl-3	ANK 5	260	IDAVDIKSGRSPLIHAVENNSSMVQLLLQHGAN
IκBα		209	VNAQEPCNGRTALHLAVDLONPDLVSLLLKCGAD
Bcl-3	ANK 6	294	VNAQMYSGSSALHSASGRGLLPLVRTLVRSGAD
IκBα		243	VNRVTYQGYYSPYQLTWGRPSTRIQQQLGQLTLE
Bcl-3	ANK 7	327	SSLKNCHNDTPLMVARSRRVIDILRG

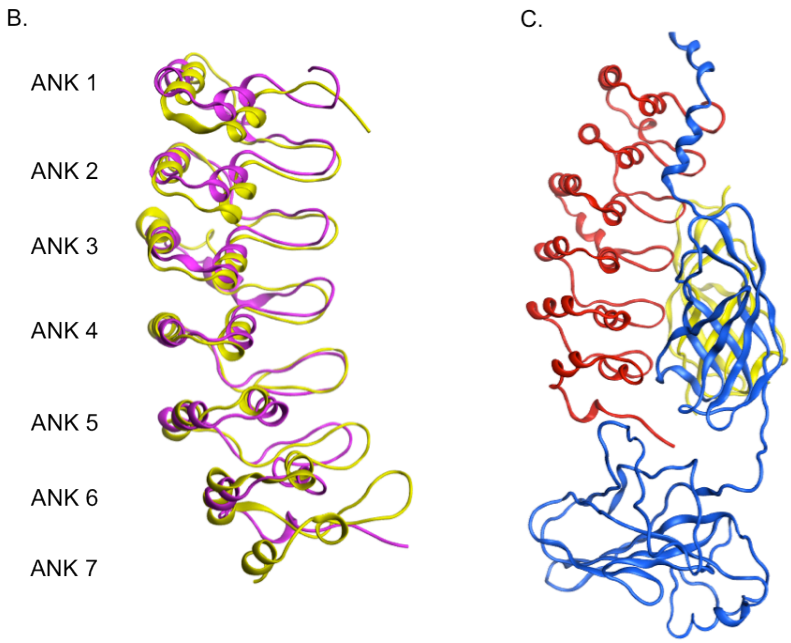

Figure 4.4 Comparison of Bcl-3 and IκBα structure

A. Sequence alignment of ankyrin repeats of Bcl-3 and IκBα. The respective ankyrin repeats are labelled and described by residues numbers. Identical residues are highlighted in red. **B.** Structural alignment by superposition of Bcl-3 (yellow) and IκBα (purple) molecule. **C.** A model of IκBα (red) in a complex with p65 (blue)/p50 (yellow) heterodimer.

4.4 Generation of Bcl-3 models

4.4.1 Model of Bcl-3-p50 and Bcl-3-p52 complex

Models were constructed by superimposing the ankyrin repeat of Bcl-3 and p50 or p52 homodimer onto the structure of the IκBα-p65/p50 complex. Two molecules of Bcl-3 have been observed to bind a single p50 or p52 homodimer (Bundy and McKeithan, 1997), therefore a second molecule of Bcl-3 was added using pseudo-dyad symmetry of the p50 or p52 homodimer as published previously (Pang et al., 2004). In order to refine generated models and evaluate their stability, models were minimized using Amber 99 forcefield and subjected to molecular dynamic simulation using Gromacs software as described in materials and methods (section 2.7). A model of the Bcl-3-p50 and Bcl-3-p52 complex is shown in Figure 4.5A&B respectively and demonstrates similar overall structure.

4.4.1.1 Validation of the model of Bcl-3-p50 complex

Our model was found to be relatively stable over period of 5 ns as confirmed by molecular dynamic simulation (Figure 4.6A&B). The structural stability of Bcl-3 model was assessed by calculation of the root-mean-square deviation (rmsd). The rmsds values of all protein atoms from the starting point are shown as a function of the simulation time either comparing rmsd values against original state (Figure 4.6C) or against the rmsd value of previous step (Figure 4.6D). In both cases the rmsd profile indicated that the conformation of the protein appears to be equilibrated in a short time at the beginning of the simulation and the values of rmsd are stabilized near to 0.8Å.

The final state of the model after 5 ns of molecular dynamic simulation was extracted and further characterised. All the residue parameters (bond angle, dihedral angle and bond length) fell within their acceptable ranges. The model was validated using the general Ramachadran plot, where the backbone dihedral angles, ψ, were plotted against amino acids dihedral angles, Φ, and showed that the majority of dihedral angles of amino acids are within acceptable ranges (Figure 4.6E).

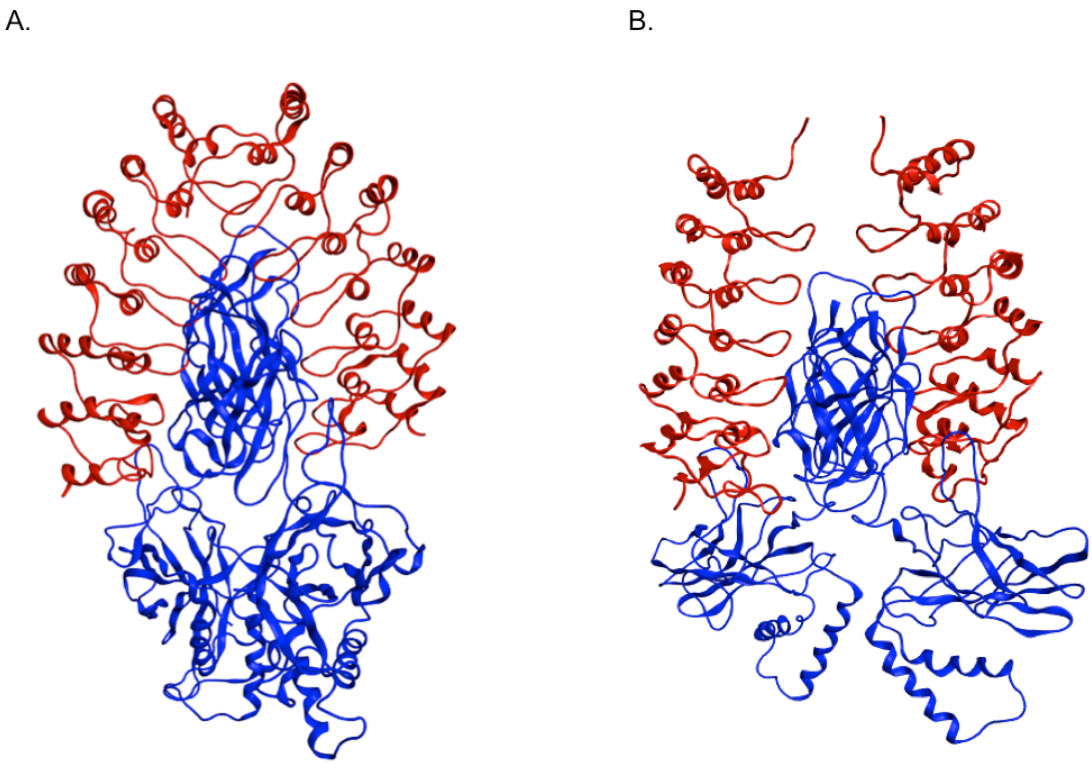

Figure 4.5 Model of Bcl-3 in a complex with p50 and p52 homodimers
Models were constructed by superposing Bcl-3 and p50 or p52 molecule onto IκBα-p65/p50 complex. **A**. Two Bcl-3 molecules (red) bind p50 homodimer (blue). **B.** Two Bcl-3 molecules (red) bind p52 homodimer (blue).

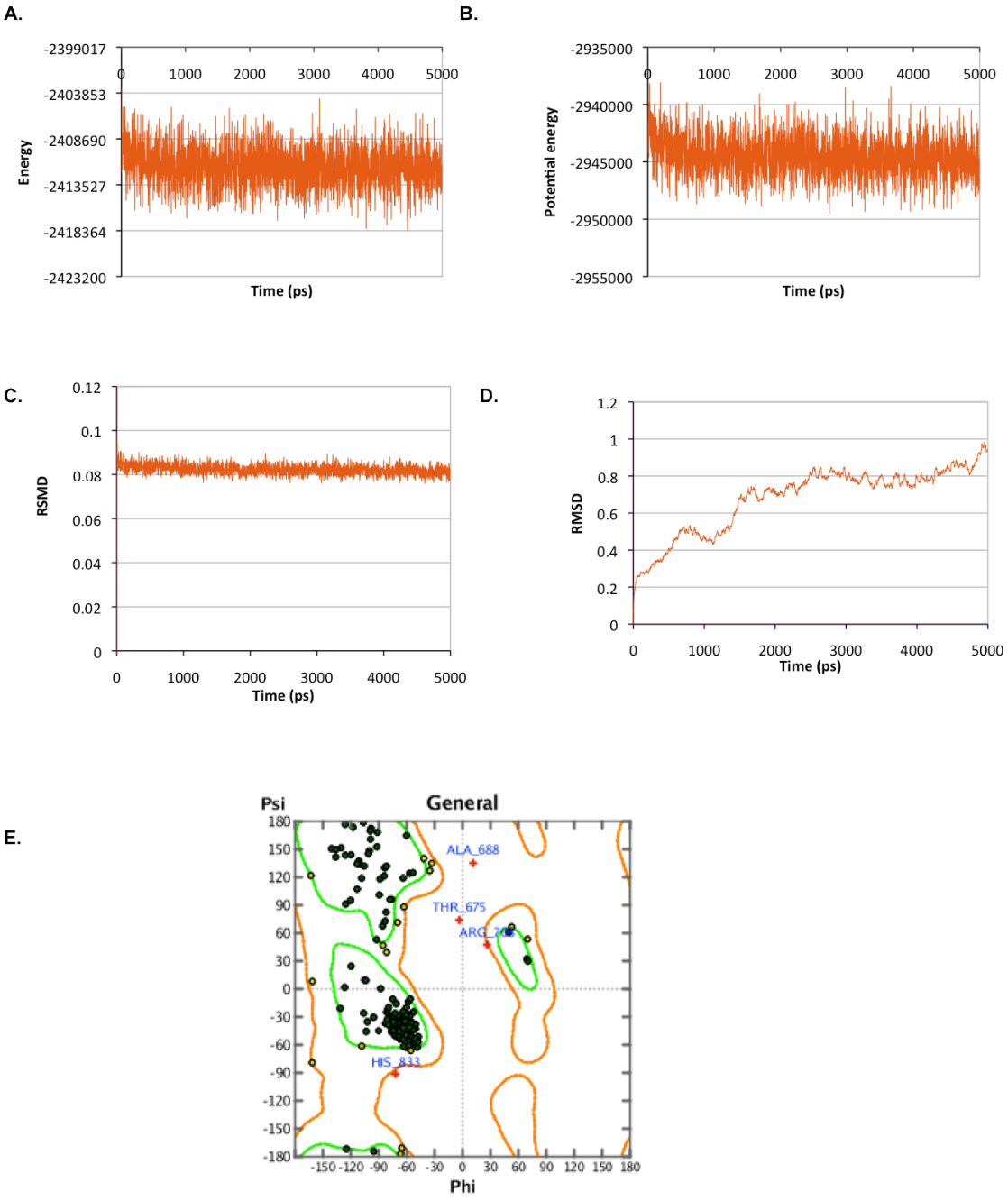

Figure 4.6 Validation of the model of Bcl-3-p50 complex

A. Changes in energy over time period of 5000 ps. **B.** Changes in potential energy over time period of 5000 ps. **C.** Changes in rmsd during 5000 ps dynamic simulation comparing rmsd changes against initial value. **D.** A plot showing changes in RMSD during 5000 ps dynamic simulation comparing rmsd changes against value of previous steps. **E.** Ramachadran plot: Backbone dihedral angles ψ were plotted against amino acids dihedral angles Φ. Majority of dihedral angles of amino acids fall within acceptable ranges (in areas limited by green lines).

4.5 Structure-based virtual screening

In our study we used a structure-based approach to perform a virtual screening in following steps. Firstly, the binding sites for p50 on the three-dimensional structure of Bcl-3 were characterised and the hydrophobic binding pocket was identified within Bcl-3 ankyrin repeats 6 and 7. Performing docking analysis of large databases could be time-consuming, therefore it is preferred to run a pharmacophore search (Kitchen et al., 2004). A pharmacophore is a set of three-dimensional chemical features designed based on ligand's interacting residues that a compound must have in order to bind in a protein's binding site. The pharmacophore model is used as a filter to search through large databases to identify compounds with similar features. During the pharmacophore search, compounds from databases were aligned with the pharmacophore in best possible manner and ranked based on the similarity with the designed pharmacophore (Young, 2009). Only compounds that satisfy the pharmacophore query were then docked and scored using three different scoring functions. In addition, final highest ranked 121 compounds were subjected to visual inspection, which can add another dimension to the selection process.

4.5.1 Identification of binding sites for p50

Binding sites for p50 were determined using a Site Finder feature in Moe (MOE, 2009.10) in our developed Bcl-3-p50 model. The dimer interface exhibits an extensive network of hydrophobic interactions and hydrogen bonds within ankyrin repeat 4 and 7 in correspondence with previous molecular modelling studies (Michel et al., 2001, Pang et al., 2004). Importantly, we observed a hydrophobic binding pocket within ankyrin repeat 6 and 7 (Figure 4.7A-C). This novel pocket has not been described previously; therefore we have termed it "MYSGS", based on the principal residues forming this p50 binding pocket. Ankyrin repeats 6 and 7 of Bcl-3 are of particular interest, as IκBα does not share structural similarity within this area therefore it can serve as a unique target on Bcl-3. The overall structure of the "MYSGS" binding pocket did not change significantly during MD simulation, therefore it can be considered a stable pocket and may be used for virtual screening.

4.5.2 Characterisation of a novel binding pocket

The interacting residues within the “MYSGS” binding pocket are depicted in Figure 4.8. p50 residues (mainly Lys 275, Asp 297, Ser 299, Pro 300, Thr 301, Asp 302, Val 303, His 304, Arg 305) interact with Bcl-3 residues from the ankyrin repeat six (Met 298, Tyr 299, Ser 300, Gly 301, Ser 302, Ser 303, His 306, Ser 307) and unique ankyrin repeat seven (Asn 331, Cys 332, His 333, Asn 334, Asp 335, Val 340, Arg 342). The most important residues for the interaction are described below in more detail.

Many hydrogen bonds and hydrophobic interactions are formed in the “MYSGS” binding pocket. Briefly, the carboxylate oxygens of the p50 residue Asp 297 are predicted to form two hydrogen bonds with the amino groups of Arg 342. Additionally, the oxygen atom in Bcl-3 residue Asn 331 is in close proximity to the backbone amide of p50 residue Pro 300 (4.13 Å) and therefore forms a hydrogen bond. The carboxyl group of the p50 residue Asp 302 forms a hydrogen bond with the hydroxyl group of Bcl-3 residue Ser 300, while the distance between these two atoms is 3.74 Å. The imidazol of p50 residue His 304 forms stacking interaction with Bcl-3 residue Cys 332. Moreover, the amino groups of p50 residue Arg 305 are in close proximity to Bcl-3 residue Asn 334.

Considering the presence of a hydrophobic binding pocket with a network of strong interactions, we predict that disruption of binding within this region, via use of a small molecule inhibitor, will prevent Bcl-3 binding to p50.

4.5.3 Generation of a pharmacophore model

Properties of p50 interacting residues in the “MYSGS” binding pocket were used to set up a pharmacophore model in MOE (MOE, 2009.10). The query was a collection of features representing the ligand (H-bond donor, H-bond acceptor and hydrophobic contacts) and volume restrictions describing the overall structure of the binding site (Figure 4.7D). The result of the database search was a set of compounds for which all, or at least three out of four restrictions of the pharmacophore query were satisfied.

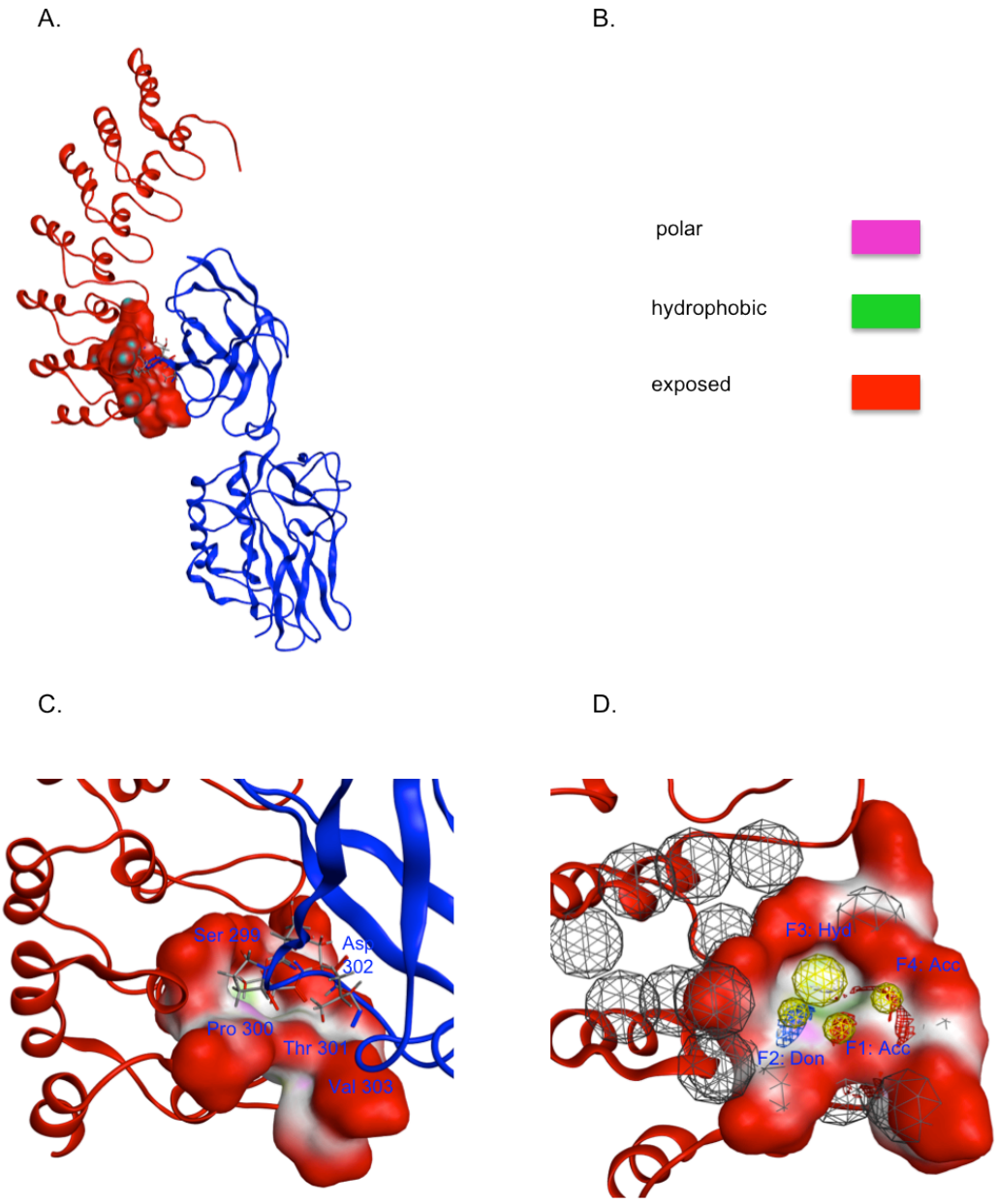

Figure 4.7 Characterisation of novel binding pocket for p50
A. Bcl-3 molecule (red) with highlighted binding pocket for p50 molecule (blue) within ankyrin repeat six and seven. **B.** The colour representation for the binding pocket. **C.** The binding pocket of Bcl-3 (red) with p50 (blue) interacting residues. **D.** A pharmacophore model was constructed based on p50 interacting residues. Main features (H-bond donor, H-bond acceptor and hydrophobic contacts) and volume restriction balls are shown.

A.

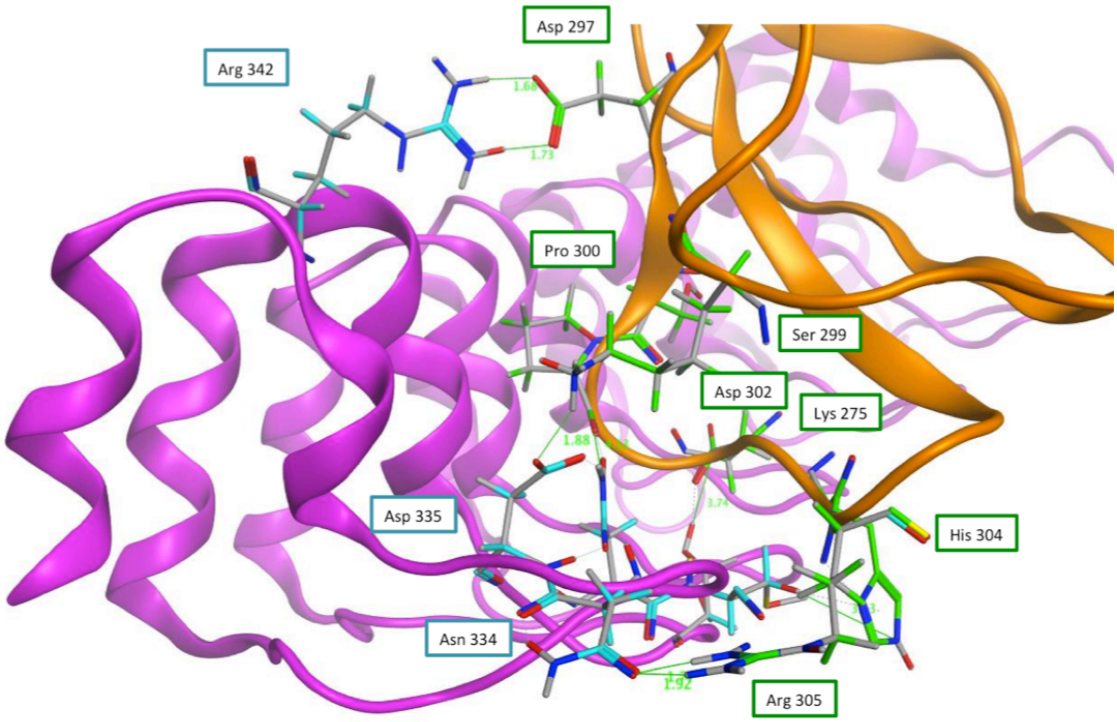

B.

Bcl-3 residues	ANK 6	Met 298, Tyr 299, Ser 300, Gly 301, Ser 302, Ser 303, His 306, Ser 307
	ANK 7	Asn 331, Cys 332, His 333, Asn 334, Asp 335, Val 340, Arg 342
p 50 residues		Lys 275, Asp 297, Ser 299, Pro 300, Thr 301, Asp 302, Val 303, His 304, Arg 305

Figure 4.8 Interacting residues in the "MYSGS" binding pocket

A. Bcl-3 molecule (purple) and p50 molecule (gold) are shown. Interacting residues are shown in ball and stick representation, while nitrogen and oxygen atoms are shown in blue and red respectively. Bcl-3 interacting residues are colored cyan and labelled, p50 interacting residues are colored light green and labelled. Green dashed lines represent distances in angstroms between respective atoms. Only interacting residues are shown for clear visualization. **B.** Interacting residues involved in the binding pocket of Bcl-3 and p50.

4.5.4 Virtual screening for inhibitors of Bcl-3-p50 interaction

Our developed pharmacophore model was used to search a database of 360 000 commercially available molecules from Specs database (Delft, The Netherlands). Output data consisted of 27 013 molecules that satisfy the pharmacophore query. A standard filter of molecular weight between 200-450 was employed to get 23 138 compounds, even though compounds that are known to target protein-protein interactions are usually larger. The selection process is outlined in Figure 4.9. In brief, molecules were clustered into groups based on more than 95% similarity before being docked and evaluated by programs GLIDE (Friesner et al., 2006), FlexX (BiosolveITGmbH) and PLANTS (Korb et al., 2006) (used algorithms described in section 4.2). The molecules were clustered into groups with similar molecules, because it was shown that using this approach the compound ranking is improved and the diversity of hits is increased (Su et al., 2001). A combination of three programs was used, because a combination of elements covering a wide range of scoring functions leads to significantly higher performance than any of the individual functions (Charifson et al., 1999). Results from three scoring functions were combined and 121 molecules with the best results in all three functions were minimized using MMFF94 force field and rescored using MOE software package (MOE, 2009.10) to further increase the accuracy of selection. This part of selection using developed scoring algorithms has to be followed by used-defined selection as outlined in Figure 4.9 B.

All final 121 compounds shared similar overall structure, comprising mostly of three either heterocyclic or aromatic rings linked with various linker chains (mainly 1-4 atoms in length). Final compounds were evaluated based on structural requirements of the binding pocket and by the strength of protein-ligand interaction. Ultimately, 10 compounds were selected according to visual inspection, and purchased from Specs database (Delft, The Netherlands) to be biologically evaluated.

The chemical structures of 10 purchased compound are shown in Table 4.1 and the scoring results are listed and explained in Table 4.2.

4.5.5 Evaluation of selected compounds for Bcl-3-p52 inhibition

Bcl-3-p50 and Bcl-3-p52 models demonstrated similar overall structure and binding interface. As expected, a binding pocket for p52 was identified within ankyrin repeats 6 and 7 of Bcl-3, formed mainly by Bcl-3 residues M298, Y299, S300, G301, K330, N331. Ten selected compounds were rescored using MOE (MOE, 2009.10) and results are shown in Table 4.2. Interestingly, the majority of compounds demonstrate protein-ligand interaction comparable to interactions seen within the Bcl-3-p50 interface.

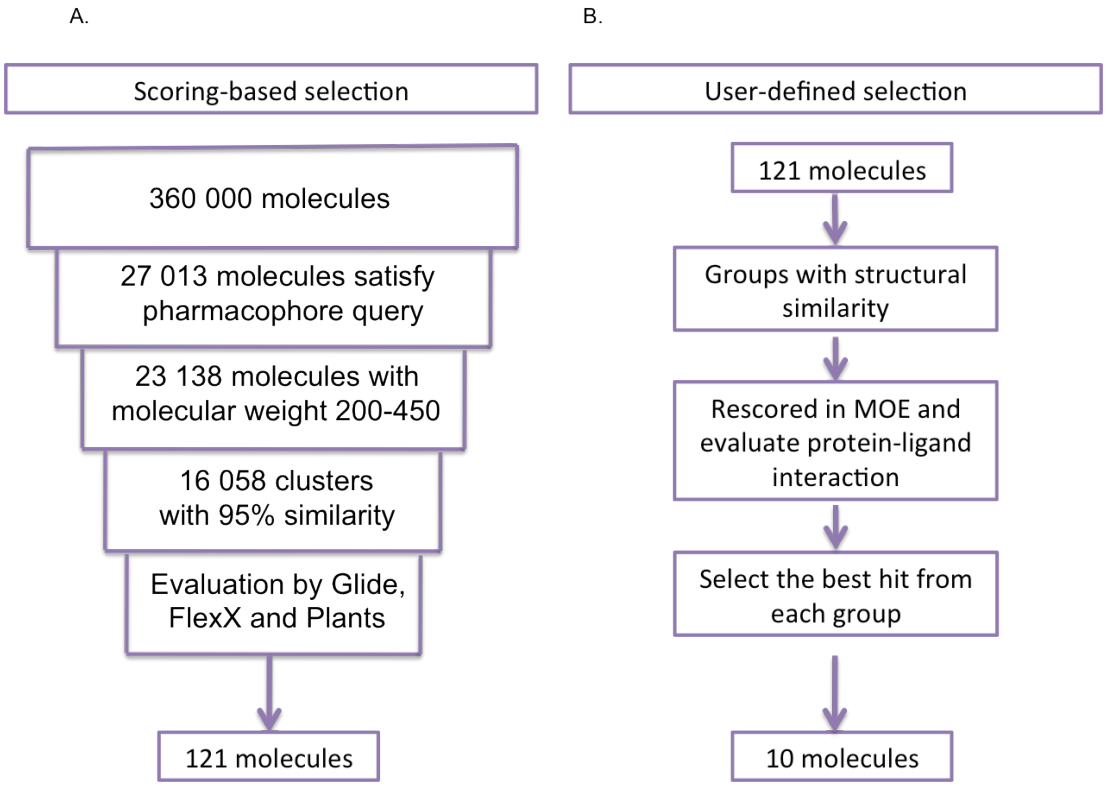

Figure 4.9 Selection process
A schematic representation of the selection process using scoring algorithms (**A.**) and the user-defined selection (**B.**).

1. 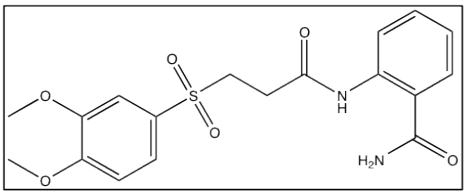

2. 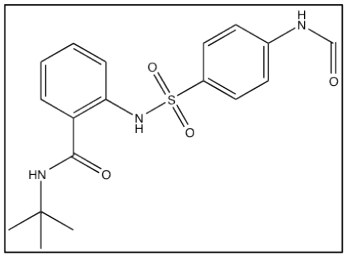

3. 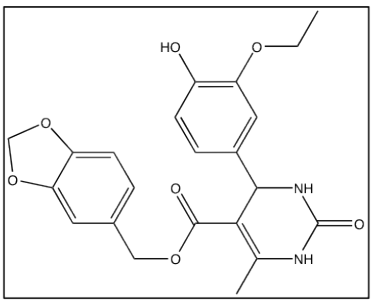

4. 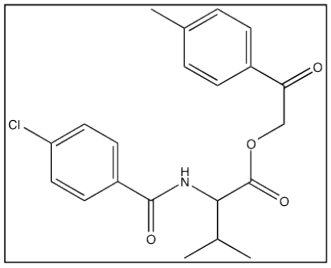

5. 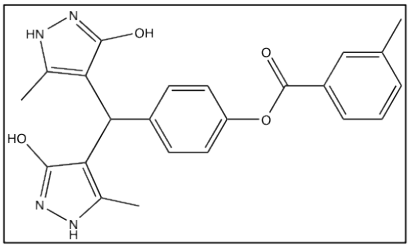

6. 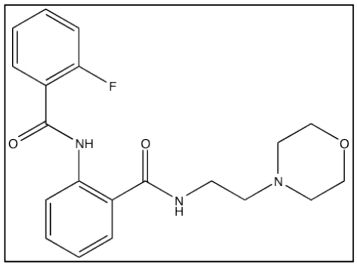

7. 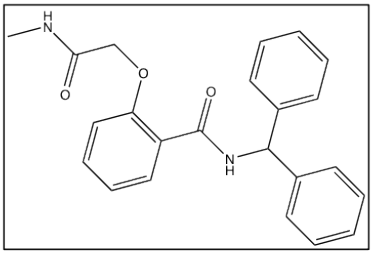

8. 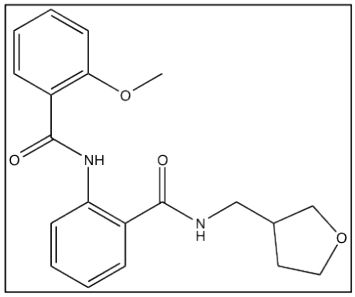

9. 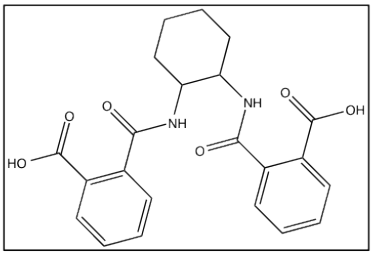

10. 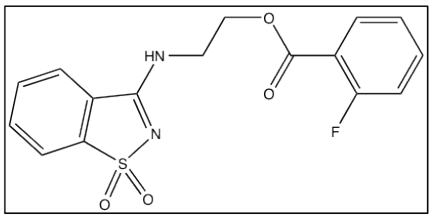

Table 4.1 Structures of 10 purchased compounds

Compound	Specs No.	FlexX	Plants	Glide	MOE	MOE p52
1.	A0-022/43452477	-16.892	-65.541	-6.625	-10.9163	-9.4260
2.	AO-080/42479276	-15.928	-73.586	-5.992	-10.213	-9.1394
3.	AG-205/37136062	-17.431	-70.479	-5.667	-11.592	-10.3953
4.	AK-918/40864467	-11.936	-65.741	-5.653	-10.045	-9.2752
5.	AH-487/40911940	-15.449	-67.499	-5.619	-13.233	-12.8786
6.	AO-365/43402787	-13.803	-75.304	-5.429	-11.083	-10.4343
7.	AO-080/42573748	-13.465	-72.212	-5.281	-10.707	-9.0189
8.	AN-329/43197657	-12.767	-69.870	-5.144	-10.938	-13.4147
9.	AN-329/40826196	-14.223	-66.634	-5.097	-12.052	-8.6166
10.	AM-879/41237197	-12.335	-74.489	-5.019	-10.476	-9.0717

Table 4.2 Scoring results for 10 purchased compounds

Scoring programs FlexX, Plants, Glide and MOE were used to score compounds designed to interrupt Bcl-3-p50 binding. Results shown here represent experimental relative binding energy calculated by respective algorithms. Stronger protein-ligand interactions were found when lower dimensionless value representing binding energy was calculated. Values in column MOE-p52 represent scoring results for compounds rescored in Bcl-3-p52 interface using MOE.

4.5.6 Predicted binding of compound 1

The strength of protein-ligand interactions and the fit into the "MYSGS" binding pocket was visually evaluated for the selected 121 compounds. Compounds were numbered according to the scoring results from FlexX scoring function; i.e. compound 1 exhibits the strongest interactions. Consequently, compounds were evaluated by other scoring functions as mentioned, without having an effect on the order of the compounds.

Figure 4.10 shows the ligand-protein interaction for compound 1. The ligand was observed to form interactions with Bcl-3 residues Glu 277, His 306, Ser 307, Arg 311 and Asn 331, which is in correspondence with interacting residues of p50 homodimer.

Most importantly, the phenyl ring forms arene-cation interactions with Arg 311 (3.69 Å). The carboxylate group of Glu 277 forms a hydrogen bond with the amide group of the ligand (1.91 Å); additional hydrogen bonds are formed between the hydroxyl group of serine and NH of the ligand's linker chain (1.95 Å) and the amino group of Asn 331 and oxygen from the sulfonyl group of the ligand (1.69Å).

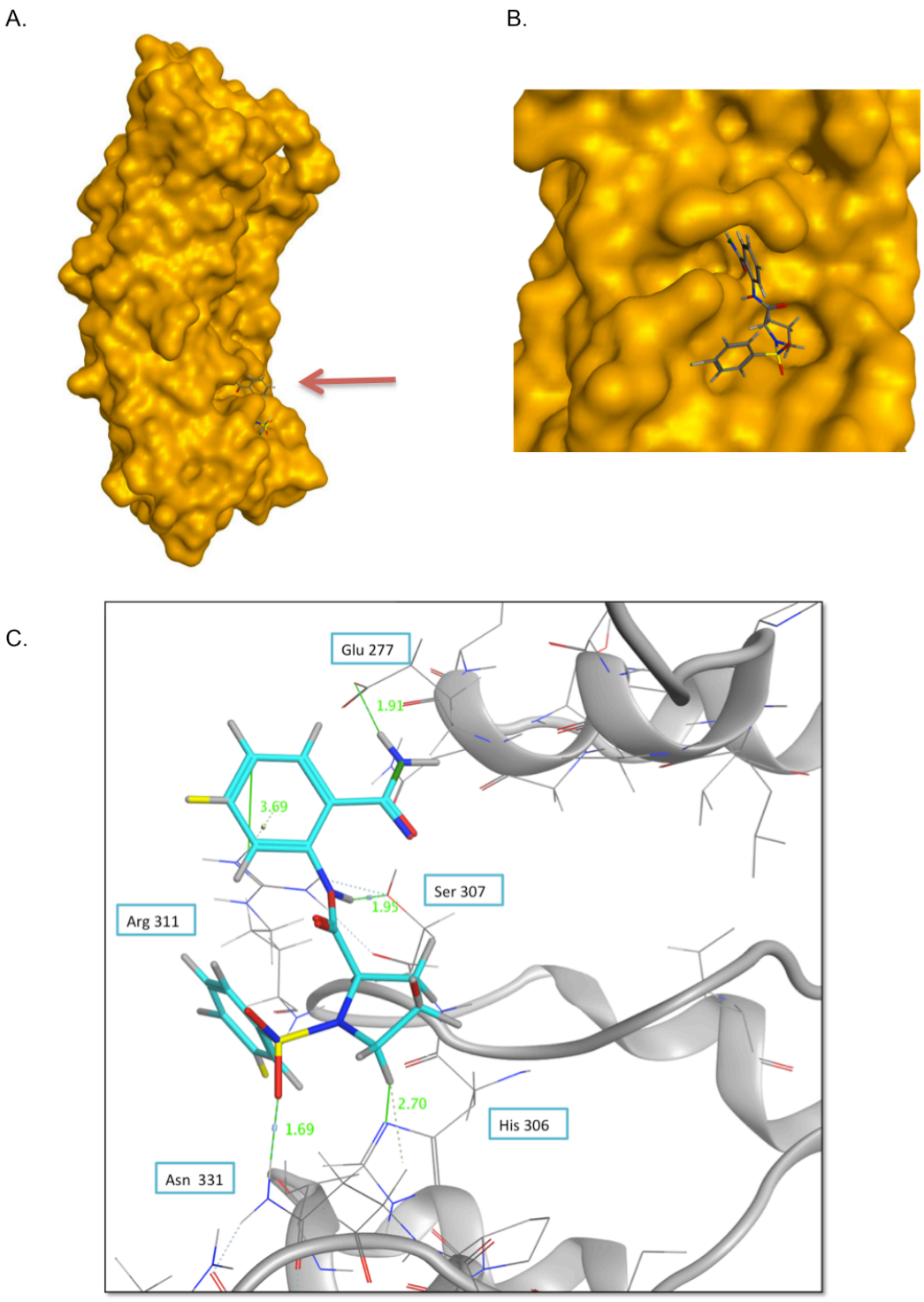

Figure 4.10 Compound 1 docked into Bcl-3

A. The surface of Bcl-3 is shown with docked compound 1 to the "MYSGS" binding pocket. **B.** An enlarged view of the binding pocket with docked compound 1. **C.** Compound 1 is shown in ball and stick representation in cyan. Interacting residues of Bcl-3 are shown in grey and labelled using cyan borders. Nitrogen, oxygen and sulphur atoms are shown in blue, red and yellow respectively. Green dashed lines represent distances in angstroms between respective atoms. Not all Bcl-3 residues are shown for clear visualization.

4.6 Biological evaluation of selected compounds

Selected compounds from virtual screening were evaluated using the cell-based assays in the previously described model systems (Chapter 3). Below is an overview of the cell lines used with a description of their expression status.

HEK-293	Description	MDA-MB-231	Description
WT	WT	WT	WT
Bcl-3 WT	↑ FLAG Bcl-3 WT	Bcl-3 WT	↑ FLAG Bcl-3 WT
Bcl-3 ANK M123	↑ FLAG Bcl-3 ANK M123 = binding mutant	Bcl-3 ANK M123	↑ FLAG Bcl-3 ANK M23 = binding mutant
WT-p52	↑ p52 WT		
Bcl-3 WT-p52	↑ p52 WT ↑ FLAG Bcl-3 WT		
Bcl-3 ANK M123-p52	↑ p52 WT ↑ FLAG Bcl-3 ANK M123 = binding mutant		

Table 4.3 Model system used for biological evaluation
Abbreviations for cell lines with the expression status (shown by arrows) used in cell-based assays. FLAG-tagged Bcl-3 constructs as described in Material and methods (section 2.1.2) were used to over express either Bcl-3 WT or Bcl-3 ANK M123 binding mutant in HEK-293 and MDA-MB-231 cell line. HEK-293 cell lines overexpressing p52 WT were also used.

4.6.1 Cell toxicity

Selected compounds were dissolved in DMSO and diluted to a highest concentration of 10 µM (0.1% DMSO). Selected compounds were tested for cell toxicity in HEK-293 and MDA-MB-231 cells before being used in cell-based assays. Cell toxicity was evaluated using the Cell Titre Blue viability assay over a range of molarities for 24hrs. The effect of selected compounds on cell viability was always normalised against DMSO control.

Compounds were well tolerated in both cell lines (Figure 4.11) and were therefore used at 10 µM in subsequent experiments.

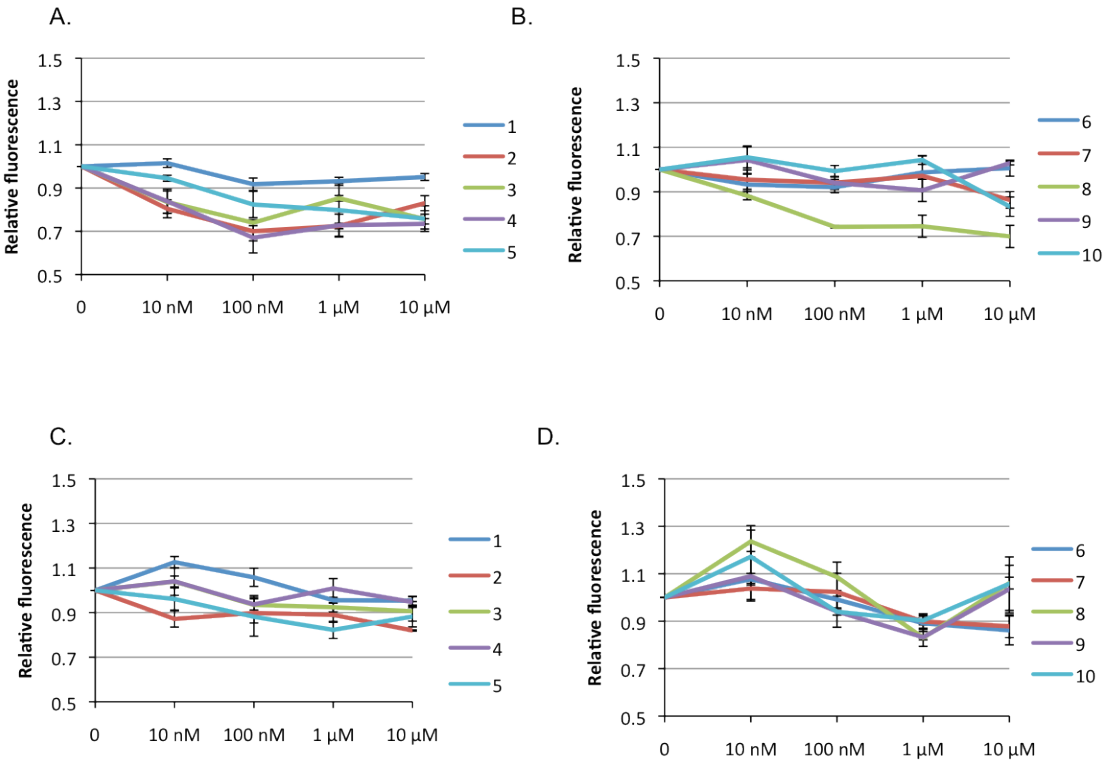

Figure 4.11 Cell toxicity

HEK-293 cells (**A+B)** and MDA-MB-231 cells (**C+D)** were cultivated with compounds 1-10 over a range of molarities in adherent growth conditions. Cell viability was determined after 24hrs by the Cell Titre Blue viability assay and resulting fluorescence was normalised against fluorescence of DMSO control. Data represent average of six wells and error bars represent ± SEM.

4.6.2 Biological evaluation of disruption of Bcl-3-p50 binding

Initially, compounds were tested on whether they had the ability to disrupt Bcl-3-p50 binding using the previously developed Indirect Sandwich ELISA assay (as described in Section 2.5.4) in HEK-293 cells. Subsequently, we looked at the functional output using NF-κB assay and motility assay.

4.6.2.1 Indirect Sandwich ELISA assay

HEK-293 Bcl-3 WT cells were cultivated with compounds at 10 μM concentration for 24hrs before cell lysates were obtained under non-denaturing conditions. The protein concentration was determined and equal loading was verified by Indirect ELISA assay using Bcl-3 antibody as shown in Figure 4.12A.

Indirect Sandwich ELISA (Figure 4.12B) revealed significantly decreased signals for p50 bound to Bcl-3 for 4 out of 10 compounds, with compound 6 having the most significant effect on disruption of Bcl-3-p50 binding.

4.6.2.2 NF-κB assay

The effect of selected compounds on NF-κB activity was analysed using NF-κB luciferase assay in HEK-293 and MDA-MB-231 cells (Figure 4.13). HEK-293 Bcl-3 WT and MDA-MB-231 Bcl-3 WT cells were cultivated with compounds at 10 μM concentration for 24hrs before being transfected with NF-κB luciferase reporter plasmid for 48hrs together with controls and analysed for NF-κB activity. The outcome of selected compounds on NF-κB activity was comparable between HEK-293 and MDA-MB-231 cells, with compound 5 and 6 having significant effect in both cell lines.

4.6.2.3 Cell motility assay

As shown in section 3.2.1.4, disruption of Bcl-3-p50 binding significantly decreased cell migration ability in MDA-MB-231 cell line. This cellular phenotype is a key clinically relevant outcome of Bcl-3 inhibition; therefore next we wanted to establish whether selected compounds would have a similar effect on cell motility via use of the Boyden motility chamber assay. We tested compound 6 and 10 and only compound 6 significantly decreased cell motility, although this was to a lesser level than the Bcl-3 overexpressing ANK M123 binding mutant (Figure 4.14).

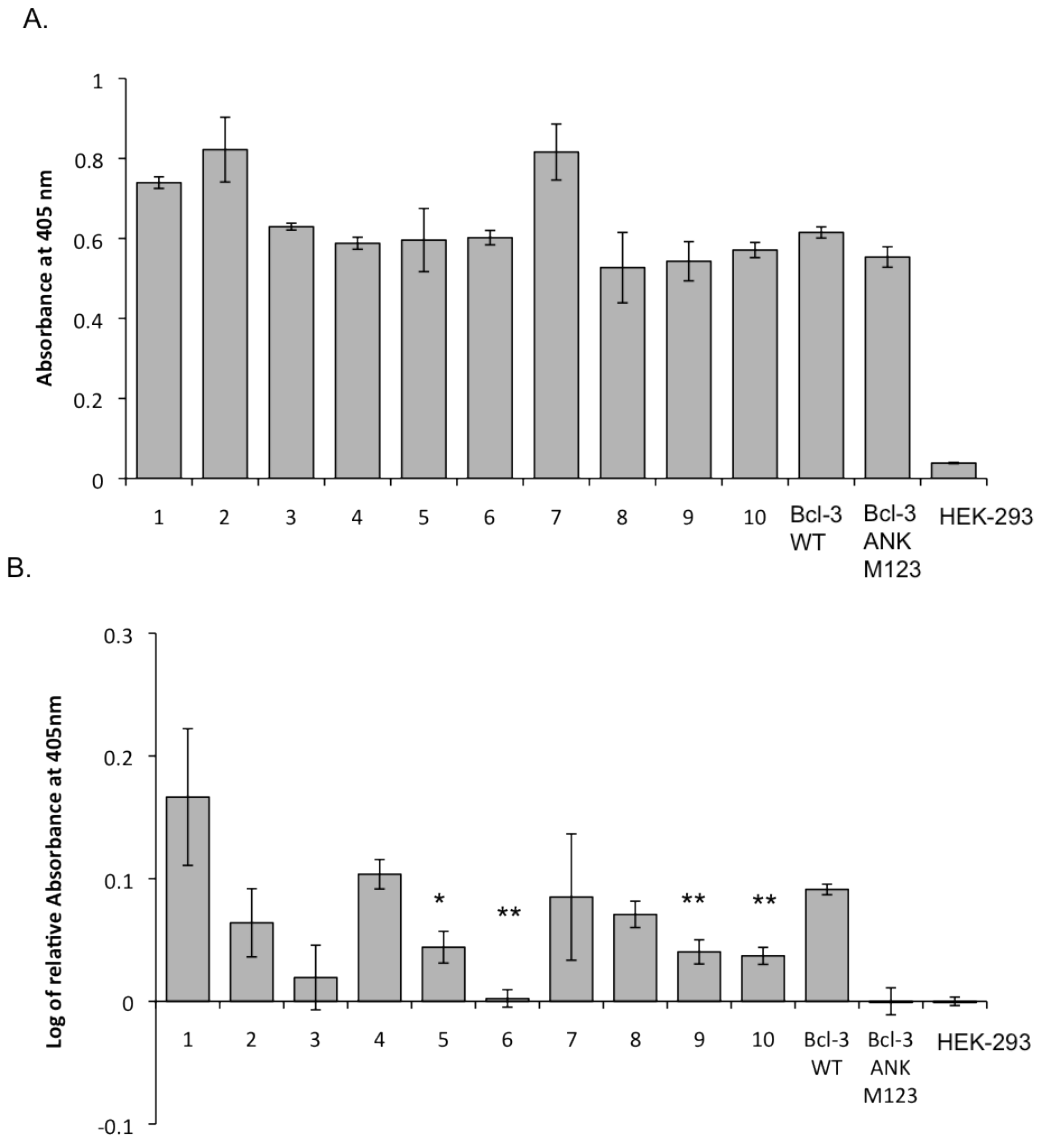

Figure 4.12 ELISA assay evaluating Bcl-3-p50 binding

HEK-293 Bcl-3 WT cells were cultivated with compounds 1-10 (10 µM) for 24hrs. Cell lysates from these cells and controls (HEK-293, Bcl-3 WT and Bcl-3 ANK M123) were prepared under non-denaturing condition. **A**. Indirect ELISA assay was performed on FLAG coated ELISA plates using Bcl-3 antibody. Absorbance was measured at 405 nm. Error bars represent ± SEM of three independent wells. **B**. Indirect sandwich ELISA assay was performed on FLAG coated ELISA plates using p50 antibody. Absorbance was measured at 405 nm, normalised to that of Bcl-3 ANK M123 and is plotted on a log scale. Error bars represent ± SEM of six independent wells. (T-test, *=$p<0.05$ and **=$p<0.01$ as compared to Bcl-3 WT).

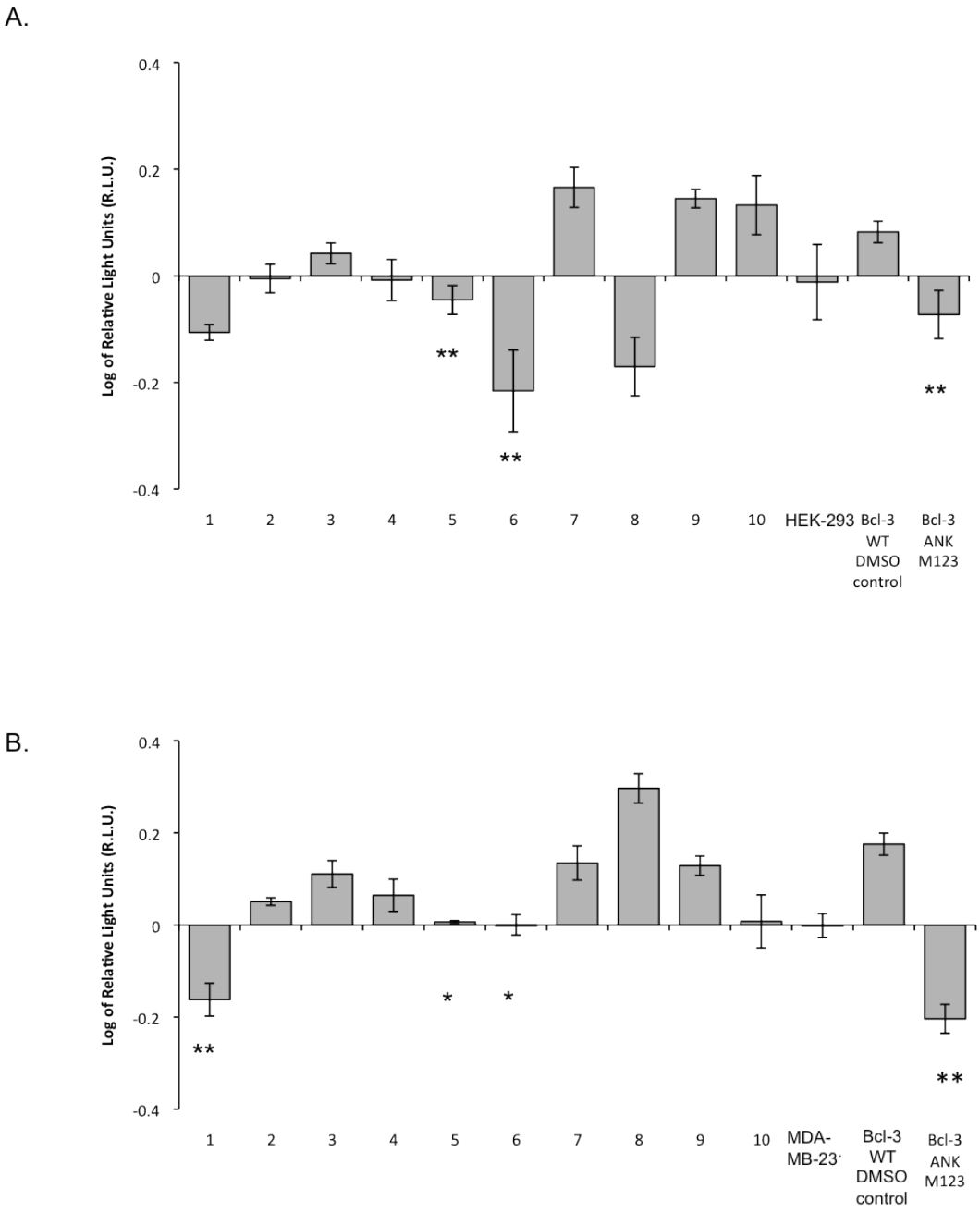

Figure 4.13 NF-κB assay in HEK-293 and MDA-MB-231 cells

HEK-293 Bcl-3 WT cells (**A.**) and MDA-MB-231 Bcl-3 WT (**B.**) were cultivated with compounds 1-10 (10 μM) or DMSO control for 24hrs before being transfected with NF-κB luciferase reporter for 48hrs together with controls. NF-κB activity is plotted on a log scale as relative light units and normalised to the NF-κB activity of HEK-293 and MDA-MB-231 cells respectively. Error bars represent ± SEM of nine independent transfections. (T-test, *=$p<0.05$ and **=$p<0.01$ as compared to HEK-293 Bcl-3 WT or MDA-MB-231 Bcl-3 WT.

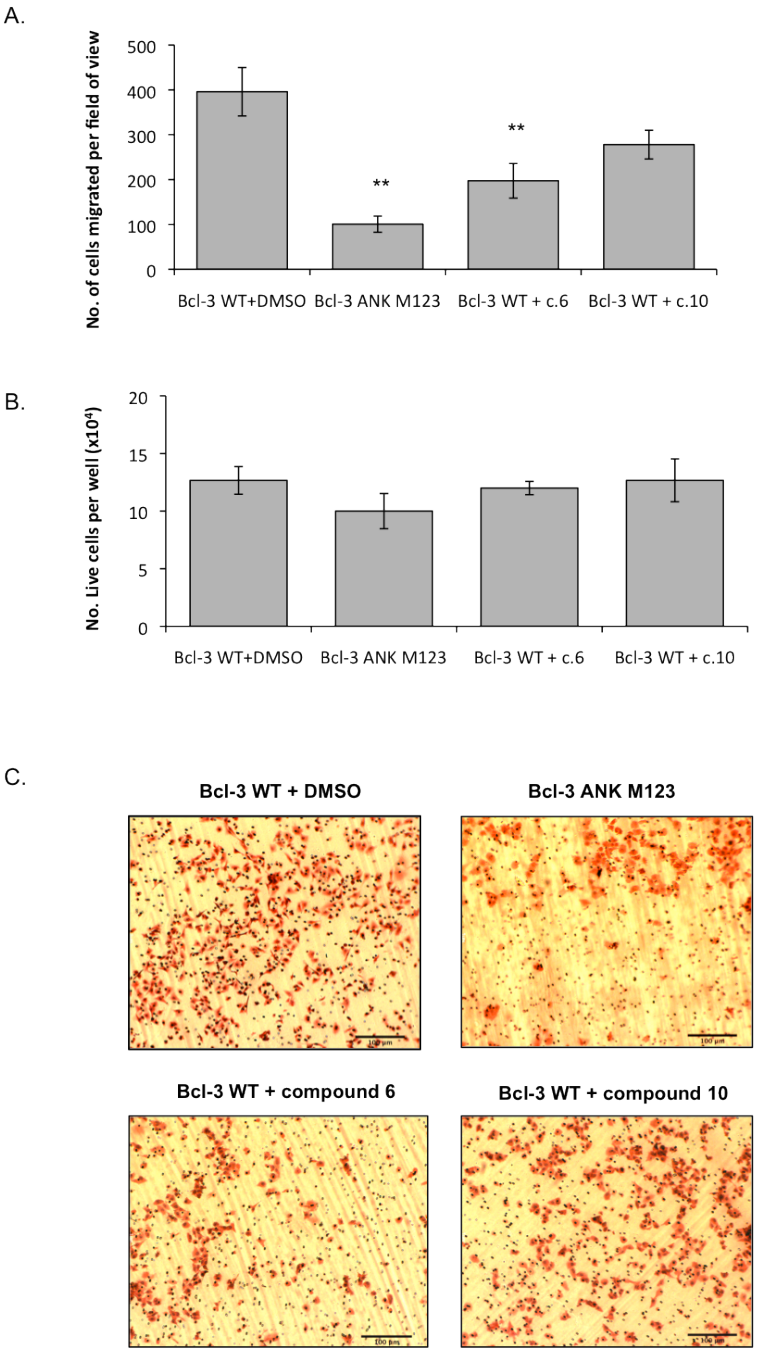

Figure 4.14 Cell motility assay in MDA-MB-231

A. MDA-MB-231 Bcl-3 WT cells were cultivated with compounds 6 or 10 (10 µM) in normal adherent growth conditions for 24hrs before being seeded onto Boyden motility chambers for 24hrs together with controls. Migrated cells were counted from three fields of view of each of three replicate Boyden chambers. Error bars represent ± SEM. (T-test, **=p<0.01). **B.** Same cells were seeded in normal adherent growth conditions for 24hrs and counted. **C.** Representative images of migrated cells for Bcl-3 WT+DMSO, Bcl-3 ANK M123, Bcl-3 WT + compound 6 and Bcl-3 WT + compound 10 cells. Scale bars represent 100 µm.

4.6.3 Biological evaluation of disruption of Bcl-3-p52 binding

As determined previously by modelling studies (section 4.5.5), p52 binds to Bcl-3 in a similar manner as to p50 in a binding pocket formed by similar residues as that for p50. Thus we wanted to determine whether selected compounds have the ability to disrupt Bcl-3-p52 binding as well. Previously we have shown that co-expression of Bcl-3 and p52 significantly increase NF-κB activity (Figure 3.17), therefore we treated these cells with selected compounds at 10 μM concentration and analysed for NF-κB activity using NF-κB luciferase assay.

Consistent with previous results, compound 6 significantly decreased NF-κB activity (Figure 4.15), suggesting that compound 6 is able to disrupt Bcl-3-p52 binding in addition to its effects on p50 binding.

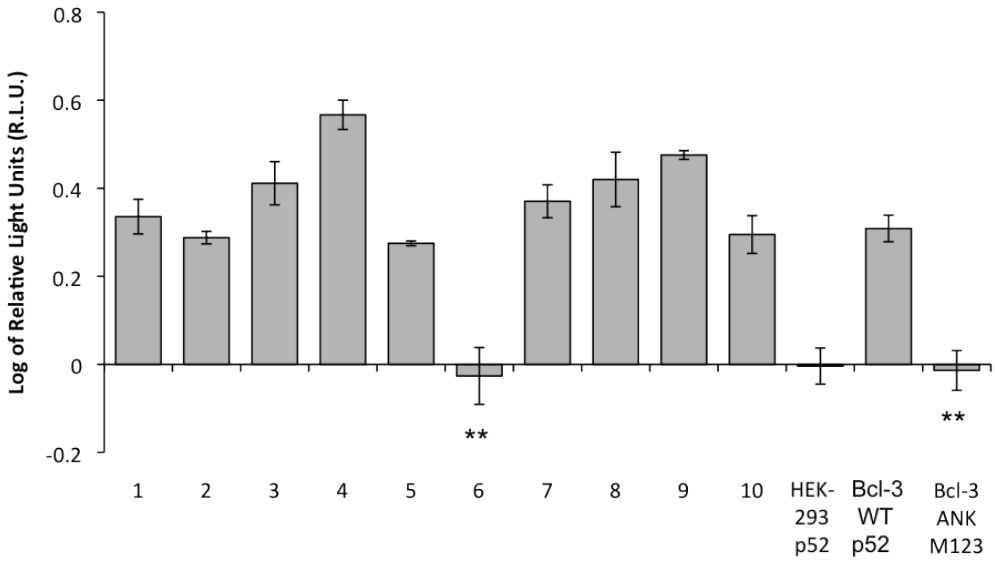

Figure 4.15 NF-κB assay in HEK-293-p52

A. HEK-293 Bcl-3 WT p52 cells were cultivated with compounds 1-10 (10 μM) or DMSO control for 24hrs before being transfected with NF-κB luciferase reporter for 48hrs together with controls. NF-κB activity is plotted on a log scale as relative light units and normalised to HEK-293. Error bars represent ± SEM of six independent transfections. (T-test, **=p<0.01 as compared to HEK-293 Bcl-3 WT p52).

4.7 Discussion

Previously we have established that the function of Bcl-3 could be inhibited by disruption of its binding to proteins p50 and p52 from NF-κB family (Chapter 3). This chapter, therefore aimed to generate and evaluate small-molecule inhibitors targeting Bcl-3-p50 interactions using molecular modelling tools.

4.7.1 Generation and optimisation of a Bcl-3-p50 and Bcl-3-p52 complex

In order to generate novel inhibitors targeting Bcl-3-p50/p52 interface using a structure based modelling approach, the model of Bcl-3 in a complex with p50 or p52 homodimers was constructed. The crystal structure of Bcl-3 was solved by Michel *et al.* (2001), however the crystal structure of Bcl-3 in a complex with p50 or 52 has not yet been revealed. Therefore, the models of Bcl-3 – p50 or p52 complexes were generated by superimposing the crystal structure of seven ankyrin repeats of Bcl-3 and crystal structure of either p50 or p52 homodimers bound to DNA onto the structure of IκBα crystallized in a complex with a p65/p50 heterodimer (Jacobs and Harrison, 1998). We were able to use this approach because IκBα shares 35% sequence identity with Bcl-3 and has similar overall structure. Two Bcl-3 molecules were observed to bind to p50 or p52 homodimers (Bundy and McKeithan, 1997), thus the second Bcl-3 molecule was added to the complex using pseudo-dyad symmetry (symmetry of the DNA backbone).

Even though Bcl-3 and other members of IκB family possess similar overall structure, they regulate NF-κB signalling in different ways. Bcl-3 is a nuclear protein and acts as an co-activator of NF-κB signalling by binding to p50 and p52 heterodimers (Bours et al., 1993, Franzoso et al., 1992, Hatada et al., 1992), however other members of the IκB family, such as IκBα, IκBβ or IκBγ act as inhibitors of NF-κB signalling by retaining various NF-κB dimers in an inactive form in the cytoplasm (Perkins, 2007). Bcl-3 shares 35% sequence identity with IκBα and affinity of Bcl-3 inhibitors towards IκBα is undesirable.

We aimed, therefore to design specific small-molecule inhibitors of Bcl-3 targeted against the additional ankyrin repeat 7 of Bcl-3 molecule as other members of IκB family have only 6 ankyrin repeats and a C-terminal PEST domain

(Michel et al., 2001). We have identified a hydrophobic binding pocket within ankyrin repeats 6 and 7 of Bcl-3 molecule, which could act as a unique site for specific targeting of Bcl-3. The pocket was named "MYSGS" binding pocket after the main Bcl-3 residues forming this pocket (Figure 4.7).

A molecular dynamic simulation was run on both, Bcl-3-p50 and Bcl-3-p52 complexes to further optimise the complex and validate the stability of the whole complex with the newly identified "MYSGS" binding pocket (Figure 4.6). The p50 and p52 homodimers were crystallized bound to DNA, therefore the final complex contained Bcl-3 bound to p50 or p52 homodimers that were bound to DNA. We decided, however to run the molecular dynamic on complexes without the DNA backbone for a multitude of reasons. Firstly the IκBα-p65/p50 complex used as a template for construction of our model was crystallized without DNA because IκBα binds p65/p50 heterodimer in the cytoplasm. The position of DNA backbone, therefore could not be optimised and several residues of the seventh ankyrin repeat of Bcl-3 were observed to have steric clashes with DNA. Moreover, Bcl-3 can bind to p50 and p52 heterodimers not only bound to DNA, but also in a free state in the cytoplasm (Watanabe et al., 1997).

4.7.2 Virtual screening for Bcl-3 inhibitors

We performed a structure based virtual screening in order to select suitable candidates from a library of commercially available compounds (Specs database, Delft, The Netherlands). Firstly we created a pharmacophore model using features of p50 residues binding in the "MYSGS" binding pocket (Figure 4.7D). The pharmacophore model is commonly used as a filter to search through large databases to identify compounds with similar features and is more time efficient than performing docking analysis on the whole set of compounds (Kitchen et al., 2004). Only compounds that satisfied the pharmacophore query were then docked and scored using three different scoring functions (described in section 4.2). Finally, highest ranked 121 compounds were subjected to visual inspection. For *in-vitro* biological evaluation we aimed to include structurally diverse candidates, therefore the final 121 compounds were sorted into groups of similarity and the compound(s) with strongest protein-ligand interactions from each group were then selected for

biological evaluation. Overall, 10 compounds were selected for biological evaluation (Table 4.1, Table 4.2).

4.7.3 Biological evaluation of potential inhibitors in cell based assays

We used previously generated tumorigenic and non-tumorigenic cell models overexpressing either Bcl-3 WT or Bcl-3 ANK M123 binding mutant (Chapter 3) for biological evaluation. In general, cells overexpressing Bcl-3 WT were treated with 10 selected compounds at 10 μM concentration and the functional outcome in various cell-based assays was compared to that of controls (parental cells and cells overexpressing Bcl-3 ANK M123 binding mutant).

Firstly we determined the toxicity of the 10 selected compounds in non-tumorigenic HEK-293 cells and tumorigenic MDA-MB-231 cells. Even at concentration of 10 μM, the selected compounds did not decrease cell viability below 70% in either of the cell line used and were therefore used at a maximum dose of 10 μM in subsequent assays.

We optimised three different assays to evaluate the potential inhibitors. Firstly, the disruption of protein-protein interactions was monitored by Indirect Sandwich ELISA assay. This was followed by the NF-κB luciferase assay which aimed to establish the effect on NF-κB activity and finally, the Boyden chamber motility assay was used in order to assess the effect of the compounds on cell migration ability (Figure 4.12, Figure 4.13, Figure 4.14).

In addition, a cell model of HEK-293 cells overexpressing p52 was used to evaluate the ability of selected compounds to disrupt Bcl-3-p52 binding by determining the functional outcome on NF-κB activity (Figure 4.15).

A combination of three cell based assays was used in order to establish the effect of these compounds not only on disruption of Bcl-3-p50 binding but also on the related suppression of NF-κB activity and cell motility. Compound 6 was selected as a lead compound with significant effect in all three assays.

4.8 Summary

We have generated a model of the Bcl-3-p50 and Bcl-3-p52 complex using molecular modelling and identified a novel binding pocket, which we called the “MYSGS” binding pocket. Properties of this binding pocket and of p50 interacting

residues were used for virtual screening of a library of commercially available compounds. A panel of selected compounds was tested using Indirect Sandwich ELISA assay to evaluate the effect of disruption of binding. The functional outcomes were evaluated *in vitro* using NF-κB luciferase assay and Boyden chamber motility assay. The lead compound was selected and the structure activity relationships (SARs) will be determined in Chapter 5.

Chapter 5

Establishing the Structure-Activity Relationship (SAR)

5. Establishing the Structure-Activity Relationships (SAR)

Compound 6 was selected as our lead compound after biological evaluation (Chapter 4). Here we aimed to design structural analogues of compound 6, which would then be synthesised and biologically tested in order to determine structure-activity relationship (SAR) of the lead compound. By fully evaluating the SAR study we are be able to determine the importance of individual functional groups within the structure and design novel inhibitors that are effective at lower concentrations.

The lead compound 6 was observed to form hydrogen bonds with Bcl-3 residues Arg 269, Glu 277, Ser 307 and Arg 311 (Figure 5.1A&B). Specifically, the phenyl ring forms arene-cation interactions with Arg 269. The carboxylate group of Glu 277 forms a hydrogen bond with the NH group of the morpholine ring; additional hydrogen bonds are form between the oxygen of the amide group of the ligand and Ser 307 and Arg 311.

A.

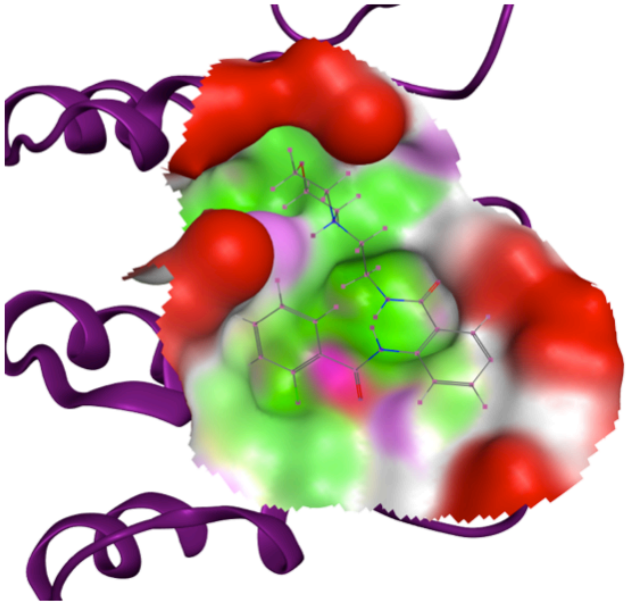

B.

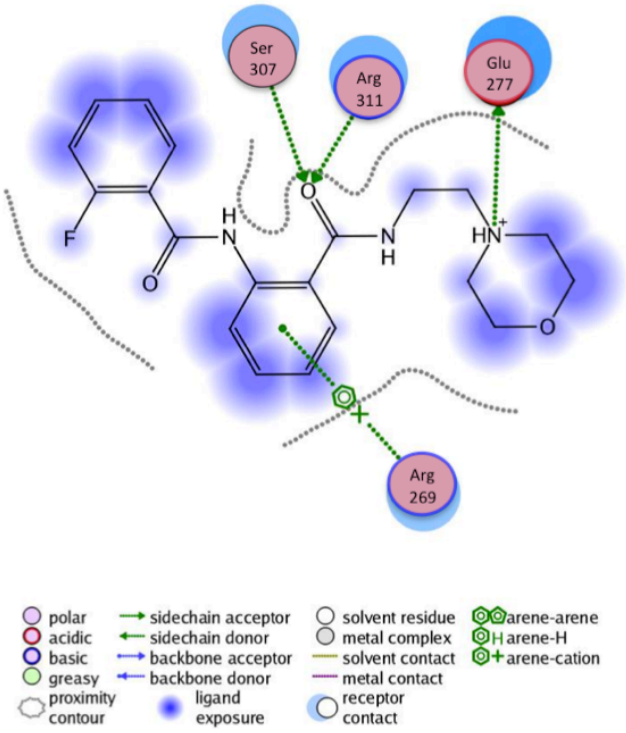

Figure 5.1 Ligand interaction of the lead compound 6 in the "MYSGG" binding pocket

A. An enlarged view of the "MYSGG" binding pocket with the lead compound 6 docked. A part of Bcl-3 molecule is shown in purple ribbon representation. Compound 6 is shown in ball and stick representation in grey. **B.** Ligand interaction diagram with explanation below. Green arrows show ligand interactions and blue spots represent areas exposed to water.

5.1 Design of novel analogues

2-benzamido-*N*-methylbenzamide was identified as an important moiety during molecular modelling studies and was also present in other compounds from virtual screening. This core structure was therefore kept unchanged in designed analogues and only one substitution at a time was introduced to give three novel series of analogues.

The figure below summarises the main modifications that were introduced in the lead structure. The main modifications carried out included:

- Modification of the substituent of the phenyl ring – series 1
- Modification of the linker chain length and substituent – series 2
- Modification of the substituent of the benzamide ring – series 3

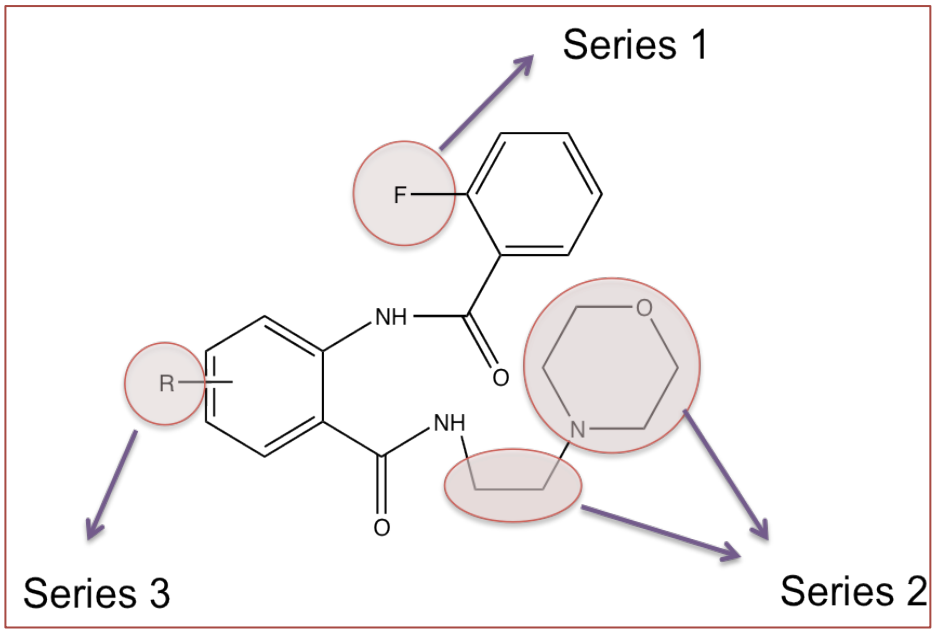

Figure 5.2 Modification of the lead compound
Modifications introduced to the lead compound are highlighted and gave rise to three series of structure analogues.

5.2 General method for synthesis

An efficient two-step synthetic route has been developed under mild conditions and is outlined below (Scheme 5.1). The cyclocondensation reaction of commercially available substituted anthranilic acid (**A**) with substituted benzoyl chloride (**B**) was carried out following a previously described method (Gilmore et al., 1996, Hsieh et al., 2005, Hsieh et al., 2010). The reaction was carried out in pyridine

at room temperature and gave rise to the intermediate product (**C**) in high yield (on average 85%). Reaction of intermediate (**C**) with commercially available amines (**D**) in the presence of diisopropylethylamine (DIPEA) at room temperature overnight as described previously (Strakovs et al., 2002) gave the target compound (**E**).

The suggested mechanism of the synthesis is outlined in Scheme 5.2. In a first step of the reaction, the lone pair electrons on the nitrogen of the primary amine of anthranilic acid attack the carbonyl of the benzoyl chloride in a nucleophilic substitution reaction. Subsequently, the ammonium cation is formed and the lone pair of electrons on the hydroxyl group attack the carbonyl, which leads to a cyclisation reaction. After elimination of water the intermediate is formed. In the second step DMF is used as a polar and aprotic solvent and DIPEA as a base. The lone pair of electrons on the nitrogen of the primary amine group attack the carbonyl on the heterocyclic ring formed during the first step cyclisation reaction, which triggers the breakage of the ring and electron re-arrangements to form the final compound.

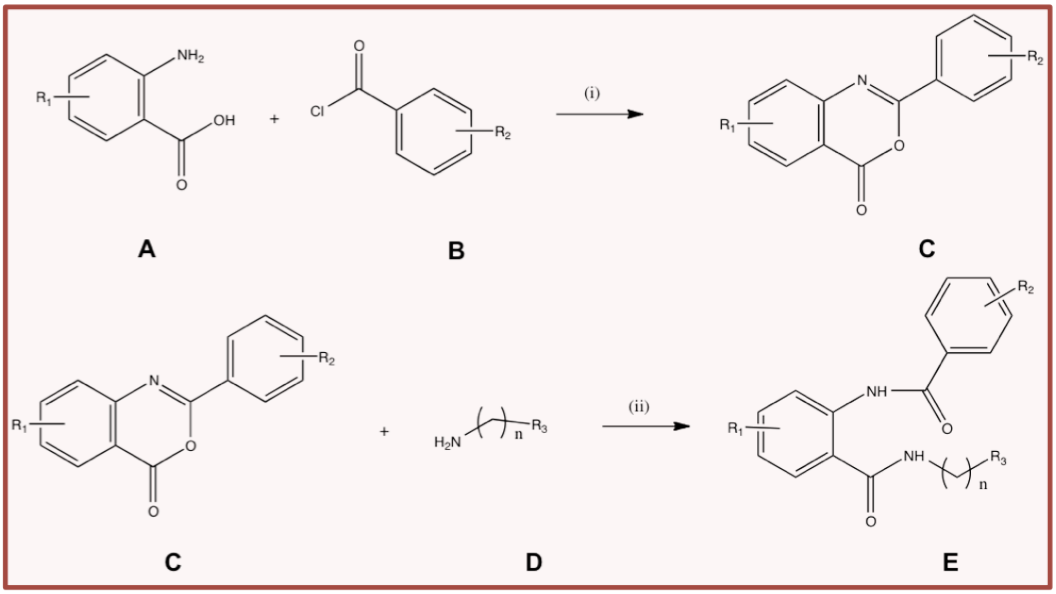

Reagents and conditions: (i) pyridine, r.t, 1 hour; (ii) iPr2EtNH, DMF, r.t, 16 hrs.

Scheme 5.1 General synthesis route

The cyclocondensation reaction of substituted anthranilic acid gave rise to intermediate **C**, which was then reacted with primary amines to obtain a final product **E**.

Step I.

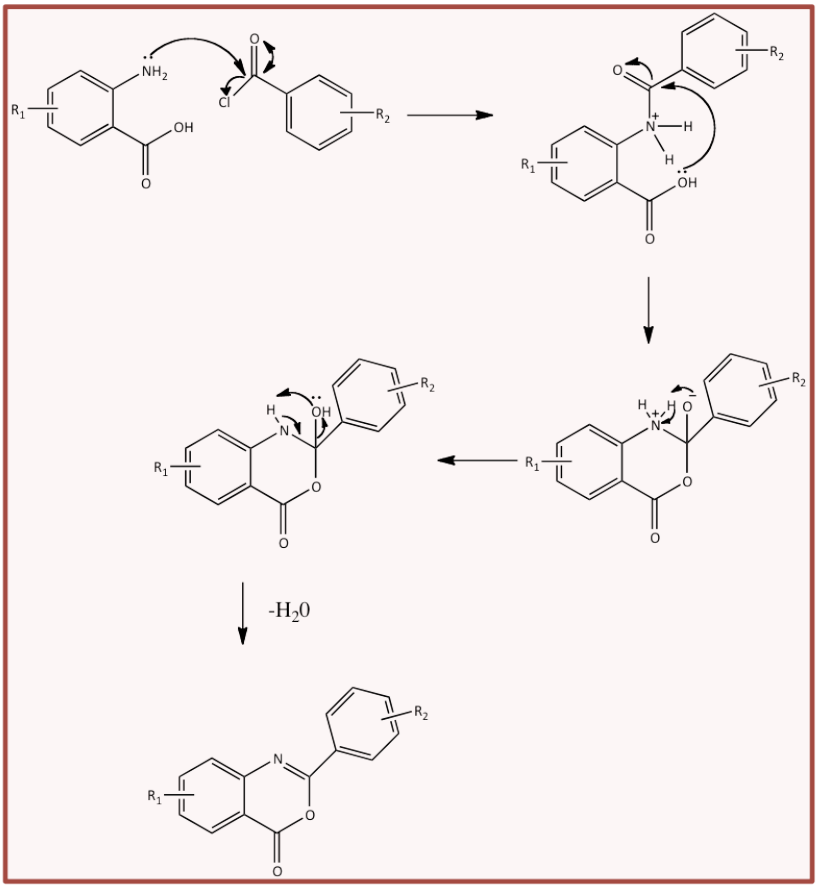

Step II.

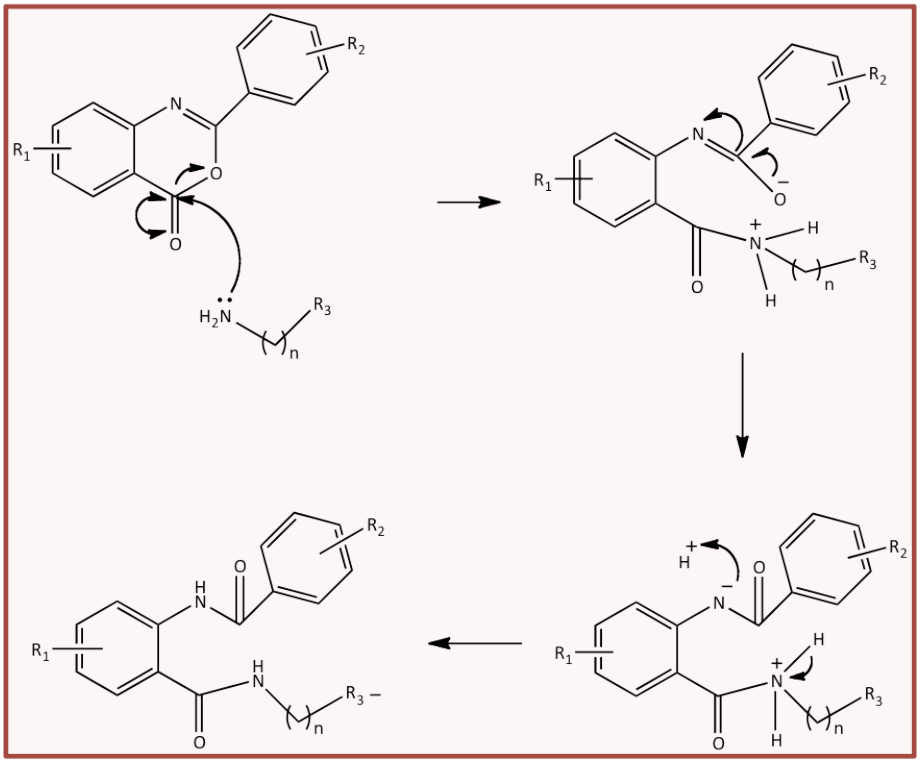

Scheme 5.2 Suggested mechanism of the two-step synthesis

5.3 Results of synthesis

Three series of analogues were synthesised following the method described in section 5.2. The full experimental data are in Chapter 6.

5.3.1 Synthesis of series 1

A wide variety of commercially available mono-substituted benzoyl chlorides were used to explore every position around the phenyl ring. A variety of substituents with electron-donating/electron-withdrawing character (F, OCH_3, NO_2) were used. Di and tri substituted benzoyl chlorides were also used (15l-15q). The second step reaction gave the final products of series 1 in a yield of 8-61%. The synthesis of analogues 15b, 15d, 15h and 15k was not achieved due to problems with purification of the final compound and if required should be repeated using a different purification method. The relatively low yield of the second step reactions is likely due to the requirement for recrystallisation and the fact that some of the final product may have been lost during the purification. The obtained compounds, however, are pure, as confirmed by elemental analysis. The full NMR data of these final compounds as well as those of intermediates are in chapter 6 (section 6.2).

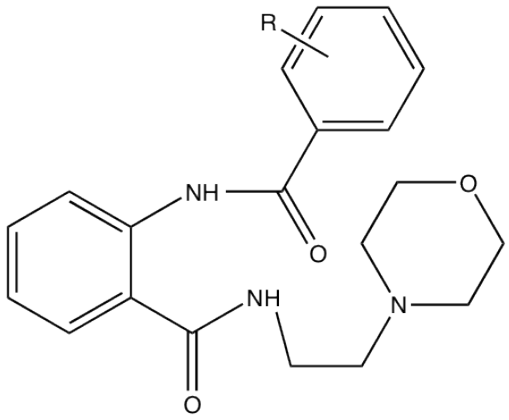

15a-k

15a: R= 2-F
15b: R= 3-F
15c: R= 4-F
15d: R= 2-OCH_3
15e: R= 3-OCH_3
15f: R= 4-OCH_3
15g: R= 2-NO_2
15h: R= 3-NO_2
15i: R= 4-NO_2
15j: R= 2-CH_3
15k: R= H
15l: R= 3,4-OCH_3
15m: R= 3,5-OCH_3
15n: R= 3,4,5-OCH_3
15o: R= 3,5-F
15p: R= 2,6-F
15q: R= 2,4-F

Series 1		
Name	Mw	Yield
15a	371.41	47%
15b	371.41	-
15c	371.41	8%
15d	383.44	-
15e	383.44	44%
15f	383.44	32%
15g	398.16	49%
15h	398.16	-

Series 1		
Name	Mw	Yield
15i	398.16	51%
15j	367.44	14%
15k	353.41	-
15l	413.20	22%
15m	413.20	58%
15n	443.21	52%
15o	389.16	40%
15p	389.16	61%
15q	389.16	55%

Scheme 5.3 Synthesis of series 1

5.3.2 Synthesis of series 2

The purpose of synthesising analogues from series 2 was to explore the effect of prolonging the linker chain, and the effect of replacing the morpholine ring with other heterocycles. For the first aim commercially available 3-morpholinopropan-1-amine was used and the importance of the morpholine ring in this position was explored using commercial available aliphatic heterocycles, such as pyridine, piperidine or pyrrolidine. Similarly, the second step reaction gave the final product in a yield of range of 17-55%. The synthesis of the analogue 17e was not achieved due to poor crystallization from ethanol and if required should be repeated using different purification method. The purity after recrystallisation from ethanol was confirmed by elemental analysis and the full NMR data of these final compounds are in chapter 6 (section 6.3).

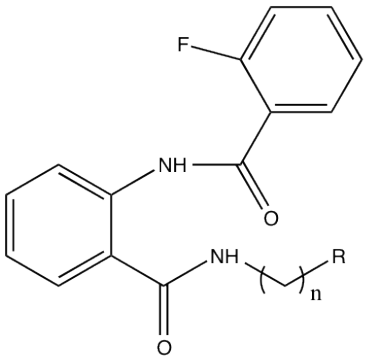

17a-f

17a: R= 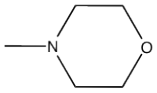 n=3

17b: R= 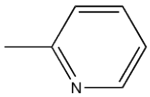 n=2

17c: R= 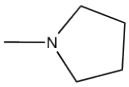 n=2

17d: R= 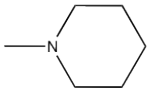 n=2

17e: R= 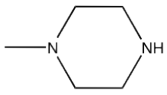 n=2

17f: R=  n=2

Series 2		
Name	Mw	Yield
17a	385.43	17%
17b	363.38	44%
17c	363.38	40%
17d	369.43	51%
17e	370.42	-
17f	301.32	43%

Scheme 5.4 Synthesis of series 2

5.3.3 Synthesis of series 3

Analogues from series 3 aimed to determine whether the activity of the lead compound could be improved by substitution on the anthranilic acid ring. We used commercially available substituted anthranilic acids, such as methoxy or methyl. The second step gave rise to the final product with a yield of 14-42%. The synthesis of analogue 20c was not achieved due to poor crystallization from ethanol

and if required should be repeated using different purification method. Similarly, these compounds were purified by recrystallisation from ethanol and the purity was confirmed by elemental analysis. The full NMR data of these final compounds as well as those of intermediates are in chapter 6 (section 6.4).

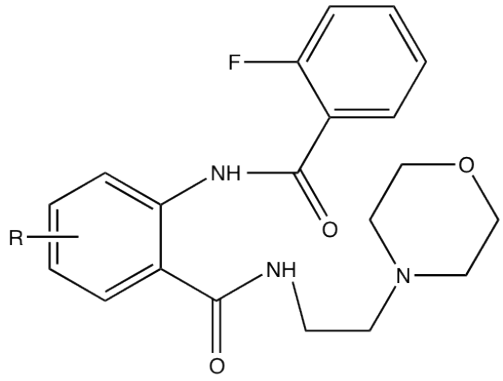

20a-d

20 a: R= 3-OCH3
20 b: R= 3-CH3
20 c: R= 5-I
20 d: R= 6-Cl

Series 3		
Name	Mw	Yield
20a	401.43	14%
20b	385.43	42%
20c	497.30	-
20d	405.85	33%

Scheme 5.5 Synthesis of series 3

5.4 Characterization of the lead compound (15a)

Before carrying out the series of modifications, previously purchased compound 6 from Specs (Delft, The Netherlands) was resynthesized as compound 15a. The synthesis was successfully achieved with 96% yield in the first step and 47% yield in the second step of the reaction. The purification of the final compound was performed by recrystallisation with ethanol. The 1H and 13C NMR Spectra was in agreement with those provided by Specs and the purity of the compound was confirmed by elemental analysis.

We established that the solubility of this compound in most commonly used solvents is very low (Table 5.1A), which represents an issue for biological evaluation. Therefore a hydrochloric salt of the lead compound was synthesised (full procedure and 1H and 13C NMR Spectra in Chapter 6, section 6.5) and the solubility was analysed. The obtained salt had improved solubility in water and methanol (Table 5.1B), however was not soluble (< 0.1 g/100 ml) in Phosphate Buffered Saline (PBS). PBS is a water-based salt solution containing sodium chloride, sodium phosphate, potassium chloride and potassium phosphate, while the buffer's phosphate groups help to maintain a constant pH. PBS is non-toxic and is commonly used as an isotonic buffered solution for cell-based assays and animal studies.

A.

Solvent	Solubility (g/100ml)
Water	< 0.01
Methanol	0.20
Ethanol	0.09
Dimethyl sulfoxide	3.71
Ethyl acetate	0.34
Dichloromethane	2.91
Diethyl ether	0.09

B.

Solvent	Solubility (g/100ml)
Water	0.95
Methanol	0.59
Ethanol	0.19
Dimethyl sulfoxide	< 0.01
Ethyl acetate	0.02
Dichloromethane	0.90
Diethyl ether	< 0.01

Table 5.1 Solubility of the lead compound in organic solvents
The solvents are in order of decreasing polarity. The solubility is represented in grams of the compound that are soluble in 100 ml of corresponding solvent. Solubility > 0.1 g/100 ml is considered as soluble. **A.** Solubility for the lead compound 6. **B.** Solubility of the hydrochloric salt of the lead compound 6.

5.4.1 Cell toxicity of the lead compound *in vitro*

The toxicity of the lead compound was evaluated *in vitro* using human breast cancer cell lines. To compare the toxicity in tumorigenic as well as in non-tumorigenic breast cancer cells, we selected MCF-10A as a non-tumorigenic human breast cancer cell line and MDA-MB-231 and SKBR3 as cell models of tumorigenic human breast cancer cell line.

MCF-10 cells were derived from a mammary tissue from a 36-year-old woman in a good health and the immortalized MCF-10A line can grow in culture and has a stable, near-diploid karyotype (Soule et al., 1990) with modest genetic modifications typical of culture-adapted breast epithelial cells, including loss of p16 locus (Yaswen et al., 2002). The cells express normal p53 (Merlo et al., 1995) and they do not grow in immuno-compromised mice (Miller et al., 1993).

The lead compound (15a) was dissolved in DMSO and diluted in media in a highest concentration of 1mM (10^{-3}M). Cell toxicity was evaluated using the Cell Titre Blue viability assay over a range of molarities for 24hrs. The effect of the lead compound on cell viability was always normalised against DMSO control and the dose-response curve was generated using GraphPad software (Figure 5.3).

The lead compound (15a) did not caused a 50% decrease in cell viability in any of the cell lines, however we could see a difference in cell toxicity between non-tumorigenic and tumorigenic cell lines. At the highest concentration of 1mM, the viability in MCF-10A cell line was 96%, 72% in MDA-MB-231 and 57% in SKBR3 compared to DMSO control (100%).

The concentration causing 50% loss in cell viability was calculated using GraphPad software by extrapolating the dose-response curve, giving values of 14.9 mM for MCF-10A, 2.70 mM for MDA-MB-231 and 1.37 mM for SKBR3.

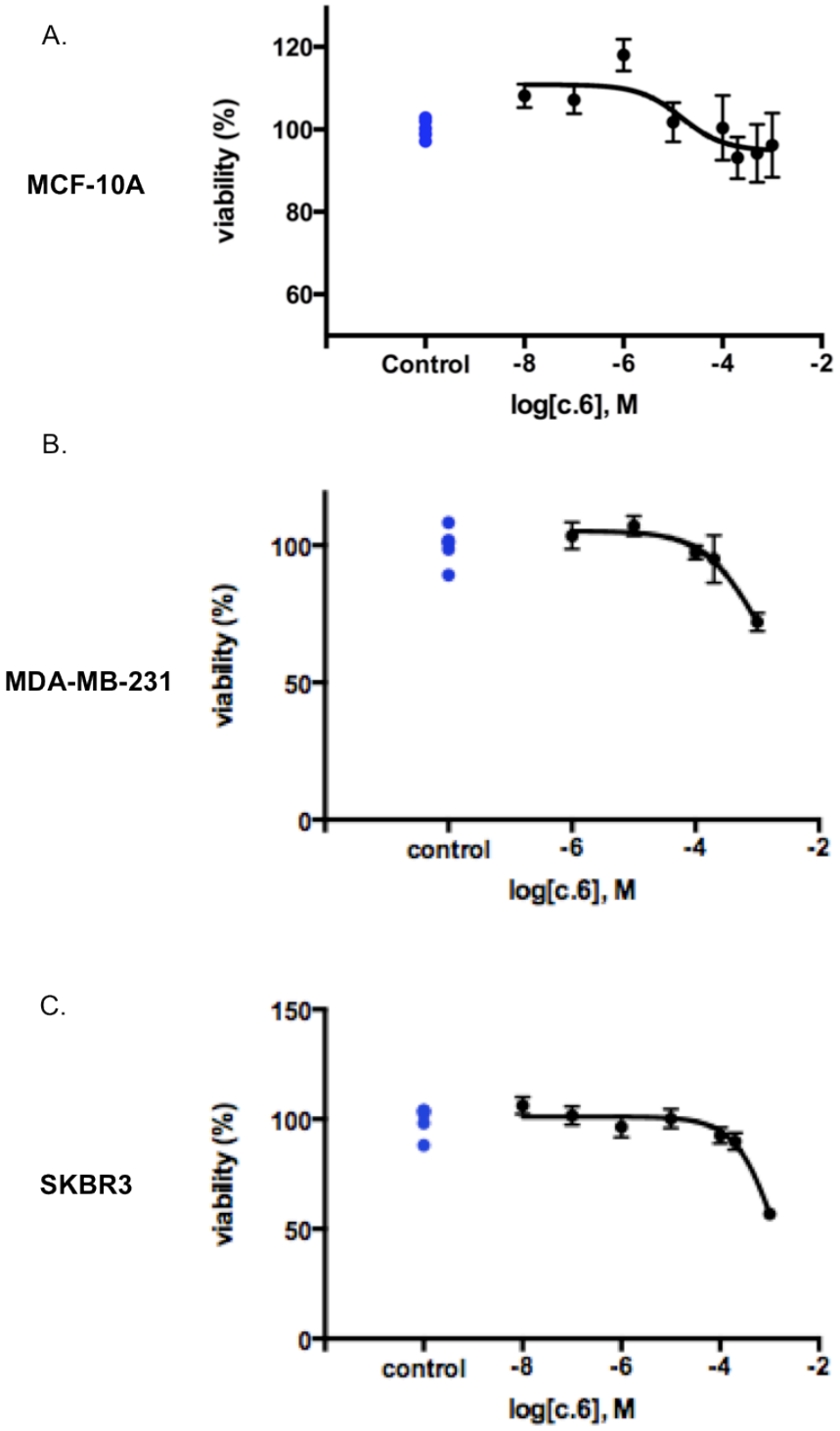

Figure 5.3 Cell toxicity of the lead compound

MCF-10A (**A.**), MDA-MB-231 (**B.**) and SKBR3 (**C.**) cells were cultivated with the lead compound 15a over a range of molarities in adherent growth conditions. Cell viability was determined after 24hrs by the Cell Titre Blue viability assay and resulting fluorescence was normalised against fluorescence of control cells treated with DMSO in relevant concentration. Data represent average of six wells and error bars represent ± SEM. Dose response curves were generated using GraphPad software.

5.4.2 Establishing IC_{50} of the lead compound by Indirect Sandwich ELISA assay

HEK-293 Bcl-3 WT cells were cultivated with the lead compound over a range of molarities for 24hrs before cell lysates were obtained under non-denaturing conditions. The dose response curve was generated using GraphPad software (Figure 5.4A). The determined IC_{50} was 447.0 nM.

Indirect ELISA assay was performed using Bcl-3 antibody to show an equal loading across samples treated with compound 15a (Figure 5.4B) and controls (Figure 5.4C).

5.4.3 Establishing IC_{50} of the lead compound by NF-κB assay

The effect of the lead compound (15a) on NF-κB activity was determined by NF-κB luciferase assay in MDA-MB-231, HEK-293 and HEK-293 p52 cells. Respective Bcl-3 WT overexpressing cells were cultivated with the lead compound (15a) over a range of molarities for 24hrs before being transfected with NF-κB luciferase reporter plasmid for 48hrs and analysed for NF-κB activity. The dose response curve was generated using GraphPad software (Figure 5.5). The determined IC_{50} in MDA-MB-231 cells was 49.43 nM, 159.6 nM HEK-293 cells and 210.6 nM in HEK-293 p52 overexpressing cells.

5.4.4 Establishing IC_{50} of the lead compound by cell motility assay

It was previously determined that the lead compound significantly suppressed migration ability in MDA-MB-231 cells at 10 μM. We therefore generated a dose response curve to determine an IC_{50} in this assay.

MDA-MB-231 Bcl-3 WT cells were cultivated with the lead compound and DMSO control over a range of molarities for 24hrs before being seeded onto Boyden migration chambers. The constant number of live cells present during this assay across samples was monitored by cell count. The dose response curve was generated using GraphPad software (Figure 5.6). The determined IC_{50} was 310.4 nM.

A.

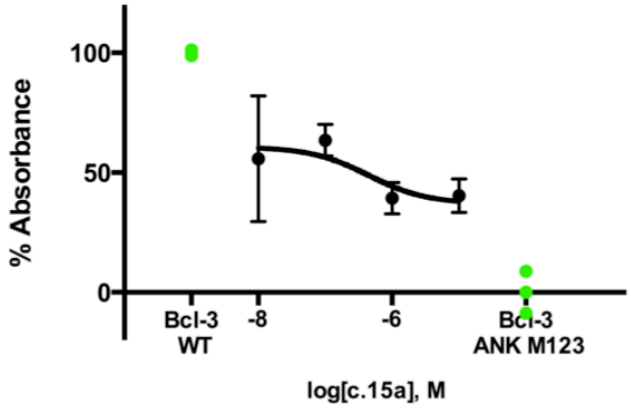

B.

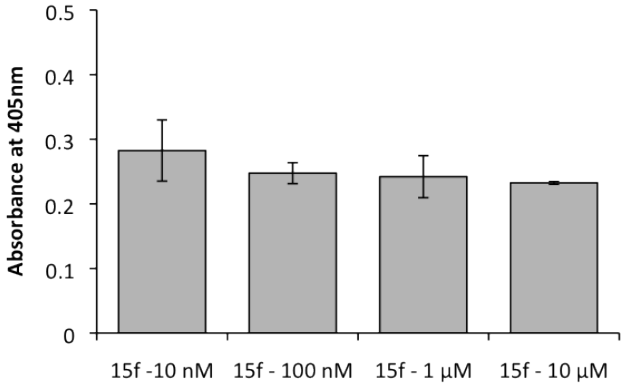

C.

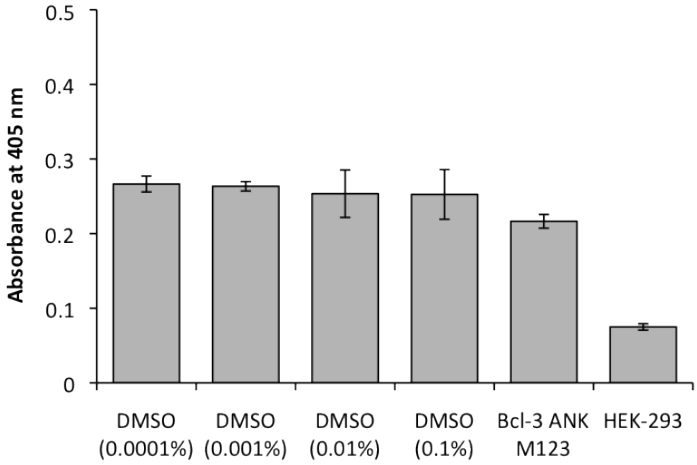

Figure 5.4 Establishing IC_{50} of the lead compound by Indirect Sandwich ELISA assay
HEK-293 Bcl-3 WT cells were cultivated with compound 15a or DMSO in a range of molarities in normal adherent growth conditions for 24hrs. Cell lysates were prepared under non-denaturing conditions. **A**. Indirect sandwich ELISA assay was performed on FLAG coated ELISA plates using p50 antibody. Absorbance was measured at 405 nm and normalised to that of DMSO control. Error bars represent ± SEM of three independent wells. The dose response curve was generated using GraphPad software. **B+C.** Indirect ELISA assay was performed on FLAG coated ELISA plates using Bcl-3 antibody. Absorbance was measured at 405 nm. Error bars represent ± SEM of three independent wells.

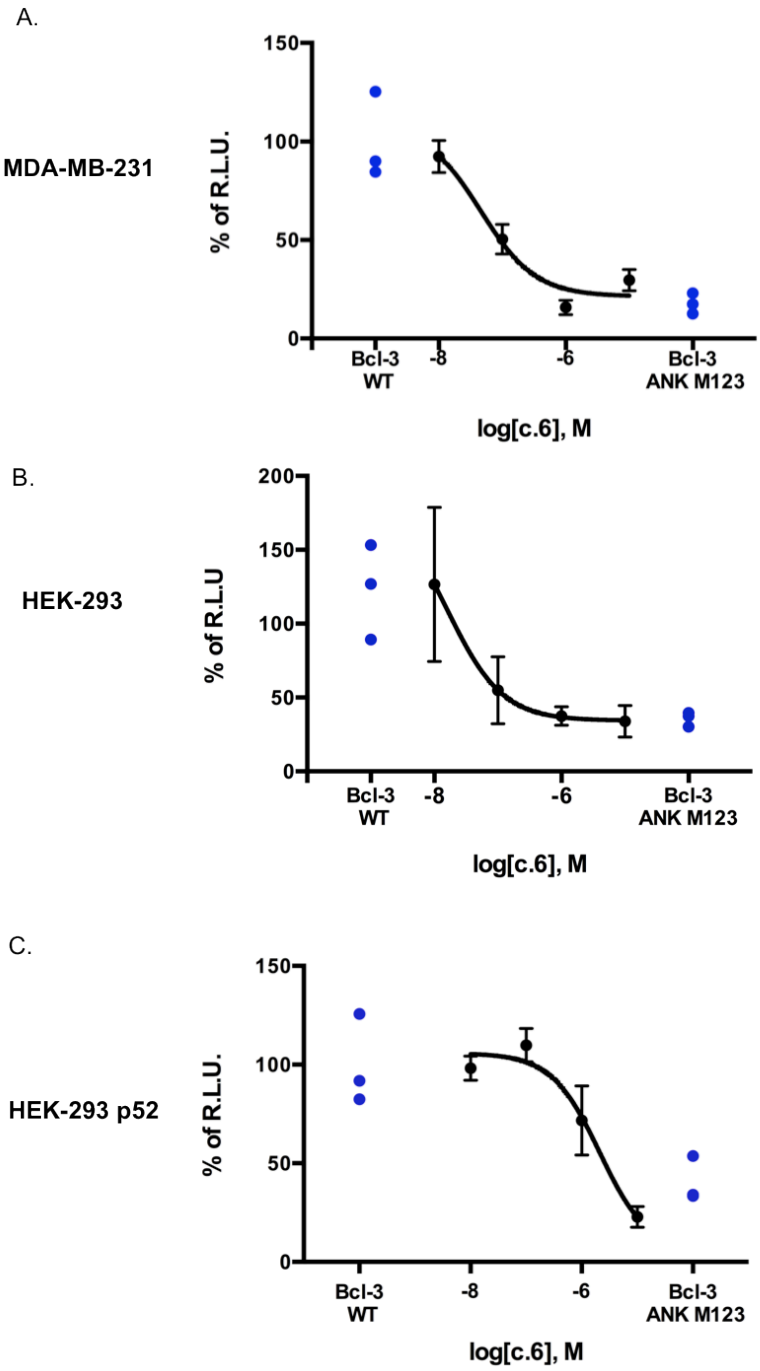

Figure 5.5 Establishing IC_{50} of the lead compound by NF-κB assay

A-C. MDA-MB-231 Bcl-3 WT, HEK-293 Bcl-3 WT and HEK-293 Bcl-3 WT p52 cells were cultivated with the lead compound 15a or DMSO control in a range of molarities for 24hrs before being transfected with NF-κB luciferase reporter for 48hrs together with controls. NF-κB activity is represented in % of DMSO control. Error bars represent ± SEM of three independent transfections. The dose response curve was generated using GraphPad software.

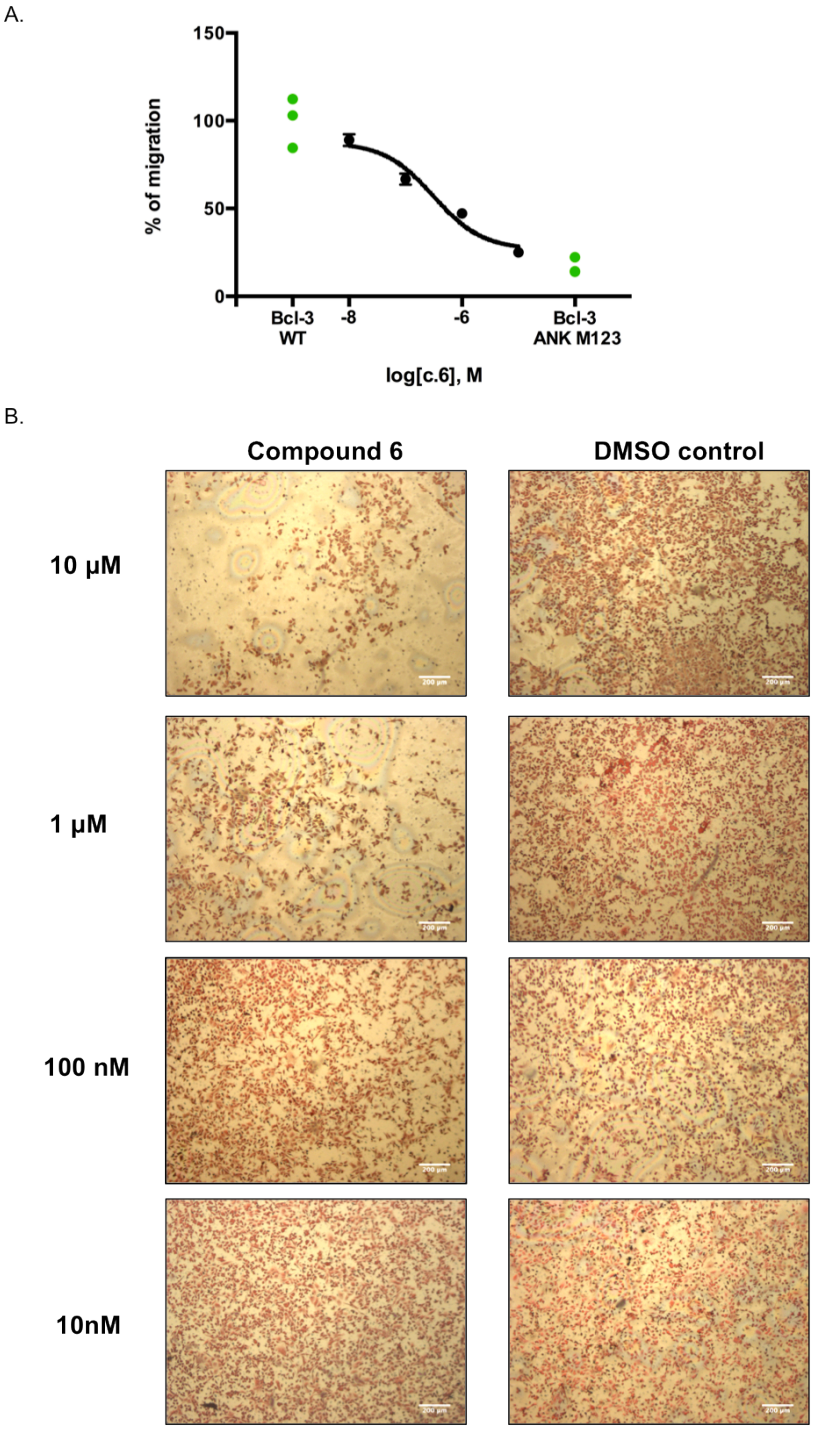

Figure 5.6 Establishing IC_{50} of the lead compound by cell motility assay
A. MDA-MB-231 Bcl-3 WT cells were cultivated with compound 15a (10 µM, 1 µM, 100 nM, 10 nM) or DMSO in corresponding concentration in normal adherent growth conditions for 24hrs before being seeded onto Boyden motility chambers for 24hrs together with Bcl-3 ANK M123 control. Migrated cells were counted from three fields of view of each of three replicate Boyden chambers. Error bars represent ± SEM. The dose response curve was generated using GraphPad software **B.** Representative images of migrated cells for Bcl-3 WT + compound 6 and Bcl-3 WT + DMSO in corresponding concentrations. Scale bars represent 200 µm.

5.5 Biological evaluation of mono substituted analogues

5.5.1 Cell toxicity

Selected compounds were dissolved in DMSO and diluted to a highest concentration of 10 µM (0.1% DMSO). In all assays, a DMSO control was always used. Selected compounds were tested for cell toxicity in HEK-293 and MDA-MB-231 cells before being used in cell-based assays. Cell toxicity was evaluated using the Cell Titre Blue viability assay over a range of molarities for 24hrs (Figure 5.7).

Compounds were well tolerated in both cell lines and cell viability was above 70% even at 10 µM concentration.

5.5.2 NF-κB assay

The effect of selected analogues on NF-κB activity was determined by NF-κB luciferase assay in MDA-MB-231 cells. MDA-MB-231 Bcl-3 WT cells were cultivated with compounds from series 1-3 at 1 µM concentration for 24hrs before being transfected with NF-κB luciferase reporter plasmid for 48hrs together with controls and analysed for NF-κB activity (Figure 5.8).

The NF-κB activity of analogues from series 1 was comparable to that of the lead compound (15a), with a significant decrease of in NF-κB activity observed for the lead compound 15a and the analogue 15f as compared to Bcl-3 WT DMSO control.

From series 2 analogue 17a and 17d significantly decreased NF-κB activity as compared to Bcl-3 WT DMSO control. Only analogue 17a, however, showed comparable activity with the lead compound 15a, all other analogues did not have improved effect.

From series 3 analogue 20a had comparable effect on NF-κB activity with the lead compound 15a. Analogue 20c also showed significant decrease in NF-κB activity as compared to Bcl-3 WT DMSO control, however not to the same level as the lead compound 15a.

Based on the results for the series of analogues, we have established dose response curve for selected analogues from series 1 (15f), from series 2 (17a and 17c) and from series 3 (20a) over a range of molarities. MDA-MB-231 Bcl-3 WT cells

were cultivated with selected compounds from series 1-3 over a range of molarities for 24hrs before being transfected with NF-κB luciferase reporter plasmid for 48hrs together with controls and analysed for NF-κB activity (Figure 5.9). We observed an improvement in the determined IC_{50} for analogue 15f (6.97 nM). Other analogues showed decreased ability to suppress NF-κB activity than the lead compound. The determined IC_{50} for analogue 17a was 2.50 µM, 2.49 µM for analogue 17c and 1.07 µM for analogue 20a.

5.5.2.1 Indirect Sandwich ELISA assay

The ability to disrupt Bcl-3-p50 binding was determined by Indirect Sandwich ELISA assay for selected analogues (15f, 17a, 17c, 20a).

HEK-293 Bcl-3 WT cells were cultivated with selected compounds over a range of molarities for 24hrs before cell lysates were obtained under non-denaturing conditions. The dose response curve for selected analogues was generated using GraphPad software (Figure 5.10A-D). We observed improved IC_{50} as compared to the lead compound 15a for analogues 15f and 20a, with IC_{50} values 60.17 nM and 119.3 nM respectively. The IC_{50} could not be established for analogues from series 2, 17a and 17c, and was calculated from the dose response curve using GraphPad software with IC_{50} of 76.25 µM for analogue 17a and 10.41 µM for analogue 17c.

Indirect ELISA assay was performed using Bcl-3 antibody to show an equal loading across samples treated with compounds 15f, 17a, 17c, and 20a (Figure 5.10E-H). The equal loading for controls was shown previously (Figure 5.4C).

5.5.2.2 Cell motility assay

As shown in section 5.4.4, the lead compound 15a caused a significant decrease in cell motility with an IC_{50} value of 310.4 nM. Therefore we wanted to establish whether designed analogues have similar or improved ability to suppress cell migration. MDA-MB-231 Bcl-3 WT cells were cultivated with selected analogues (15f, 17a, 17c, 20a) and DMSO control over a range of molarities for 24hrs before being seeded onto the Boyden motility chambers. Migrated cells were visualised and counted after 24hrs. The dose response curves were generated using GraphPad

software (Figure 5.11). The constant number of live cells present during this assay across samples was monitored by cell count.

Consistent with results from NF-κB assay and Indirect Sandwich ELISA assay, the analogue 15f showed an improved ability to suppress cell migration, with IC_{50} value of 28.93 nM. Interestingly, the cell migration was suppressed below 50% even at 10 nM concentration. Other analogues showed decreased ability to suppress cell motility than the lead compound 15a. The determined IC_{50} for analogue 17a was 1.33 µM, 3.65 µM for analogue 17c and 900 nM for analogue 20a.

5.5.2.2.1 The effect of analogue 15f on cell viability

The activity of the analogue 15f was improved as compared to the original compound 6 (15a); therefore next we determined the toxicity of this analogue in MDA-MB-231 cell line.

The lead compound (15a) was dissolved in DMSO and diluted in media to a highest concentration of 2mM. Cell toxicity was evaluated using the Cell Titre Blue viability assay over a range of molarities for 24hrs. The effect of the lead compound on cell viability was always normalised against DMSO control and the dose-response curve was generated using GraphPad software (Figure 5.12). Cell viability was decreased by 50% at 781.3 µM concentration of compound 15f.

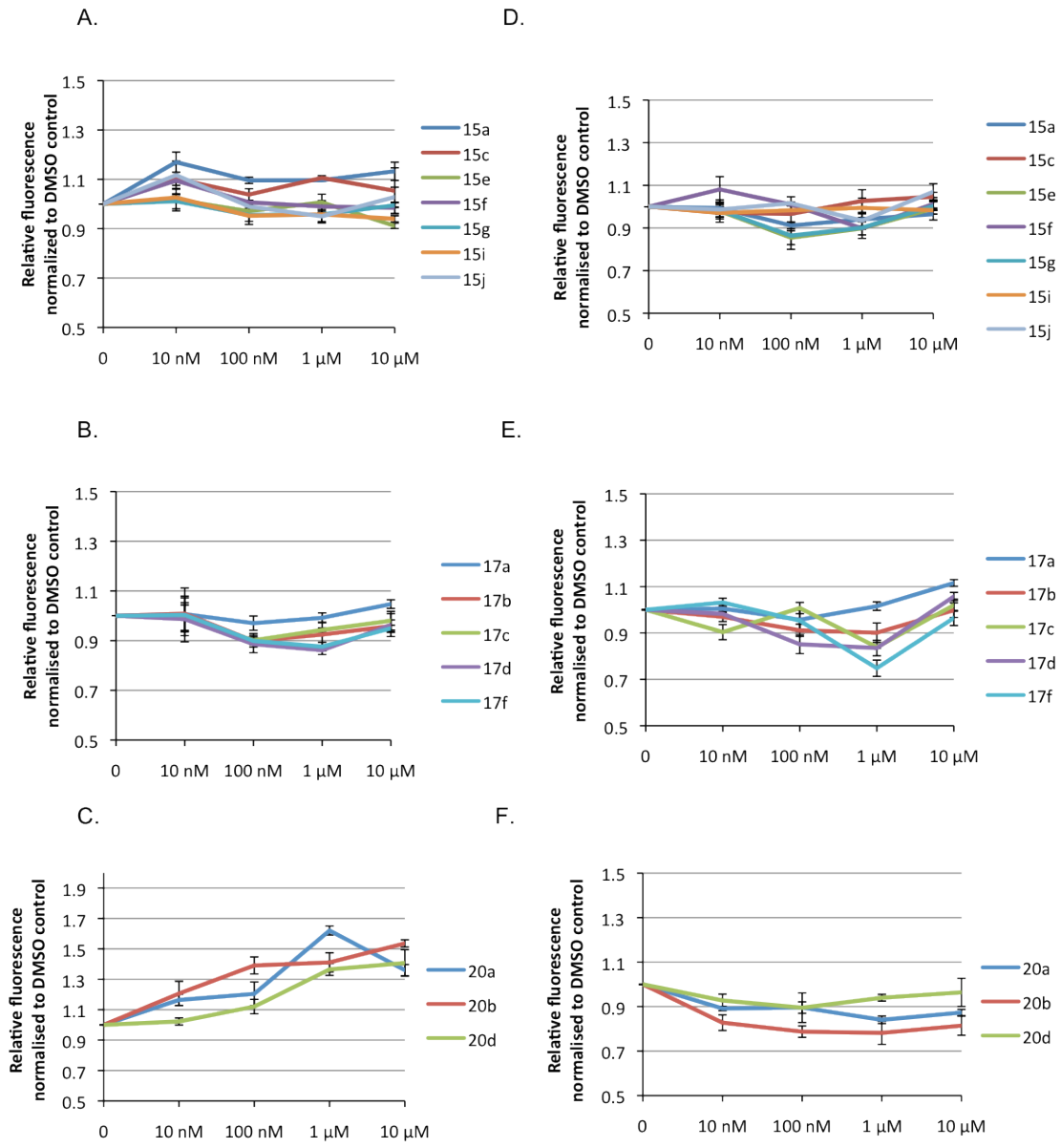

Figure 5.7 Cell toxicity

MDA-MB-231 cells (**A&B&C)** and HEK-293 cells (**D&E&F)** were cultivated with compounds from series 1, 2 or 3 (10 nM, 100 nM, 1 µM and 10 µM) in adherent growth conditions. Cell viability was determined after 24hrs by the Cell Titre Blue viability assay and resulting fluorescence was normalised against that of respective cells treated with DMSO under the same conditions. Data represent average of six wells and error bars represent ± SEM.

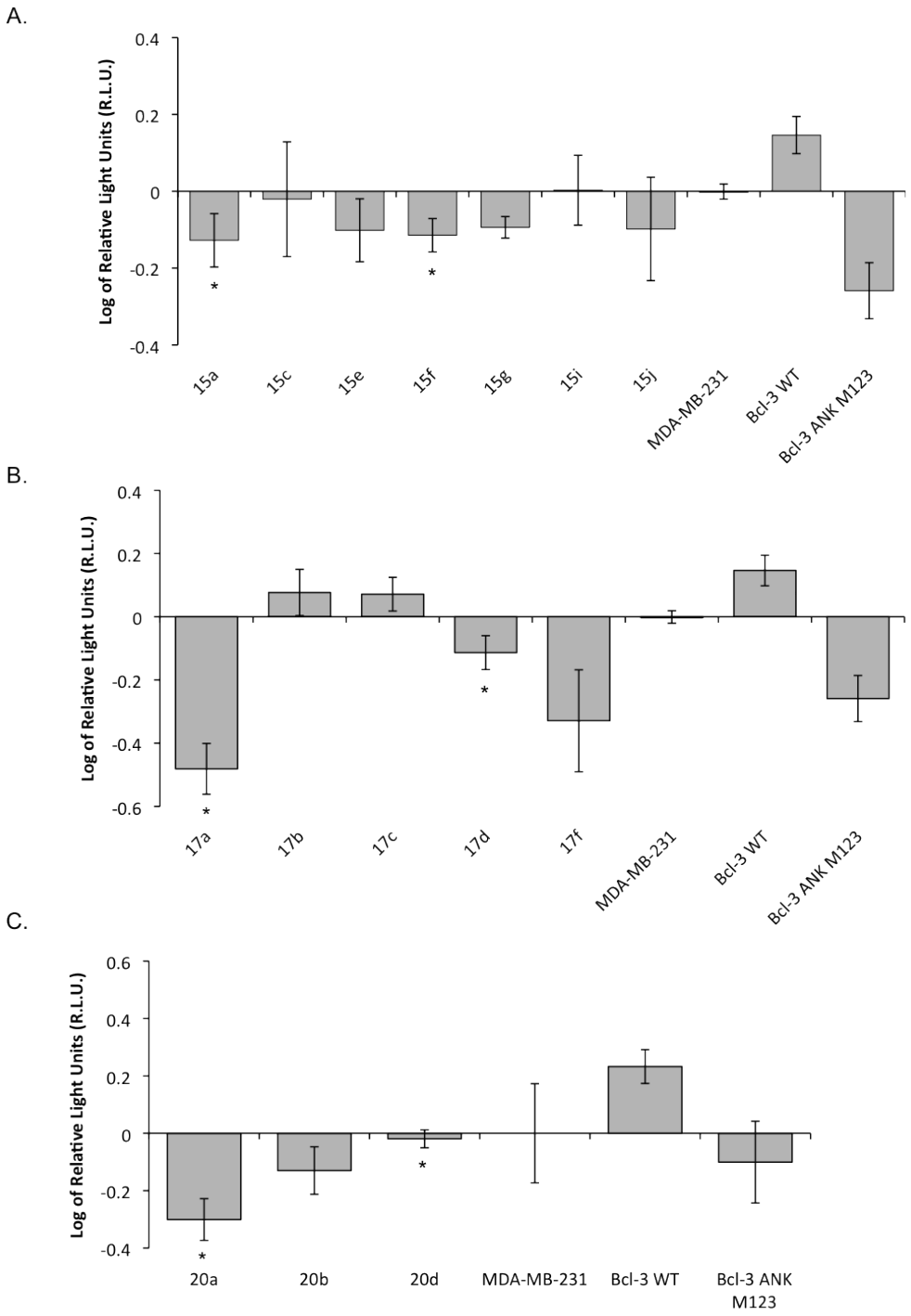

Figure 5.8 NF-κB assay in MDA-MB-231 cells

MDA-MB-231 Bcl-3 WT cells were cultivated with compounds from series 1 (**A.**), 2 (**B.**) and 3 (**C.**) at 1 µM concentration or DMSO control for 24hrs before being transfected with NF-κB luciferase reporter for 48hrs together with controls. NF-κB activity is plotted on a log scale as relative light units and normalised to the NF-κB activity of MDA-MB-231 cells. Error bars represent ± SEM of three independent transfections. (T-test, *=$p<0.05$ as compared to MDA-MB-231 Bcl-3 WT).

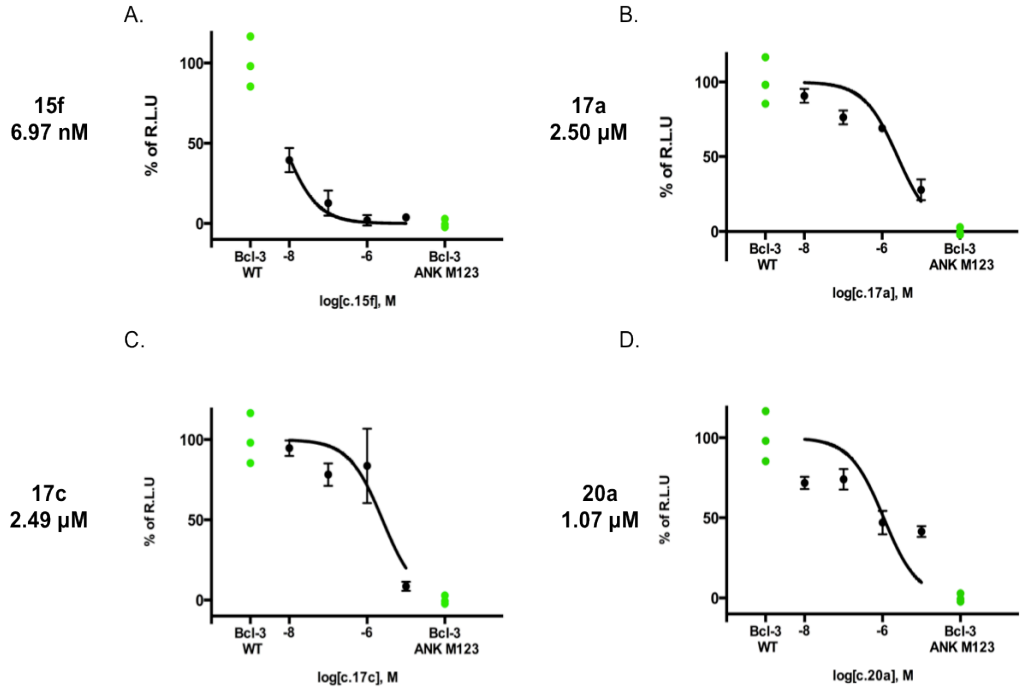

Figure 5.9 Establishing IC_{50} of selected analogues by NF-κB assay in MDA-MB-231 cells

MDA-MB-231 Bcl-3 WT cells were cultivated with analogues 15f (**A.**), 17a (**B.**), 17c (**C.**) and 20a (**D.**) or DMSO control in a range of molarities for 24hrs before being transfected with NF-κB luciferase reporter for 48hrs together with controls. NF-κB activity is represented in % of DMSO control. Error bars represent ± SEM of three independent transfections. The dose response curve was generated using GraphPad software.

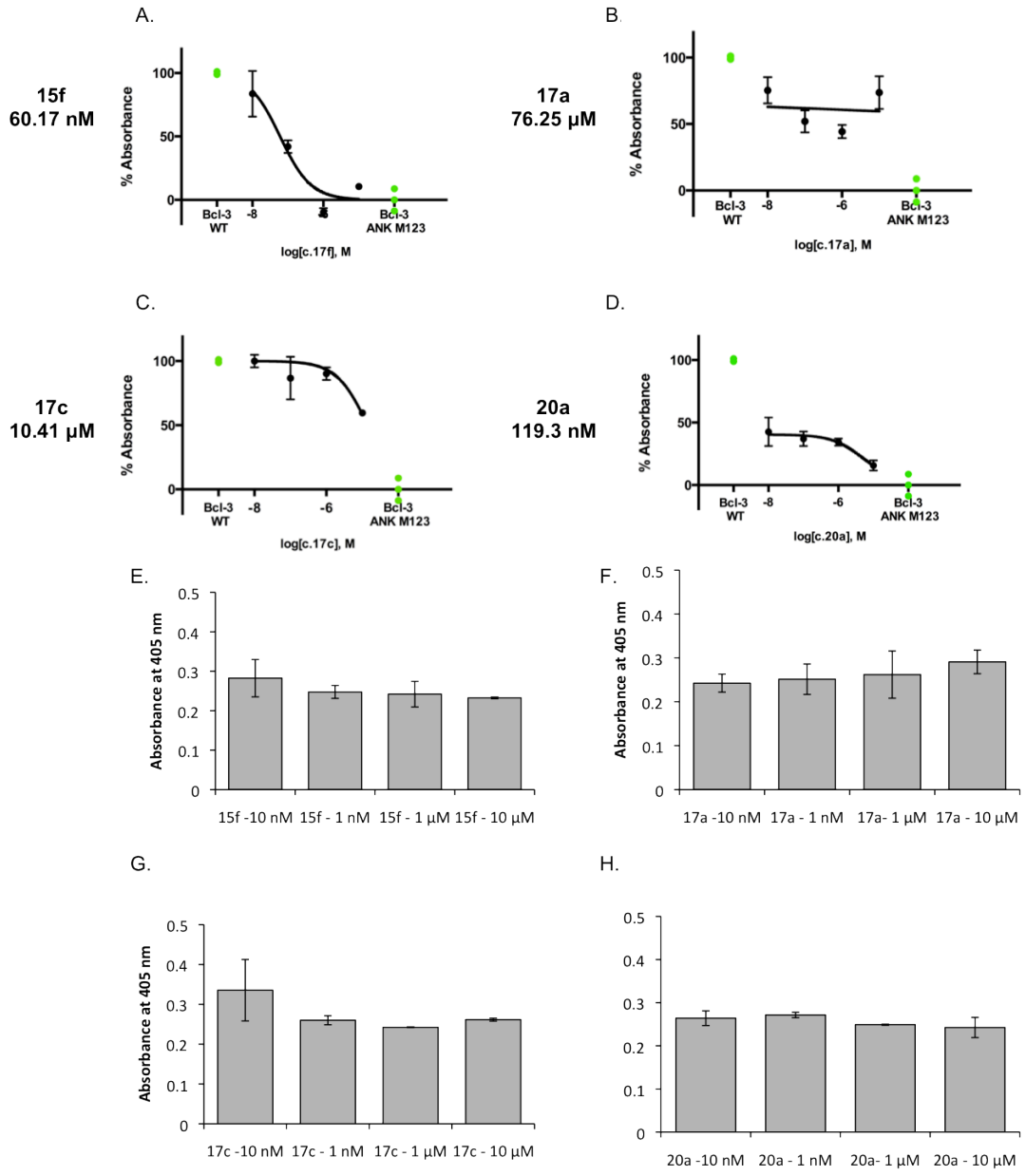

Figure 5.10 Establishing IC_{50} of selected analogues by Indirect Sandwich ELISA assay

HEK-293 Bcl-3 WT cells were cultivated with compound 15f (**A.**), 17a (**B.**), 17c (**C.**) and 20a (**D.**) or DMSO in a range of molarities in normal adherent growth conditions for 24hrs. Cell lysates were prepared under non-denaturing conditions. **A-D**. Indirect sandwich ELISA assay was performed on FLAG coated ELISA plates using p50 antibody. Absorbance was measured at 405 nm and normalised to that of DMSO control. Error bars represent ± SEM of three independent wells. The dose response curve was generated using GraphPad software. **D-H.** Indirect ELISA assay was performed on FLAG coated ELISA plates using Bcl-3 antibody. Absorbance was measured at 405 nm. Error bars represent ± SEM of three independent wells.

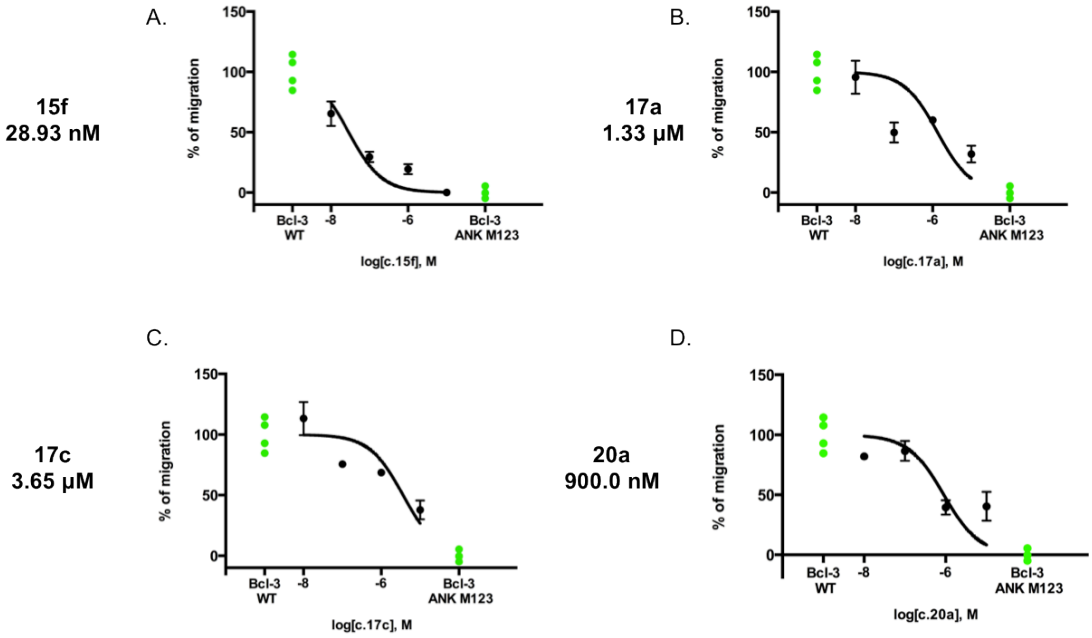

Figure 5.11 Establishing IC_{50} of selected analogues by cell motility assay
MDA-MB-231 Bcl-3 WT cells were cultivated with compounds 15f (**A.**), 17a (**B.**), 17c (**C.**) and 20a (**D.**) or DMSO in a range of molarities in normal adherent growth conditions for 24hrs before being seeded onto Boyden motility chambers for 24hrs together with Bcl-3 ANK M123 control. Migrated cells were counted from three fields of view of each of three replicate Boyden chambers. Error bars represent ± SEM. The dose response curve was generated using GraphPad software.

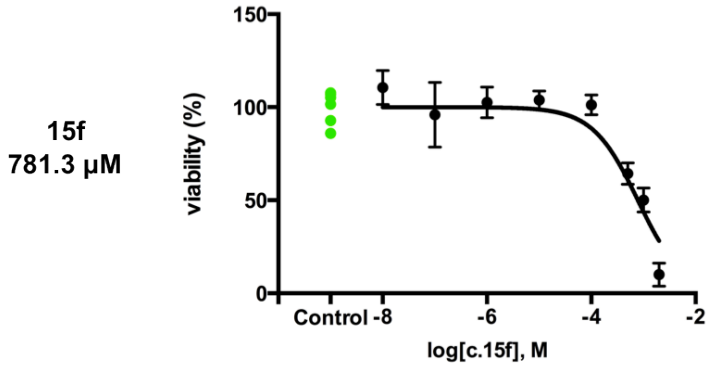

Figure 5.12 The effect of analogue 15f on cell viability
MDA-MB-231 cells were cultivated with the analogue 15f over a range of molarities in adherent growth conditions. Cell viability was determined after 24hrs by the Cell Titre Blue viability assay and resulting fluorescence was normalised against fluorescence of control cells treated with DMSO in relevant concentration. Data represent average of six wells and error bars represent ± SEM. Dose response curves were generated using GraphPad software.

5.6 Biological evaluation of di- and tri- substituted analogues

5.6.1 Cell toxicity

Selected compounds were dissolved in DMSO and diluted to a highest concentration of 10 µM (0.1% DMSO). In all assays, a DMSO control was always used. Selected di- and tri- substituted compounds from series 1 (15l-q) were tested for cell toxicity in MDA-MB-231 cells before being used in cell-based assays. Cell toxicity was evaluated using the Cell Titre Blue viability assay over a range of molarities for 24hrs (Figure 5.13A&B).

Compounds were well tolerated in both cell lines and cell viability was above 90% even at 10 µM concentration.

5.6.2 NF-κB assay

The effect of selected analogues on NF-κB activity was determined by NF-κB luciferase assay in MDA-MB-231 cells. MDA-MB-231 Bcl-3 WT cells were cultivated with compounds from series 1-3 at 1 µM concentration for 24hrs before being transfected with NF-κB luciferase reporter plasmid for 48hrs together with controls and analysed for NF-κB activity. Only the original compound 6 (15a) caused a significant suppression of NF-κB activity as compared to Bcl-3 WT overexpressing MDA-MB-231 cells (Figure 5.13C).

IC_{50} values were established for three selected analogues (15o-q). All three tested analogues showed decreased ability to suppress NF-κB activity than the lead compound 6 (15a). The determined IC_{50} for analogue 15o was 2237.80 nM, 705.90 nM for analogue 15p and 988.87 nM for analogue 15q (Figure 5.14).

A.

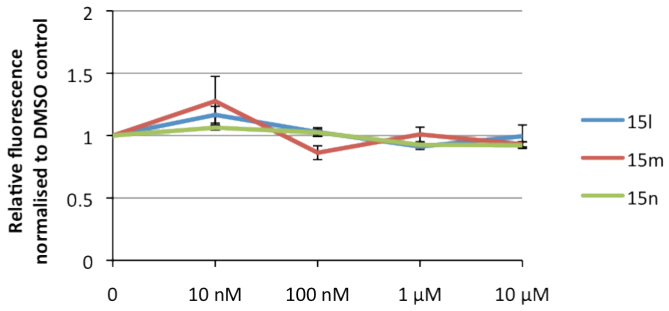

B.

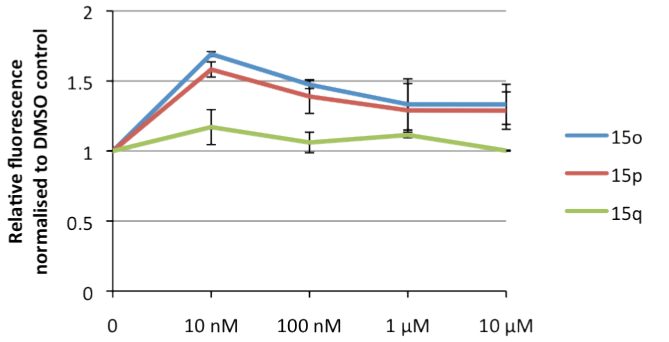

C.

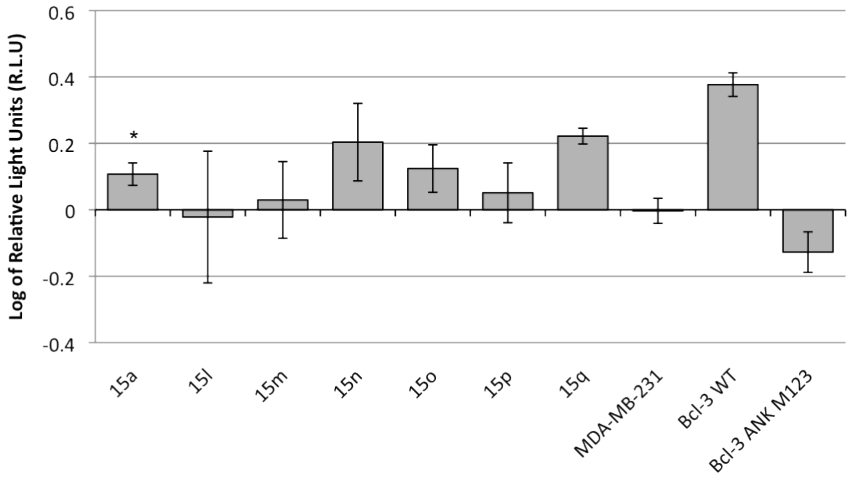

Figure 5.13 Biological evaluation of di- and tri- substituted analogues

A&B. MDA-MB-231 cells were cultivated with di- and tri- substituted compounds from series 1 (15l-q) over a range of molarities in adherent growth conditions. Cell viability was determined after 24hrs by the Cell Titre Blue viability assay and resulting fluorescence was normalised against that of respective cells treated with DMSO under the same conditions. Data represent average of six wells and error bars represent ± SEM. **C.** MDA-MB-231 Bcl-3 WT cells were cultivated with compounds from series 1 (15l-q) at 1 µM concentration or DMSO control for 24hrs before being transfected with NF-κB luciferase reporter for 48hrs together with controls. NF-κB activity is plotted on a log scale as relative light units and normalised to the NF-κB activity of MDA-MB-231 cells. Error bars represent ± SEM of three independent transfections. (T-test, *=$p<0.05$ as compared to MDA-MB-231 Bcl-3 WT).

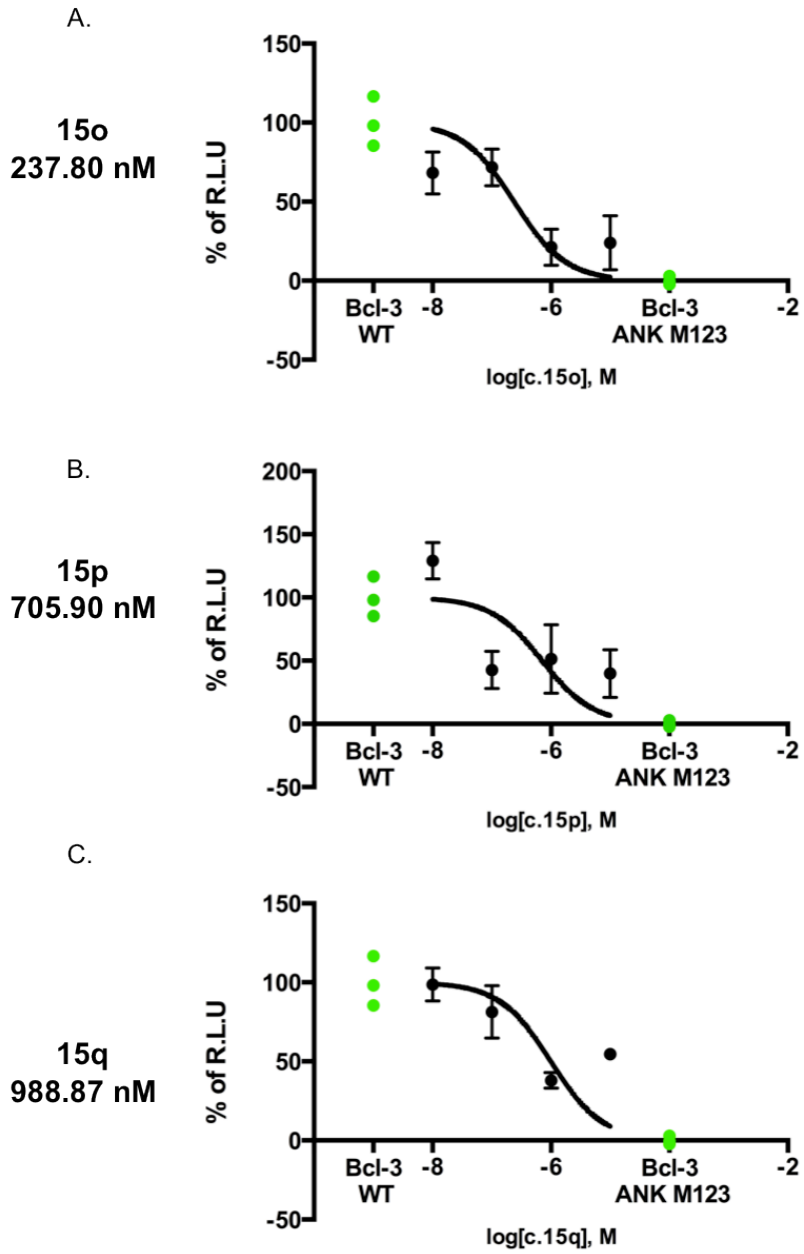

Figure 5.14 Establishing IC_{50} of selected di- and tri- substituted analogues by NF-κB assay in MDA-MB-231 cells

MDA-MB-231 Bcl-3 WT cells were cultivated with analogues 15o (**A.**), 15p (**B.**), 15q (**C.**) or DMSO control at a range of molarities for 24hrs before being transfected with NF-κB luciferase reporter for 48hrs together with controls. NF-κB activity is represented in % of DMSO control. Error bars represent ± SEM of three independent transfections. The dose response curve was generated using GraphPad software.

5.7 Discussion

Compound 6 was selected as our lead compound after biological evaluation (Chapter 4). Novel analogues of the lead compound were designed and aimed to explore structure-activity relationship. We have introduced three types of changes, giving rise to three series of analogues.

Molecular modelling is a very useful tool to distinguish between active and non-active compounds, however it is not suitable for predicting activity at low µM concentration. Based on the activity we observed with the lead compound, we predicted that newly designed analogues would have similar low µM activity. Therefore when designing novel analogues we have chosen a systematic approach of chemical modification rather than an approach based on molecular modelling.

Series 1 introduced mono substitution of F, OCH_3 and NO_2 on every position on the phenyl ring. Di- and tri- substitutions of F and OCH_3 were also introduced. Series 2 aimed to explore the effect of lengthening the linker chain, and the effect of replacing the morpholine ring with other heterocycles. However, based on the protein-ligand interactions observed for the lead compound in the binding pocket, we predicted that the amino group on the morpholine ring is an important moiety for interactions and its replacement would decrease the activity. Series 3 aimed to explore whether substitution on the benzamide ring would affect the activity.

An efficient two-step synthetic route has been developed under mild conditions. Final compounds were obtained by recrystalization from ethanol and the high purity was confirmed by elemental analysis. The importance of an efficient and cost-effective synthetic method will be fully appreciated when synthesising many novel analogues in the future.

5.7.1 Characterisation of the lead compound

Firstly we wanted to further characterise the lead compound. The toxicity was established in non-tumorigenic MCF-10A breast cancer cell line, in HER2+ SKBR3 and in triple negative MDA-MB-231 breast cancer cell lines. The lead compound was not toxic in any of the cell lines tested, however we observed lower cell viability in the SKBR3 cell line as compared to MDA-MB-231 and MCF-10A cells

(Figure 5.3), which might reflect differences in cell viability observed in these cell lines when Bcl-3 was suppressed by siRNA (Chapter 3).

The IC_{50} of the lead compound was determined using previously described cell based assays (Indirect Sandwich ELISA, NF-κB luciferase reporter assay, cell migration assay) and was in the nM range in all three assays (Figure 5.4, Figure 5.5, Figure 5.6).

In order to increase the solubility of the lead compound in aqueous solution, the synthesis of hydrochloride salt was successfully attempted using hydrochloride acid in methanol. The full experimental procedure is described in Chapter 6, section 6.5. The obtained salt had improved solubility in water and methanol (Table 5.1B), however was not soluble (< 0.1 g/100 ml) in Phosphate Buffered Saline (PBS). Therefore the solubility of the lead compound would have to be improved in order to continue with *in vivo* evaluation, either via synthesis of a different type of salt or by an introduction of novel substituent(s).

5.7.2 Biological evaluation of mono-substituted analogues

Newly designed and synthesised analogues were biologically evaluated in cell based assays similarly to the first round of selection of the 10 purchased compounds.

Firstly we determined the toxicity in both cell lines, HEK-293 and MDA-MB-231 and similarly, even at concentration of 10 μM, selected compounds did not decrease cell viability below 70% in either of the cell lines used (Figure 5.7).

The effect of novel analogues on NF-κB activity was established at 1 μM concentration in MDA-MB-231 cells and compared to the original compound 6 (Figure 5.8). Next we determined IC_{50} using Indirect Sandwich ELISA assay, NF-κB reporter assay and cell migration assay for 4 selected analogues, 15f from series 1, 17a and 17c from series 2 and 20a from series 3.

The comparison of IC_{50} values for five selected mono substituted analogues is shown in Table 5.2. Briefly, the activity of analogue from series 1, 15f, showed an improved IC_{50} in all three cell based assays. These findings suggested that replacement of the fluoro substituent with an electron-donating group on the benzoyl ring, such as 3-methoxy (15f) might further improve the activity of the lead compound.

On the other hand, elongation of a linker chain or replacement of the morpholine ring with other heterocycles caused decreased activity in all three assays as represented by analogues from series 2, 17a and 17c.

Substitution on the anthranilic acid ring as represented by analogues from series 3, did not improve the activity, however the activity was not decreased to such a level as in the case of analogues from series 2.

The replacement of a fluoro group with a methoxy group not only increased the efficacy, but also solubility of this analogue. However, the toxicity in MDA-MB-231 cells was increased from EC_{50} 2.70 mM (15a) to EC_{50} 781.3 µM (15f). The increase in toxicity could reflect the increase in efficacy, as we previously demonstrated that suppression of Bcl-3 by siRNA in MDA-MB-231 decreases cell viability. The toxicity in a non-tumorigenic cell line, such as MCF-10A, should be established and compared to a toxicity in a tumorigenic cell line(s).

5.7.3 Biological evaluation of di- and tri- substituted analogues

Di- and tri- substituted analogues from series 1 (15l-q) were firstly evaluated for cell toxicity. Compounds were well tolerated in both cell lines and cell viability was above 90% even at 10 µM concentration.

Next the effect of novel analogues on NF-κB activity was established at 1 µM concentration in MDA-MB-231 cells and compared to the original compound 6 (Figure 5.13). However, the di- or tri- substituted analogues did not improve the suppression of NF-κB activity as compared to the original lead compound.

IC_{50} values were established for three selected analogues (15o-q). All three tested analogues showed decreased ability to suppress NF-κB activity than the lead compound 6 (15a) and the comparison of IC_{50} values is shown in Table 5.2.

A.

	ELISA	NF-κB	Motility
15a	447.00 nM	45.43 nM	310.4 nM
15f	60.17 nM	6.97 nM	28.93 nM
17a	76.25 μM	2.50 μM	1.33 μM
17c	10.41 μM	2.49 μM	3.65 μM
20a	119.5 nM	1.07 μM	0.90 μM

B.

Analogue	NF-κB assay
15o	237.80 μM
15p	705.90 μM
15q	988.87 μM

Table 5.2 Comparison of novel analogues

A. The IC_{50} was measured for selected mono-substituted analogues by Indirect Sandwich ELISA assay, NF-κB assay and Cell motility assay. **B.** The IC_{50} was measured for di- and tri-substituted analogues by NF-κB assay.

Chapter 6

Experimental chemistry

6. Experimental chemistry

6.1 General information

All chemicals used in this investigation were obtained from commercial suppliers (Sigma Aldrich) and were used without further purification. All glassware were washed and dried before each experiment. Solvents were evaporated using the Buchi Rotavapor. Melting points were measured on a Griffin apparatus using a capillary method.

The ^{1}H, ^{13}C NMR spectra were recorded on a Bruker AVANCE 500 spectrometer at 500 and 126 MHz respectively, at 25°C. Chemical shifts (δ) are reported in parts per million (ppm). J values are reported in Hertz (Hz). Dimethyl sulfoxide (DMSO) was used as a solvent. Used abbreviations include s (singlet), d (doublet), t (triplet), q (quadruplet), m (multiplet), dd (doublet of doublets), dt (doublet of triplets), td (triplet of doublets).

TLC was performed using Merck TLC silica gel 60 plates F_{254} (40-60 μM) with detection by UV light (254-366 nm).

Mass spectrometry was run using electron ionisation (EI) and electrospray (ES) on a Waters GCT Premier or a Waters LCT Premier XE, respectively. The mass spectrometry was performed as a service by School of Chemistry, Cardiff University. Elemental analysis (CHN) microanalysis was performed as a service by MEDAC Ltd, Surrey. High resolution mass spectrometry was performed on LTQ Orkitrap XL by the EPSRC National Mass Spectrometry Service (Swansea, UK).

6.2 Synthesis of series 1

The series 1 of analogues was synthesised following the method outlined in Scheme 6.1.

6.2.1 General method for the first step

In the first step, anthranilic acid **11** was dissolved in pyridine (5 ml) and 2.2 equivalent of substituted benzoyl chlorides **12a-k** and stirred at r.t. The reaction was monitored by TLC and stopped after approximately an hour after complete disappearance of the anthranilic acid **11**. The reaction mixture was poured into 10% solution of sodium carbonate (3 g sodium carbonate, 27 ml distilled water). The formed precipitate was collected by filtration under reduced pressure as intermediate **13a-k**.

6.2.2 General method for the second step

In the second step, to a stirred solution of intermediates **13a-k** in DMF (10 ml) were added 2 equivalents of DIPEA and 2.2 equivalents of 2-morpholinoethanamine **14**. The reaction mixture was stirred at r.t overnight. The complete disappearance of starting materials (**13a-k**) was monitored by TLC. The reaction mixture was dissolved in DCM and washed three times with water. The product was evaporated under reduced pressure and the obtained solid was recrystallized from ethanol.

All synthesised compounds were analysed by ^{1}H, ^{13}C NMR spectra and mass spectrometry. The purity of final compounds was also confirmed by elemental analysis.

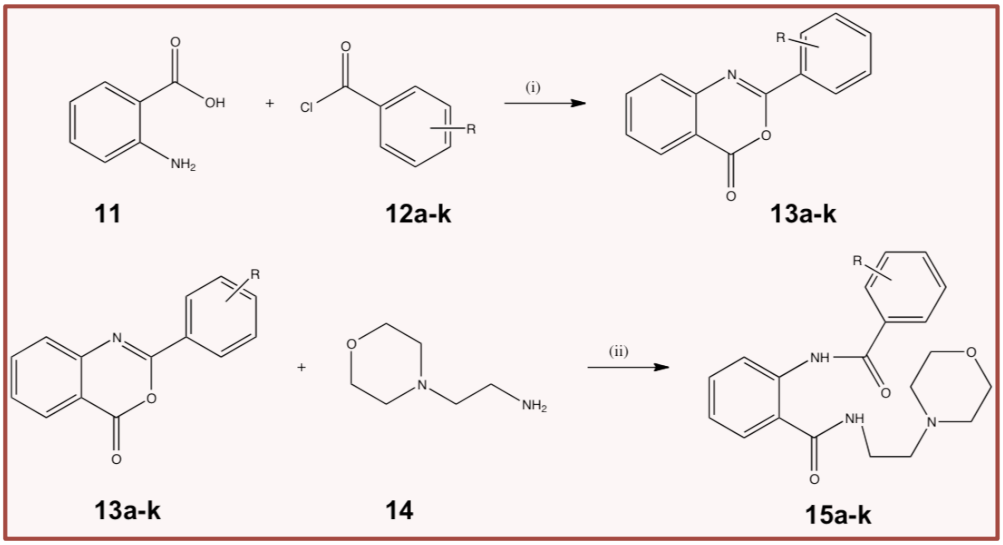

Reagents and conditions: (i) pyridine, room temperature, 1 h; (ii) iPr2EtNH, DMF, room temperature, 16hrs.

12, 13, 15a: R= 2-F
12, 13, 15b: R= 3-F
12, 13, 15c: R= 4-F
12, 13, 15d: R= 2-OCH_3
12, 13, 15e: R= 3-OCH_3
12, 13, 15f: R= 4-OCH_3
12, 13, 15g: R= 2-NO_2
12, 13, 15h: R= 3-NO_2
12, 13, 15i: R= 4-NO_2
12, 13, 15j: R= 2-CH_3
12, 13, 15k: R= H
12,13,15l: = 3,4-OCH_3
12,13,15m: R= 3,5-OCH_3
12,13,15n: R= 3,4,5-OCH_3
12,13,15o: R= 3,5-F
12,13,15p: R= 2,6-F
12,13,15q: R= 2,4-F

Scheme 6.1 Synthesis of series 1

6.2.3 Synthesis of 2-(2-fluorophenyl)-4*H*-3,1-benzoxazin-4-one (**13 a**)

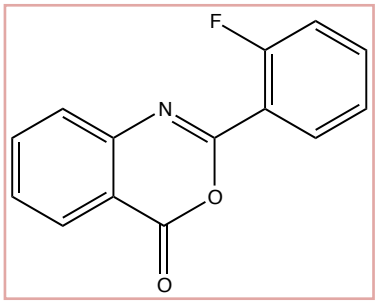

Chemical Formula: $C_{14}H_8FNO_2$

Molecular Weight: 241.22

The synthetic procedure followed the general method in section 6.2.1 using anthranilic acid **11** (0.50 g, 3.65 mmol) dissolved in pyridine (5 ml) and 2.2 equivalent of 2-fluorobenzoyl chloride **12a** (0.96 ml, 8.02 mmol). Collected as a white solid, yield 85% (0.75 g), mp 97°C.

^{1}H NMR (500 MHz, DMSO-d_6) δ 8.18 (dd, *J* = 8.0, 1.5 Hz, 1H, ArH), 8.10 (td, *J* = 7.8, 1.8 Hz, 1H, ArH), 7.98 (td, *J* = 9.1, 2.2 Hz, 1H, ArH), 7.74 (d, J = 7.9 Hz, 1H, ArH), 7.68 (td, *J* = 7.6, 1.2 Hz, 2H, ArH), 7.47 – 7.40 (m, 2H, ArH).

^{13}C NMR (126 MHz, DMSO-d_6) δ 160.48 (d, J_{C-F} = 258.3 Hz, ArC-F), 158.66 (ArC=O), 154.23 (ArC), 146.03 (ArC), 136.88 (ArCH), 134.52 (d, J_{C-F} = 8.8 Hz, ArCH), 131.10 (ArCH), 129.02 (ArCH), 127.98 (ArCH), 127.03 (ArCH), 124.83 (d, J_{C-F} = 3.8 Hz, ArCH), 118.66 (d, J_{C-F} = 10.1 Hz, ArC), 117.21 (d, J_{C-F} = 21.4 Hz, ArCH), 116.92 (ArC).

MS (APCI^{+}): 242.05 [M+1].

6.2.4 Synthesis of 2-(3-fluorophenyl)-4*H*-3,1-benzoxazin-4-one (**13b**)

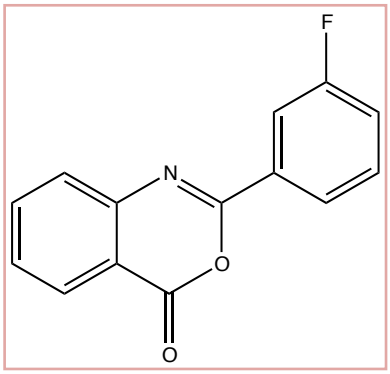

Chemical Formula: $C_{14}H_8FNO_2$

Molecular Weight: 241.22

The synthetic procedure followed the general method in section 6.2.1 using anthranilic acid **11** (0.50 g, 3.65 mmol) dissolved in pyridine (5 ml) and 2.2 equivalent of 3-fluorobenzoyl chloride **12b** (0.98 ml, 8.02 mmol). Collected as a white solid, yield 80% (0.71 g), mp 96°C.

^{1}H NMR (500 MHz, DMSO-d_6) δ 8.48 (d, *J* = 8.3 Hz, 1H, ArH), 8.17 (d, *J* = 7.9 Hz, 1H, ArH), 8.06 – 7.93 (m, 2H, ArH), 7.87 (d, J = 10.4 Hz, 1H, ArH), 7.81 (d, J = 10.1 Hz, 1H, ArH), 7.77 – 7.48 (m, 1H, ArH), 7.27 (t, *J* = 7.7 Hz, 1H, ArH).

^{13}C NMR (126 MHz, DMSO-d_6) δ 162.17 (d, $J_{C\text{-}F}$ = 245.7 Hz, ArC-F), 158.56 (ArC=O), 145.93 (ArC), 139.71 (ArC), 136.89 (ArCH), 134.20 (ArCH), 131.28 (d, $J_{C\text{-}F}$ = 8.2 Hz, ArCH), 130.64 (ArCH), 128.90 (ArCH), 127.00 (ArCH), 123.69 (d, $J_{C\text{-}F}$ = 2.8 Hz, ArCH), 121.14 (ArC), 119.35 (d, $J_{C\text{-}F}$ = 88.2 Hz, ArCH), 117.37 (d, $J_{C\text{-}F}$ = 85.7 Hz, ArC).

MS (APCI^{+}): 242.06 [M+1].

6.2.5 Synthesis of 2-(4-fluorophenyl)-4*H*-3,1-benzoxazin-4-one (**13c**)

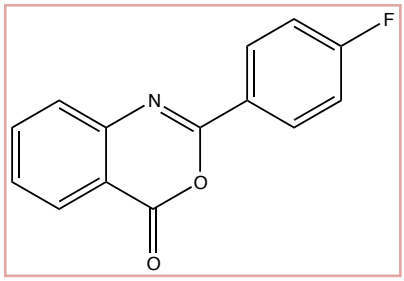

Chemical Formula: $C_{14}H_8FNO_2$

Molecular Weight: 241.22

The synthetic procedure followed the general method in section 6.2.1 using anthranilic acid **11** (0.50 g, 3.65 mmol) dissolved in pyridine (5 ml) and 2.2 equivalent of 4-fluorobenzoyl chloride **12c** (0.95 ml, 8.02 mmol). Collected as a white solid, yield 91% (0.80 g), mp 159°C.

^{1}H NMR (500 MHz, DMSO-d_6) δ 8.26 (td, J = 14.1, 5.4 Hz, 2H, ArH), 8.16 (dd, *J* = 8.0, 1.5 Hz, 1H, ArH), 7.96 (t, J = 15.8 Hz, 1H, ArH), 7.72 (d, *J* = 8.1 Hz, 1H, ArH), 7.63 (td, *J* = 7.6, 1.2 Hz, 1H, ArH), 7.48 – 7.40 (m, 2H, ArH).

^{13}C NMR (126 MHz, DMSO-d_6) δ 164.74 (d, J_{C-F} = 251.4 Hz, ArC-F), 158.72 (ArC=O), 155.58 (ArC), 146.18 (ArC), 136.87 (ArCH), 130.53 (d, J_{C-F} = 9.4 Hz, ArCH), 128.57 (ArCH), 128.05 (ArCH), 126.83 (d, J_{C-F} = 3.8 Hz, ArCH), 126.61 (ArC), 116.81 (ArC), 116.17 (d, J_{C-F} = 22.3 Hz, ArCH).

MS (APCI$^+$): 242.06 [M+1].

6.2.6 Synthesis of 2-(2-methoxyphenyl)-4*H*-3,1-benzoxazin-4-one (**13d**)

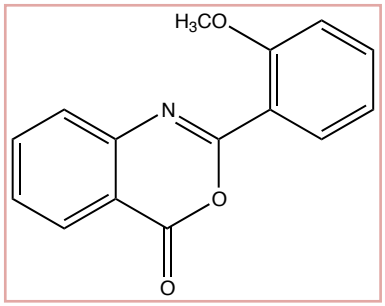

Chemical Formula: $C_{15}H_{11}NO_3$

Molecular Weight: 253.25

The synthetic procedure followed the general method in section 6.2.1 using anthranilic acid **11** (0.50 g, 3.65 mmol) dissolved in dry pyridine (5 ml) under anhydrous conditions in nitrogen atmosphere and 2.2 equivalent of 2-methoxybenzoyl chloride **12d** (1.19 ml, 8.02 mmol). Collected as a white solid, yield 98% (0.91 g), mp 107°C.

^{1}H NMR (500 MHz, DMSO-d_6) δ 8.17 (dd, *J* = 7.9, 1.6 Hz, 1H, ArH), 7.97 (td, 16.0, 1.1 Hz, 1H, ArH), 7.78 (dd, *J* = 7.7, 1.8 Hz, 1H, ArH), 7.71 (d, 7.9 Hz, 1H, ArH), 7.66 (td, *J* = 7.6, 1.2 Hz, 1H, ArH), 7.60 (td, *J* = 8.8, 1.8 Hz, 1H, ArH), 7.24 (d, *J* = 8.4 Hz, 1H, ArH), 7.12 (t, *J* = 7.5 Hz, 1H, ArH), 3.88 (s, 3H, OCH_3).

^{13}C NMR (126 MHz, DMSO-d_6) δ 159.15 (ArC=O), 157.89 (ArC), 157.16 (ArC), 146.31 (ArC), 136.88 (ArCH), 133.24 (ArCH), 130.97 (ArCH), 128.81 (ArCH), 127.90 (ArCH), 126.89 (ArCH), 120.36 (ArCH), 120.27 (ArC), 116.53 (ArC), 112.56 (ArCH), 55.66 (OCH_3).

MS (APCI$^+$): 254.07 [M+1].

6.2.7 Synthesis of 2-(3-methoxyphenyl)-4*H*-3,1-benzoxazin-4-one (**13e**)

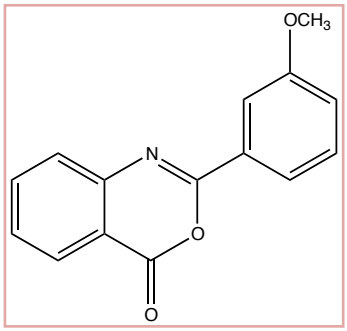

Chemical Formula: $C_{15}H_{11}NO_3$

Molecular Weight: 253.25

The synthetic procedure followed the general method in section 6.2.1 using anthranilic acid **11** (0.50 g, 3.65 mmol) dissolved in dry pyridine (5 ml) under anhydrous conditions in nitrogen atmosphere and 2.2 equivalent of 3-methoxybenzoyl chloride **12e** (1.13 ml, 8.02 mmol). Collected as a white solid, yield 97% (0.90 g), mp 103°C.

^{1}H NMR (500 MHz, DMSO-d_6) δ 8.14 (dd, *J* = 7.9, 1.5 Hz, 1H, ArH), 7.94 (t, J = 7.9 Hz, 1H, ArH), 7.76 (d, *J* = 7.7, Hz, 1H, ArH), 7.71 (d, *J* = 8.1 Hz, 1H, ArH), 7.66 – 7.58 (m, 2H, ArH), 7.50 (t, *J* = 8.0 Hz, 1H, ArH), 7.21 (dd, *J* = 8.4, 2.6 Hz, 1H, ArH), 3.85 (s, 3H, OCH_3).

^{13}C NMR (126 MHz, DMSO-d_6) δ 159.42 (ArC=O), 158.79 (ArC), 156.10 (ArC), 146.09 (ArC), 136.86 (ArCH), 131.27 (ArC), 130.16 (ArCH), 128.64 (ArCH), 128.01 (ArCH), 126.90 (ArCH), 120.15 (ArCH), 118.72 (ArCH), 116.79 (ArC), 112.36 (ArCH), 55.35 (OCH_3).

MS (APCI$^+$): 254.07 [M+1].

6.2.8 Synthesis of 2-(4-methoxyphenyl)-4*H*-3,1-benzoxazin-4-one (**13f**)

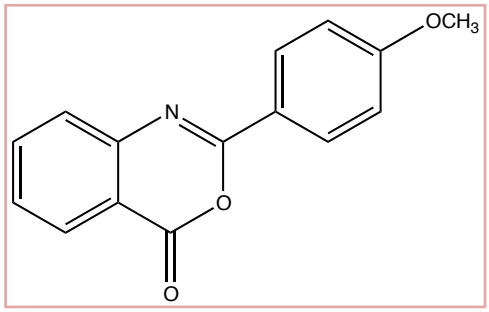

Chemical Formula: $C_{15}H_{11}NO_3$

Molecular Weight: 253.25

The synthetic procedure followed the general method in section 6.2.1 using anthranilic acid **11** (0.50 g, 3.65 mmol) dissolved in dry pyridine (5 ml) under anhydrous conditions in nitrogen atmosphere and 2.2 equivalent of 4-methoxybenzoyl chloride **12f** (1.09 ml, 8.02 mmol). Collected as a white solid, yield 71% (0.66 g), mp 121°C.

^{1}H NMR (500 MHz, DMSO-d_6) δ 8.14 (td, J = 17.8, 1.8 Hz, 3H, ArH), 7.93 (td, *J* = 8.5, 1.6 Hz, 1H, ArH), 7.68 (d, J = 7.9 Hz, 1H, ArH), 7.59 (td, *J* = 7.4, 1.2 Hz, 1H, ArH), 7.14 (d, J = 9.0 Hz, 2H, ArH), 3.88 (s, 3H, OCH_3).

^{13}C NMR (126 MHz, DMSO-d_6) δ 162.88 (ArC=O), 158.95 (ArC), 156.39 (ArC), 146.59 (ArC), 136.80 (ArCH), 132.66 (ArCH), 129.80 (ArCH), 126.61 (ArCH), 122.10 (ArCH), 120.18 (ArC), 116.55 (ArC), 114.45 (ArCH), 55.56 (OCH_3).

MS ($APCI^+$): 254.08 [M+1].

6.2.9 Synthesis of 2-(2-nitrophenyl)-4*H*-3,1-benzoxazin-4-one (**13g**)

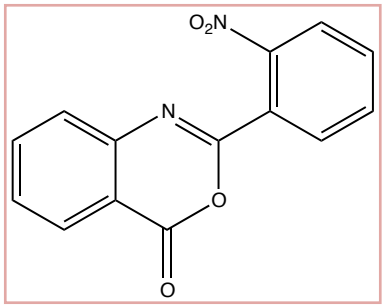

Chemical Formula: $C_{14}H_8N_2O_4$

Molecular Weight: 268.22

The synthetic procedure followed the general method in section 6.2.1 using anthranilic acid **11** (0.50 g, 3.65 mmol) dissolved in pyridine (5 ml) and 2.2 equivalent of 2-nitrobenzoyl chloride **12g** (1.06 ml, 8.02 mmol). Collected as a yellow solid, yield 77% (0.75 g), mp 169°C.

^{1}H NMR (500 MHz, DMSO-d_6) δ 8.22 (dd, *J* = 7.8, 1.5 Hz, 1H, ArH), 8.17 (dd, *J* = 8.0, 1.3 Hz, 1H, ArH), 8.10 (dd, *J* = 7.6, 1.5 Hz, 1H, ArH), 8.02 (td, *J* = 7.7, 1.6 Hz, 1H, ArH), 7.96 (td, *J* = 7.6, 1.3 Hz, 1H, ArH), 7.91 (td, *J* = 7.8, 1.6 Hz, 1H, ArH), 7.76 – 7.69 (m, 2H, ArH).

^{13}C NMR (126 MHz, DMSO-d_6) δ 158.20 (ArC=O), 154.50 (ArC), 148.15 (ArC), 145.58 (ArC), 137.26 (ArCH), 133.60 (ArCH), 132.97 (ArCH), 131.16 (ArCH), 129.61 (ArCH), 128.22 (ArCH), 127.04 (ArCH), 124.98 (ArC), 124.57 (ArCH), 116.68 (ArC).

MS (APCI$^+$): 269.05 [M+1].

6.2.10 Synthesis of 2-(3-nitrophenyl)-4*H*-3,1-benzoxazin-4-one (**13h**)

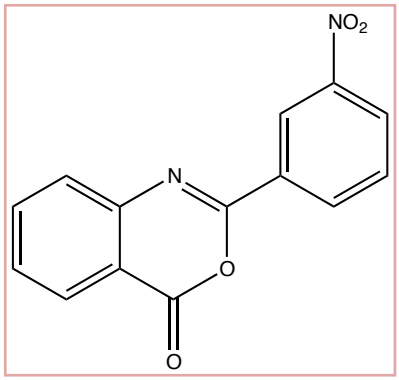

Chemical Formula: $C_{14}H_8N_2O_4$

Molecular Weight: 268.22

The synthetic procedure followed the general method in section 6.2.1 using anthranilic acid **11** (0.50 g, 3.65 mmol) dissolved in pyridine (5 ml) and 2.2 equivalent of 3-nitrobenzoyl chloride **12h** (1.06 ml, 8.02 mmol). Collected as a yellow solid, yield 96% (0.94 g), mp 115°C.

^{1}H NMR (500 MHz, DMSO-d_6) δ 8.74 (t, *J* = 2.0 Hz, 1H, ArH), 8.48 (dd, *J* = 8.3, 1.1 Hz, 1H, ArH), 8.37 (dd, *J* = 8.5, 1.3 Hz, 2H, ArH), 7.99 (dd, *J* = 7.9, 1.6 Hz, 1H, ArH), 7.91 (t, *J* = 8.0 Hz, 1H, ArH), 7.70 (td, *J* = 8.5, 1.7 Hz, 1H, ArH), 7.30 (td, *J* = 7.6, 1.3 Hz, 1H, ArH).

^{13}C NMR (126 MHz, DMSO-d_6) δ 167.70 (ArC=O), 162.76 (ArC), 148.00 (ArC), 139.20 (ArC), 135.84 (ArC), 133.98 (ArCH), 133.23 (ArCH), 130.69 (ArCH), 126.53 (ArCH, 124.09 (ArCH), 122.02 (ArCH), 118.95 (ArC).

MS (APCI$^+$): 269.06 [M+1].

6.2.11 Synthesis of 2-(4-nitrophenyl)-4*H*-3,1-benzoxazin-4-one (**13i**)

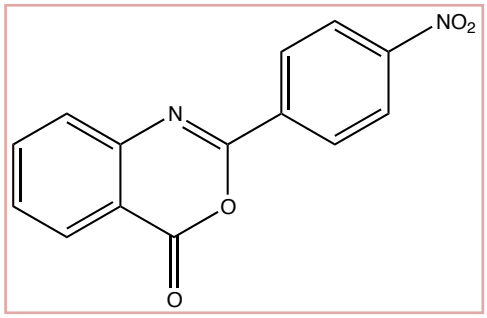

Chemical Formula: $C_{14}H_8N_2O_4$

Molecular Weight: 268.22

The synthetic procedure followed the general method in section 6.2.1 using anthranilic acid **11** (0.50 g, 3.65 mmol) dissolved in pyridine (5 ml) and 2.2 equivalent of 4-nitrobenzoyl chloride **12i** (1.49 g, 8.02 mmol). Collected as a yellow solid, yield 96% (0.94 g), mp 169°C.

^{1}H NMR (500 MHz, DMSO-d_6) δ 8.19 (t, *J* = 7.8 Hz, 2H, ArH), 8.00 (t, *J* = 7.8 Hz, 2H, ArH), 7.79 (d, *J* = 8.1 Hz, 2H, ArH), 7.69 (t, *J* = 7.6 Hz, 2H, ArH).

^{13}C NMR (126 MHz, DMSO-d_6) δ 158.43 (ArC=O), 154.74 (ArC), 149.62 (ArC), 145.77 (ArC), 136.98 (ArCH), 135.81 (ArC), 129.37 (ArCH), 129.13 (ArCH), 128.13 (ArCH), 127.24 (ArCH), 124.08 (ArCH), 117.20 (ArC).

MS (APCI$^+$): 269.08 [M+1].

6.2.12 Synthesis of 2-(*o*-tolyl)-4*H*-3,1-benzoxazin-4-one (**13j**)

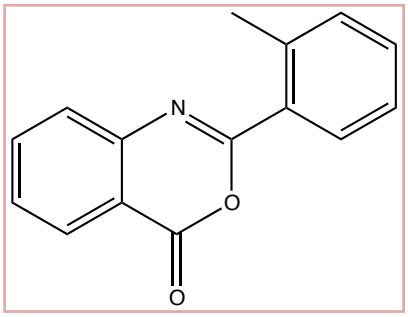

Chemical Formula: $C_{15}H_{11}NO_2$

Molecular Weight: 237.25

The synthetic procedure followed the general method in section 6.2.1 using anthranilic acid **11** (0.50 g, 3.65 mmol) dissolved in pyridine (5 ml) and 2.2 equivalent of 2-methyl benzoyl chloride **12j** (1.05 ml, 8.02 mmol). Collected as a yellow solid, yield 99% (0.86 g), mp 102°C.

^{1}H NMR (500 MHz, DMSO-d_6) δ 8.17 (d, *J* = 8.0 Hz, 1H, ArH), 7.99 – 7.90 (m, 2H, ArH), 7.71 (d, *J* = 8.1 Hz, 1H, ArH), 7.65 (t, *J* = 7.6 Hz, 1H, ArH), 7.51 (t, *J* = 7.5 Hz, 1H, ArH), 7.40 (t, *J* = 6.9 Hz, 2H, ArH), 2.66 (s, 3H, CH_3).

^{13}C NMR (126 MHz, DMSO-d_6) δ 159.07 (ArC=O), 157.59 (ArC), 146.17 (ArC), 138.32 (ArC), 136.74 (ArCH), 131.69 (ArCH), 131.48 (ArCH), 129.88 (ArC), 129.79 (ArCH), 128.69 (ArCH), 127.84 (ArCH), 126.93 (ArCH), 126.07 (ArCH), 116.68 (ArC), 21.31 (CH_3).

MS (APCI$^+$): 238.07 [M+1].

6.2.13 Synthesis of 2-phenyl-4*H*-3,1-benzoxazin-4-one (**13k**)

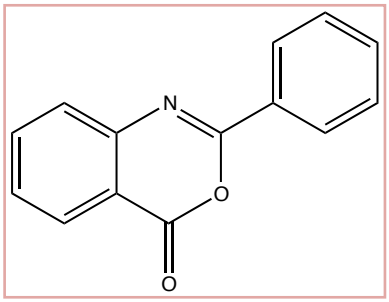

Chemical Formula: $C_{14}H_9NO_2$

Molecular Weight: 223.23

The synthetic procedure followed the general method in section 6.2.1 using anthranilic acid **11** (0.50 g, 3.65 mmol) dissolved in pyridine (5 ml) and 2.2 equivalent of benzoyl chloride **12k** (0.93 ml, 8.02 mmol). Collected as a yellow solid, yield 95% (0.77 g), mp 91°C.

^{1}H NMR (500 MHz, DMSO-d_6) δ 8.22 (dd, *J* = 7.3, 1.7 Hz, 1H, ArH), 8.03 (dd, *J* = 7.9, 1.6 Hz, 1H, ArH), 7.98 (dd, 8.1, 1.6 Hz, 2H, ArH), 7.72 – 7.64 (m, 2H, ArH), 7.62 (dd, *J* = 8.1, 6.6 Hz, 3H, ArH).

^{13}C NMR (126 MHz, DMSO-d_6) δ 168.04 (ArC=O), 164.76 (ArC), 140.25 (ArC), 136.87 (ArCH), 134.33 (ArCH), 132.19 (ArCH), 130.69 (ArCH), 129.00 (ArCH), 127.03 (ArCH), 123.34 (ArCH), 120.75 (ArCH), 116.99 (ArC).

MS (APCI$^+$): 224.08 [M+1].

6.2.14 2-(3,4-dimethoxyphenyl)-4*H*-3,1-benzoxazin-4-one (**13l**)

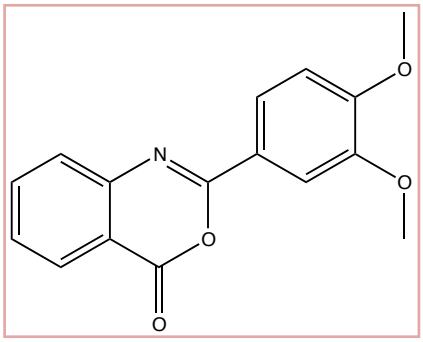

Chemical Formula: $C_{16}H_{13}NO_4$

Molecular Weight: 283.28

The synthetic procedure followed the general method in section 6.2.1 using anthranilic acid **11** (0.50 g, 3.65 mmol) dissolved in pyridine (5 ml) and 2.2 equivalent of benzoyl chloride **12l** (1.61 g, 8.02 mmol). Collected as a white solid, yield 83% (0.86 g), mp 166°C.

^{1}H NMR (500 MHz, DMSO-d_6) δ 8.15 (dd, J = 7.8, 1.6 Hz, 1H, ArH), 7.94 (td, J = 8.4, 1.6 Hz, 1H, ArH), 7.83 (dd, J = 8.5, 2.1 Hz, 1H, ArH) 7.71 (dd, J = 6.8, 1.7 Hz, 2H, ArH), 7.60 (td, J = 8.3, 1.1 Hz, 1H, ArH), 7.18 (d, J = 8.6 Hz, 1H, ArH), 3.89 (d, J = 4.7 Hz, 6H, OCH_3).

^{13}C NMR (126 MHz, DMSO-d_6) δ 159.35 (ArC=O), 158.95 (ArC), 152.82 (ArC), 148.79 (ArC), 146.56 (ArC), 136.84 (ArCH), 128.09 (ArCH), 126.65 (ArCH), 122.07 (ArC), 121.86 (ArCH), 116.65 (ArC), 111.56 (ArCH), 110.19 (ArCH), 55.77 (OCH_3), 55.63 (OCH_3).

MS (EI^+): 283.1.

6.2.15 2-(3,5-dimethoxyphenyl)-4*H*-3,1-benzoxazin-4-one (**13m**)

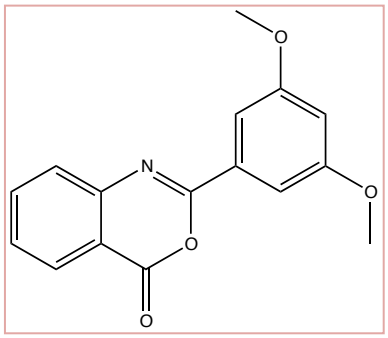

Chemical Formula: $C_{16}H_{13}NO_4$

Molecular Weight: 283.28

The synthetic procedure followed the general method in section 6.2.1 using anthranilic acid **11** (0.50 g, 3.65 mmol) dissolved in pyridine (5 ml) and 2.2 equivalent of benzoyl chloride **12m** (1.61 g, 8.02 mmol). Collected as a white solid, yield 93% (0.97 g), mp 165°C.

^{1}H NMR (500 MHz, DMSO-d_6) δ 8.71 (dd, J = 7.8, 1.6 Hz, 1H, ArH), 7.97 (t, J = 7.6 Hz, 1H, ArH), 7.75 (dd, J = 8.0, 2.1 Hz, 1H, ArH), 7.65 (t, J = 7.6 Hz, 1H, ArH), 7.31 (d, J = 2.5 Hz, 2H, ArH), 6.81 (d, J = 2.3 Hz, 1H, ArH), 3.86 (s, 6H, OCH_3)

^{13}C NMR (126 MHz, DMSO-d_6) δ 160.72 (ArC=O), 158.76 (ArC), 152.82 (ArC), 146.11 (ArC), 145.80 (ArC), 136.84 (ArCH), 132.01 (ArC), 131.55 (ArCH), 128.73 (ArCH), 128.08 (ArCH), 126.99 (ArCH), 116.96 (ArC), 105.49 (ArCH), 104.83 (ArCH), 55.59 (OCH_3).

MS (EI^+): 283.1.

6.2.16 2-(3,4,5-trimethoxyphenyl)-4*H*-3,1-benzoxazin-4-one (**13n**)

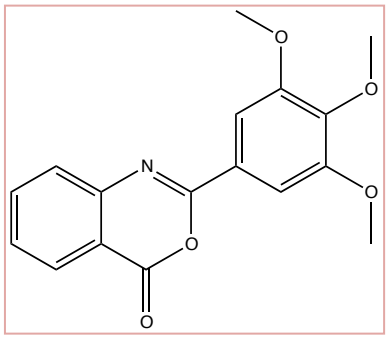

Chemical Formula: $C_{17}H_{15}NO_5$

Molecular Weight: 313.30

The synthetic procedure followed the general method in section 6.2.1 using anthranilic acid **11** (0.50 g, 3.65 mmol) dissolved in pyridine (5 ml) and 2.2 equivalent of benzoyl chloride **12n** (1.85 g, 8.02 mmol). Collected as a white solid, yield 91% (1.04 g), mp 165°C.

^{1}H NMR (500 MHz, DMSO-d_6) δ 8.17 (dd, J=9.3, 1.8 Hz, 1H, ArH), 7.98-7.94 (m, 1H, ArH), 7.75 (d, J=2.9 Hz, 1H, ArH), 7.63 (td, J=15.7, 1.2 Hz, 1H, ArH), 7.49 (s, 2H, ArH), 3.92 (s, 6H, OCH_3), 3.80 (s, 3H, OCH_3).

^{13}C NMR (126 MHz, Chloroform) δ 159.61 (ArC=O), 156.82 (ArC), 153.34 (ArC), 147.07 (ArC), 142.21 (ArC), 136.58 (ArCH), 128.64 (ArCH), 128.09 (ArCH), 127.09 (ArCH), 125.23 (ArC), 116.78 (ArC), 105.60 (ArCH), 61.01 (OCH_3), 56.42 (OCH_3).

MS (EI^+): 313.1.

6.2.17 2-(3,5-difluorophenyl)-4*H*-3,1-benzoxazin-4-one (**13o**)

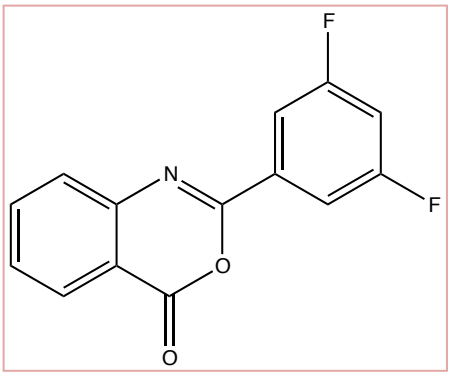

Chemical Formula: $C_{14}H_7F_2NO_2$

Molecular Weight: 259.21

The synthetic procedure followed the general method in section 6.2.1 using anthranilic acid **11** (0.50 g, 3.65 mmol) dissolved in pyridine (5 ml) and 2.2 equivalent of benzoyl chloride **12o** (0.95 ml, 8.02 mmol). Collected as a white solid, yield 94% (0.89 g), mp 122°C.

^{1}H NMR (500 MHz, Chloroform) δ 8.28 (dd, J = 9.4, 1.6 Hz, 1H, ArH), 7.88 (m, 3H, ArH), 7.74 (dd, 8.1, 0.6 Hz, 1H, ArH), 7.60 (tt, 15.3, 1.4 Hz, 1H, ArH), 7.05 (m, 1H, ArH).

^{13}C NMR (126 MHz, Chloroform) δ 164.11 (d, $J_{C\text{-}F}$ = 10.1 Hz, ArC-F), 162.12 (d, $J_{C\text{-}F}$ = 18.1 Hz, ArC-F), 158.78 (ArC=O), 146.35 (ArC), 136.78 (ArCH), 133.75 (ArC), 128.98 (ArCH), 128.78 (ArCH), 127.49 (ArCH), 117.14 (ArC), 111.40 (d, $J_{C\text{-}F}$ = 7.7 Hz, ArCH), 111.23 (d, $J_{C\text{-}F}$ = 7.2 Hz, ArCH), 107.93 (ArCH), 105.93 (ArC).

MS (EI^{+}): 259.1.

6.2.18 2-(2,6-difluorophenyl)-4*H*-3,1-benzoxazin-4-one (**13p**)

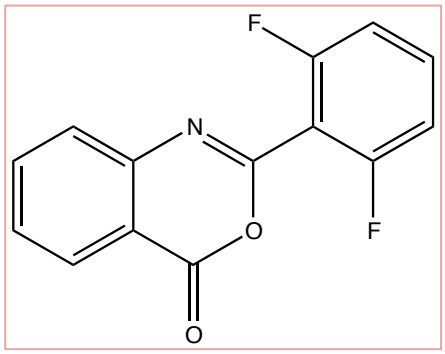

Chemical Formula: $C_{14}H_7F_2NO_2$

Molecular Weight: 259.21

The synthetic procedure followed the general method in section 6.2.1 using anthranilic acid **11** (0.50 g, 3.65 mmol) dissolved in pyridine (5 ml) and 2.2 equivalent of benzoyl chloride **12p** (1.01 ml, 8.02 mmol). Collected as a white solid, yield 97% (0.92 g), mp 119°C.

^{1}H NMR (500 MHz, Chloroform-*d*) δ 8.31 (dd, J = 7.8, 2.0 Hz, 1H, ArH), 7.92-7.88 (m, 1H, ArH), 7.76 (dd, J = 8.1, 1.7 Hz, 1H, ArH), 7.64 (td, J = 7.3, 1.2 Hz, 1H, ArH), 7.52 (tt, J = 8.5, 6.2 Hz, 1H, ArH), 7.08 (tt, J = 7.1, 4.5 Hz, 2H, ArH).

^{13}C NMR (126 MHz, DMSO-d_6) δ 161.85 (d, $J_{C\text{-}F}$ = 6.2 Hz, ArC-F), 159.75 (d, $J_{C\text{-}F}$ = 7.4 Hz, ArC-F), 158.91 (C=O), 150.95 (ArC), 146.19 (ArC), 136.68 (ArCH), 133.55 (ArC), 133.03 (t, $J_{C\text{-}F}$ = 21.1 Hz, ArCH), 129.38 (ArCH), 128.68 (ArCH), 127.49 (ArCH), 117.26 (ArC), 112.25 (d, $J_{C\text{-}F}$ = 4.2 Hz, ArCH), 112.07 (d, $J_{C\text{-}F}$ = 4.4 Hz, ArCH).

MS (EI^+): 259.1.

6.2.19 2-(2,4-difluorophenyl)-4*H*-3,1-benzoxazin-4-one (**13q**)

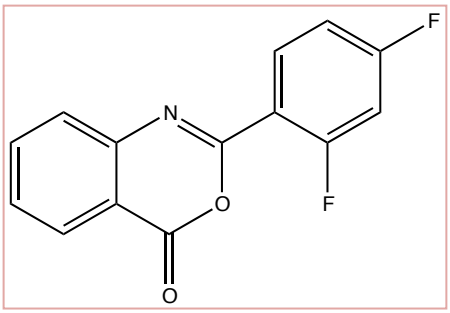

Chemical Formula: $C_{14}H_7F_2NO_2$

Molecular Weight: 259.21

The synthetic procedure followed the general method in section 6.2.1 using anthranilic acid **11** (0.50 g, 3.65 mmol) dissolved in pyridine (5 ml) and 2.2 equivalent of benzoyl chloride **12q** (0.99 ml, 8.02 mmol). Collected as a white solid, yield 81% (0.76 g), mp 102°C.

^{1}H NMR (500 MHz, Chloroform-*d*) δ 8.28 (dd, J = 7.9, 0.6 Hz, 1H, ArH), 8.20 (td, J = 8.6, 6.4 Hz, 1H, ArH), 7.91-7.84 (m, 1H, ArH), 7.73 (dd, J = 8.2, 0.6 Hz, 1Hz, ArH), 7.59 (td, J = 7.8, 1.2 Hz, 1H, ArH), 7.08 (m, 2H, ArH).

^{13}C NMR (126 MHz, DMSO-d_6) δ 164.50 (d, $J_{C\text{-}F}$ = 252.9 Hz, ArC-F), 162.20 (d, $J_{C\text{-}F}$ = 289.0 Hz, ArC-F), 158.99 (ArC=O), 146.63 (ArC), 136.68 (ArCH), 132.85 (ArCH), 128.78 (ArCH), 128.62 (ArCH), 127.48 (ArCH), 116.97 (ArC), 113.95 (ArC), 112.00 (d, $J_{C\text{-}F}$ =21.9 Hz), 107.25 (ArC), 105.63 (ArCH).

MS (EI^+): 259.0.

6.2.20 Synthesis of 2-[(2-fluorobenzoyl)amino]-N-(2-morpholin-4-ylethyl)benzamide (**15a**)

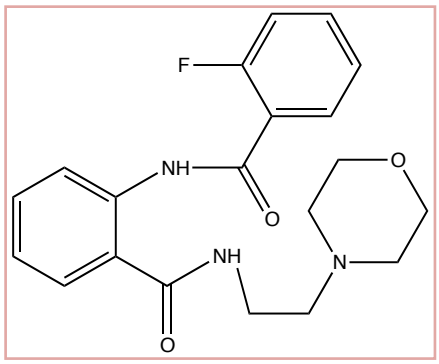

Chemical Formula: $C_{20}H_{22}FN_3O_{3c}$

Molecular Weight: 371.41

The synthetic procedure followed the general method in section 6.2.2 using 2-(2-fluorophenyl)-4*H*-3,1-benzoxazin-4-one **13a** (1.00 g, 4.15 mmol) in DMF (10 ml), 2 equivalents of DIPEA (1.19 ml, 8.29 mmol) and 2.2 equivalents of 2-morpholinoethanamine **14** (1.44 ml, 9.12 mmol). The product was recrystallized from ethanol as a white solid. Yield 47% (0.73 g), mp 131°C.

^{1}H NMR (500 MHz, DMSO-d_6) δ 12.00 (s, 1H, NH), 8.72 (s, 1H, NH), 8.57 (d, *J* = 8.3 Hz, 1H, ArH), 7.89 (td, *J* = 7.7, 1.9 Hz, 1H, ArH), 7.76 (dd, *J* = 8.0, 1.5 Hz, 1H, ArH), 7.68 – 7.64 (m, 1H, ArH), 7.57 (td, *J* = 8.6, 1.5 Hz, 1H, ArH), 7.46 – 7.35 (m, 2H, ArH), 7.24 (td, *J* = 7.6, 1.2 Hz, 1H, ArH), 3.53 (t, *J* = 4.6 Hz, 4H, CH_2), 3.40 (q, *J* = 6.4 Hz, 2H, CH_2), 2.51 (t, *J* = 6.7 Hz, 2H, CH_2), 2.47 (t, *J* = 4.7 Hz, 4H, CH_2).

^{13}C NMR (126 MHz, DMSO-d_6) δ 168.03 (C=O), 160.86 (d, J_{C-F} = 146.2 Hz, ArC-F), 158.28 (C=O), 138.32 (ArC), 133.77 (d, J_{C-F} = 8.8 Hz, ArCH), 131.83 (ArCH), 130.62 (d, J_{C-F} = 1.3 Hz, ArCH), 128.02 (ArCH), 125.04 (d, J_{C-F} = 3.8 Hz, ArCH), 123.30 (ArCH), 122.94 (d, J_{C-F} = 13.9 Hz, ArC) 121.73 (ArC), 120.96 (ArCH), 116.57 (d, J_{C-F} =22.7 Hz, ArCH), 66.15 (CH_2), 56.98 (CH_2), 53.18 (CH_2), 36.43 (CH_2).

MS (ES^+): 372.19 [M+1].

Calculated analysis for $C_{20}H_{22}FN_3O_3$ (371.41): C, 64.68; H, 5.97; N, 11.31. Found C, 64.49; H, 6.08; N, 11.29.

6.2.21 Synthesis of 2-[(3-fluorobenzoyl)amino]-N-(2-morpholin-4-ylethyl)benzamide (**15b**)

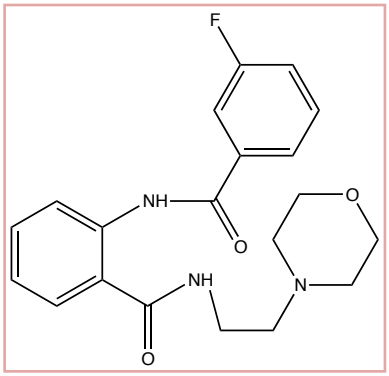

Chemical Formula: $C_{20}H_{22}FN_3O_3$

Molecular Weight: 371.41

The synthetic procedure followed the general method in section 6.2.2 using 2-(3-fluorophenyl)-4*H*-3,1-benzoxazin-4-one **13b** (0.50 g, 2.07 mmol) in DMF (5 ml), 2 equivalents of DIPEA (0.60 ml, 4.18 mmol) and 2.2 equivalents of 2-morpholinoethanamine **14** (0.30 ml, 2.27 mmol). The product was not obtained due to poor crystallization from ethanol.

6.2.22 Synthesis of 2-[(4-fluorobenzoyl)amino]-N-(2-morpholin-4-ylethyl)benzamide (**15c**)

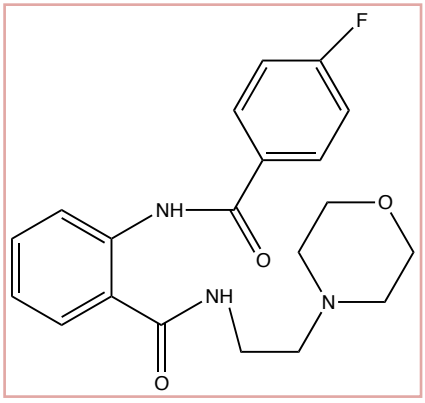

Chemical Formula: $C_{20}H_{22}FN_3O_3$

Molecular Weight: 371.41

The synthetic procedure followed the general method in section 6.2.2 using 2-(4-fluorophenyl)-4*H*-3,1-benzoxazin-4-one **13c** (0.50 g, 2.06 mmol) in DMF (8 ml), 2 equivalents of DIPEA (0.72 ml, 4.12 mmol) and 2.2 equivalents of 2-morpholinoethanamine **14** (0.60 ml, 4.54 mmol). The product was recrystallized from ethanol as a white solid. Yield 8% (0.05 g), mp 129°C.

^{1}H NMR (500 MHz, DMSO-d_6) δ 12.52 (s, 1H, NH), 8.80 (s, 1H, NH), 8.61 (d, *J* = 8.3 Hz, 1H, ArH), 8.0 (td, *J* = 14.1, 2.1 Hz, 2H, ArH), 7.83 (dd, *J* = 7.9, 1.5 Hz, 1H, ArH), 7.58 (td, *J* = 8.2, 7.8, 1.5 Hz, 1H, ArH), 7.45 (t, *J* = 17.6 Hz, 2H, ArH), 7.23 (t, *J* = 7.6, 1H, ArH), 3.55 (t, *J* = 4.6 Hz, 4H, CH_2), 3.44 (q, *J* = 6.5 Hz, 2H, CH_2), 2.51 (q, *J* = 6.3 Hz, 6H, CH_2).

^{13}C NMR (126 MHz, DMSO-d_6) δ 168.50 (C=O), 164.29 (d, $J_{C\text{-}F}$ = 253.3 Hz, ArC-F), 158.31 (C=O), 139.17 (ArC), 132.15 (ArCH), 131.05 (d, $J_{C\text{-}F}$ = 3.8 Hz, ArC), 129.61 (d, $J_{C\text{-}F}$ = 10.1 Hz, ArCH), 128.10 (ArCH), 122.94 (ArCH), 120.58 (ArC), 120.38 (ArCH), 115.98 (d, $J_{C\text{-}F}$ = 20.2 Hz, ArCH), 66.17 (CH_2), 56.96 (CH_2), 53.20 (CH_2), 36.55 (CH_2).

MS (ES^+): 372.20 [M+1].

Calculated analysis for $C_{20}H_{22}FN_3O_3$ (371.41): C, 64.62; H, 6.09; N, 11.32. Found C, 64.49; H, 6.08; N, 11.29.

6.2.23 Synthesis of 2-[(2-methoxybenzoyl)amino]-N-(2-morpholin-4-ylethyl)benzamide (**15d**)

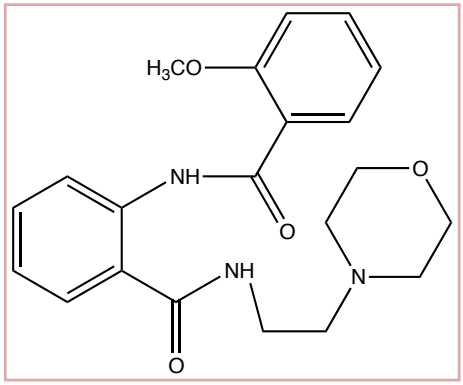

Chemical Formula: $C_{21}H_{25}N_3O_4$

Molecular Weight: 383.44

The synthetic procedure followed the general method in section 6.2.2 using 2-(2-methoxyphenyl)-4*H*-3,1-benzoxazin-4-one **13d** (0.50 g, 1.97 mmol) in DMF (8 ml), 2 equivalents of DIPEA (0.69 ml, 3.94 mmol) and 2.2 equivalents of 2-morpholinoethanamine **14** (0.57 ml, 4.34 mmol). The product was not obtained due to poor crystallization from ethanol.

6.2.24 Synthesis of 2-[(3-methoxybenzoyl)amino]-N-(2-morpholin-4-ylethyl)benzamide (**15e**)

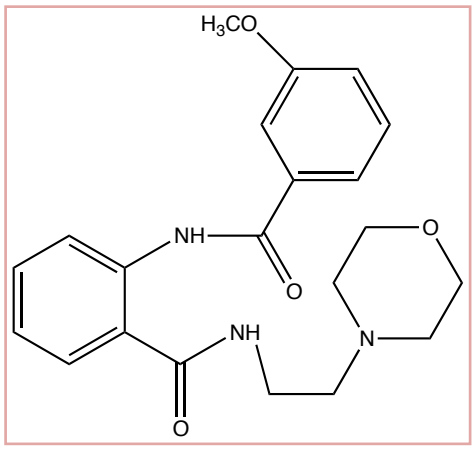

Chemical Formula: $C_{21}H_{25}N_3O_4$

Molecular Weight: 383.44

The synthetic procedure followed the general method in section 6.2.2 using 2-(3-methoxyphenyl)-4*H*-3,1-benzoxazin-4-one **13e** (0.50 g, 1.97 mmol) in DMF (8 ml), 2 equivalents of DIPEA (0.69 ml, 3.94 mmol) and 2.2 equivalents of 2-morpholinoethanamine **14** (0.57 ml, 4.34 mmol). The product was recrystallized from ethanol as a white solid. Yield 0.33 g (44%), mp 105°C.

^{1}H NMR (500 MHz, DMSO-d_6) δ 12.49 (s, 1H, NH), 8.80 (s, 1H, NH), δ 8.63 (d, *J* = 8.5 Hz, 1H, ArH), 7.82 (dd, *J* = 7.9, 1.6 Hz, 1H, ArH), 7.58 (td, J = 17.0, 1.2 Hz, 1H, ArH), 7.52 (d, *J* = 6.5, Hz, 2H, ArH), 7.48 (t, *J* = 3.2 Hz, 1H, ArH), 7.25 – 7.16 (m, 2H, ArH), 3.86 (s, 3H, CH_3), 3.54 (t, *J* = 4.7 Hz, 4H, CH_2), 3.44 (q, *J* = 6.5 Hz, 2H, CH_2), 2.50 (d, *J* = 15.1 Hz, 2H, CH_2), 2.42 (t, *J* = 4.7 Hz, 4H, CH_2).

^{13}C NMR (126 MHz, DMSO-d_6) δ 168.50 (C=O), 164.09 (C=O), 159.52 (ArC), 139.19 (ArC), 136.01 (ArC), 132.14 (ArCH), 130.13 (ArCH), 128.10 (ArCH), 122.87 (ArCH), 120.55 (ArC), 120.27 (ArCH), 118.80 (ArCH), 117.63 (ArCH), 112.46 (ArCH), 66.17 (CH_2), 56.99 (CH_2), 55.28 (OCH_3), 53.18 (CH_2), 36.53 (CH_2).

MS (ES^+): 384.19 [M+1].

Calculated analysis for $C_{21}H_{25}N_3O_4$ (383.44): C, 65.78; H, 6.57; N, 10.95. Found C, 65.71; H, 6.77; N, 10.98.

6.2.25 Synthesis of 2-[(4-methoxybenzoyl)amino]-N-(2-morpholin-4-ylethyl)benzamide (**15f**)

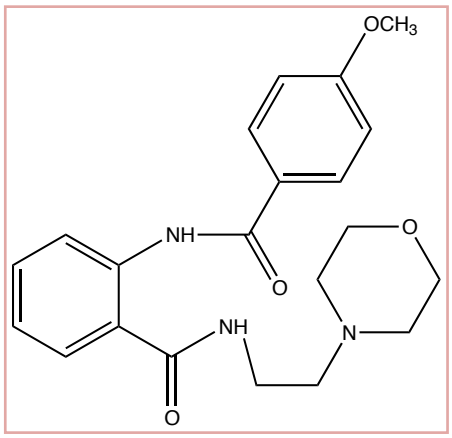

Chemical Formula: $C_{21}H_{25}N_3O_4$

Molecular Weight: 383.44

The synthetic procedure followed the general method in section 6.2.2 using 2-(4-methoxyphenyl)-4*H*-3,1-benzoxazin-4-one **13f** (0.50 g, 1.97 mmol) in DMF (8 ml), 2 equivalents of DIPEA (0.69 ml, 3.94 mmol) and 2.2 equivalents of 2-morpholinoethanamine **14** (0.57 ml, 4.34 mmol). The product was recrystallized from ethanol as a white solid. Yield 32% (0.24 g), mp 110°C.

^{1}H NMR (500 MHz, DMSO-d_6) δ 12.44 (s, 1H, NH), 8.78 (s, 1H, NH), 8.65 (d, *J* = 8.3 Hz, 1H, ArH), 7.92 (d, J =8.9 Hz, 2H, ArH), 7.81 (dd, *J* = 8.0, 1.5 Hz, 1H, ArH), 7.56 (td, *J* = 8.7, 1.5 Hz, 1H, ArH), 7.19 (d, *J* = 15.5, 1.3 Hz, 3H, ArH), 3.86 (s, 3H, OCH_3), 3.55 (t, *J* = 4.6 Hz, 4H, CH_2), 3.45 (q, *J* = 6.4 Hz, 2H, CH_2), 2.51 (m, 3H, CH_2), 2.43 (d, *J* = 9.1 Hz, 3H, CH_2).

^{13}C NMR (126 MHz, DMSO-d_6) δ 168.60 (C=O), 163.87 (C=O), 162.20 (ArC), 140.73 (ArC), 132.10 (ArCH), 128.80 (ArCH), 128.06 (ArCH), 126.63 (ArC), 122.50 (ArCH), 120.23 (ArC), 120.18 (ArCH), 114.18 (ArCH), 66.18 (CH_2), 56.98 (CH_2), 55.45 (OCH_3), 53.21 (CH_2), 36.54 (CH_2).

MS (ES^+): 384.19 [M+1].

Calculated analysis for $C_{21}H_{25}N_3O_4$ (383.44): C, 65.78; H, 6.57; N, 10.95. Found C, 65.63; H, 6.62; N, 10.95.

6.2.26 Synthesis of 2-[(2-nitrobenzoyl)amino]-N-(2-morpholin-4-ylethyl)benzamide (**15g**)

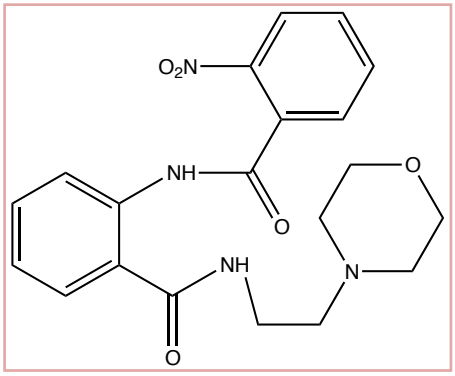

Chemical Formula: $C_{20}H_{22}N_4O_5$

Molecular Weight: 398.16

The synthetic procedure followed the general method in section 6.2.2 using 2-(2-nitrophenyl)-4*H*-3,1-benzoxazin-4-one **13g** (0.50 g, 1.87 mmol) in DMF (8 ml), 2 equivalents of DIPEA (0.65 ml, 3.74 mmol) and 2.2 equivalents of 2-morpholinoethanamine **14** (0.54 ml, 4.11 mmol). The product was recrystallized from ethanol as a white solid. Yield 49% (0.37 g), mp 139°C.

^{1}H NMR (500 MHz, DMSO-d_6) δ 12.02 (s, 1H, NH), 8.75 (s, 1H, NH), 8.41 (d, *J* = 8.2 Hz, 1H, ArH), 8.13 (d, *J* = 8.3, 1H, ArH), 7.91 (t, J =15.2 Hz, 1H, ArH), 7.82 (m, 3H, ArH), 7.59 (t, *J* = 8.2 Hz, 1H, ArH), 7.27 (td, *J* = 7.6, 1.3 Hz, 1H, ArH), 3.53 (t, *J* = 4.6 Hz, 4H, CH_2), 3.37 (q, *J* = 6.5 Hz, 2H, CH_2), 2.46 (t, *J* = 6.8 Hz, 2H, CH_2), 2.39 (t, *J* = 4.7 Hz, 4H, CH_2)

^{13}C NMR (126 MHz, DMSO-d_6) δ 168.01 (C=O), 163.35 (C=O), 147.02 (ArC), 138.23 (ArC), 134.11 (ArCH), 132.02 (ArC), 131.58 (ArCH), 131.68 (ArCH), 128.38 (ArCH), 128.11 (ArCH), 124.57 (ArCH), 123.67 (ArCH), 121.76 (ArC), 120.89 (ArCH), 66.14 (CH_2), 56.95 (CH_2), 53.19 (CH_2), 36.48 (CH_2).

MS (ES^+): 399.19 [M+1].

Calculated analysis for $C_{20}H_{22}N_4O_5$ (398.16): C, 60.29; H, 5.57; N, 14.06. Found C, 60.34; H, 5.61; N, 13.97.

6.2.27 Synthesis of 2-[(3-nitrobenzoyl)amino]-N-(2-morpholin-4-ylethyl)benzamide (**15h**)

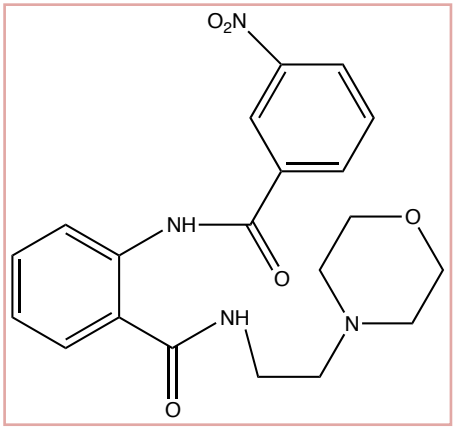

Chemical Formula: $C_{20}H_{22}N_4O_5$

Molecular Weight: 398.16

The synthetic procedure followed the general method in section 6.2.2 using 2-(3-nitrophenyl)-4*H*-3,1-benzoxazin-4-one **13h** (0.50 g, 1.87 mmol) in DMF (8 ml), 2 equivalents of DIPEA (0.65 ml, 3.74 mmol) and 2.2 equivalents of 2-morpholinoethanamine **14** (0.54 ml, 4.11 mmol). The product was not obtained due to poor crystallization from ethanol.

6.2.28 Synthesis of 2-[(4-nitrobenzoyl)amino]-N-(2-morpholin-4-ylethyl) benzamide (**15i**)

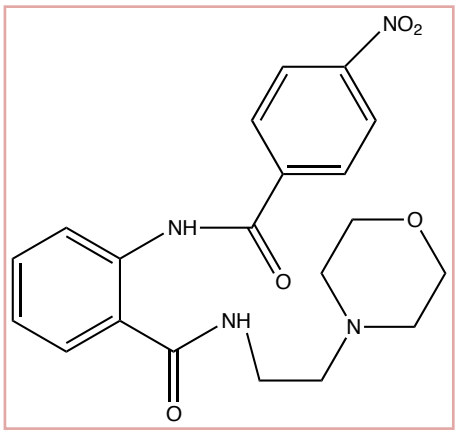

Chemical Formula: $C_{20}H_{22}N_4O_5$

Molecular Weight: 398.16

The synthetic procedure followed the general method in section 6.2.2 using 2-(4-nitrophenyl)-4*H*-3,1-benzoxazin-4-one **13i** (0.50 g, 1.87 mmol) in DMF (8 ml), 2 equivalents of DIPEA (0.65 ml, 3.74 mmol) and 2.2 equivalents of 2-morpholinoethanamine **14** (0.54 ml, 4.11 mmol). The product was recrystallized from ethanol as a white solid. Yield 51% (0.38 g), mp 148°C.

^{1}H NMR (500 MHz, DMSO-d_6) δ 12.70 (s, 1H, NH), 8.83 (s, 1H, NH), 8.59 (d, *J* = 8.4 Hz, 1H, ArH), 8.44 (d, 8.9 Hz, 2H, ArH), 8.16 (d, 8.9 Hz, 2H, ArH), 7.85 (dd, *J* = 8.0, 1.5 Hz, 1H, ArH), 7.60 (td, *J* = 8.6, 1.5 Hz, 1H, ArH), 7.27 (td, *J* = 7.5, 1.2 Hz, 1H, ArH), 3.54 (t, *J* = 4.6 Hz, 4H, CH_2), 3.44 (q, *J* = 6.5 Hz, 2H, CH_2), 2.44 (m, 6H, CH_2).

^{13}C NMR (126 MHz, DMSO-d_6) δ 168.38 (C=O), 162.69 (C=O), 149.41 (ArC), 140.10 (ArC), 138.76 (ArC), 132.21 (ArCH), 128.43 (ArCH), 128.15 (ArCH), 124.13 (ArCH), 123.47 (ArCH), 120.92 (ArC), 120.64 (ArCH), 66.17 (CH_2), 56.93 (CH_2), 53.20 (CH_2), 36.58 (CH_2).

MS (ES^+): 399.21 [M+1].

Calculated analysis for $C_{20}H_{22}N_4O_5$ (398.16): C, 60.29; H, 5.57; N, 14.06. Found C, 60.36; H, 5.54; N, 14.05.

6.2.29 Synthesis of 2-[(2-methylbenzoyl)amino]-N-(2-morpholin-4-ylethyl) benzamide (**15j**)

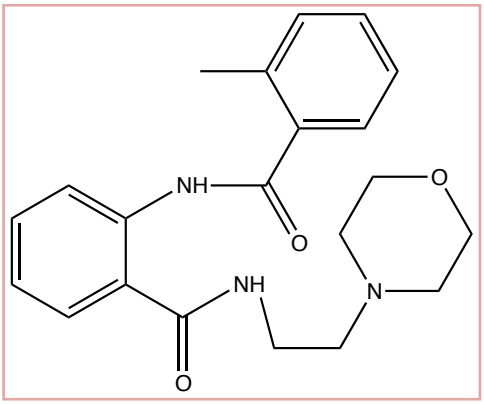

Chemical Formula: $C_{21}H_{25}N_3O_3$

Molecular Weight: 367.44

The synthetic procedure followed the general method in section 6.2.2 using 2-(2-methylphenyl)-4*H*-3,1-benzoxazin-4-one **13j** (0.50 g, 2.11 mmol) in DMF (8 ml), 2 equivalents of DIPEA (0.61 ml, 4.64 mmol) and 2.2 equivalents of 2-morpholinoethanamine **14** (0.74 ml, 4.22 mmol). The product was recrystallized from ethanol as a white solid. Yield 14% (0.11 g), mp 76°C.

^{1}H NMR (500 MHz, DMSO-d_6) δ 11.78 (s, 1H, NH), 8.72 (s, 1H, NH), 8.59 (d, *J* = 8.3 Hz, 1H, ArH), 7.78 (dd, *J* = 7.8, 1.5 Hz, 1H, ArH), 7.56 (q, J =23.6 Hz, 2H, ArH), 7.43 (td, *J* = 7.5, 1.4 Hz, 1H, ArH), 7.34 (dt, *J* = 7.3, 3.4 Hz, 2H, ArH), 7.22 (td, *J* = 7.6, 1.2 Hz, 1H, ArH), 3.53 (t, *J* = 4.6 Hz, 4H, CH_2), 3.37 (q, *J* = 6.5 Hz, 2H, CH_2), 2.45 (d, *J* = 3.9 Hz, 5H, $CH_{2/3}$), 2.39 (t, *J* = 4.7 Hz, 4H, CH_2).

^{13}C NMR (126 MHz, DMSO-d_6) δ 168.22 (C=O), 167.10 (C=O), 138.96 (ArC), 136.44 (ArC), 135.82 (ArC), 131.96 (ArCH), 131.14 (ArCH), 130.24 (ArCH), 128.04 (ArCH), 126.75 (ArCH), 126.07 (ArCH), 122.92 (ArCH), 121.00 (ArC), 120.32 (ArCH), 66.14 (CH_2), 56.99 (CH_2), 53.19 (CH_2), 36.43 (CH_2), 19.59 (CH_3).

MS (ES^+): 368.22 [M+1].

Calculated analysis for $C_{21}H_{25}N_3O_3$ (367.44): C, 68.64; H, 6.86; N, 11.44. Found C, 68.27; H, 6.71; N, 11.28.

6.2.30 Synthesis of 2-benzamido-N- (2-morpholin-4-ylethyl)benzamide (**15k**)

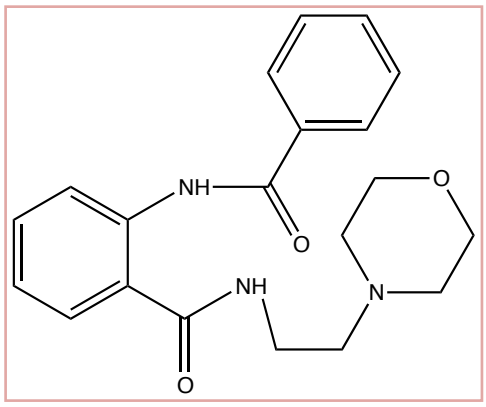

Chemical Formula: $C_{20}H_{23}N_3O_3$

Molecular Weight: 353.41

The synthetic procedure followed the general method in section 6.2.2 using 2-phenyl-4*H*-3,1-benzoxazin-4-one **13k** (0.50 g, 2.11 mmol) in DMF (8 ml), 2 equivalents of DIPEA (0.78 ml, 4.48 mmol) and 2.2 equivalents of 2-morpholinoethanamine **14** (0.65 ml, 4.93 mmol). The obtained solid was a starting material.

6.2.31 Synthesis of 3,4-dimethoxy-*N*- (2-[(2-morpholin-4-ylethyl) carbamoyl] phenyl) benzamide (**15l**)

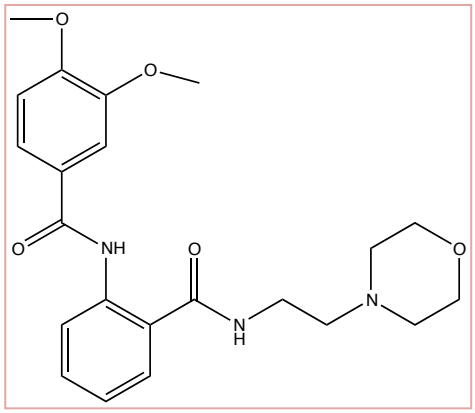

Chemical Formula: $C_{22}H_{27}N_3O_5$

Molecular Weight: 413.47

The synthetic procedure followed the general method in section 6.2.2 using 2-(3,4-dimethoxyphenyl)-4*H*-3,1-benzoxazin-4-one **13l** (0.25 g, 0.88 mmol) in DMF (8 ml), 2 equivalents of DIPEA (0.31 ml, 1.77 mmol) and 2.2 equivalents of 2-morpholinoethanamine **14** (0.26 ml, 1.94 mmol). The product was recrystallized from ethanol as a white solid. Yield 22% (0.19 g), mp 106°C.

^{1}H NMR (500 MHz, DMSO-d_6) δ 12.47 (s, 1H,NH), 8.79 (s, 1H, NH), 8.64 (d, J = 8.4 Hz, 1H, ArH), 7.81 (d, J = 7.8 Hz, 1H, ArH), 7.60-7.50 (m, 3H, ArH), 7.23-7.13 (m, 2H, ArH), 3.86 (s, 6H, OCH_3), 3.55 (t, J = 4.4 Hz, 4H, CH_2), 3.45 (q, J = 6.5 Hz, 2H, CH_2), 2.42 (t, J = 4.6 Hz, 6H, CH_2).

^{13}C NMR (126 MHz, DMSO-d_6) δ 168.62 (C=0), 163.98 (ArC), 151.93 (ArC), 148.69 (ArC), 139.52 (ArC), 132.12 (ArCH), 128.06 (ArCH), 126.83 (ArC), 122.50 (ArCH), 120.26 (ArC), 120.07 (ArCH), 119.86 (ArCH), 111.38 (ArCH), 110.45 (ArCH), 66.17 (CH_2), 56.98 (CH_2), 55.70 (OCH_3), 55.45 (OCH_3), 53.20 (CH_2), 36.52 (CH_2).

MS (EI^+): 413.2.

Calculated analysis for $C_{22}H_{27}N_3O_5$ (413.47): C, 63.91; H, 6.58; N, 10.16. Found C, 63.54; H, 6.86; N, 10.11.

6.2.32 Synthesis of 3,5-dimethoxy-*N*- (2-[(2-morpholin-4-ylethyl) carbamoyl] phenyl) benzamide (**15m**)

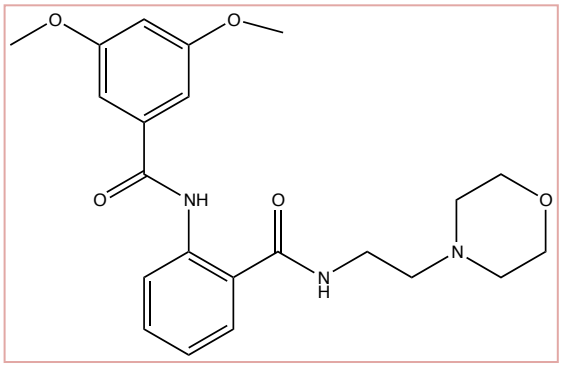

Chemical Formula: $C_{22}H_{27}N_3O_5$

Molecular Weight: 413.47

The synthetic procedure followed the general method in section 6.2.2 using 2-(3,5-dimethoxyphenyl)-4*H*-3,1-benzoxazin-4-one **13m** (0.25 g, 0.88 mmol) in DMF (8 ml), 2 equivalents of DIPEA (0.31 ml, 1.77 mmol) and 2.2 equivalents of 2-morpholinoethanamine **14** (0.26 ml, 1.94 mmol). The product was recrystallized from ethanol as a white solid. Yield 58% (0.21 g), mp 120°C

^{1}H NMR (500 MHz, DMSO-d_6) δ 12.46 (s, 1H, NH), 8.79 (s, NH), 8.61 (dd, J = 8.4, 1.2 Hz, 1H, ArH), 7.81 (dd, J = 7.9 Hz, 1H, ArH), 7.57 (t, J = 7.6 Hz, 1H, ArH), 7.22 (td, J = 7.5, 1.3 Hz, 1H, ArH), 7.07 (d, J = 2.2 Hz, 2H, ArH), 6.77 (t, J = 2.2 Hz, 1H, ArH), 3.84 (d, J = 1.5 Hz, 6H, OCH_3), 3.54 (t, J = 4.6 Hz, 4H, CH_2), 3.44 (q, J = 6.4 Hz, 2H, CH_2), 2.49 (t, J = 6.8 Hz, 2H, CH_2), 2.42 (t, J = 4.7 Hz, 4H, CH_2)

^{13}C NMR (126 MHz, DMSO-d_6) δ 168.49 (C=0), 163.95 (ArC), 160.70 (ArC), 139.12 (ArC), 136.72 (ArC), 132.13 (ArCH), 128.09 (ArCH), 122.89 (ArCH), 120.59 (ArC), 120.22 (ArCH), 104.99 (ArCH), 103.43 (ArCH), 66.16 (CH_2), 56.99 (CH_2), 55.44 (OCH_3), 53.21 (CH_2), 36.52 (CH_2).

MS (EI$^+$): 413.2.

Calculated analysis for $C_{22}H_{27}N_3O_5$ (413.47): C, 63.91; H, 6.58; N, 10.16. Found C, 63.66; H, 6.43; N, 10.03.

6.2.33 Synthesis of 3,4,5-trimethoxy-*N*- (2-[(2-morpholin-4-ylethyl) carbamoyl] phenyl) benzamide (**15n**)

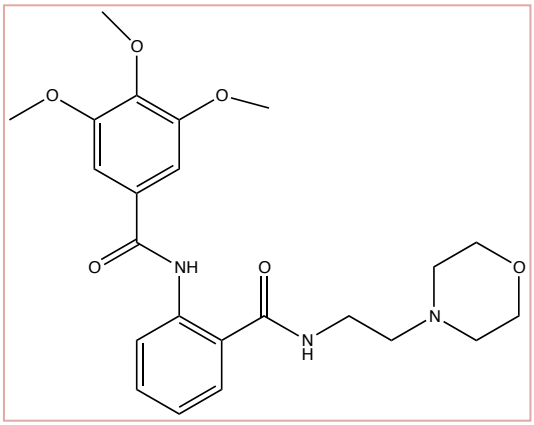

Chemical Formula: $C_{23}H_{29}N_3O_6$

Molecular Weight: 443.21

The synthetic procedure followed the general method in section 6.2.2 using 2-(3,4,5-trimethoxyphenyl)-4*H*-3,1-benzoxazin-4-one **13n** (0.25 g, 0.80 mmol) in DMF (8 ml), 2 equivalents of DIPEA (0.28 ml, 1.60 mmol) and 2.2 equivalents of 2-morpholinoethanamine **14** (0.23 ml, 1.76 mmol). The product was recrystallized from ethanol as a white solid. Yield 52% (0.18 g), mp 117°C.

^{1}H NMR (500 MHz, DMSO-d_6) δ 11.78 12.49 (s, 1H, NH), 8.80 (s, 1H, NH), 8.59 (dd, J = 8.3, 1.3 Hz, 1H, ArH), 7.81 (dd, J = 7.9, 1.5 Hz, 1H, ArH), 7.57 (td, J = 8.8, 2.0 Hz, 1H, ArH), 7.26 (s, 2H, ArH), 7.21 (td, J = 8.8, 1.4 Hz, 1H, ArH), 3.89 (s, 6H, OCH_3), 3.77 (s, 3H, OCH_3), 3.54 (t, J = 4.7 Hz, 4H, $CH_{2'}$), 3.43 (q, J = 6.5 Hz, 2H, CH_2), 2.49 (d, J = 6.8 Hz, 2H, CH_2), 2.41 (t, J = 7.3 Hz, 4H, CH_2).

^{13}C NMR (126 MHz, DMSO-d_6) δ 168.54 (C=O), 163.92 (ArC), 152.90 (ArC), 140.63 (ArC), 139.25 (ArC), 132.12 (ArCH), 129.91 (ArC), 128.08 (ArCH), 122.77 (ArCH), 120.62 (ArC), 120.14 (ArCH), 104.56 (ArCH), 66.15 (CH_2), 60.13 (OCH_3), 56.99 (CH_2), 55.94 (OCH_3), 53.20 (CH_2), 36.49 (CH_2).

MS (EI^+): 443.2.

Calculated analysis for $C_{23}H_{29}N_3O_6$ (443.21): C, 62.29; H, 6.59; N, 9.47. Found C, 62.29; H, 6.46; N, 9.49.

6.2.34 Synthesis of 3,5-difluoro -*N*- (2-[(2-morpholin-4-ylethyl) carbamoyl] phenyl) benzamide (**15o**)

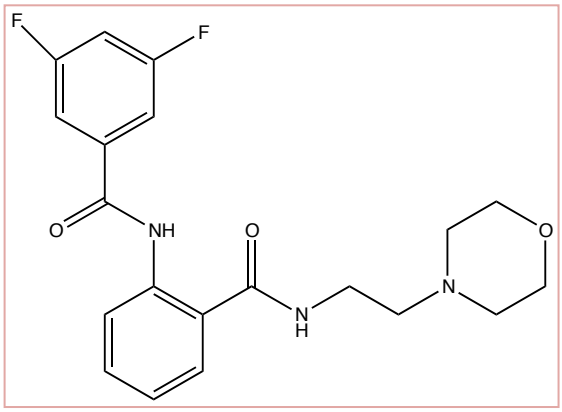

Chemical Formula: $C_{20}H_{21}F_2N_3O_3$

Molecular Weight: 389.40

The synthetic procedure followed the general method in section 6.2.2 using 2-(3,5-difluorophenyl)-4*H*-3,1-benzoxazin-4-one **13o** (0.25 g, 0.96 mmol) in DMF (8 ml), 2 equivalents of DIPEA (0.33 ml, 1.92 mmol) and 2.2 equivalents of 2-morpholinoethanamine **14** (0.28 ml, 2.11 mmol). The product was recrystallized from ethanol as a white solid. Yield 40% (0.15 g), mp 116°C.

^{1}H NMR (500 MHz, DMSO-d_6) δ 12.54 (s, 1H, NH), 8.81 (s, 1H, NH), 8.52 (dd, J = 8.4, 1.2 Hz, 1H, ArH), 7.83 (dd, J = 7.9, 1.5 Hz, 1H, ArH), 7.61-7.59 (m, 1H, ArH), 7.59-7.55 (m, 3H, ArH), 7.26 (td, J = 7.6, 1.3 Hz, 2H, ArH), 3.55 (t, J = 4.6 Hz, 4H, CH_2), 3.44 (q, J = 6.1 Hz, 2H, CH_2), 2.49 (d, J = 6.8 Hz, 1H, CH_2), 2.42 (t, J = 6.5 Hz, 4H, CH_2).

^{13}C NMR (126 MHz, DMSO-d_6) δ 168.33 (C=O), 163.50 (d, J_{C-F} = 13.1 Hz, ArC-F), 161.50 (d, J_{C-F} = 11.2 Hz, ArC-F), 150.10 (ArC), 143.55 (ArC), 138.5 (d, J_{C-F} = 37.7 Hz, ArC), 132.15 (ArCH), 128.16 ArCH), 123.47 (ArCH), 121.16 (ArC), 120.69 (ArCH), 110.50 (d, J_{C-F} = 7.04 Hz, ArCH), 110.29 (d, J_{C-F} = 6.7 Hz, ArCH), 107.50 (ArCH), 66.15 (CH_2), 56.98 (CH_2), 53.21 (CH_2), 36.56 (CH_2).

MS (EI^+): 389.2.

Calculated analysis for $C_{20}H_{21}F_2N_3O_3$ (389.40): C, 61.69; H, 5.44; N, 10.79. Found C, 61.56; H, 5.27; N, 10.68.

6.2.35 Synthesis of 2,6-difluoro -*N*- (2-[(2-morpholin-4-ylethyl) carbamoyl] phenyl) benzamide (**15p**)

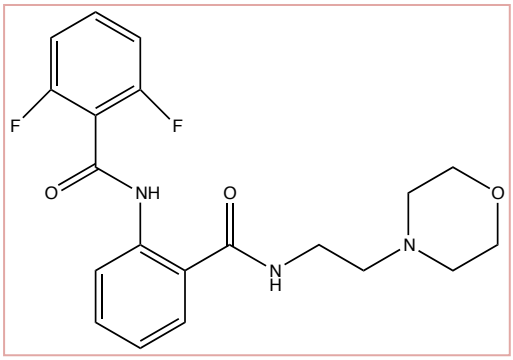

Chemical Formula: $C_{20}H_{21}F_2N_3O_3$

Molecular Weight: 389.40

The synthetic procedure followed the general method in section 6.2.2 using 2-(2,6-difluorophenyl)-4*H*-3,1-benzoxazin-4-one **13p** (0.25 g, 0.96 mmol) in DMF (8 ml), 2 equivalents of DIPEA (0.33 ml, 1.92 mmol) and 2.2 equivalents of 2-morpholinoethanamine **14** (0.28 ml, 2.11 mmol). The product was recrystallized from ethanol as a white solid. Yield 61% (0.25 g), mp 136°C.

^{1}H NMR (500 MHz, DMSO-d_6) δ 12.03 (s, 1H, NH), 8.76 (s, 1H, NH), 8.52 (dd, J = 8.3, 1.2 Hz, 1H, ArH), 7.79 (dd, J = 8.0, 1.6 Hz, 1H, ArH), 7.66-7.62 (m, 1H, ArH), 7.62-7.57 (m, 1H, ArH), 7.28 (td, J = 7.9, 6.2 Hz, 3H, ArH), 3.53 (t, J = 4.7 Hz, 4H, CH_2), 3.37 (q, J = 6.4 Hz, 2H, CH_2), 2.46 (t, J = 6.8 Hz, 2H, CH_2), 2.39 (t, J = 5.0 Hz, 4H, CH_2).

^{13}C NMR (126 MHz, DMSO-d_6) δ 167.96 (C=O), 159.76 (d, J_{C-F} = 7.1 Hz, ArC-F), 157.72 (d, J_{C-F} = 5.5 Hz, ArC-F), 137.98 (ArC), 132.79 (t, J_{C-F}=20.4 Hz, ArCH), 132.13 (ArCH), 128.14 (ArCH), 127.75 (ArC), 123.77 (ArCH), 121.32 (ArC), 120.54 (ArCH), 112.52 (d, J_{C-F} = 3.8 Hz, ArCH), 112.34 (d, J_{C-F}= 4.2 Hz, ArCH), 111.50 (ArC), 66.13 (CH_2), 56.92 (CH_2), 53.18 (CH_2), 36.45 (CH_2).

MS (EI^+): 389.2.

Calculated analysis for $C_{20}H_{21}F_2N_3O_3$ (389.40): C, 61.69; H, 5.44; N, 10.79. Found C, 61.68; H, 5.31; N, 10.82.

6.2.36 Synthesis of 2,4-difluoro -*N*- (2-[(2-morpholin-4-ylethyl) carbamoyl] phenyl) benzamide (**15q**)

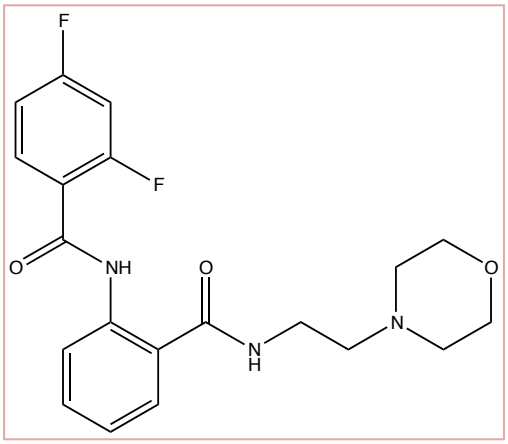

Chemical Formula: $C_{20}H_{21}F_2N_3O_3$

Molecular Weight: 389.40

The synthetic procedure followed the general method in section 6.2.2 using 2-(2,4-difluorophenyl)-4*H*-3,1-benzoxazin-4-one **13q** (0.25 g, 0.96 mmol) in DMF (8 ml), 2 equivalents of DIPEA (0.33 ml, 1.92 mmol) and 2.2 equivalents of 2-morpholinoethanamine **14** (0.28 ml, 2.11 mmol). The product was recrystallized from ethanol as a white solid. Yield 55% (0.21 g), mp 121°C.

^{1}H NMR (500 MHz, DMSO-d_6) δ 12.00 (s, 1H, NH), 8.72 (s, 1H, NH), 8.55 (d, J = 8.3 Hz, 1H, ArH), 7.98 (tt, J = 8.8, 6.6 Hz, 1H, ArH), 7.76 (dd, J = 7.9, 1.6 Hz, 1H, ArH), 7.57 (td, J = 8.5, 1.5 Hz, 1H, ArH), 7.49 (td, J = 11.6, 2.5 Hz, 1H, ArH), 7.30 (td, J = 8.4, 3.8 Hz, 1H, ArH), 7.24 (td, J = 7.6, 1.2 Hz, 1H, ArH), 3.53 (t, J = 5.6 Hz, 4H, CH_2), 3.39 (q, J = 6.3 Hz, 2H, CH_2), 2.48 (t, J = 6.7 Hz, 2H, CH_2), 2.41 (t, J = 4.6 Hz, 4H, CH_2).

^{13}C NMR (126 MHz, DMSO-d_6) δ 168.02 (C=O), 163.20 (d, $J_{C\text{-}F}$ = 5.3 Hz, ArC-F), 158.10 (d, $J_{C\text{-}F}$ = 10.5 Hz, ArC-F), 138.24 (d, $J_{C\text{-}F}$ = 5.4 Hz, ArC), 132.69 (d, $J_{C\text{-}F}$ = 14.9 Hz, ArC), 131.83 (ArCH), 128.02 (ArCH), 123.38 (ArCH), 121.80 (ArC), 121.04 (ArCH), 119.75 (ArC), 112.57 (d, $J_{C\text{-}F}$ = 3.3 Hz, ArCH), 112.41 (d, $J_{C\text{-}F}$ = 3.7 Hz, ArCH), 104.99 (ArCH), 66.16 (CH_2), 56.98 (CH_2), 53.18 (CH_2), 36.44 (CH_2).

MS (EI^+): 389.2.

Calculated analysis for $C_{20}H_{21}F_2N_3O_3$ (389.40): C, 61.69; H, 5.44; N, 10.79. Found C, 61.59; H, 5.24; N, 10.70.

6.3 Synthesis of series 2

The series 2 of analogues were synthesised following the method outlined in Scheme 6.2 using **13a** intermediate as a starting material.

To a stirred solution of 2-(2-fluorophenyl)-4*H*-3,1-benzoxazin-4-one **13a** in DMF (10 ml) were added 2 equivalents of DIPEA and 2.2 equivalents of appropriate amines **16a-f**. The reaction mixture was stirred at r.t overnight. The complete disappearance of the starting material (**13a**) was monitored by TLC. The reaction mixture was dissolved in DCM and washed three times with water. The obtained solid was recrystallized from ethanol.

All synthesised compounds were analysed by ^{1}H, ^{13}C NMR spectra and mass spectrometry and elemental analysis.

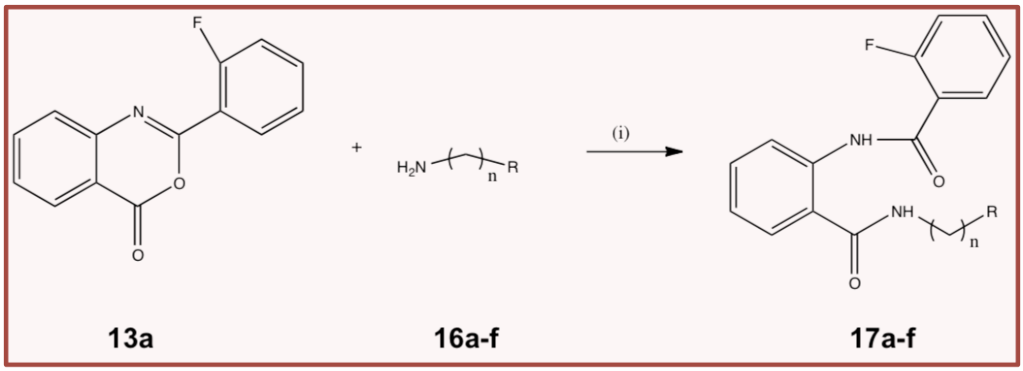

Reagents and conditions: (i) iPr2EtNH, DMF, room temperature, 16 hours.

16, 17a: R= 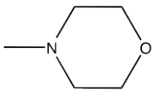 n=3

16, 17d: R= 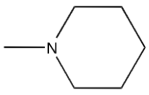 n=2

16, 17b: R= 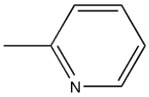 n=2

16, 17e: R= 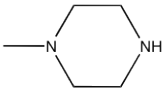 n=2

16, 17c: R= 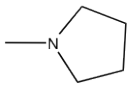 n=2

16, 17f: R=  n=2

Scheme 6.2 Synthesis of series 2

6.3.1 Synthesis of 2-[(2-fluorobenzoyl)amino]-N-(2-morpholin-4-ylpropyl)benzamide (**17a**)

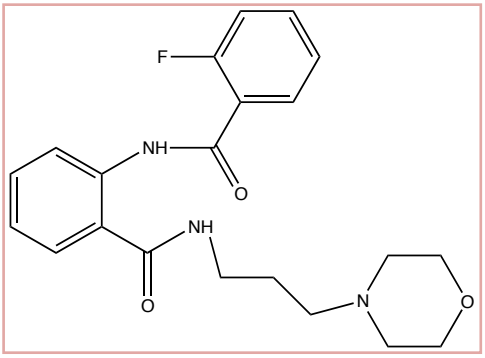

Chemical Formula: $C_{21}H_{24}FN_3O_3$

Molecular Weight: 385.43

The synthetic procedure followed the general method in section 6.3 using 2-(2-fluorophenyl)-4*H*-3,1-benzoxazin-4-one **13a** (0.50 g, 2.07 mmol) in DMF (8 ml), 2 equivalents of DIPEA (0.72 ml, 4.14 mmol) and 2.2 equivalents of 3-morpholinopropan-1-amine **16a** (0.67 ml, 4.56 mmol). The product was recrystallized from ethanol as a white solid. Yield 17% (0.14 g), mp 108°C.

^{1}H NMR (500 MHz, DMSO-d_6) δ 12.06 (s, 1H, NH), 8.82 (s, 1H, NH), 8.58 (d, *J* = 8.3 Hz, 1H, ArH), 7.89 (td, *J* = 7.7, 1.9 Hz, 1H, ArH), 7.77 (dd, *J* = 7.9, 1.5 Hz, 1H, ArH), 7.69 – 7.61 (m, 1H, ArH), 7.57 (td, *J* = 8.6, 1.5 Hz, 1H, ArH), 7.44 – 7.36 (m, 2H, ArH), 7.23 (td, *J* = 7.6, 1.2 Hz, 1H, ArH), 3.55 (t, *J* = 4.6 Hz, 4H, CH_2), 3.30 (dd, *J* = 7.0 Hz, 2H, CH_2), 2.32 (t, *J* = 6.6 Hz, 6H, CH_2), 1.69 (p, *J* = 7.0 Hz, 2H, CH_2).

^{13}C NMR (126 MHz, DMSO-d_6) δ 168.01 (C=O), 160.86 (d, J_{C-F} = 146.2 Hz, ArC-F), 158.29 (C=O), 138.37 (ArC), 133.76 (d, J_{C-F} = 8.8 Hz, ArCH), 131.78 (ArCH), 130.64 (d, J_{C-F} = 1.3 Hz, ArCH), 128.01 (ArCH), 125.01 (d, J_{C-F} = 3.8 Hz, ArCH), 123.24 (ArCH), 122.91 (ArC), 121.70 (ArC), 120.94 (ArCH), 116.64 (d, J_{C-F} = 22.9 Hz, ArCH), 66.16 (CH_2), 55.99 (CH_2), 53.30 (CH_2), 37.75 (CH_2), 25.59 (CH_2).

MS (ES^+): 386.18 [M+1].

Calculated analysis for $C_{21}H_{24}FN_3O_3$ (385.43): C, 65.44; H, 6.28; N, 10.09. Found C, 65.44; H, 6.39; N, 10.94.

6.3.2 Synthesis of 2-[(4-fluorobenzoyl)amino]-N-(pyridin-3-ylmethyl)benzamide (**17b**)

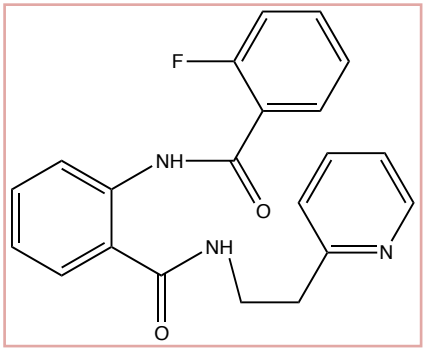

Chemical Formula: $C_{21}H_{18}FN_3O_2$

Molecular Weight: 363.38

The synthetic procedure followed the general method in section 6.3 using 2-(2-fluorophenyl)-4*H*-3,1-benzoxazin-4-one **13a** (0.50 g, 2.07 mmol) in DMF (8 ml), 2 equivalents of DIPEA (0.72 ml, 4.14 mmol) and 2.2 equivalents of 2-(pyridin-2-yl) ethanamine **16b** (0.55 ml, 4.56 mmol). The product was recrystallized from ethanol as a brown solid. Yield 44% (0.34 g), mp 88°C.

^{1}H NMR (500 MHz, DMSO-d_6) δ 11.99 (s, 1H, NH), 8.89 (s, 1H, NH), 8.57 (d, *J* = 8.4 Hz, 1H, ArH), 8.48 (d, J = 6.6 Hz, 1H, ArH), 7.88 (td, *J* = 7.8, 1.8 Hz, 1H, ArH), 7.72 (dd, *J* = 7.8, 1.6 Hz, 1H, ArH), 7.68 (m, 2H, ArH), 7.56 (td, J = 17.4, 1.3 Hz, 1H, ArH), 7.41 (m, 2H, ArH), 7.27 (d, *J* = 7.7 Hz, 1H, ArH), 7.22 (td, *J* = 7.6, 1.3 Hz, 1H, ArH), 7.16 (td, *J* = 7.5, 1.2 Hz, 1H, ArH), 3.63 (m, 2H, CH_2), 3.00 (t, *J* = 7.2 Hz, 2H, CH_2).

^{13}C NMR (126 MHz, DMSO-d_6) δ 168.03 (C=O), 160.88 (d, $J_{C\text{-}F}$ = 144.9 Hz, ArC-F), 158.94 (ArC), 158.30 (ArC), 148.97 (ArCH), 138.37 (ArC), 136.33 (ArCH), 133.76 (d, $J_{C\text{-}F}$ = 8.8 Hz, ArCH), 131.81 (ArCH), 130.60 (d, $J_{C\text{-}F}$ = 1.3 Hz, ArCH), 127.99 (ArCH), 125.02 (d, $J_{C\text{-}F}$ = 2.6 Hz, ArCH), 123.23 (ArCH), 123.12 (ArCH), 121.60 (ArC), 121.42 (ArCH), 120.89 (ArCH), 116.49 (d, $J_{C\text{-}F}$ = 22.7 Hz, ArCH), 36.98 (CH_2).

MS (ES^+): 362.13 [M+1].

High resolution MS: 364.1456 [M-1] – Composition $\underline{C_{21}H_{19}FN_3O_2}$ (delta ppm 0.1) or $C_{18}H_{21}F_5O_2$ (delta ppm -0.1).

6.3.3 Synthesis of 2-[(4-fluorobenzoyl)amino]-N-(pyrrolidin-3-ylmethyl)benzamide (**17c**)

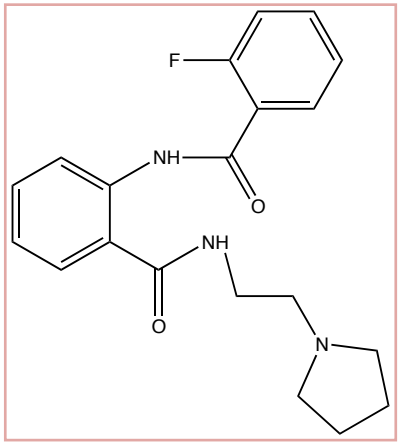

Chemical Formula: $C_{20}H_{22}FN_3O_2$

Molecular Weight: 355.17

The synthetic procedure followed the general method in section 6.3 using 2-(2-fluorophenyl)-4*H*-3,1-benzoxazin-4-one **13a** (0.50 g, 2.07 mmol) in DMF (8 ml), 2 equivalents of DIPEA (0.72 ml, 4.14 mmol) and 2.2 equivalents of 2-(pyrrolidin-1-yl) ethanamine **16c** (0.58 ml, 4.56 mmol). The product was recrystallized from ethanol as a yellow/brown solid. Yield 41% (0.30 g), mp 89°C.

^{1}H NMR (500 MHz, DMSO-d_6) δ 12.04 (s, 1H, NH), 8.74 (s, 1H, NH), 8.58 (d, *J* = 8.4 Hz, 1H, ArH), 7.88 (td, *J* = 7.7, 1.9 Hz, 1H, ArH), 7.77 (dd, *J* = 7.9, 1.5 Hz, 1H, ArH), 7.66 (m, 1 H, ArH), 7.57 (td, *J* = 8.6, 1.5 Hz, 1H, ArH), 7.41 (m, 2H, ArH), 7.23 (td, *J* = 7.6, 1.2 Hz, 1H, ArH), 3.38 (q, *J* = 6.5 Hz, 2H, CH_2), 2.57 (t, *J* = 6.8 Hz, 2H, CH_2), 2.47 (t, *J* = 6.6, Hz, 4H, CH_2), 1.71 – 1.60 (m, 4H, CH_2).

^{13}C NMR (126 MHz, DMSO-d_6) δ 167.98 (C=O), 161.44 (d, $J_{C\text{-}F}$ = 144.9 Hz, ArC-F), 158.29 (C=O), 138.38 (ArC), 133.77 (d, $J_{C\text{-}F}$ = 8.6 Hz, ArCH), 131.83 (ArCH), 130.60 (ArCH), 128.04 (ArCH), 125.03 (d, $J_{C\text{-}F}$ = 3.8 Hz, ArCH), 123.27 (ArCH), 122.91 (d, $J_{C\text{-}F}$ = 12.6 Hz, ArC), 121.59 (ArCH), 120.93 (ArCH), 116.58 (d, $J_{C\text{-}F}$ = 22.7 Hz, ArC), 54.49 (CH_2), 53.56 (CH_2), 38.58 (CH_2), 23.12 (CH_2).

MS (ES^+): 356.15 [M+1].

Calculated analysis for $C_{20}H_{22}FN_3O_2$ (355.17): C, 67.59; H, 6.24; N, 11.82. Found C, 67.66; H, 6.19; N, 11.67.

6.3.4 Synthesis of 2-[(4-fluorobenzoyl)amino]-N-(piperidin-3-ylmethyl)benzamide (**17d**)

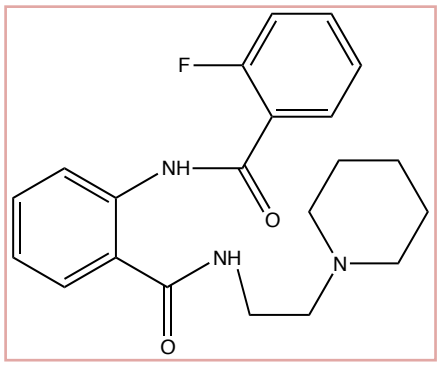

Chemical Formula: $C_{21}H_{24}FN_3O_2$

Molecular Weight: 369.43

The synthetic procedure followed the general method in section 6.3 using 2-(2-fluorophenyl)-4*H*-3,1-benzoxazin-4-one **13a** (0.50 g, 2.07 mmol) in DMF (8 ml), 2 equivalents of DIPEA (0.72 ml, 4.14 mmol) and 2.2 equivalents of 2-(piperidin-1-yl) ethanamine **16d** (0.65 ml, 4.56 mmol). The product was recrystallized from ethanol as a white solid. Yield 51% (0.39 g), mp 94°C.

^{1}H NMR (500 MHz, DMSO-d_6) δ 11.99 (s, 1H, NH), 8.69 (s, 1H, NH), 8.57 (d, *J* = 8.3 Hz, 1H, ArH), 7.88 (td, *J* = 17.1, 1.7 Hz, 1H, ArH), 7.76 (d, *J* = 9.1 Hz, 1H, ArH), 7.67 – 7.62 (m, 1H, ArH), 7.56 (t, *J* = 16.4 Hz, 1H, ArH), 7.42 – 7.37 (m, 1H, ArH), 7.23 (t, *J* = 15.4 Hz, 2H, ArH), 3.36 (q, *J* = 19.6 Hz, 2H, CH_2), 2.43 (t, *J* = 14.1 Hz, 2H, CH_2), 2.35 (t, *J* = 18.6 Hz, 4H, CH_2), 1.44 (q, *J* = 22.6 Hz, 4H, CH_2), 1.34 (d, J=15.1 Hz, 2H, CH_2).

^{13}C NMR (126 MHz, DMSO-d_6) δ 167.99 (C=O), 160.89 (d, J_{C-F} = 155.0 Hz, ArC-F), 158.31 (C=O), 154.28 (ArC), 138.39 (ArC), 133.76 (d, J_{C-F} = 8.8 Hz, ArCH), 131.77 (ArCH), 130.60 (d, J_{C-F} = 1.8 Hz, ArCH), 128.01 (ArCH), 125.00 (d, J_{C-F} = 3.7 Hz, ArCH), 123.26 (ArCH), 121.81 (ArC), 120.97 (ArCH), 116.56 (d, J_{C-F} = 22.8 Hz, ArCH), 57.31 (CH_2), 53.96 (CH_2), 36.87 (CH_2), 25.56 (CH_2), 23.99 (CH_2).

MS (EI^+): 369.19.

Calculated analysis for $C_{21}H_{24}FN_3O_2$ (369.43): C, 68.27; H, 6.55; N, 11.37. Found C, 67.95; H, 6.82; N, 11.44.

6.3.5 Synthesis of 2-[(4-fluorobenzoyl)amino]-N-(piperazin-3-ylmethyl)benzamide (**17e**)

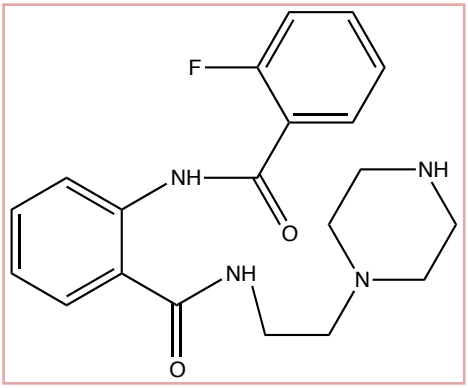

Chemical Formula: $C_{20}H_{23}FN_4O_2$

Molecular Weight: 370.42

The synthetic procedure followed the general method in section 6.3 using 2-(2-fluorophenyl)-4*H*-3,1-benzoxazin-4-one **13a** (0.50 g, 2.07 mmol) in DMF (8 ml), 2 equivalents of DIPEA (0.72 ml, 4.14 mmol) and 2.2 equivalents of 2-(piperazin-1-yl) ethanamine **16e** (0.53 ml, 4.56 mmol). The product could not be purified by recrystallisation.

6.3.6 Synthesis of *N*- (2-aminoethyl)-2-(2-fluorobenzamido) benzamide (**17f**)

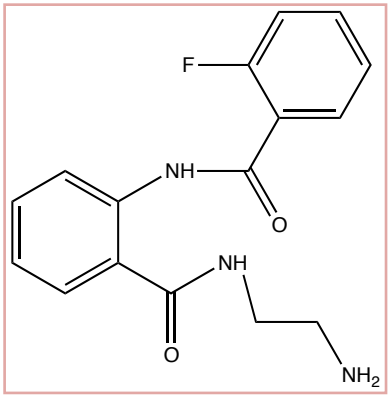

Chemical Formula: $C_{16}H_{16}FN_3O_2$

Molecular Weight: 301.32

The synthetic procedure followed the general method in section 6.3 using 2-(2-fluorophenyl)-4*H*-3,1-benzoxazin-4-one **13a** (0.50 g, 2.07 mmol) in DMF (8 ml), 2 equivalents of DIPEA (0.72 ml, 4.14 mmol) and 2.2 equivalents of ethane-1,2-diamine **16f** (0.31 ml, 4.56 mmol). The product was recrystallized from ethanol as a yellow solid. Yield 43% (0.27 g), mp 96°C.

^{1}H NMR (500 MHz, DMSO-d_6) δ 12.51 (s, 1H, NH), 11.62 (s, 2H, NH_2), 8.80 (s, 1H, NH), 8.60 (dd, *J* = 9.4, 1.1 Hz, 1H, ArH), 8.03 (dd, *J* = 9.4, 1.6 Hz, 1H, ArH), 7.98 (dd, *J* = 9.7, 1.6 Hz, 2H, ArH), 7.72-7.64 (m, 2H, ArH), 7.62 (td, *J* = 16.6, 1.9 Hz, 1H, ArH), 7.26 (td, *J* = 16.4, 1.1 Hz, 1H, ArH), 3.91 (s, 4H, CH_2).

^{13}C NMR (126 MHz, DMSO-d_6) δ 168.24 (C=O), 160.87 (d, J_{C-F} = 151.5 Hz, ArC-F), 158.29 (C=O), 154.31 (ArC), 138.41 (ArC), 133.74 (d, J_{C-F} = 9.5 Hz, ArCH), 131.80 (ArCH), 130.61 (d, J_{C-F} = 1.8 Hz, ArCH), 128.21 (ArCH), 125.02 (d, J_{C-F} = 3.6 Hz, ArCH), 123.22 (ArCH), 121.65 (ArC), 120.86 (ArCH), 116.57 (d, J_{C-F} =22.5 Hz, ArCH), 42.79 (CH_2), 40.88 (CH_2).

MS (EI^+): 301.12.

High resolution MS: 302.1301 [M-1]. Composition: $C_{21}H_{18}O_2$ (delta ppm -0.1), $C_{13}H_{19}O_2F_5$ (delta ppm 0.4), $\underline{C_{16}H_{17}O_2N_3F_1}$ (delta ppm 0.6).

6.4 Synthesis of series 3

The series 3 of analogues were synthesised following the method outlined in Scheme 6.3.

6.4.1 General method for the first step

In the first step, substituted anthranilic acids **18a-d** were dissolved in pyridine (5 ml) and 2.2 equivalent of 2-fluorobenzoyl chloride **12a** was added and the mixture was stirred at r.t. The reaction was monitored by TLC and stopped after approximately an hour after complete disappearance of substituted anthranilic acids **18a-d**. The reaction mixture was poured into 10% solution of sodium carbonate (3 g sodium carbonate, 27 ml distilled water). The formed precipitate was collected by filtration under reduced pressure as intermediate **19a-d**.

6.4.2 General method for the second step

In the second step, to a stirred solution of intermediates **19a-d** in DMF (10 ml) were added 2 equivalents of DIPEA and 2.2 equivalents of 2-morpholinoethanamine **14**. The reaction mixture was stirred at r.t overnight. The complete disappearance of the starting material (**19a-d**) was monitored by TLC. The reaction mixture was dissolved in DCM and washed three times with water. The product was evaporated under reduced pressure and the obtained solid was recrystallized from ethanol.

All synthesised compounds were analysed by ^{1}H, ^{13}C NMR spectra and mass spectrometry. The purity of final compounds was also confirmed by elemental analysis.

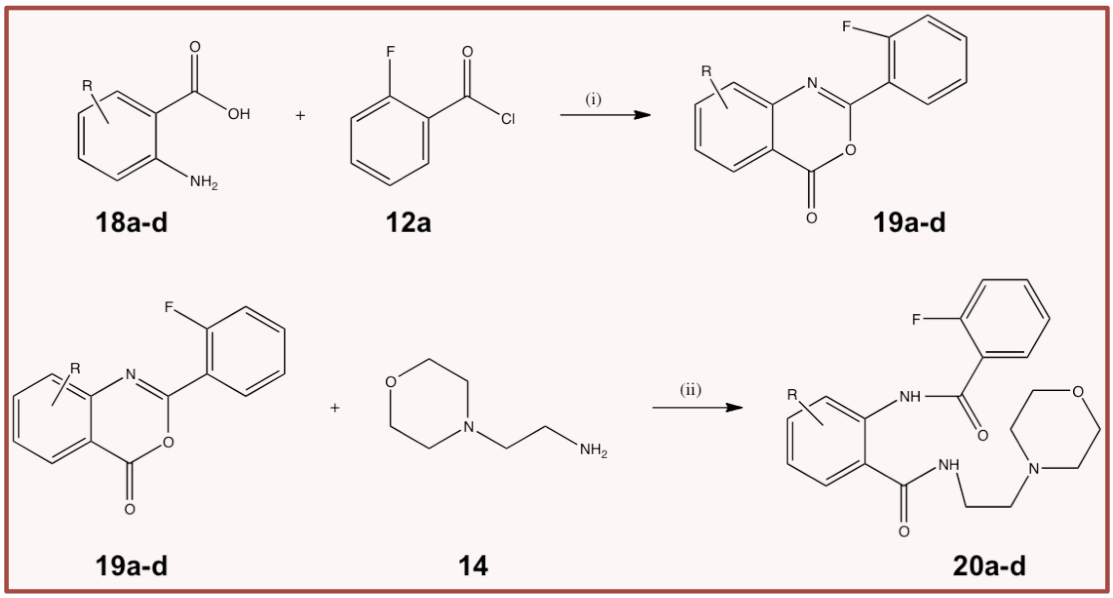

Reagents and conditions: (i) pyridine, room temperature, 1 hour; (ii) iPr2EtNH, DMF, room temperature, 16 hours.

18, 19, 20 a: R= 3-OCH3
18, 19, 20 b: R= 3-CH3
18, 19, 20 c: R= 5-I
18, 19, 20 d: R= 6-Cl

Scheme 6.3 Synthesis of series 3

6.4.3 Synthesis of 2-(2-fluorophenyl)-8-methoxy-3,1-benzoxazin-4-one (**19a**)

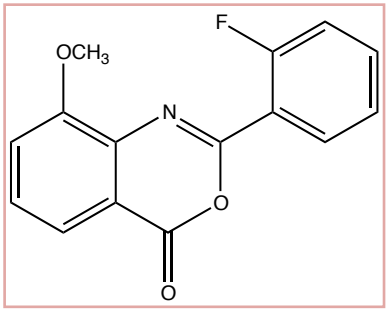

Chemical Formula: $C_{15}H_{10}FNO_3$

Molecular Weight: 271.24

The synthetic procedure followed the general method in section 6.4.1 using 2-amino-3-methoxybenzoic acid **18a** (0.50 g, 2.99 mmol) dissolved in pyridine (5 ml) and 2.2 equivalent of 2-fluorobenzoyl chloride **12a** (0.79 ml, 6.58 mmol). Collected as a white solid, yield 92% (0.75 g), mp 131°C.

^{1}H NMR (500 MHz, DMSO-d_6) δ 8.08 (td, *J* = 7.7, 1.8 Hz, 1H, ArH), 7.72 (d, J = 1.6 Hz, 1H, ArH), 7.71 (d, J = 1.6 Hz, 1H, ArH), 7.63 – 7.54 (m, 2H, ArH), 7.42 (m, 2H, ArH), 3.97 (s, 3H, OCH_3).

^{13}C NMR (126 MHz, DMSO-d_6) δ 160.31 (d, J_{C-F} = 257.0 Hz, ArC-F), 158.73 (ArC=O), 154.15 (ArC), 152.92 (ArC), 135.83 (ArC), 134.31 (d, J_{C-F} = 8.8 Hz, ArCH), 131.14 (ArCH), 129.48 (ArCH), 124.79 (d, J_{C-F} = 3.8 Hz, ArCH), 118.90 (d, J_{C-F} = 10.1 Hz, ArC), 118.78 (ArCH), 118.32 (ArCH), 117.22 (d, J_{C-F} = 21.4 Hz, ArCH), 56.34 (OCH_3).

MS (APCI$^+$): 272.07 [M+1].

6.4.4 Synthesis of 2-(2-fluorophenyl)-8-methoxy-3,1-benzoxazin-4-one (**19b**)

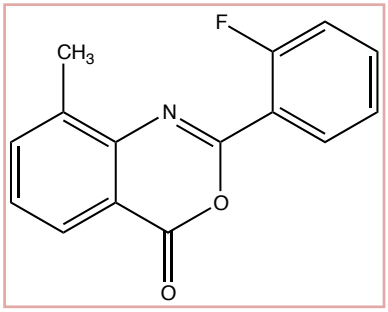

Chemical Formula: $C_{15}H_{10}FNO_2$

Molecular Weight: 255.21

The synthetic procedure followed the general method in section 6.4.1 using 2-amino-3-methylbenzoic acid **18b** (0.50 g, 3.31 mmol) dissolved in pyridine (5 ml) and 2.2 equivalent of 2-fluorobenzoyl chloride **12a** (0.87 ml, 7.28 mmol). Collected as a white solid, yield 97% (0.81 g), mp 106°C.

^{1}H NMR (500 MHz, DMSO-d_6) δ 8.13 (td, *J* = 7.7, 1.9 Hz, 1H, ArH), 8.0 (d, J = 8.8Hz, 1H, ArH), 7.84 (d, *J* = 8.8, 1H, ArH), 7.75 – 7.67 (m, 1H, ArH), 7.55 (t, *J* = 7.7 Hz, 1H, ArH), 7.47 – 7.40 (m, 2H, ArH), 2.58 (s, 3H, CH_3).

^{13}C NMR (126 MHz, DMSO-d_6) δ 160.51 (d, J_{C-F} = 259.6 Hz, ArC-F), 159.01 (ArC=O), 153.06 (ArC), 144.29 (ArC), 137.40 (ArCH), 135.61 (ArC), 134.44 (d, J_{C-F} = 8.82 Hz, ArCH), 131.07 (ArCH), 128.42 (ArCH), 125.54 (ArCH), 124.82 (d, J_{C-F} = 3.8 Hz, ArCH), 118.93 (d, J_{C-F} = 1.3 Hz, ArC), 117.32 (d, J_{C-F} = 21.4 Hz, ArC), 116.78 (ArCH), 16.50 (CH_3).

MS (APCI$^+$): 256.07 [M+1].

6.4.5 Synthesis of 2-(2-fluorophenyl)-8-methoxy-3,1-benzoxazin-4-one (**19c**)

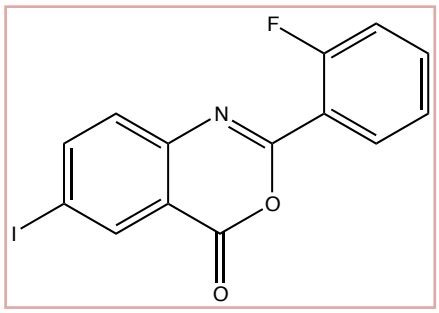

Chemical Formula: $C_{14}H_7FINO_2$

Molecular Weight: 367.11

The synthetic procedure followed the general method in section 6.4.1 using 2-amino-5-iodobenzoic acid **18c** (0.50 g, 1.90 mmol) dissolved in pyridine (5 ml) and 2.2 equivalent of 2-fluorobenzoyl chloride **12a** (0.50ml, 4.18 mmol). Collected as a white solid, yield 90% (0.63 g), mp 159°C.

^{1}H NMR (500 MHz, DMSO-d_6) δ 8.41 (d, *J* = 2.0 Hz, 1H, ArH), 8.26 (dd, *J* = 8.4, 2.0 Hz, 1H, ArH), 8.09 (td, *J* = 7.8, 1.8 Hz, 1H, ArH), 7.75-7.69 (m, 1H, ArH), 7.50 (d, *J* = 8.4 Hz, 1H, ArH), 7.44 (m, 2H, ArH).

^{13}C NMR (126 MHz, DMSO-d_6) δ 160.48 (d, J_{C-F} = 258.3 Hz, ArC-F), 157.35 (ArC=O), 154.59 (ArC), 145.39 (ArC), 145.12 (ArCH), 135.85 (ArCH), 134.74 (d, J_{C-F} = 8.8 Hz, ArCH), 131.10 (ArCH), 128.95 (ArCH), 124.86 (d, J_{C-F} = 3.8 Hz, ArCH), 118.82 (ArC), 118.45 (d, J_{C-F} = 8.8 Hz, ArC), 117.28 (d, J_{C-F} = 21.4 Hz, ArCH), 93.91 (ArC-I).

6.4.6 Synthesis of 5-chloro-2- (2-fluorophenyl)-3,1-benzoxazin-4-one (**19d**)

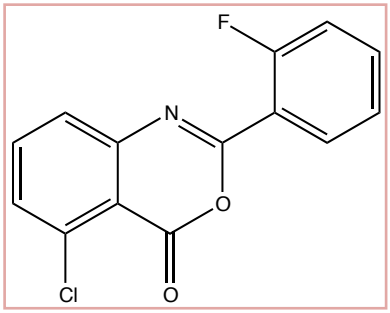

Chemical Formula: $C_{14}H_7ClFNO_2$

Molecular Weight: 275.66

The synthetic procedure followed the general method in section 6.4.1 using 2-amino-6-chlorobenzoic acid **18d** (0.50 g, 2.91 mmol) dissolved in pyridine (5 ml) and 2.2 equivalent of 2-fluorobenzoyl chloride **12a** (0.76 ml, 6.41 mmol). Collected as a white solid, yield 89% (0.71 g), mp 104°C.

^{1}H NMR (500 MHz, DMSO-d_6) δ 8.01 (td, *J* = 17.6, 1.8 Hz, 1H, ArH), 7.90 (t, *J* = 16.1 Hz, 1H, ArH), 7.71 (dd, *J* = 9.1, 1.2 Hz, 2H, ArH), 7.67 (dd, J = 9.1, 1.2 Hz, 1H, ArH), 7.46-7.42 (m, 2H, ArH),

^{13}C NMR (126 MHz, DMSO-d_6) δ 160.53 (d, J_{C-F} = 256.9 Hz, ArC-F), 155.43 (ArC=O), 148.53 (ArC), 144.39 (ArC), 136.6 (ArCH), 134.81 (d, J_{C-F} = 10.1 Hz, ArCH), 134.01 (ArC), 131.09 (ArCH), 130.93 (ArCH), 126.44 (ArCH), 124.86 (d, J_{C-F} = 3.9 Hz, ArCH), 118.18 (d, J_{C-F} = 10.3 Hz, ArC), 117.28 (d, J_{C-F} = 22.3 Hz, ArCH), 114.77 (ArC-Cl).

MS (EI^+): 275.01.

6.4.7 Synthesis of 2-[(2-fluorobenzoyl)amino]-3-methoxy-N-(2-morpholin-4-ylethyl) benzamide (**20a**)

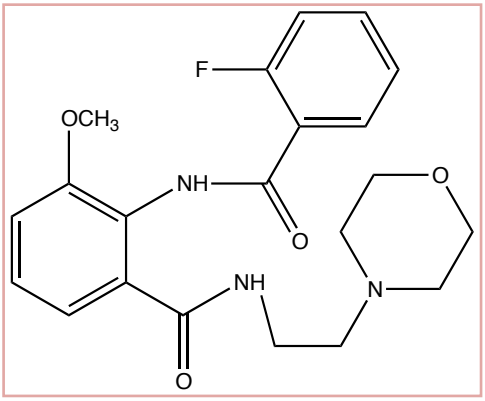

Chemical Formula: $C_{21}H_{24}FN_3O_4$

Molecular Weight: 401.43

The synthetic procedure followed the general method in section 6.4.2 using 2-(2-fluorophenyl)-8-methoxy-3,1-benzoxazin-4-one (**19a**) (0.50 g, 1.84 mmol) in DMF (8 ml), 2 equivalents of DIPEA (0.64 ml, 3.69 mmol) and 2.2 equivalents of 2-morpholinoethanamine **14** (0.53 ml, 4.06 mmol). The product was recrystallized from ethanol as a white solid. Yield 14% (0.27 g), mp 131°C.

^{1}H NMR (500 MHz, DMSO-d_6) δ 9.53 (s, 1H, NH), 8.02 (s, 1H, NH), 7.79 (t, J = 15.1 Hz, 1H, ArH), 7.60 (q, *J* = 7.0 Hz, 1H, ArH), 7.38-7.30 (m, 3H, ArH), 7.21 (d, *J* = 8.2 Hz, 1H, ArH), 7.12 (d, *J* = 7.7 Hz, 1H, ArH), 3.81 (s, 3H, OCH_3), 3.31 (t, *J* = 10.1 Hz, 6H, CH_2), 2.33 (m, 6H, CH_2).

^{13}C NMR (126 MHz, DMSO-d_6) δ 166.71 (C=O), 159.56 (d, $J_{C\text{-}F}$ = 249.5 Hz, ArC-F), 154.59 (C=O), 144.51 (ArC), 138.35 (ArC), 134.90 (d, $J_{C\text{-}F}$ = 1.3 Hz, ArC), 133.09 (d, $J_{C\text{-}F}$ = 1.3 Hz, ArCH), 130.62 (ArCH), 127.27 (ArCH), 124.50 (ArCH), 119.74 (ArCH), 118.6 (ArC), 116.34 (d, $J_{C\text{-}F}$ = 22.7 Hz, ArCH), 113.45 (ArCH), 66.05 (CH_2), 57.03 (CH_2), 56.04 (OCH_3), 53.14 (CH_2), 36.23 (CH_2).

MS (ES^+): 402.21 [M+1].

Calculated analysis for $C_{21}H_{24}FN_3O_4$ (401.43): C, 62.83; H, 6.03; N, 10.47. Found C, 62.76; H, 6.17; N, 10.53.

6.4.8 Synthesis of 2-[(2-fluorobenzoyl)amino]-3-methyl-N-(2-morpholin-4-ylethyl) benzamide (**20b**)

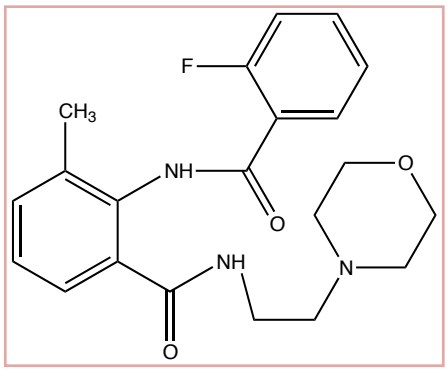

Chemical Formula: $C_{21}H_{24}FN_3O_3$

Molecular Weight: 385.43

The synthetic procedure followed the general method in section 6.4.2 using 2-(2-fluorophenyl)-8-methyl-3,1-benzoxazin-4-one (**19b**) (0.50 g, 1.96 mmol) in DMF (8 ml), 2 equivalents of DIPEA (0.68 ml, 3.91 mmol) and 2.2 equivalents of 2-morpholinoethanamine **14** (0.57 ml, 4.31 mmol). The product was recrystallized from ethanol as a white solid. Yield 42% (0.32 g), mp 165°C.

^{1}H NMR (500 MHz, DMSO-d_6) δ 9.96 (s, 1H, NH), 8.12 (s, 1H, NH), 7.80 (td, J = 7.6, 1.9 Hz, 1H, ArH), 7.61 (td, J = 7.4, 1.9 Hz, 1H, ArH), 7.37 (m, 4H, ArH), 7.30 (t, *J* = 7.6 Hz, 1H, ArH), 3.32 (d, J = 5.4 Hz, 4H, CH_2), 2.39 (t, J = 6.8 Hz, 2H, CH_2), 2.32 (m, 6H, CH_2), 2.27 (s, 3H, CH_3).

^{13}C NMR (126 MHz, DMSO-d_6) δ 167.43 (C=O), 162.08 (d, $J_{C\text{-}F}$ = 206.6 Hz, ArC-F), 158.45 (C=O), 135.89 (ArC), 133.90 (ArC), 133.42 (ArC), 133.04 (d, $J_{C\text{-}F}$ = 8.8 Hz, ArCH), 131.88 (ArCH), 130.36 (d, $J_{C\text{-}F}$ = 1.3 Hz, ArCH), 126.37 (ArCH), 125.59 (ArCH), 125.10 (ArCH), 124.62 (d, $J_{C\text{-}F}$ = 2.5 Hz, ArC), 116.30 (d, $J_{C\text{-}F}$ = 22.7 Hz, ArCH), 66.08 (CH_2), 57.04 (CH_2), 53.16 (CH_2), 36.30 (CH_2), 18.22 (CH_3).

MS (ES^+): 386.22 [M+1].

Calculated analysis for $C_{21}H_{24}FN_3O_3$ (385.43): C, 65.44; H, 6.28; N, 10.90. Found C, 65.66; H, 6.27; N, 10.96.

6.4.9 Synthesis of 2-[(2-fluorobenzoyl)amino]-5-iodo-N-(2-morpholin-4-ylethyl) benzamide (**20c**)

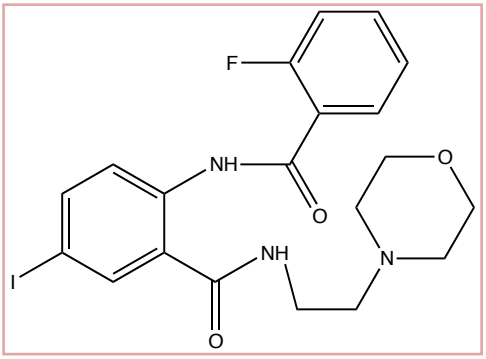

Chemical Formula: $C_{20}H_{21}FIN_3O_3$

Molecular Weight: 497.30

The synthetic procedure followed the general method in section 6.4.2 using 2-(2-fluorophenyl)-6-iodo-3,1-benzoxazin-4-one (**19c**) (0.50 g, 1.36 mmol) in DMF (8 ml), 2 equivalents of DIPEA (0.48 ml, 2.72 mmol) and 2.2 equivalents of 2-morpholinoethanamine **14** (0.39 ml, 2.99 mmol). The product could not be purified by recrystallisation.

6.4.10 Synthesis of 2-[(2-fluorobenzoyl)amino]-2-chloro-N-(2-morpholin-4-ylethyl) benzamide (**20d**)

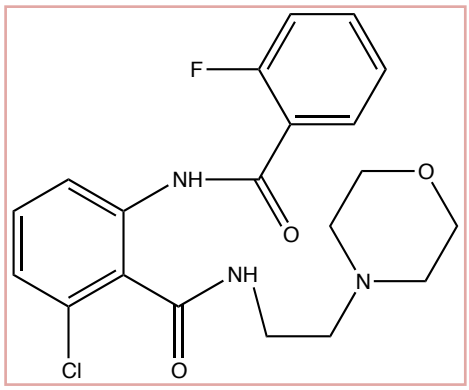

Chemical Formula: $C_{20}H_{21}FClN_3O_3$

Molecular Weight: 405.85

The synthetic procedure followed the general method in section 6.4.2 using 2-(2-fluorophenyl)-5-chloro-3,1-benzoxazin-4-one (**19d**) (0.50 g, 1.83 mmol) in DMF (8 ml), 2 equivalents of DIPEA (0.64 ml, 3.65 mmol) and 2.2 equivalents of 2-morpholinoethanamine **14** (0.53 ml, 4.02 mmol). The product was recrystallized from ethanol as a yellow solid. Yield 33% (0.25 g), mp 121°C.

^{1}H NMR (500 MHz, DMSO-d_6) δ 9.60 (s, 1H, NH), 8.60 (s, 1H, NH), 7.97 (dd, *J* = 8.6 Hz, 1H, ArH), 7.87 (td, *J* = 15.6, 1.8 Hz, 1H, ArH), 7.67-7.63 (m, 1H, ArH), 7.48 (t, 16.5 Hz, 1H, ArH), 7.42-7.36 (m, 3H, ArH), 3.48 (t, *J* = 9.3 Hz, 4H, CH_2), 3.38 (q, J = 19.5 Hz, 2H, CH_2), 2.43 (t, *J* = 13.7 Hz, 2H, CH_2), 2.33 (s, 4H, CH_2).

^{13}C NMR (126 MHz, DMSO-d_6) δ 164.21 (C=O), 162.52 (d, J_{C-F} = 114.8 Hz, ArC-F), 158.45 (C=O), 155.98 (ArC), 142.8 (ArC), 136.0 (ArC), 133.97 (d, J_{C-F} = 9.4 Hz, ArCH), 130.87 (ArCH), 130.24 (ArCH, 130.20 (d, J_{C-F} = 19.9 Hz, ArC), 125.94 (ArCH), 124.99 (d, J_{C-F} = 3.4 Hz, ArCH), 122.60 (ArCH), 116.44 (d, J_{C-F} = 23.0 Hz, ArCH), 66.08 (CH_2), 56.74 (CH_2), 53.16 (CH_2), 36.47 (CH_2).

MS (EI^+): 405.12.

Calculated analysis for $C_{20}H_{21}FClN_3O_3$ (405.85): C, 59.19; H, 5.22; N, 10.35. Found C, 59.40; H, 5.21; N, 10.38.

6.5 Synthesis of hydrochloride salt of 2-fluoro-*N*- (2-((2-morpholinoethyl) carbamoyl) phenyl) benzamide (HCl salt of 15a)

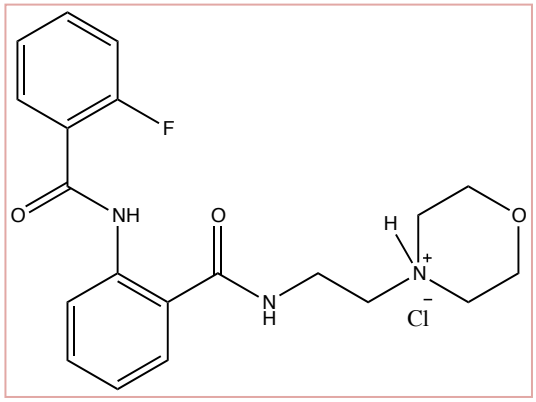

Chemical Formula: $C_{20}H_{23}FN_3O_3^+Cl^-$

Molecular Weight: 372.41

2-[(2-fluorobenzoyl)amino]-N-(2-morpholin-4-ylethyl)benzamide (15a) (0.31g, 0.81mmol) was dissolved in 150ml of methanol. Hydrogen chloride in methanol (1.2ml, 1.25M) was added and the mixture was stirred at r.t. for an hour. Methanol was evaporated from the mixture, following by addition and evaporation of hexane. DCM (2ml) was added to the mixture followed by addition of hexane and the formed white precipitate was filtered under reduced pressure. Yield 79% (0.26g), mp 145˚C.

^{1}H NMR (500 MHz, Chloroform) δ 11.61 (s, 1H, NH), 9.00 (s, 1H, NH), 8.65 (d, J = 8.2 Hz, 1H, ArH), 8.00 (td, J = 7.6, 2.0 Hz, 2H, ArH), 7.50 - 7.43 (m, 2H, ArH), 7.25 (t, J = 7.5 Hz, 1H, ArH), 7.15 (t, J = 5.3 Hz, 1H, ArH), 7.12 (d, J = 7.0 Hz, 1H, ArH), 4.06 (t, J = 12.2 Hz, 2H,CH_2), 3.93 - 3.78 (m, 4H, CH_2) 3.56 (d, J = 11.8 Hz, 2H, CH_2), 3.20 (s, 2H,CH_2), 3.01 (s, 1H, NH^+), 2.87 (t, J = 8.3, 7.6 Hz, 2H, CH_2).

^{13}C NMR (126 MHz, DMSO-d_6) δ 169.51 (C=O), 162.15 (ArC-F), 162.16 (ArC), 161.23 (ArC), 159.24 (ArC), 139.50 (ArC), 133.25 (d, J_{C-F} = 8.8 Hz, ArC), 132.85 (ArCH), 131.70 (d, J_{C-F} = 2.2 Hz, ArCH), 128.40 (ArCH), 124.69 (d, J_{C-F} = 3.4 Hz, ArCH), 123.73 (ArCH), 122.04 (ArCH), 120.17 (ArC), 116.35 (d, J_{C-F} = 23.9 Hz, ArCH), 63.53 (CH_2), 58.72 (CH_2), 53.11 (CH_2), 34.00 (CH_2).

Calculated analysis for $C_{20}H_{23}FN_3O_3^+Cl^-$ (372.41): C, 58.90; H, 5.68; N, 10.30; Cl 8.69. Found C, 59.08; H, 5.68; N, 10.32; Cl, 9.18.

MS (EI^+): 372.2.

Chapter 7

General Discussion

7. Discussion and future work

An increasing body of evidence on the role of NF-κB signalling in cancer development indicates that NF-κB is an interesting target for the development of novel therapeutics. The NFκB family of transcription factors regulate expression of numerous genes that control apoptosis, cell adhesion, cell proliferation, immunity and inflammation (Perkins, 2007). Interestingly, a high level of NF-κB activation was found in 86% of HER2+/ER- breast cancers and in 33% of basal-like cancers (Biswas and Iglehart, 2006). These subtypes of breast cancers are associated with a shortened disease-free interval, poor survival and resistance to cancer therapy (Schlotter et al., 2008), therefore a development of novel targeted therapy is clearly needed. The positive link between HER2 expression and NF-κB activation suggested that HER2+ breast tumours could be preferential targets of NF-κB inhibitors (Biswas and Iglehart, 2006, Zhou et al., 2005).

The discovery of a novel, druggable target within the NF-κB signalling pathway is essential for the development of novel therapeutics. In particular, strategies to modulate, rather than completely inhibit NF-κB pathway have a strong potential (Perkins, 2012).

One candidate approach that we adopted is to target a co-activator of NF-κB signalling, Bcl-3, which is a known oncogene that was found overexpressed in various types of cancers. A recent study in our lab showed that Bcl-3 specifically promoted the formation of metastasis of ErbB2 driven tumours *in vivo* (Wakefield et al., 2013). The occurrence of developed lung metastasis in a Bcl-3 deficient ErbB2 (MMTV/neu) mouse model was reduced by 40%, moreover a reduction in mitotic index (Ki-67) and increase in apoptosis (cleaved caspase 3) was observed in secondary lung lesions (Wakefield et al., 2013).

The fact that primary tumour growth was unaffected however suggested that Bcl-3 suppression might be therapeutically beneficial specifically for the prevention of secondary-tumour seeding and spread at distal sites (Wakefield et al., 2013). Further studies are needed to determine whether the suppression of Bcl-3 could inhibit the growth and spread of existing metastatic lesions in addition to its effect on secondary tumour seeding and spread at distal sites.

The evidence that Bcl-3 deficiency *in vivo* did not affect normal mammary function (Wakefield et al., 2013) and Bcl-3 deficient mice appeared developmentally normal and healthy, only susceptible to certain pathogens (such as S. pneumoniae or Toxoplasma gonidii) (Franzoso et al., 1997, Schwarz et al., 1997) supports the therapeutic potential of Bcl-3 inhibition.

With this in mind, the main aims of this project were to (1) further investigate the oncogenic potential of Bcl-3 in HER2+ and HER2- human breast cancer cell lines; (2) determine whether Bcl-3 could be inhibited by disruption of binding to its binding partners from the NF-κB family; (3) explore Bcl-3 structure using molecular modelling and select potential small molecule inhibitors by virtual screening.

7.1 Bcl-3 as a therapeutic target

In previous studies in our lab, the deletion of Bcl-3 in an ErbB2 murine mammary cancer cell line, MG1361, resulted in an 80% decrease in metastatic formation *in vivo* in a metastatic model of breast cancer as compared to control xenografts (Wakefield et al., 2013). Moreover, suppression of Bcl-3 *in vitro* by siRNA in MG1361 cell line resulted in a significant decrease in cell migratory capacity without affecting cell proliferation (Wakefield et al., 2013). Furthermore, in a similar study using various human breast cancer cell lines, Bcl-3 suppression led to a decrease in cell proliferation in addition to a concomitant decrease in cell migration observed in murine breast cancer cells (Wakefield, 2012). This finding is of particular interest, because it would mean that suppression of Bcl-3 could inhibit growth of existing metastasis or even primary human tumours. Therefore we wanted to further explore the role of Bcl-3 not only in metastasis progression but also in cell proliferation in human breast cancer cell lines.

It was demonstrated previously that Bcl-3 expression correlates with HER2 status (Wakefield, 2012). We confirmed that HER2+ SKBR3 cell line had higher level of Bcl-3 expression as opposed to low Bcl-3 levels in triple negative MDA-MB-231 cell line and in ER+ ZR-75-1 cell line (Chapter 3). Consequently Bcl-3 was suppressed in these three human breast cancer cell lines by Bcl-3 siRNA. Interestingly, only in SKBR3 and MDA-MB-231 cell lines did we observe a decrease in cell viability when Bcl-3 was suppressed. This was attributed to an increase in cell death and an

increase in the percentage of cells resting in the G0/1 phase of the cell cycle (Chapter 3). In SKBR3 and MDA-MB-231 cells we also observed a decrease in NF-κB activity when Bcl-3 was suppressed, which is not surprising as Bcl-3 is a known co-activator of NF-κB signalling. However we did not detect any changes in expression of cyclin D1, NF-κB regulated gene responsive for cell proliferation, suggesting that Bcl-3 regulates cell proliferation via other NF-κB regulated gene(s), which have yet to be identified.

We did not observe any effect either on cell proliferation or NF-κB activity when Bcl-3 was suppressed in the ER+ ZR-75-1 cell line (Chapter 3), which further supports the hypothesis that inhibition of Bcl-3 would be therapeutically beneficial mainly in ER- mammary tumours.

7.2 Modelling disruption of Bcl-3-p50 binding in MDA-MB-231 cell line

Currently there is no available Bcl-3 inhibitor. In order to identify a potential mechanism for molecular inhibition we aimed to determine whether Bcl-3 function could be inhibited by disruption of its binding to proteins p50 and p52 from the NF-κB family. For this purpose we used a Bcl-3 binding mutant ANK M123 (construct described in section 2.1.2), which was proven not to be able to bind to protein p50 and p52 (Keutgens et al., 2010).

Using modelling studies it was found that Bcl-3 binds p50 and p52 proteins as a dimer (Michel et al., 2001), therefore we hypothesised that the Bcl-3 binding mutant ANK M123 could act in a dominant negative manner by binding to endogenous Bcl-3 and therefore preventing it from acting.

We overexpressed the Bcl-3 ANK M123 construct in MDA-MB-231 cells, these cells were chosen because of their metastatic phenotype and low level of endogenous Bcl-3 expression. Bcl-3 ANK M123 overexpressing cells responded *in vitro* similarly to cells with Bcl-3 suppressed by siRNA, supporting the hypothesis that these cells act in a dominant negative manner. Despite this, however our hypothesis still remains to be formally demonstrated.

We observed a significant decrease in NF-κB activity along with down regulation of cyclin D1 and decrease in cell viability and cell migration ability (Chapter3). Moreover, overexpression of Bcl-3 ANK M123 significantly reduced the

migratory capacity of MDA-MB-231 cells by 30% as compared to parental MDA-MB-231 control (Chapter3).

Consistent with *in vitro* results, when Bcl-3 ANK M123 cells were injected orthotopically into 8 week old immune compromised female virgin mice, (Hsd: Athymic Nude-Foxn 1^{nu}), a significantly reduced growth rate was observed as compared to parental MDA-MB-231 cells with a longer latency in tumour formation. Interestingly, primary tumours formed from Bcl-3 ANK M123 overexpressing cells exhibited a significant reduction in mitotic index (Ki-67) and an increase in apoptosis (cleaved caspase-3) with a histological appearance less aggressive and invasive than controls, properties previously observed only at secondary lesions (Dr. Richard Clarkson and Steffan Seal, unpublished data).

7.3 Does Bcl-3 act as an oncogene?

Bcl-3 has been shown to stimulate cell growth as well as provide a survival function in various cell lines *in vitro* (Rebollo et al., 2000, Na et al., 1999). However the role of Bcl-3 *in vivo* is rather controversial. H16N2 cells overexpressing Bcl-3 did not form tumours in nude mice (Westerheide et al., 2001), however Bcl-3 expressing NIH3T3 cells formed tumours when injected in nude mice (Viatour et al., 2004a), suggesting that the oncogenic potential of Bcl-3 might be cell specific or under a tight regulation in various mouse models.

We aimed to further explore the effect of Bcl-3 WT overexpression in MDA-MB-231 cell line. Despite the increase in NF-κB activity and cyclin D1 expression caused by Bcl-3 WT overexpression, we observed a decrease in cell viability as compared to parental MDA-MB-231 cells (Chapter 3). This rather surprising observation was compounded by the fact that a lower percentage of cells in G0/G1 phase of the cell cycle was observed, which would suggest re-entry into the cell cycle and thus should lead to an increase in cell proliferation (Chapter 3). However, the overexpression of Bcl-3 WT led to an expected increase in migratory capacity of MDA-MB-231 cells by 40% as compared to parental MDA-MB-231 control. These discrepancies between the outcome of Bcl-3 WT overexpression on cell proliferation as opposed to cell migration are discussed in Chapter 3.

In Chapter 3 we also pointed out that unnatural overexpression of Bcl-3 could lead to physiological suppression of Bcl-3 function, which might be attributed

to a tight regulation of Bcl-3 function. A presence of NF-κB-Bcl-3 auto regulatory loop was suggested by Brasier *et al.* (2001) and Bundy *et al.* (1997) suggested that Bcl-3 in higher concentrations form inhibitory complexes with p52 homodimers. Moreover, Bcl-3 oncogenicity is also attenuated by GSK3-dependent phosphorylation on its C-terminal domain as this phosphorylation triggers Bcl-3 degradation via the proteasome pathway. This mechanism physiologically limits intracellular levels of Bcl-3 and therefore prevents Bcl-3 oncogenicity in normal cells (Viatour et al., 2004a).

The overall negative effect of Bcl-3 overexpression on cell numbers *in vitro* was recently reflected in a mouse xenograft study, where a significantly reduced growth rate was observed as compared to parental MDA-MB-231 cells with a longer latency in tumour formation (Dr. Richard Clarkson and Steffan Seal, unpublished data). Moreover, recombinant tumours exhibited a significantly reduction in mitotic index (Ki-67) and apoptosis (cleaved caspase-3).

The results here may indicate that Bcl-3 is in fact a disease modifying gene rather than a driving oncogene. Furthermore Bcl-3 expression failed to correlate with diagnostic indicators of aggressiveness in correlative analyses, which points to a modifying role of Bcl-3 as opposed to primarily causing an aggressive phenotype (Steffan Seal, unpublished data).

7.4 Targeting Bcl-3-p50 protein-protein interactions

Based on provided evidence, the inhibition of Bcl-3 seems a promising therapeutic strategy, especially for HER2+ and triple negative breast cancers. Using a Bcl-3 ANK M123 binding mutant we have shown that Bcl-3 function can be inhibited by disruption to its binding partner p50 and p52 from the NF-κB family. Therefore our next aim was to generate and evaluate small-molecule inhibitors targeting Bcl-3-p50 interface using molecular modelling tools.

The design of specific inhibitors targeting protein-protein interactions (PPIs) is an emerging, and alternative, paradigm in drug design. The conventional enzymatic targets offer usually structurally well characterised, hydrophobic pockets with dimensions appropriate to the design of small molecule inhibitors. In contrast, protein-protein interfaces are predominantly large and featureless, and have been proven difficult to target. However, in recent years, the use of *in silico* modelling

helped to understand the nature of the protein-protein interface and revealed that even planar protein-protein interfaces often contain a so-called hotspot, consisting of polar amino acids (frequently tyrosine, tryptophan and arginine) that have been shown to play a key role in coordinating protein-protein interactions but also provide a molecular target for the design of small molecule inhibitors (Jubb et al., 2012, Garner et al., 2011).

Indeed, a number of small molecule inhibitors targeting PPIs have been developed and progressed to clinical evaluation. The recent development against targets such as p53/Mdm2 (Wang et al., 2012) or Bcl2/Bax (Thomas et al., 2013) changed the perception of PPIs as non viable drug targets and supports further development of small molecule inhibitors of PPIs.

7.4.1 Virtual screening targeted against a novel Bcl-3 binding pocket

In order to generate novel inhibitors targeting the Bcl-3-p50 interface we have constructed a model of Bcl-3 in a complex with p50 and identified a novel hydrophobic binding pocket within ankyrin repeats 6 and 7 of the Bcl-3 molecule. The pocket was named the “MYSGS” binding pocket after the main Bcl-3 residues forming this pocket and could act as a unique site for specific targeting of Bcl-3 (Chapter 4).

We performed a structure based virtual screening in order to select suitable candidates from a library of commercially available compounds (Specs database, Delft, The Netherlands). After multi-step selection (described in Chapter 4) we chose 10 compounds for biological evaluation.

7.4.2 Biological evaluation of potential inhibitors in cell based assays

We have biologically evaluated 10 selected compounds from virtual screening using previously described tumorigenic MDA-MB-231 cell line overexpressing either Bcl-3 WT or Bcl-3 ANK M123 and also in non-tumorigenic human embryonic kidney HEK-293 cells. HEK-293 cells were chosen as a cell model to study Bcl-3 interactions with NF-κB subunits, because they are easily manipulated and express negligible levels of endogenous Bcl-3 (A. Chariot, Personal Communication). An indirect sandwich ELISA was optimised to detect Bcl-3-p50

interactions and found as a suitable method for monitoring Bcl-3-p50 PPIs (Chapter 3).

After determining the toxicity in both of the selected cell lines, compounds were tested in three optimised cell based assays. A combination of three cell based assays were used in order to establish the effect of these compounds not only on disruption of Bcl-3-p50 binding but also the related suppression of NF-κB activity and cell motility (Chapter 4). Compound 6 (B3JS6) was then selected as a lead compound with low nM activities in all three assays.

7.4.3 Structure activity relationships of a lead compound

Novel analogues of the lead compound were designed and aimed to explore structure-activity relationships. We have introduced three types of changes giving rise to three series of analogues (Chapter 5). An efficient two-step synthetic route has been developed under mild conditions. Final compounds were obtained by recrystalization from ethanol and the high purity was confirmed by elemental analysis (Chapter 6).

Series 1 introduced mono substitution of F, OCH_3 and NO_2 on every position on the phenyl ring. Di- and tri- substitutions of F and OCH_3 were also introduced. Series 2 aimed to explore the effect of prolonging the linker chain, and the effect of replacing the morpholine ring with other heterocycles. Series 3 aimed to explore whether substitution on the benzamide ring would affect the activity.

21 newly designed and synthesised analogues were biologically evaluated in cell based assays similarly to the first round selection of 10 purchased compounds (Chapter 5). SAR results indicate that the length of the linker chain and the presence of a morpholine ring are important moieties for the activity. Furthermore, substitution on the benzoyl ring could increase the activity, as demonstrated with almost 10 fold increase in activity when 3-methoxy substitution was introduced. On the other hand, di- and tri- substituted analogues on the benzoyl ring showed a decrease in the activity. Similarly, substitution on the anthranilic ring decreased the activity (summarised in Figure 7.1).

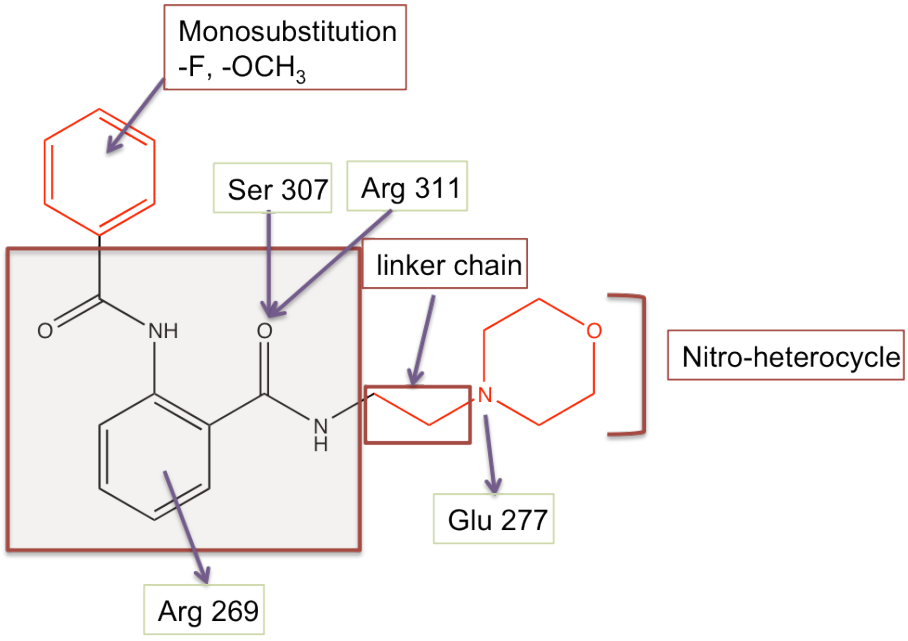

Figure 7.1 Structure activity relationships (SAR) of the lead compound
The core structure that was not modified in our SAR study is shown in a red box. Four Bcl-3 residues (in green boxes) were observed to interact with the lead compound. The importance of the length of the linker chain and a presence of a nitro-heterocycle (such as morpholine) for the activity was demonstrated. Monosubstitution on the benzoyl ring (–F, –OCH_3) is important to retain or further increase the activity.

7.5 Future directions

7.5.1 Further chemical modification of structural analogues

Synthesis of more structural analogues to further explore the SAR of the lead compound will be performed in the near future. The new analogues will aim to further increase the efficacy and drug like properties of the lead compound.

The novelty of structural analogues already analysed in cell based assays was determined via Scifinder and Pubchem search in order to provide bases for a patent application. Unfortunately, the lead compound and a few structural analogues (such as 15f) were already evaluated in various biological assay, and even though none of the assays found them active, still can not be considered as completely novel compounds. Therefore novel structural analogues will be designed considering the current SAR results in order to be in a stronger position for a patent application.

Modelling studies could evaluate the potential of the selected compounds to bind IκBα and (or) other members of the IκB family. Further *in vitro* assays will also aim to confirm the selectivity of selected compounds towards Bcl-3.

7.5.2 Further *in vivo* studies to support therapeutic potential of Bcl-3

Further studies are needed in order to proceed with potential Bcl-3 inhibitors towards a clinical setting. Previously we have shown that suppression of Bcl-3 in murine breast cancer cell line, MG1361, resulted in an 80% decrease in metastatic formation *in vivo* in a metastatic model of breast cancer as compared to control xenografts (Wakefield et al., 2013). Current studies are evaluating whether Bcl-3 suppression in human breast cancer cell line, MDA-MB-231, would have the same effect on inhibition of initial secondary tumour seeding and spread at distal sites in an *in vivo* xenograft model.

Having identified that the Bcl-3 ANK M123 binding mutant acts in a dominant negative manner, we are looking at whether MDA-MB-231 cells overexpressing Bcl-3 ANK M123 injected by tail vein in a xenografts experiment would suppress the growth and spread of existing metastatic lesion in addition to the effect on initial seeding and spread.

Even though MDA-MB-231 Bcl-3 WT overexpressing cells did not promote primary tumour growth in orthotopic xenografts models, the effect on formation and growth of lung metastasis is currently being evaluated in a tail vein xenografts experiment.

7.5.3 Future perspectives of Bcl-3 inhibitors

Toxicology studies are being done in collaboration with Dr. Annette Byrne (Royal College of Surgeons, Dublin, Ireland) using C57 BI 6 mouse strain. The lead compound was not found toxic up to concentration of 3.5 mg/kg; unfortunately higher concentration could not be used because of low aqueous solubility. Pharmacodynamic studies are clearly needed to establish the drug like properties and bioavailability *in vivo* and are planned in the near future.

In the meantime, *in vivo* experiments are evaluating the efficacy of designed inhibitors, firstly of 15a and 15f. With the use of luciferase expressing MDA-MB-231 cells we will be able to visualise any formed metastasis in a tail vein xenografts experiment and evaluate the effect of Bcl-3 suppression with the use of our potential inhibitors on seeding, spread and eventually, growth of secondary tumours.

Other future *in vitro* and *in vivo* studies should aim to establish whether adjuvant administration of Bcl-3 inhibitors to current breast cancer therapy would be of benefit and importantly which combination would improve the therapeutic outcome of breast cancer patients.

Bcl-3 was found overexpressed in various types of cancers as discussed in the general introduction (Chapter 1), therefore it would be of interest to evaluate whether Bcl-3 inhibition would be beneficial for other cancers in addition to breast cancers. Further studies should also aim to determine which subclass of patient would most likely benefit from Bcl-3 inhibitors and how to quickly evaluate that in the clinic.

References

Ahmed, S. U. & Milner, J. 2009. Basal Cancer Cell Survival Involves JNK2 Suppression of a Novel JNK1/c-Jun/Bcl-3 Apoptotic Network. *PLos ONE,* 4**,** e7305.

Andela, V. B., Schwarz, E. M. & Puzas, J. E. 2000. Tumor Metastasis and the Reciprocal Regulation of Prometastatic and Antimetastatic Factors by Nuclear Factor kB. *Cancer Res,* 60**,** 6557-6562.

Au, W. Y., Horsman, D. E., Ohno, H., Klasa, R. J. & Gascoyne, R. D. 2002. Bcl-3/IgH translocation (14;19)(q32;q13) in Non-Hodgkin's Lymphomas. *Leukemia&Lymphoma,* 43**,** 813-816.

Baldwin, A. S. 2001. Control of oncogenesis and cancer therapy resistance by the transcription factor NF-κB. *J. Clin. Invest.,* 107**,** 241-246.

Bartkova, J., Lukas, J., Müller, H., Lützhøt, D., Strauss, M. & Bartek, J. 1994. Cyclin D1 protein expression and function in human breast cancer. *Int. J. Cancer,* 57**,** 353-361.

Basseres, D. & Baldwin, A. 2006. Nuclear factor-kB and inhibitor of kB kinase pathways in oncogenic initiation and progression. *Oncogene,* 25**,** 6817-6830.

Bauer, A., Villunger, A., Labi, V., Fischer, S. F., Strasser, A., Wagner, H., Schmid, R. M. & Hacker, G. 2006. The NF-κB regulator Bcl-3 and the BH3-only proteins Bim and Puma control the death of activated T cells. *Proc Natl Acad Sci U S A,* 103**,** 10979-10984.

BCCResearch 2008. Cancer therapies:Technologies and global markets.

Beg, A. A., Sha, W., Bronso, R., Ghosh, S. & Baltimore, D. 1995. Embryonic lethality and liver degeneration in mice lacking the RelA component of NF-kB. *Nature,* 376**,** 167-170.

Bild, A. H., Parker, J. S., Gustafson, A. M., Acharya, C. R., Hoadley, K. A., Anders, C., Marcom, P. K., Carey, L. A., Potti, A., Nevins, J. R. & Perou, C. M. 2009. An integration of complementary strategies for gene-expression analysis to reveal novel therapeutic opportunities for breast cancer. *Breast Cancer Res,* 11.

BiosolveITGmbH FlexX 3.0. Sannkt Augustin, Germany.

Biswas, D. K., Cruz, A. P., Gansberger, E. & Pardee, A. B. 2000. Epidermal growth factor-induced nuclear factor κB activation: A major pathway of cell-cycle progression in estrogen-receptor negative breast cancer cells. *PNAS,* 97**,** 8542-8547.

Biswas, D. K. & Iglehart, J. D. 2006. Linkage Between EGFR Family Receptors and Nuclear Factor KappaB (NF-kB) Signaling in Breast Cancer. *J Cell Physiol,* 209**,** 645-652.

Biswas, D. K., Martin, K. J., McAlister, C., Cruz, A. P., Graner, E., Dai, S.-c. & Pardee, A. B. 2003. Apoptosis Caused by Chemotherapeutic Inhibition of Nuclear Factor-κB Activation. *Cancer Res,* 63**,** 290-295.

Biswas, D. K., Shi, Q., Baily, S., Strickland, I., Ghosh, S., Pardee, A. B. & Iglehart, J. D. 2004. NF-κB activation in human breast cancer specimens and its role in cell proliferation and apoptosis. *Proc Natl Acad Sci U S A,* 101**,** 10137-10142.

Bonvin, A. M. 2006. Flexible protein-protein docking. *Curr. Opin. Struct. Biol.,* 16**,** 194-200.

Bours, V., Franzoso, G., Azarenko, V., Park, S., Kanno, T., Brown, K. & Siebenlist, U. 1993. The oncoprotein Bcl-3 directly transactivates through kappa B motifs via association with DNA-binding p50B homodimers. *Cell,* 72**,** 729-739.

Brasier, A. R., Lu, M., Hai, T., Lu, Y. & Boldogh, I. 2001. NF-kappa B-inducible BCL-3 expression is an autoregulatory loop controlling nuclear p50/NF-kappa B1 residence. *J. Biol. Chem.,* 276**,** 32080-32093.

Brocke-Heindrich, K., Ge, B., Cvijic, H., Pfeifer, G., Loffler, D., Henze, C., McKeithan, T. & Horn, F. 2006. BCL3 is induced by IL-6 via Stat3 binding to intronic enhancer HS4 and represses its own transcription. *Oncogene,* 25**,** 7297-7304.

Bundy, D. L. & McKeithan, T. W. 1997. Diverse Effects of BCL3 Phosphorylation on Its Modulation of NF-κB p52 Homodimer Binding to DNA. *J. Biol. Chem.,* 272**,** 33132-33139.

Carey, L., Perou, C., Livasy, C., Dressier, L., Cowan, D., COnway, K., Karaca, G., Troester, M., Tse, C., Edmiston, S., Deming, S., Geradts, J., Cheang, M., Nielsen, T., Moorman, P., Earp, H. & Milikan, R. 2006. Race, breast cancer subtypes, and survival in the Carolina Breast Cancer Study. *JAMA,* 21**,** 2492-2502.

Carey, L. A. 2010. Through a glass darkly: Advances in understanding breast cancer biology, 2000-2010. *Clin breast cancer,* 10**,** 188-195.

Carney, W. P., Leitzel, K., Ali, S., Neumann, R. & Lipton, A. 2007. HER-2/neu diagnostics in breast cancer. *Breast Cancer Res,* 9**,** 1186.

Charafe-Jauffret, E., Ginestier, C., Iovino, F., Wicinski, J., Cervera, N., Finetti, P., Hur, M., Diebel, M., Monville, F., Dutcher, J., Brown, M., Viens, P., Xerri, L., Bertucci, F., Stassi, G., Dontu, G., Birnbaum, D. & Wicha, M. 2009. Breast cancer cell lines contain functional cancer stem cells with metastatic capacity and a distinct molecular signature. *Cancer Res,* 2009**,** 1302-1313.

Charifson, P. S., Corkery, J. J., Murcko, M. A. & Walters, W. P. 1999. Consensus Scoring: A Method for Obtaining Improved Hit Rates from Docking Databases of Three-Dimensional Structures into Proteins. *J. Med. Chem.,* 42**,** 5100-5109.

Choi, H. J., Lee, J. M., Kim, H., Nam, H. J., Shin, H.-J. R., Kim, D., Ko, E., Noh, D.-Y., Kim, K. & Baek, J. H. K. S. H. 2010. Bcl3-dependent stabilization of CtBP1 is crucial for the inhibition of apoptosis and tumor progression in breast cancer. *Biochem. Biophys. Res. Commun.,* 400**,** 396-402.

Chua, H. L., Bhat-Nakshatri, P., Clare, S. E., Morimiya, A., Badve, S. & Nakshatri, H. 2007. NF-kappaB represses E-cadherin expression and enhances epithelial to mesenchymal transition of mammary epithelial cells: potential involvement of ZEB-1 and ZEB-2. *Oncogene,* 26**,** 711-24.

Clarkson, R. W., Heeley, J. L., Chapman, R., Aillet, F., Hay, R. T., Wyllie, A. & Watson, C. J. 2000. NF-kappaB inhibits apoptosis in murine mammary epithelia. *J Biol Chem,* 275**,** 12737-42.

Cogswell, P. C., Guttridge, D. C., Funkhouser, W. K. & Baldwin, A. S. 2000. Selective activation of NF-kB subunits in human breast cancer: potential roles for NF-kB2/p52 and for Bcl-3. *Oncogene,* 19**,** 1123-1131.

Curtis, C., Shah, S. P., Chin, S.-F., Turashvili, G., Rueda, O. M., Dunning, M. J., Speed, D., Lynch, A. G., Samarajiwa, S., Yuan, Y., Gra, S., Ha, G., Haffari, G., Bashashati, A., Russell, R., McKinney, S., Langerød, A., Green, A.,

Provenzano, E., Wishart, G., Pinder, S., Watson, P., Markowetz, F., Murphy, L., Ellis, I., Purushotham, A., Børresen-Dale, A.-L., Brenton, J. D., Tavare, S., Caldas, C. & Aparicio, S. 2012. The genomic and transcriptomic architecture of 2,000 breast tumours reveals novel subgroups. *Nature,* 486**,** 346-352.

Dechend, R., Hirano, F., Lehnamm, K., Heissmeyer, V., Ansieau, S., Wulczyn, F. G., Scheidereit, C. & Leutz, A. 1999. The Bcl-3 oncoprotein acts as a bridging factor between NF-kappaB/Rel and nuclear co-regulators. *Oncogene,* 18**,** 3316-3323.

Dey, A., Tergaonkar, V. & Lane, D. P. 2008. Double-edged swords as cancer therapeutics: simultaneously targeting p53 and NF-kB pathways. *Nature Reviews Drug Discovery,* 7**,** 1031-1040.

Dontu, G., Al-Hajj, M., Abdallah, W., Clarke, M. & Wicha, M. 2003. Stem cells in normal breast development and breast cancer. *Cell Proliferation,* 36**,** 59-72.

Eckhardt, B. L., Francis, P. A., Parker, B. S. & Anderson, R. L. 2012. Strategies for the discovery and development of therapies for metastatic breast cancer. *Nat Rev Drug Discov,* 11**,** 479-497.

Ferlay, J., Shin, H., Bray, F., Forman, D., Mathers, C. & Parkin, D. 2010. GLOBOCAN 2008 v1.2, Cancer Incidence and Mortality Worldwide: IARC CancerBase No. 10. *IARC.*

Foulkes, W. D., Brunet, J.-S., Stefansson, I. M., Straume, O., Chappuis, P. O., Begin, L. R., Hamel, N., Goffin, J. R., Wong, N., Trudel, M., Kapusta, L., Porter, P. & Akslen, L. A. 24. The Prognostic Implication of the Basal-Like (Cyclin Ehigh/p27low/p53/ Glomeruloid-Microvascular-Proliferation) Phenotype of BRCA1-Related Breast Cancer. *Cancer Res,* 64**,** 830-835.

Franzoso, G., Bours, V., Azarenko, V., Park, S., Tomita-Yamaguchi, M., Kanno, T., Brown, K. & Siebenlist, U. 1993. The oncoprotein Bcl-3 can facilitate NF-kappa B-mediated transactivation by removing inhibiting p50 homodimers from select kappa B sites. *The EMBO Journal,* 12**,** 3893-3901.

Franzoso, G., Bours, V., Park, S., Tomita-Yamaguchi, M., Kelly, K. & Siebenlist, U. 1992. The candidate oncoprotein Bcl-3 is an antagonist of p50/NF-kappa B-mediated inhibition. *Nature,* 359**,** 339-342.

Franzoso, G., Carlson, L., Poljak, L., Shores, E., Epstein, S., Leonardi, A., Grinberg, A., Tran, T., Scharton-Kersten, T., Anver, M., Love, P., Brown, K. & Siebenlist, U. 1998. Mice deficient in nuclear factor (NF)-kappa B/p52 present with defects in humoral responses, germinal center reactions, and splenic microarchitecture. *J. Exp. Med.,* 19**,** 147-159.

Franzoso, G., Carlson, L., Scharton-Kersten, T., Shores, E. W., Epstein, S., Grinberg, A., Tran, T., Shacter, E., Leonardi, A., Anver, M., Paul-Love, Sher, A. & Siebenlist, U. 1997. Critical Roles for the Bcl-3 Oncoprotein in T Cell–Mediated Immunity, Splenic Microarchitecture, and Germinal Center Reactions. *Immunity,* 6**,** 479-490.

Friesner, R. A., Murphy, R. B., Repasky, M. P., Frye, L. L., Greenwood, J. R., Halgren, T. A., Sanschagrin, P. C. & Mainz, D. T. 2006. Extra Precision Glide: Docking and Scoring Incorporating a Model of Hydrophobic Enclosure

for Protein-Ligand Complexes. *J. Med. Chem.,* 49**,** 6177-6196.

Fujita, T., Nolan, G. P., Liou, H.-C., L.Scott, M. & Baltimore, D. 1993. The candidate proto-oncogene bcl-3 encodes a transcriptional coactivator that activates through NF-kappa B p50 homodimers. *Genes & Development,* 7**,** 1354-1363.

Garner, A. L. & Janda, K. D. 2011. Protein-Protein Interactions and Cancer: Targeting the Central Dogma. *Curr. Topics Med. Chem.,* 11**,** 258-280.

Gildea, J. J., Seraj, M. J., Oxford, G., Harding, M. A., Hampton, G. M., Moskaluk, C. A., Frierson, H. F., Conaway, M. R. & Theodorescu, D. 2002. RhoGDI2 is an invasion and metastasis suppressor gene in human cancer. *Cancer Res,* 62**,** 6418-23.

Gilmore, J. L., Hays, S. J., Caprathe, B. W., Lee, C., Emmerling, M. R., Michael, W. & Jaen, J. C. 1996. Synthesis and evaluation of 2-aryl-4H-3,1-benzoxazin-4-ones as C1r serine protease inhibitors. *Bioorg. Med. Chem. Lett.,* 6**,** 679-682.

Gilmore, T. 2006. Introduction to NF-κB: players, pathways, perspectives. *Oncogene,* 25.

Guan, Y., Yao, H., Zheng, Z., Qiu, G. & Sun, K. 2011. MiR-125b targets BCL3 and suppresses ovarian cancer proliferation. *Int. J. Cancer,* 128**,** 2274-2283.

Guardavaccaro, D., Corrente, G., Covone, F., Micheli, L., D'Agnano, I., Starace, G., Caruso, M. & Tirone, F. 2000. Arrest of G(1)-S progression by the p53-inducible gene PC3 is Rb dependent and relies on the inhibition of cyclin D1 transcription. *Mol Cell Biol.,* 20**,** 1797-1815.

Guarino, M. 2007. Epithelial–mesenchymal transition and tumour invasion. *Int. J. Biochem. Cell Biol.,* 39**,** 2153-2160.

Haffner, M. C., Berlato, C. & Doppler, W. 2006. Exploiting Our Knowledge of NF-κB Signaling for the Treatment of Mammary Cancer. *J Mammary Gland Biol Neoplasia,* 11**,** 63-73.

Harrison, H., Farnie, G., Howell, S., Rock, R., Stylianou, S., Brennan, K., Bundred, N. & Clarke, R. 2010. Regulation of breast cancer stem cell activity by signaling through the Notch4 receptor. *Cancer Res,* 70**,** 709-718.

Hatada, E. N., Nieters, A., Wulczyn, F. G., Naumann, M., Meyer, R., Nucifora, G., McKeithan, T. W. & Scheidereit, C. 1992. The ankyrin repeat domains of the NF-kappa B precursor p105 and the protooncogene bcl-3 act as specific inhibitors of NF-kappa B DNA binding. *Proc Natl Acad Sci U S A* 89**,** 2489-2493.

Hayden, M. S. & Ghosh, S. 2004. Signaling to NF-κB. *Genes & Development,* 18**,** 2195-2224.

Heissmeyer, V., Krappann, D., Wulczyn, F. G. & Scheidereit, C. 1999. NF-kB p105 is a target of IkB kinases and controls signal induction of Bcl-3–p50 complexes. *The EMBO Journal,* 18**,** 4766-4778.

Helbig, G., Christopherson, K. W., 2nd, Bhat-Nakshatri, P., Kumar, S., Kishimoto, H., Miller, K. D., Broxmeyer, H. E. & Nakshatri, H. 2003. NF-kappaB promotes breast cancer cell migration and metastasis by inducing the expression of the chemokine receptor CXCR4. *J Biol Chem,* 278**,** 21631-8.

Hennessy, B. T., Gonzalez-Angulo, A.-M., Stemke-Hale, K., Gilcrease, M. Z., Krishnamurthy, S., Lee, J.-S., Fridlyand, J., Sahin, A., Agarwal, R., Joy, C., Liu, W., Stivers, D., Baggerly, K., Carey, M., Lluch, A., Monteagudo, C., He, X., Weigman, V., Fan, C., Palazzo, J., Hortobagyi, G. N., Nolden, L. K., Wang, N. J., Valero, V., Gray, J. W., Perou, C. M. & Mills, G. B. 2009. Characterization of a Naturally Occurring Breast Cancer Subset Enriched in Epithelial-to-Mesenchymal Transition and Stem Cell Characteristics. *Cancer Res,* 69**,** 4116-4124.

Hennessy, C., Henry, J. A., May, F. E. B., Westley, B. R., Angus, B. & Lennard, T. W. J. 1991. Expression of the Antimetastatic Gene nm23 in Human Breast Cancer: An Association WIth Good Prognosis. *J Natl Cancer Inst,* 83**,** 281-285.

Hess, B., Kutzner, C., Spoel, D. V. d. & Lindahl, E. 2008. Algorithms for highly efficient, load-balanced, and scalable molecular simulation. *J. Chem. Theory Comput.,* 4**,** 435-447.

Higgins, M. J. & JOSE BASELGA, M. D. 2011. Targeted therapies for breast cancer. *J. Clin. Invest.,* 121**,** 3797-3803.

Hoelder, S., Clarke, P. A. & Workman, P. 2012. Discovery of small molecule cancer drugs: Successes, challenges and opportunities. *Mol. Oncol.,* 6**,** 155-176.

Horikawa, T., Yang, J. & kondo, S. 2007. Twist and epithelial-mesenchymal transition are induced by the EBV oncoprotein latent membrane protein 1 and are associated with metastatic nasopharyngeal carcinomea. *Cancer Res,* 67**,** 1970-1978.

Hsieh, P.-W., Hwang, T.-L., Wu, C.-C., Chang, F.-R., Wanga, T.-W. & Wu, Y.-C. 2005. The evaluation of 2,8-disubstituted benzoxazinone derivatives as anti-inflammatory and anti-platelet aggregation agents. *Bioorg. Med. Chem. Lett.,* 15**,** 2786-2789.

Hsieh, P.-W., Yu, H.-P., Chang, Y.-J. & Hwang, T.-L. 2010. Synthesis and evaluation of benzoxazinone derivatives on activity of human neutrophil elastase and on hemorrhagic shock-induced lung injury in rats. *Eur. J. Med. Chem.,* 45**,** 3111-3115.

Huber, M., Kraut, N. & Beug, H. 2005. Molecular requirements for epithelial-mesenchymal transition during tumor progression. *Curr Opin Cell Biol,* 15**,** 548-558.

Huber, M. A., Azoitei, N., Baumann, B., Grunert, S., Sommer, A., Pehamberger, H., Kraut, N., Beug, H. & Wirth, T. 2004a. NF-kappaB is essential for epithelial-mesenchymal transition and metastasis in a model of breast cancer progression. *J Clin Invest,* 114**,** 569-81.

Huber, M. A., Beug, H. & Wirth, T. 2004b. Epithelial-mesenchymal transition: NF-kappaB takes center stage. *Cell Cycle,* 3**,** 1477-80.

Izzo, J., Malhotra, U. & Wu, T. 2007. Clinical biology of esophageal adenocarcinoma after surgery is influenced by nuclear factor-kappaB expression. *Proc Natl Acad Sci U S A,* 104**,** 12790-12795.

Jacobs, M. D. & Harrison, S. C. 1998. Structure of an IkappaBalpha/NF-kappaB complex. *Cell,* 95**,** 749-758.

Janda, E., Lehmann, K., Killisch, I., Jechlinger, M., Herzig, M., Downward, J., Beug, H. & Grünert, S. 2002. Ras and TGF cooperatively regulate epithelial cell plasticity and metastasis: dissection of Ras signaling pathways. *J. Cell Biol.,* 156**,** 299-313.

Jubb, H., Higueruelo, A., Winter, A. & Blundell, T. 2012. Structural biology and drug discovery for protein-protein interactions. *Trends Pharmacol. Sci.,* 33**,** 241-248.

Karin, M., Cao, Y., Gretan, F. R. & Li, Z.-W. 2002. NF-κB in cancer: From innocent bystander to major culprit. *Nat. Rev. Cancer,* 2**,** 301-310.

Karin, M., Yamamoto, Y. & Wang, Q. M. 2004. The IKK NF-κB System: A Treasure Trove For Drug Development. *Nat. Rev. Cancer,* 3**,** 17-26.

Kashatus, D., Cogswell, P. & Baldwin, A. S. 2006. Expression of the Bcl-3 proto-oncogene suppresses p53 activation. *Genes & Development,* 20**,** 225-235.

Kerr, L. D., Duckett, C. S., Wamsley, P., Zhang, Q., Chiao, P., Nabel, G., McKeithan, T. W., Baeuerle, P. A. & Verma, I. M. 1992. The proto-oncogene BCL-3 encodes an IKB protein. *Genes & Development,* 6**,** 2352-2363.

Keutgens, A., Zhang, X., Shostak, K., Robert, I., Olivier, S., Vanderplasschen, A., Chapelle, J.-P., Viatour, P., Merville, M.-P., Bex, F., Gothot, A. & Chariot, A. 2010. BCL-3 Degradation Involves Its Polyubiquitination through a FBW7-independent Pathway and Its Binding to the Proteasome Subunit PSMB1. *J. Biol. Chem.,* 285**,** 25831-25840.

Kim, D. W., Sovak, M. A., Zanieski, G., Genevieve, N., Romieu-Mourez, R., Lau, A. W., J.Hafer, L., Yaswen, P., Stampfer, M., Rogers, A. E., Russo, J. & Sonenshein, G. E. 2000. Activation of NF-kB/Rel occurs early during neoplastic transformation of mammary cells. *Carcinogenesis,* 21**,** 871-879.

Kim, H., Hawke, N. & Baldwin, A. 2006. NF-κB and IKK as therapeutic targets in cancer. *Cell Death Diff.,* 13**,** 738-747.

Kitchen, D. B., Decornez, H., Furr, J. R. & Bajorath, J. r. 2004. Docking and scoring in virtual screening for drug discovery: methods and applications *Nat. Rev. Drug Discovery,* 3**,** 935-949.

Korb, O., Stutzle, T. & E.Exner, T. 2009. Empirical scoring functions for andvanced protein-ligand docking with PLANTS. *J. Chem. Inf. Model.,* 49**,** 84-96.

Korb, O., Stutzle, T. & Exner, T. 2006. Ant Colony Optimization and Swarm Intelligence, 5th International Workshop. *ANTS LNCS4150, 247-258.*

Korkaya, H., Paulson, A., Iovino, F. & Wicha, M. 2008. HER2 regulates the mammary stem/progenitor cell population driving tumorigenesis and invasion. *Oncogene,* 27**,** 6120-6130.

Kramer, B., Rarey, M. & Lengauer, T. 1999. Evaluation of the FlexX incremental construction algorithm for protein-ligand docking. *J. Mol. Biol.,* 37**,** 228-241.

Kuwata, H., Watanabe, Y., Miyoshi, H., Yamamoto, M., Kaisho, T., Takeda, K. & Akira, S. 2003. IL-10-inducible Bcl-3 negatively regulates LPS-induced TNF-α production in macrophages. *Blood,* 102**,** 4123-4129.

Laurentiis, M. D., Cianniello, D., Caputo, R., Stanzione, B., Arpino, G., Cinieri, S., Lorusso, V. & Placido, S. D. 2010. Treatment of triple negative breast cancer (TNBC): current options and future perspectives. *Cancer Treat. Rev.,* 36**,** S80-S86.

Leach, A. R. 2001. *Molecular Modelling Principles and Applications*, Pearson Education Limited.

Lehmann, B. D., Bauer, J. A., Chen, X., Sanders, M. E., Chakravarthy, A. B., Shyr, Y. & Pietenpol, J. A. 2011. Identification of human triple-negative breast cancer subtypes and preclinical models for selection of targeted therapies. *J. Clin. Invest.,* 121**,** 2750-2767.

Liu, W., Bagaitkar, J. & Watabe, K. 2007. Roles of AKT signal in breast cancer. *Frontiers in Bioscience,* 12**,** 4011-4019.

Liu, Z. G., Hsu, H. L., Goeddel, D. V. & Karin, M. 1996. Dissection of TNF receptor 1 effector functions: JNK activation is not linked to apoptosis while NF-kappaB activation prevents cell death. *Cell,* 87**,** 565-576.

Livasy, C. A., Perou, C. M., Karaca, G., Cowan, D. W., Maia, D., SusanJackson, Tse, C.-K., Nyante, S. & Mililikan, R. C. 2007. Identification of a basal-like subtype of breast ductal carcinoma in situ. *Human Pathology,* 38**,** 197-204.

MacDonald, I. C., Groom, A. C. & Chambers, A. F. 2002. Cancer spread and micrometastasis development: quantitative approaches for in vivo models. *BioEssays,* 24**,** 885-893.

Maldonado, V., Espinosa, M., Prueferer, F., Patino, N., Ceballos-Cancino, G., Urzua, U., Juretic, N. & Melendez-Zajgla, J. 2010. Gene Regulation by BCL3 in a Cervical Cancer Cell Line. *Folia Biologica,* 56**,** 183-193.

Massoumi, R., Chmielarska, K., Hennecke, K., Pfeifer, A. & Fassler, R. 2006. Cyld Inhibits Tumor Cell Proliferation by Blocking Bcl-3-Dependent NF-kB Signaling. *Cell,* 125**,** 665-677.

Mathas, S., Johrens, K., Joos, S., Lietz, A., Hummel, F., Janz, M., Jundt, F., Anagnostopoulos, I., Bommert, K., Lichter, P., Stein, H., Scheidereit, C. & Dorken, B. 2005. Elevated NF-kappaB p50 complex formation and Bcl-3 expression in classical Hodgkin, anaplastic large-cell, and other peripheral T-cell lymphomas. *Blood,* 106**,** 4287-93.

McKeihan, T. W., Hitoshi Ohno, G. T., timothy W.Mc Keithan, Dickstein, J. & Hume, E. 1994. Genomic structure of the candidate proto-oncogene BCL3. *Genomics,* 24**,** 120-126.

McKeithan, T. W., Ohno, H. & O.Diaz, M. 1990. Identification of a transcriptional unit adjacent to the breakpoint in the 14;19 translocation of chronic lymphocytic leukemia. *Genes, Chromosomes and Cancer,* 1**,** 247-255.

Meckhofer, E., Cogswell, P. & Baldwin, A. 2010. Her2 activates NF-kB and induces invasion through the canonical pathway involving IKKalfa. *Oncogene,* 29**,** 1238-1248.

Mehlen, P. & Puisieux, A. 2006. Metastasis: a question of life or death. *Nat. Rev.,* 6**,** 449-458.

Meng, S., Tripathy, D., Frenkel, E. P., Shete, S., Naftalis, E. Z., Huth, J. F., Beitsch, P. D., Leitch, M., Hoover, S., Euhus, D., Haley, B., Morrison, L., Fleming, T. P., Herlyn, D., Terstappen, L. W. M. M., Fehm, T., Tucker, T. F., Lane, N., Wang, J. & Uhr, J. W. 2004. Circulating Tumor Cells in Patients with Breast Cancer Dormancy. *Clin. Cancer Res.,* 10**,** 8152-8162.

Merlo, G. R., Basolo, F., Fiore, L., Duboc, L. & Hynes, N. E. 1995. p53-dependent and p53-independent Activation of Apoptosis in Mammary Epithelial Cells Reveals a Survival Function of EGF and Insulin. *J. Cell Biol.,* 128**,** 1185-1196.

Michel, F., Soler-Lopez, M., Petosa, C., Cramer, P., Siebenlist, U. & Muller, C. W. 2001. Crystal structure of the ankyrin repeat domain of Bcl-3: a unique member of the IκB family. *The EMBO Journal,* 20**,** 6180-6190.

Miller, F., Soule, H., Tait, L., Pauley, R., Wolman, S., Dawson, P. & Heppner, G. 1993. Xenograft model of progressive human proliferative breast disease. *J Natl Cancer Inst,* 3**,** 1725-1732.

Mitchell, T. C., Thompson, B. S., Trent, J. O. & Casella, C. R. 2002. A short domain within Bcl-3 is responsible for its lymphocyte survival activity. *Ann. N.Y. Acad. Sci,* 975**,** 132-147.

MOE 2009.10. Molecular-Operating-Environment. Inc. Montreal, Quebec, Canada: Chemical Computing Group.

Morrow, P. K. H., Zambrana, F. & Esteva, F. J. 2009. Advances in systemic therapy for HER2-positive metastatic breast cancer. *Breast Cancer Res,* 11**,** 207.

Musgrove, E. A., Lee, C. S. L., Buckley, M. F. & Sutherland, R. L. 1994. Cyclin D1 induction in breast cancer cells shortens G1 and is sufficient for cells arrested in G1 to complete the cell cycle. *Proc Natl Acad Sci U S A,* 91**,** 8022-8026.

Na, S.-Y., Choi, J.-E., Kim, H.-J., Jhun, B. H., Lee, Y.-C. & Lee, J. W. 1999. Bcl3, an IκB Protein, Stimulates Activating Protein-1 Transactivation and Cellular Proliferation. *J. Biol. Chem.,* 274**,** 28491-28496.

Nahta, R. & Esteva, F. J. 2006. Molecular mechanism of trastuzumab resistance. *Breast Cancer Res,* 8**,** 1186.

Naugler, W. E. & Karin, M. 2008. NF-kB and cancer - identifying targets and mechanisms. *Curr. Opin. Genet. Dev.,* 18**,** 19-26.

Naumann, M., Wulczyn, F. G. & Scheidereit, C. 1993. The NF-kappa B precursor p105 and the proto-oncogene product Bcl-3 are I kappa B molecules and control nuclear translocation of NF-kappa B. *The EMBO Journal,* 12**,** 213-222.

Nishikori, M., Maesako, Y., Ueda, C., Kurata, M., Uchiyama, T. & Ohno, H. 2003. High-level expression of BCL3 differentiates t(2;5)(p23;q35)-positive anaplastic large cell lymphoma from Hodgkin disease. *Blood,* 101**,** 2789-2796.

Nolan, G. P., Fujita, T., Bhatia, K., Huppi, C., Liou, H.-C., Scott, M. L. & Baltimore, D. 1993. The bcl-3 proto-oncogene encodes a nuclear I kappa B-like molecule that preferentially interacts with NF-kappa B p50 and p52 in a phosphorylation-dependent manner. *Mol. Cell. Biol.,* 13**,** 3557-3566.

Normanno, N., Morabito, A., Luca, A. D., Piccirillo, M. C., Gallo, M., Maiello, M. R. & Perrone, F. 2009. Target-based therapies in breast cancer: current status and future perspectives. *Endocrine-related cancer,* 16**,** 675-702.

O'Neil, B., Buzkova, P., Farrah, H., Kashatus, D., Sanoff, H., Goldberg, R., Baldwin, A. & Funkhouser, W. 2007. Expression of nuclear factor-kappaB family proteins in hepatocellular carcinomas. *Oncology,* 72**,** 97-104.

Ohno, H., Takimoto, G. & McKeithan, T. W. 1990. The candidate proto-oncogene bcl-3 is related to genes implicated in cell lineage determination and cell cycle control. *Cell,* 60**,** 991-997.

Ong, S. T., Hackbarth, M. L., Degenstein, L. C., Baunoch, D. A., Anastasi, J. & McKeithan, T. W. 1998. Lymphadenopathy, splenomegaly, and altered immunoglobulin production in BCL3 transgenic mice. *Oncogene,* 16**,** 2333-43.

Orlowski, R. Z. & Dees, E. C. 2002. Applying drugs that affect the ubiquitin-proteasome pathway to the therapy of breast cancer. *Breast Cancer Res,* 5.

Palma, M. D. & Hanahan, D. 2012. The biology of personalized cancer medicine: Facing individual complexities underlying hallmark capabilities. *Mol. Oncol.,* 6**,** 111-127.

Pang, H., Bartlam, M., Zeng, Q., Miyatake, H., Hisano, T., Miki, K., Wong, L.-L., Gao, G. F. & Rao, Z. 2004. Crystal structure of human pirin. *J. Biol. Chem.,* 279**,** 1491-1498.

Parker, J. S., Mullins, M., Cheang, M. C. U., Leung, S., Voduc, D., Vickery, T., Davies, S., Fauron, C., He, X., Hu, Z., Quackenbush, J. F., Stijleman, I. J., Palazzo, J., Marron, J. S., Nobel, A. B., Mardis, E., Nielsen, T. O., Ellis, M. J., Perou, C. M.

& Bernard, P. S. 2009. Supervised Risk Predictor of Breast Cancer Based on Intrinsic Subtypes. *J. Clin. Oncol.,* 27**,** 1160-1167.

Pasparakis, M. 2009. Regulation of tissue homeostasis by NF-κB signalling: implications for inflammatory diseases. *Nat. Rev. Immunol.,* 9**,** 778-788.

Perkins, N. D. 2007. Integrating cell-signalling pathways with NF-κB and IKK function. *Nat. Rev.,* 8**,** 49-62.

Perkins, N. D. 2012. The diverse and complex roles of NF-kB subunits in cancer. *Nat. Rev. Cancer,* 12**,** 121-132.

Perou, C. M., Sorlie, T., Eisen, M. B., van de Rijn, M., Jeffrey, S. S., Rees, C. A., Pollack, J. R., Ross, D. T., Johnsen, H., Akslen, L. A., Fluge, O., Pergamenschikov, A., Williams, C., Zhu, S. X., Lonning, P. E., Borresen-Dale, A. L., Brown, P. O. & Botstein, D. 2000. Molecular portraits of human breast tumours. *Nature,* 406**,** 747-52.

Place, A. E., Huh, S. J. & Polyak, K. 2011. The microenvironment in breast cancer progression: biology and implications for treatment. *Breast Cancer Res,* 13**,** 227.

Polyak, K. 2007. Breast cancer: origins and evolution. *J. Clin. Invest.,* 117**,** 3155-3163.

Prat, A., Parker, J. S., Karginova, O., Fan, C., Livasy, C., Herschkowitz, J. I., He, X. & Perou, C. M. 2010. Phenotypic and molecular characterization of the claudin-low intrinsic subtype of breast cancer. *Breast Cancer Res,* 12.

Prathipati, P. & Saxena, A. K. 2006. Evaluation of Binary QSAR Models Derived from LUDI and MOE Scoring Functions for Structure Based Virtual Screening. *J. Chem. Inf. Model.,* 46**,** 39-51.

Pratt, M. A. C., Bishop, T. E., White, D., Yasvinski, G., Ménard, M., Niu, M. Y. & Clarke, R. 2003. Estrogen Withdrawal-Induced NF-κB Activity and Bcl-3 Expression in Breast Cancer Cells: Roles in Growth and Hormone Independence. *Mol. Cell. Biol.,* 23**,** 6887-6900.

Puvvada, S. D., Funkhouser, W. K., Greene, K., Deal, A., Chu, H., Baldwin, A. S., Tepper, J. E. & O'Neil, B. H. 2010. NF-κB and Bcl-3 Activation Are Prognostic in Metastatic Colorectal Cancer. *Clin. Transl. Res.,* 78**,** 181-188.

Rachet, B., Maringe, C., Nur, U., Quaresma, M., Shah, A., Woods, L. M., Ellis, L., Walters, S., Forman, D., Steward, J. & Coleman, M. P. 2009. Population-based cancer survival trends in England and Wales up to 2007: an assessment of the NHS cancer plan for England. *Lancet Oncol,* 10**,** 351-69.

Rebollo, A., Dumoutier, L., Renauld, J. C., Zaballos, A., Ayllon, V. & Martinez, A. C. 2000. Bcl-3 expression promotes cell survival following interleukin-4 deprivation and is controlled by AP1 and AP1-like transcription factors. *Mol Cell Biol,* 20**,** 3407-16.

Richon, A. B. 2008. Current status and future direction of the molecular modeling industry. *Drug Discov. Today,* 13**,** 665-669.

Rocha, S., Martin, A. M., Meek, D. W. & Perkins, N. D. 2003. p53 Represses Cyclin D1 Transcription through Down Regulation of Bcl-3 and Inducing Increased Association of the p52 NF-κB Subunit with Histone Deacetylase 1. *Mol. Cell. Biol.,* 23**,** 4713-4727.

Romieu-Mourez, R., Kim, D. W., Shin, S. M., Demicco, E. G., Landesman-Bollag, E., Seldin, D. C., Cardiff, R. D. & Sonenshein, G. E. 2003. Mouse mammary tumor virus c-rel transgenic mice develop mammary tumors. *Mol Cell Biol,* 23**,** 5738-54.

Scartozzi, M., Bearzi, I. & Pierantoni, C. 2007. Nuclear factor-kB tumor expression predicts response and survival in irinotecan-refractory metastatic colorectal cancer treated with ceruximab-irinotecan therapy. *J Clinical Oncology,* 25**,** 3930-3935.

Schlotter, C. M., Vogt, U., Algayer, H. & Brandt, B. 2008. Molecular targeted therapies for breast cancer treatment. *Breast Cancer Res,* 10**,** 1186.

Schrodinger 2009. Glide. 5.5 ed. New York, NY.

Schwarz, E. M., Krimpenfort, P., Berns, A. & Verma, I. M. 1997. Immunological defects in mice with a targeted disruption in Bcl-3. *Genes & Development,* 11**,** 187-197.

Sen, R. & Baltimore, D. 1986. Multiple Nuclear Factors Interact with the lmmunoglobulin Enhancer Sequences. *Cell,* 46**,** 705-716.

Shibata, A., Nagaya, T., Imai, T., Funahashi, H., Nakao, A. & Seo, H. 2002. Inhibition of NF-kappaB activity decreases the VEGF mRNA expression in MDA-MB-231 breast cancer cells. *Breast Cancer Res Treat,* 73**,** 237-243.

Shostak, K. & Chariot, A. 2011. NF-κB, stem cells and breast cancer: the links get stronger. *Breast Cancer Res,* 13.

Sliva, D., Rizzo, M. T. & English, D. 2002. Phosphatidylinositol 3-Kinase and NF-ĸB Regulate Motility of Invasive MDA-MB-231 Human Breast Cancer Cells by the Secretion of Urokinase-type Plasminogen Activator. *J. Biol. Chem.,* 277**,** 3150-3157.

Sonenshein, G. E. 1997. Rel/NF-kB transcription factors and the control of apoptosis. *Semin. Cancer Biol,* 8**,** 113-119.

Sorlie, T., Perou, C. M., Tibshirani, R., Aas, T., Geisler, S., Johnsen, H., Hastie, T., Eisen, M. B., van de Rijn, M., Jeffrey, S. S., Thorsen, T., Quist, H., Matese, J. C., Brown, P. O., Botstein, D., Eystein Lonning, P. & Borresen-Dale, A. L. 2001. Gene expression patterns of breast carcinomas distinguish tumor subclasses with clinical implications. *Proc Natl Acad Sci U S A,* 98**,** 10869-74.

Sotiriou, C., Neo, S. Y., McShane, L. M., Korn, E. L., Long, P. M., Jazaeri, A., Martiat, P., Fox, S. B., Harris, A. L. & Liu, E. T. 2003. Breast cancer classification and prognosis based on gene expression profiles from a population-based study. *Proc Natl Acad Sci U S A,* 100**,** 10393-8.

Soule, H., Maloney, T., Wolman, S., Peterson, W., Brenz, R., McGrath, C., Russo, J., Pauley, R., Jones, R. & Brooks, S. 1990. Isolation and characterization of a spontaneously immortalized human breast epithelial cell line, MCF-10. *Cancer Res,* 15**,** 6075-6086.

Spector, N., Xia, W., El-Hariry, I., Yarden, Y. & Bacus, S. 2007. Small molecule HER-2 tyrosine kinase inhibitors. *Breast Cancer Res,* 9**,** 1186.

Strakovs, A., Tonkikh, N. N., Petrova, M., Ryzhanova, K. V. & Palitis, E. 2002. The reaction of 2-aminoethyl and 3-aminopropyl-substituted heterocycles with 2-formyl 1,3-cyclanediones and 4-oxo-3,1-benzoxazines. *Chem. Heterocycl. Compd.,* 38**,** 449-455.

Su, A., Lorber, D., Weston, G., Baase, W., Matthews, B. & Shoichet, B. 2001. Docking molecules by families to increase the diversity of hits in database screens: computational strategy and experimental evaluation. *Proteins,* 42**,** 29-293.

Tew, G., Lorimer, E., Berg, T., Zhi, H., Li, R. & Williams, C. 2007. SmgGDS regulates cell proliferation, migration, and NF-kappa B transcriptional activity in non-small cell lung carcinoma. *J Biol Chem,* 283**,** 963-976.

Thiery, J. P. 2002. Epithelial-mesenchymal transitions in tumour progression. *Nat Rev Cancer,* 2**,** 442-54.

Thiery, J. P. & Sleeman, J. P. 2006. Complex networks orchestrate epithelial–mesenchymal transitions. *Nat. Rev. Mol. Cell Biol.,* 7**,** 131-142.

Thomas, S., Quinn, B., Das, S., Dash, R., Emdad, L., Dasgupta, S., Wang, X., Dent, P., Reed, J., Pellecchia, M., Sarkar, D. & Fisher, P. 2013. Targeting the Bcl-2 family for cancer therapy. *Expert Opin. Ther. Targets,* 17**,** 61-75.

Thompson, J. E., Phillips, R. J., Erdjument-Bromage, H., Tempst, P. & Ghosh, S. 1995. IKB-p Regulates the Persistent Response in a Biphasic Activation of NF-KB. *Cell,* 80**,** 573-582.

Thornburg, N. J., Pathmanathan, R. & Raab-Traub, N. 2003. Activation of Nuclear Factor-κB p50 Homodimer/Bcl-3 Complexes in Nasopharyngeal Carcinoma. *Cancer Res.,* 63**,** 8293-8301.

Viatour, P., Dejardin, E., Warnier, M., Lair, F., Claudio, E., Bureau, F., Marine, J.-C., Merville, M.-P., Maurer, U., Green, D., Piette, J., Siebenlist, U., Bours, V. & Chariot, A. 2004a. GSK3-Mediated BCL-3 Phosphorylation Modulates Its Degradation and Its Oncogenicity. *Mol. Cell,* 16**,** 35-45.

Viatour, P., Merville, M.-P., Bours, V. & Chariot, A. 2004b. Protein phosphorylation as a key mechanism for the regulation of BCL-3 activity. *Cell Cycle,* 3**,** 1498-1501.

Viatour, P., Merville, M.-P., Bours, V. & Chariot, A. 2005. Phosphorylation of NF-kB and IkB proteins: implications in cancer and inflammation. *Trends Biochem. Sci.,* 30**,** 43-52.

Vilimas, T., Mascarenhas, J. & Palomero, T. 2007. Targeting the NF-kappa B signaling pathway in Notch1-induced T-cell leukemia. *Nat Med,* 13**,** 70-77.

Wakefield, A. 2012. PhD Thesis.

Wakefield, A., Soukupova, J., Montagne, A., Ranger, J., French, R., Muller, W. J. & Clarkson, R. W. E. 2013. Bcl3 Selectively Promotes Metastasis of ERBB2-Driven Mammary Tumors. *Cancer Res.,* 73**,** 745-755.

Wang, C.-Y., Jr., J. C. C., Liu, R. & Jr., A. S. B. 1999. Control of inducible chemoresistance: Enhanced anti-tumor therapy through increased apoptosis by inhibition of NF-κB. *Nat. Med.,* 5**,** 412-417.

Wang, W. & Hu, Y. 2012. Small molecule agents targeting the p53-MDM2 pathway for cancer therapy. *Med. Res. Rev.,* 32**,** 1159-1196.

Waszkowycz, B., Clark, D. E. & Gancia, E. 2011. Outstanding challenges in protein-ligand docking and structure-based virtual screening. *John Wiley & Sons,* 1**,** 229-259.

Watanabe, N., Iwamura, T., Shinoda, T. & Fujita, T. 1997. Regulation of NFKB1 proteins by the candidate oncoprotein BCL-3: generation of NF-kappaB homodimers from the cytoplasmic pool of p50-p105 and nuclear translocation. *The EMBO Journal,* 16**,** 3609-3620.

Watson, C. J. 2006. Post-lactational mammary gland regression: molecular basis and implications for breast cancer. *Expert Rev Mol Med,* 8**,** 1-15.

Webster, G. A. & Perkins, N. D. 1999. Transcriptional Cross Talk between NF-kB and p53. *Mol. Cell. Biol.,* 19**,** 3485.

Weichert, W., Boehm, M. & Gekeler, V. 2007. High expression of RelA/p65 is associated with activation of nuclear factor-kappaB-dependent signaling in

pancreatic cancer and marks a patient population with poor prognosis. *Br J Cancer,* 97**,** 523-530.

Weigelt, B., Peterse, J. L. & Veer, L. J. v. t. 2005. Breast Cancer Metastasis: Markers and Models. *Nat. Rev.,* 5**,** 591-602.

Westerheide, S. D., Mayo, M. W., Anest, V., Hanson, J. L. & Baldwin, A. S. 2001. The Putative Oncoprotein Bcl-3 Induces Cyclin D1 To Stimulate G1 Transition. *Mol. Cell. Biol.,* 21**,** 8428-8436.

Wu, J. T. & Kral, J. G. 2005. The NF-kB/IkB signaling system: A molecular target in breast cancer therapy. *J. Surg. Res.,* 123**,** 158-169.

Wulczyn, F. G., Naumann, M. & Scheidereit, C. 1992. Candidate proto-oncogene bcl-3 encodes a subunit-specific inhibitor of transcription factor NF-kappa B. *Nature,* 358**,** 597-599.

Yamaguchi, N., Ito, T., Azuma, S., Ito, E., Honma, R., Yanagisawa, Y., Nishikawa, A., Kawamura, M., Imai, J.-i., Watanabe, S., Semba, K. & Inoue, J.-i. 2009. Constitutive activation of nuclear factor-kappaB is preferentially involved in the proliferation of basal-like subtype breast cancer cell lines. *Cancer Sci,* 100**,** 1668-1674.

Yang, J., Pan, W., Clawson, G. & RIchmond, A. 2007. Systemic targeting inhibitor of kappaB kinase inhibits melanoma tumor growth. *Cancer Res,* 67**,** 3127-3134.

Yaswen, P. & Stampfer, M. R. 2002. Molecular changes accompanying senescence and immortalization of cultured human mammary epithelial cells. *Int. J. Biochem. Cell Biol.,* 34**,** 1382-1394.

Young, D. C. 2009. *Computational drug design*, A John Wiley & Sons.

Zhang, B., Cao, X., Liu3, Y., Cao, W., Zhang, F., Zhang, S., Li, H., Ning, L., Fu, L., Niu, Y., Niu, R., Sun, B. & Hao, X. 2008. Tumor-derived matrix metalloproteinase-13 (MMP-13) correlates with poor prognosis of invasive breast cancer. *BMC Cancer,* 8.

Zhang, Q., A.Didonato, J., Karin, M. & W.McKeithan, T. 1994. BCL3 encodes a nuclear protein which can alter the subcellular location of NF-kappa B proteins. *Mol. Cell. Biol.,* 14**,** 3915-3926.

Zhang, X., Wang, H., Claudio, E., Brown, K. & Siebenlist, U. 2007. A role for BCL-3 in control of central immunologic tolerance *Immunity,* 27**,** 438-452.

Zhou, Y., Eppenberger-Castori, S., Marx, C., Yau, C., Scott, G. K., Eppenberger, U. & Benz, C. C. 2005. Activation of nuclear factor-kB (NFkB) identifies a high-risk subset of hormone-dependent breast cancers. *Int. J. Biochem. Cell Biol.,* 37**,** 1130-1144.

Appendices

1. List of purchased and synthesised compounds

Purchased compounds	Name in thesis	SPECS Number
B3JS1	Compound 1	A0-022/43452477
B3JS2	Compound 2	AO-080/42479276
B3JS3	Compound 3	AG-205/37136062
B3JS4	Compound 4	AK-918/40864467
B3JS5	Compound 5	AH-487/40911940
B3JS6	Compound 6	AO-365/43402787
B3JS7	Compound 7	AO-080/42573748
B3JS8	Compound 8	AN-329/43197657
B3JS9	Compound 9	AN-329/40826196
B3JS10	Compound 10	AM-879/41237197

Synthesized compounds	Name in thesis	Name on tubes/ Analysis	Chemical name
B3JS6	15a	JS021	2-[(2-fluorobenzoyl)amino]-N-(2-morpholin-4-ylethyl)benzamide
B3JS11	15c	JS023	2-[(4-fluorobenzoyl)amino]-N-(2-morpholin-4-ylethyl)benzamide

B3JS12	15e	JS025	2-[(3-methoxybenzoyl)amino]-N-(2-morpholin-4-ylethyl)benzamide
B3JS13	15f	JS026	2-[(4-methoxybenzoyl)amino]-N-(2-morpholin-4-ylethyl)benzamide
B3JS14	15g	JS027	2-[(2-nitrobenzoyl)amino]-N-(2-morpholin-4-ylethyl)benzamide
B3JS15	15i	JS029	2-[(4-nitrobenzoyl)amino]-N-(2-morpholin-4-ylethyl)benzamide
B3JS16	15j	JS0210	2-[(2-methylbenzoyl)amino]-N-(2-morpholin-4-ylethyl)benzamide
B3JS17	15l	SV02	3,4-dimethoxy-*N*- (2-[(2-morpholin-4-ylethyl) carbamoyl] phenyl) benzamide
B3JS18	15m	SV04	3,5-dimethoxy-*N*- (2-[(2-morpholin-4-ylethyl) carbamoyl] phenyl) benzamide
B3JS19	15n	SV06	3,4,5-trimethoxy-*N*-(2-[(2-morpholin-4-ylethyl) carbamoyl] phenyl) benzamide
B3JS20	15o	SV14	3,5-difluoro -*N*- (2-[(2-morpholin-4-ylethyl) carbamoyl] phenyl) benzamide
B3JS21	15p	SV16	2,6-difluoro -*N*- (2-[(2-morpholin-4-ylethyl) carbamoyl] phenyl) benzamide
B3JS22	15q	SV17	2,4-difluoro -*N*- (2-[(2-morpholin-4-ylethyl) carbamoyl] phenyl) benzamide
B3JS23	17a	JS031	2-[(2-fluorobenzoyl)amino]-N-(2-morpholin-4-ylpropyl)benzamide
B3JS24	17b	JS032	2-[(4-fluorobenzoyl)amino]-N-(pyridin-3-ylmethyl)benzamide
B3JS25	17c	JS033	2-[(4-fluorobenzoyl)amino]-N-(pyrrolidin-3-ylmethyl)benzamide
B3JS26	17d	JS034	2-[(4-fluorobenzoyl)amino]-N-(piperidin-3-ylmethyl)benzamide
B3JS27	17f	JS036	*N*- (2-aminoethyl)-2-(2-fluorobenzamido) benzamide

B3JS28	20a	JS051	2-[(2-fluorobenzoyl)amino]-3-methoxy-N-(2-morpholin-4-ylethyl) benzamide
B3JS29	20b	JS052	2-[(2-fluorobenzoyl)amino]-3-methyl-N-(2-morpholin-4-ylethyl) benzamide
B3JS30	20d	JS053	2-[(2-fluorobenzoyl)amino]-2-chloro-N-(2-morpholin-4-ylethyl) benzamide